UNIVERSITY OF MESSINA

DEPARTMENT OF ENGINEERING

DOCTORAL COURSE IN "CHEMISTRY AND ENGINEERING OF MATERIALS AND CONSTRUCTIONS"

UNIVERSITY OF CÓRDOBA

DEPARTMENT OF ORGANIC CHEMISTRY

DOCTORAL COURSE IN "FINE CHEMISTRY"

XXXVI° CYCLE (SSD: CHIM/07)

Development of Innovative Technologies for the Synthesis of Materials for Sensing and Environmental Applications

Doctoral Thesis of:

Viviana Bressi

Supervisor and thesis director (UNIME):

Prof.ssa Claudia Espro

Co-supervisor (UNIME)

Dr.ssa Consuelo Celesti

Co-tutela thesis director (UCO):

Prof.ssa Alina Mariana Balu

Ph.D. Coordinator (UNIME):

Prof. Edoardo Proverbio

ACADEMIC YEAR: 2022-2023

UNIVERSIDAD DE CÓRDOBA

DEPARTAMENTO DE QUÍMICA ORGANICA

PROGRAMA DE DOCTORADO EN QUÍMICA FINA

Desarrollo de Tecnologías Innovadoras para la Síntesis de Materiales en Aplicaciones de Detección y Medio Ambiente

Development of Innovative Technologies for the Synthesis of Materials for Sensing and Environmental Applications

Tesis Doctoral:

Viviana Bressi

Directore Tesis (UCO):

Prof.a Alina Mariana Balu

Directore Tesis (UNIME):

Prof.a Claudia Espro

Responsable de la Línea de Investigación (UCO):

Prof. Antonio Angel Romero Reyes

Coordinador de Doctorado en Química Fina (UCO):

Prof. Pedro Lavela Cabello

Fecha de depósito en el Idep: 02/11/2023

Thesis Frameworks

Resumen and Abstract

These paragraphs provide a clear summary of the methods employed and the entire research work conducted.

Aim of the Thesis

This paragraph provides a brief overview of the main goals and interests that drove the development of this research project, providing an early grasp of the motivations that guided the investigations reported in the following chapters.

Chapter 1. Overview and Scientific Context

This chapter offers a comprehensive introduction to advanced materials derived from biomass conversion, along with an exploration of the synthesis techniques developed, and their potential fields of application. Additionally it delves into the insight of electrochemical sensors and electrochemical methodologies, along with adsorption processes of pollutants, as valid approaches for the environmental monitoring and mitigation.

Chapter 2. Materials and Methods

This chapter encompasses the materials employed within this thesis, focusing on the description of the raw materials, the procedural aspects of sample

preparation, and the characterization techniques deployed throughout this research endeavor. Furthermore, it offers a concise glimpse into the instrumentation utilized for electrochemical assessments.

Chapter 3. Experimental Endeavors, Outcomes, and Discussion

This chapter constitutes the focal point of this scientific work, wherein the adopted experimental approach and the attained results have been examined and discussed.

Concluding Remarks and Future Perspectives

This section summarizes the key results of the work, providing a synthesis of the main objectives achieved, highlighting the importance of the acquired results in the current context, and offering a view into possible future directions of research or development.

Other Activities

This space is dedicated to all the academic and formative activities carried out during the three years of the doctoral program.

Table of contents

3.3 Electrochemical Determination of Nitrites and Sulfites by Using Waste-derived Nanobiochar

3.4 On the Electroanalytical Detection of Zn Ions by a Novel Schiff Base Ligand-SPCE Sensor

3.5 Hydrochar from Sargassum Muticum: a Sustainable Approach for High-capacity Removal of Rhodamine B dye

Concluding Remarks and Future Perspectives

Other Activities

Resumen

Esta investigación doctoral se centra en la conversión integral de materiales de desecho y biomasas a través de enfoques sostenibles, generando materiales basados en carbono que exhiben propiedades ventajosas y capacidades cautivadoras para procesos catalíticos y detección de contaminantes ambientales. La progresión de la humanidad ha estado constantemente entrelazada con avances científicos y tecnológicos. Sin embargo, este camino ha ocurrido a lo largo de los siglos, a menudo en detrimento de los recursos de la Tierra, lo que ha llevado al cambio climático, la pérdida de biodiversidad, la depleción del ozono estratosférico, trastornos en los ciclos de nitrógeno y fósforo, acidificación oceánica, contaminación ambiental y la dispersión de gases peligrosos en la atmósfera. En los últimos años, la comunidad de investigación se ha percatado de esta dura realidad al alinearse con los 12 principios de la Química Verde y los 17 Objetivos de Desarrollo Sostenible (ODS) delineados en la agenda 2030 de las Naciones Unidas.

En este sentido, el objetivo de esta empresa de investigación fue aprovechar el potencial de las fuentes de biomasa, que podrían representar amenazas para los ecosistemas y, directa o indirectamente, para la seguridad humana. Esto se logró transformándolos en valiosos materiales carbonáceos mediante el desarrollo de procesos sencillos y respetuosos con el medio ambiente. Además, de acuerdo con los principios de la Química Verde, haciendo hincapié en la utilización de materias primas renovables y la reducción de residuos, junto con el compromiso de los ODS de mitigar los impactos del cambio climático y promover la vida acuática y el bienestar de sus habitantes, estos innovadores materiales verdes se utilizaron como adsorbentes para la eliminación de peligrosos contaminantes orgánicos, como soportes para procesos catalíticos y

como sistemas de detección selectiva y simultánea de iones de metales pesados. Estos avances han abierto las puertas a resultados prometedores, sugiriendo un avance significativo hacia el establecimiento de una comunidad científica totalmente sostenible.

Abstract

This doctoral research focuses on the comprehensive conversion of waste materials and biomasses through sustainable approaches, yielding carbon-based materials that exhibit advantageous properties and captivating capabilities for catalytic processes and detection of environmental pollutants. Humanity progression has consistently been intertwined with scientific and technological advancements. However, this route has occurred over the course of centuries, often at the detriment of the Earth's resources, leading to climate change, biodiversity loss, stratospheric ozone depletion, disorders in nitrogen and phosphorus cycles, ocean acidification, environmental pollution, and the dispersion of hazardous gases in the atmosphere. In recent years, the research community became aware of this harsh reality, by aligning itself with the 12 principles of Green Chemistry and the 17 Sustainable Development Goals (SDGs) outlined in the 2030 agenda by the United Nations.

On this account, the objective of this research endeavour was to harness the potential of biomass sources, which could pose threats to ecosystems and, directly or indirectly, to human safety. This was accomplished by transforming them into valuable carbonaceous materials through the development of straightforward and environmentally compatible processes. Moreover, according with Green Chemistry's principles, emphasizing the utilization of renewable raw materials and waste reduction, along with SDGs commitment to mitigating the impacts of climate change and promotion of aquatic life, and its inhabitants' well-being, these innovative green materials were harnessed as adsorbents for the removal of hazardous organic pollutants, as supports for catalytic processes and as selective and simultaneous sensor detection systems for heavy metal ions. These advancements have opened the doors to promising

outcomes, suggesting a significant stride towards establishing a fully sustainable scientific community.

Aim of the Thesis

This thesis summarizes and describes the research activities carried out through a collaborative effort undertaken between the Sensors Laboratory at the Department of Engineering of the University of Messina (Italy), and the FQM 383 research group at the Department of Organic Chemistry of the University of Córdoba (Spain).

The primary purpose of this work was to highlight the valorisation of waste and biomass, with the aim to enhance them into value-added materials applicable across several fields, including catalysis, adsorption and sensing. In recent years, numerous innovative waste management technologies have emerged, predominantly focused on converting organic waste into valuable resources. These high added value raw materials include essential oils, bioactive compounds, sustainable production of biogas, bioethanol, and other captivating chemicals such as furfural, pectins, lignin, cellulose, hemicellulose and acids (Reguengo *et al.*, 2022). Sustainable processes geared toward waste valorisation attend two main purposes: the extraction of bioactive materials and their utilization for synthesizing new products. Biomass conversion methods are commonly categorized into biochemical and thermochemical approaches (Awasthi *et al.*, 2023; Choudhary *et al.*, 2020). Biochemical methods harness chemical reactions facilitated by microorganisms acting directly on biomass to generate energy. Suitable biomass sources for biochemical conversion include urban wastewater and aquatic crops. In contrast, thermochemical methods employ heat to initiate chemical reactions, leading to the conversion of matter into energy. Lignocellulosic biomass is the preferred substrate for biomass conversion due to its inherent suitability. In the context of this PhD research, hydrothermal carbonization (HTC) was the central thermochemical method

employed for biomass conversion HTC consists in a thermochemical process conducted in an aqueous medium under comparatively mild conditions, in contrast to other treatments like pyrolysis or roasting. This approach holds great promise for waste valorisation, offering the distinct advantage of accommodating wet biomass, thereby mitigating a primary limitation of conventional thermochemical processes that necessitate dry feedstock.

The solid and liquid products generated through HTC of several biomass were extensively explored during this PhD research and subsequently transforming them into support for catalytic application or nanomaterials referred to as "carbon nanodots" (CDs or CNDs). CDs are novel materials lauded for their manifold properties, including nanoscale dimensions, outstanding photostability and water stability, biocompatibility, low cytotoxicity, fluorescence behaviour, and facile surface modification (Kurian and Paul, 2021). Waste biomass stands as an appealing candidate for the large-scale production of CDs, not only for its capacity to obtain these materials with exceptional properties but also for its alignment with the principles of waste management, circular economy, and Green Chemistry (Bressi *et al.*, 2023). This convergence presents an environmentally friendly solution to address waste-related challenges while advancing the pursuit of sustainability goals.

In this environmentally conscious scenario, the synthesized materials have been employed as electrochemical and fluorescent sensors for the detection of heavy metals and environmentally harmful organic molecules in water. Heavy metal ions are elements known for their potential to induce ecological harm and pose direct or indirect risks to human health even in traces. Additionally, due to their non-biodegradable nature, they accumulate in soil and water, thereby becoming significant factors in the development of severe health conditions, including but not limited to cancers, infections, and neurodegenerative diseases. The risk of toxicity increases for heavy metals like Cadmium, Lead, and Mercury, which

can exert detrimental effects even when present in low concentrations (Maftouh *et al.*, 2023). Closely associated with these inorganic compounds, various organic molecules, such as dyes or explosives, frequently contaminate water sources, primarily due to inadequate disposal practices by industries involved in their production or usage (Akram *et al.*, 2023). Given their high persistence and potential harm to both human health and the environment, these molecules are often chosen as model contaminants in studies related to wastewater treatment.

The overarching goal of this research was to develop a rapid and selective detection system of detecting and/or removing environmental pollutants. For this objective, electrochemical sensors, specifically commercial screen-printed sensors (SPCEs), were subjected to modification through drop-casting advanced materials, aimed at enhancing the electrochemical performance of the commercial carbon electrode. This was achieved by employing various voltammetric techniques, which yielded noteworthy results in the detection of organic molecules and heavy metal ions.

References

Akram, M.; Bhutto, S.U.A.; Aftab, S.; Sindhu, L.; Xu, X.; Haider, Z. Nanocomposites for Removal and Degradation of Organic Pollutants, in: Malik, J.A., Sadiq Mohamed, M.J. (Eds.), Modern Nanotechnology: Volume 1: *Environmental Sustainability and Remediation*. Springer International Publishing, **2023**, 519–558. https://doi.org/10.1007/978-3-031-31111-6_21

Awasthi, M.K.; Sar, T.; Gowd, S.C.; Rajendran, K.; Kumar, V.; Sarsaiya, S., Li, Y.; Sindhu, R.; Binod, P.; Zhang, Z.; Pandey, A.; Taherzadeh, M.J. A comprehensive review on thermochemical, and biochemical conversion methods of lignocellulosic biomass into valuable end product. *Fuel*, **2023**, 342, 127790. https://doi.org/10.1016/j.fuel.2023.127790

Bressi, V.; Balu, A.M.; Iannazzo, D.; Espro, C. Recent advances in the synthesis of carbon dots from renewable biomass by high-efficient hydrothermal and microwave green approaches. *Current Opinion in Green and Sustainable Chemistry*, **2023**, 40, 100742. https://doi.org/10.1016/j.cogsc.2022.100742

Choudhary, P.; Assemany, P.P.; Naaz, F.; Bhattacharya, A.; Castro, J. de S.; Couto, E. de A. do C.; Calijuri, M.L.; Pant, K.K.; Malik, A. A review of biochemical and thermochemical energy conversion routes of wastewater grown algal biomass. *Science of the Total Environment*, **2020**, 726, 137961. https://doi.org/10.1016/j.scitotenv.2020.137961

Fang, J.; Zhan, L.; Ok, Y.S.; Gao, B. Minireview of potential applications of hydrochar derived from hydrothermal carbonization of biomass. *Journal of Industrial and Engineering Chemistry*, **2018**, 57, 15–21. https://doi.org/10.1016/j.jiec.2017.08.026

Kurian, M.; Paul, A. Recent trends in the use of green sources for carbon dot synthesis–A short review. *Carbon Trends*, **2021**, 3, 100032. https://doi.org/10.1016/j.cartre.2021.100032

Maftouh, A.; El Fatni, O.; El Hajjaji, S.; Jawish, W.; Sillanpää, M. Comparative Review of Different Adsorption Techniques Used in Heavy Metals Removal in Water.

Biointerface Research in Applied Chemistry, **2023**, 13, 397. https://doi.org/10.33263/BRIAC134.397

Reguengo, L.M.; Salgaço, M.K.; Sivieri, K.; Maróstica Júnior, M.R. Agro-industrial by-products: Valuable sources of bioactive compounds. *Food Research International*, **2023**, 152, 110871. https://doi.org/10.1016/j.foodres.2021.110871

Satira, A.; Paone, E.; Bressi, V.; Iannazzo, D.; Marra, F.; Calabrò, P.S.; Mauriello, F.; Espro, C. Hydrothermal Carbonization as Sustainable Process for the Complete Upgrading of Orange Peel Waste into Value-Added Chemicals and Bio-Carbon Materials. *Applied Sciences*, **2021**, 11, 10983. https://doi.org/10.3390/app112210983

Chapter 1. Overview and Scientific Context

1.1 Exploring the Biomass Universe

The term "biomass" is referred to "the biodegradable fraction of products, waste, and residues originating from agriculture (including both plant and animal materials), forestry, and associated sectors such as fisheries and aquaculture, along with the biodegradable component of industrial and municipal waste" (Schnepf, 2010). Thus, biomass refers to a wide range of materials with variable compositions that can exist in the three different physical states (solid, liquid, and gaseous). Therefore, it can be defined as any organic substance of animal or plant origin that has not been fossilized and from which energy can be extracted. In general, biomass can be categorized into three categories:

- Phytomass: also called "vegetal biomasses" or "biomasses of plant origin" are the most used. They originate from agricultural waste, gardening activities, and forest maintenance. This category also includes certain plant species cultivated specifically to provide suitable materials for energy production. Examples of plant biomasses include wood, fruit pomace, fruit cores, nutshells, fruits, and vegetable peels.

- Animal Biomass: animal biomasses result from the breeding of herbivorous animals. The most frequently utilized type is manure, which contains all the gases and chemical energy produced from the grass consumed and digested by the animals. Animal biomass also encompasses materials derived from animal carcasses, although this practice is often considered controversial.

- Microbial Biomass: is obtained from soil and relies on the elements present within the soil, such as sulfur and nitrogen, as well as fungi, bacteria, and other microorganisms. Additionally, any soil where plants grow and decompose, and where animals and their waste also decompose, contains various nutrients that can serve as potential sources of energy.

Biomass offers versatility in its applications: it can be harnessed to generate thermal energy, electricity, and biofuels, as well as produce high-value by-products and bio-based chemicals. Regardless of the group they belong to, biomass represents a *carbon-neutral* sustainable source of renewable energy (Hussin *et al.*, 2023). Carbon neutrality, also known as zero emissions, involves achieving a balance between emissions and carbon absorption, which is crucial for monitoring climate change phenomena, including rising sea levels, ocean acidification, and loss of biodiversity (Wernberg *et al.*, 2024). This balance is achieved because the carbon released during biomass combustion was initially absorbed by plants during their growth. This cyclic process, known as the "carbon cycle", can contribute to mitigating the greenhouse effect. Thus, in conjunction with the 17 sustainability goals ('THE 17 GOALS | Sustainable Development', 2023), aimed at protecting the environment, the principles of

Green Chemistry focused on using renewable raw materials and reducing waste (‘Green Chemistry’, 2023), and the European Green Deal aimed to make Europe climate-neutral by 2050 (‘Green Deal europeo: la chiave per un’UE sostenibile e climaticamente neutrale’, 2020), biomass emerges as an ideal candidate for a renewable energy source. Consequently, biomass is a more sustainable energy source compared to exhaustible fossil fuels (Adeoye *et al.* 2023). Nevertheless, it is important a responsible management of biomass resources to prevent adverse environmental impacts, including deforestation and competition with food production.

1.1.1 Biomass Conversion: Current Insights

Italy’s total energy supply (TES) is still predominantly composed of fossil fuels, accounting for approximately 80%. Among these, gas and oil reach up 41% and 34% of the total energy supply, respectively, while coal contributes approximately 4% to TES (as of 2021 data), (‘IEA Bioenergy Countries’ Report – Update 2021 | Bioenergy’, 2021). In 2022, the quantity of renewable energy generated from biomass and waste reached 17.5 terawatt hours, constituting approximately 18% of the total gross electricity production from renewable sources in Italy, where bioenergy represents around 50% of the renewable energy supply, with solid biomass accounting for two-thirds of bioenergy usage, and solid biomass is primarily employed in residential applications for heating purposes (‘Italy: biomass & waste energy production 2011-2022’). As previously mentioned, biomass is considered a renewable energy source because plants and organisms can grow and regenerate over time, in contrast to fossil resources like oil and coal, which are finite and non-renewable. In fact, it has been estimated that the world's oil reserves may be adequate to sustain energy supplies and chemical production for the next 40 years (‘Statistical Review of World Energy | Energy Economics’, 2020).

Hence, the need to enhance biomass consumption and conversion becomes clear. Biomass can be harnessed for energy production through three main routes: direct production of biofuels, generation of electrical and thermal energy, and the conversion/extraction of high-value-added *chemicals* and bio-products. Methods for converting biomass can be broadly categorized into two groups: biochemical processes and thermochemical processes. Biochemical processes enable the extraction of energy through chemical reactions facilitated by microorganisms that directly act on the biomass. Biomass suitable for biochemical conversion includes urban wastewater and aquatic crops, and the processes involved are alcoholic fermentation, aerobic digestion, and anaerobic digestion. Thermochemical processes, on the other hand, rely on the application of heat to initiate the chemical reactions necessary for converting biomass into high-value materials and energy. Lignocellulosic biomass is particularly well-suited for these methods, accounting for approximately 70% of primary energy sources in 2019 (**Figure 1.1**, ('Renewable Energy Statistics',2019).

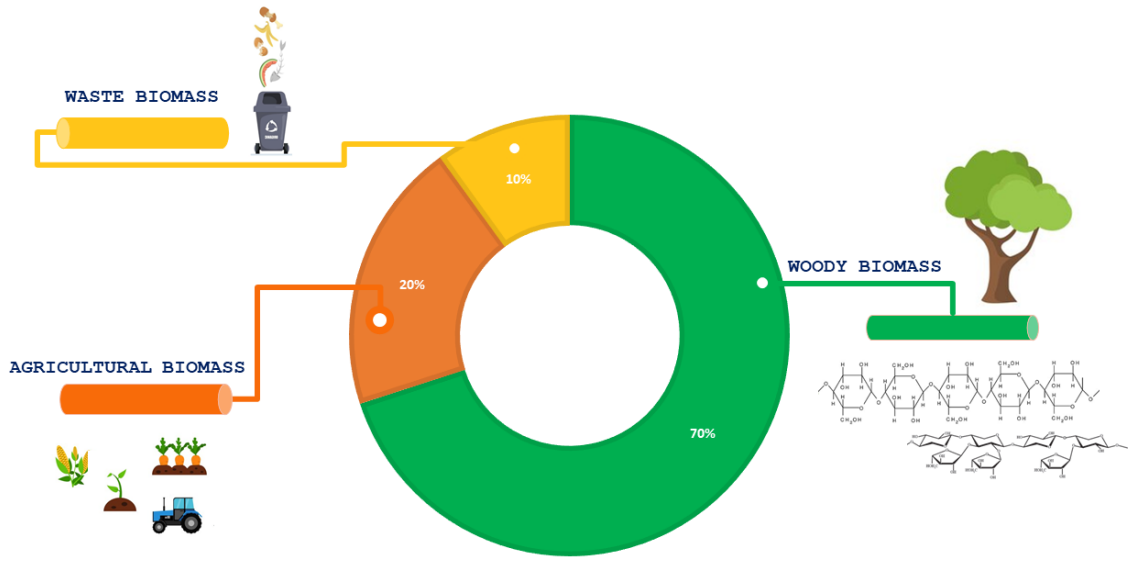

Figure 1.1. ***Distribution of the different biomass feedstock for energy in 2019 (****(Futura n.d.)****), source Eurostat and Bioenergy Europe's estimates***

The methods employed in thermochemical conversion include gasification, combustion, pyrolysis, and hydrothermal treatment (Adams *et al.*, 2018; Len *et al.*, 2022). Compared to biochemical processes, thermochemical processes offer several advantages, including greater flexibility in the types of biomass that can be treated, higher energy density, reducing production costs by eliminating the need for specific enzymes and are adaptable for large-scale applications (Sharma *et al.*, 2014). Moreover, operating at high temperatures can enhance reactivity and the speed of chemical reactions.

1.1.2 Hydrothermal Carbonization Process

Among thermochemical conversion methods, Hydrothermal Carbonization (HTC) is gaining considerable traction. HTC represents a promising green technology with several advantages over other biomass conversion processes, such as pyrolysis and gasification. These advantages include milder conditions (shorter reaction times and lower temperatures), the possibility of recovering all products (in both solid, liquid, and gaseous phases), and the utilization of raw materials with high moisture content without the need for pre-treatment (Masoumi and Dalai, 2020). This thermochemical process converts wet biomass, sewage sludge, organic waste, and crops into high-value materials operating at relatively moderate temperatures, in water media, within an anaerobic and pressure-controlled environment (Pauline and Joseph, 2020; Shen, 2020) (**Figure 1.2**).The process begins with prepared biomass being introduced into a dedicated reactor. In this controlled environment, water is added to create a moist mixture, and temperature and pressure settings are selected based on the desired end product (for example, higher temperatures, and longer reaction time favour complete conversion of the biomass into hydrochar and high heating rates control the heat mass transfer (Tasca *et al.*, 2019). The combination of high temperature, water, and anaerobic conditions

enhances biomass degradation throughout the process by passing numerous chemical events such as hydrolysis, polymerization, aromatization, and dehydration (Fang *et al.*, 2018). If the chemicals formed during the reactions are highly reactive, they can undergo recondensation: lignin fragments and polymers undergoing cellulose degradation are examples of substances with high reactivity and the ability to easily recondense (Fang *et al.*, 2018). At the conclusion of the process, three main products are obtained:

- solid product: this solid material is called hydrochar and it can be recovered and used for various purposes, such as energy production (Burguete *et al.* 2016), pollutants adsorbents (Spagnuolo *et al.*, 2023), catalyst support (Masoumi and Dalai, 2020), soil amendement or fertiliser (Antero *et al.*, 2020), and for sensing applications (Espro *et al.*, 2021; Ferlazzo *et al.*, 2023);
- liquid product: the liquid fraction is constituted byseveral substances dissolved, such as sugars, and a bio-oil undissolved fraction, rich in bio-components derived from the starting biomass (such as levulinic acid, furfural, xylose, lignin etc.), whichcan be extracted and reutilised (Satira *et al.*, 2021; Singh *et al.*, 2019; Usman *et al.*, 2019);
- gaseous product: this bio-gas, mainly composed of CO_2, can be used as a heat source, for energy purposes (Picone *et al.*, 2021), or converted into bio-methane (Pagés-Díaz and Huiliñir, 2020).

The products distribution is contingent on process conditions and the type of feedstock employed (Satira *et al.*, 2021). As a general trend, the hydrochar typically retains 50-80% of the initial biomass, while the aqueous phase, containing both inorganic and organic components, accounts for 5-20%. The gas-phase, typically represents 2-5% (Fang *et al.*, 2018).

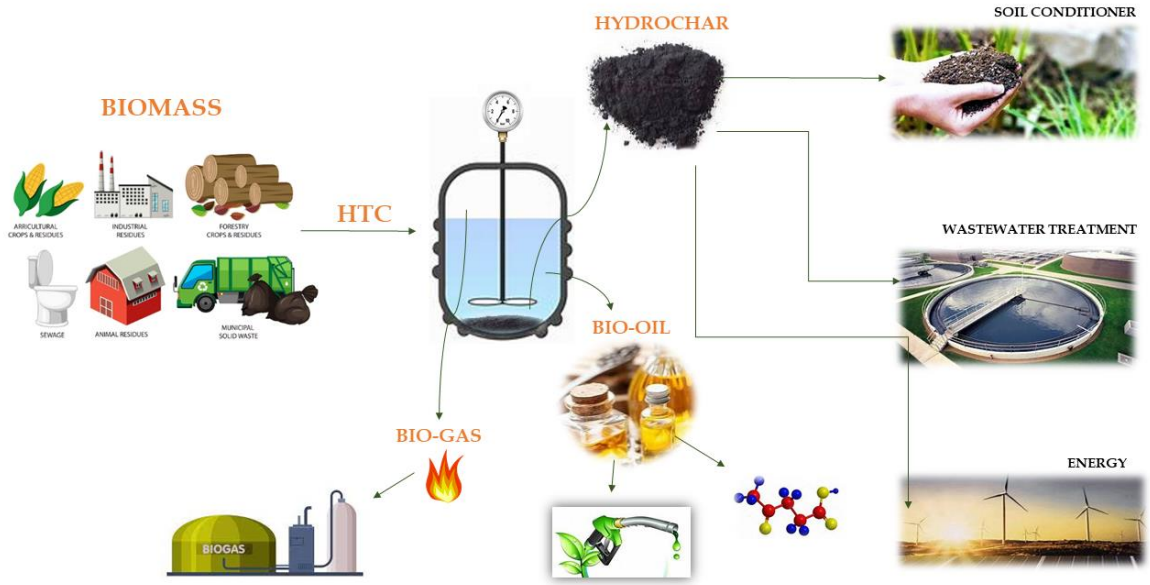

Figure 1.2. ***Schematic HTC process and products***

In summary, hydrothermal conversion is an environmentally friendly technology for transforming wet biomass and organic waste into valuable materials. Its advantages include its adaptability to high-moisture feedstocks, moderate operating temperatures, and the ability to recover various useful products, making it a promising method in the transition to more sustainable and resource-efficient energy and material production processes.

1.2 Nanomaterials derived from Biomass and Their Application in Environmental Mitigation Techniques

Carbonaceous nanomaterials are compounds with a high carbon content, a large surface area, and particles with nanoscale size (Liu *et al.*, 2018). Nano-hydrochars and nano-biochars are specifically engineered from thermo-chemically converted biomass to overcome constraints in the starting materials (biochar or hydrochar), such as poor surface area and low absorption potential (Ferlazzo *et al.*, 2023). Due to their increased surface area, abundant functional groups, enhanced microporosity, and surface hydrophobicity, nano-carbon particles exhibit superior mechanical and thermal stability (Ramanayaka *et al.*, 2020). Moreover, the presence of carbon edge defects within these functional groups ensures that the material's surface possesses a substantial number of unpaired π electrons (Ferlazzo *et al.*, 2023). These electrons play a pivotal role in accelerating electron transfer and catalytic activity in redox processes, influencing the final properties of the material and their application for a wide range of fields.

Since the discovery of fullerenes in the 1980s ("C60: Buckminsterfullerene| Nature", 1980), carbon-related materials research and engineering have gained significant attention. Carbon nanomaterials have recently emerged as highly promising candidates for a wide range of applications across several fields, owing to their captivating properties. These properties include exceptional photostability and biocompatibility, low cytotoxicity, compact size, fluorescence, and ease of surface modification (Bressi *et al.*, 2023; Zhang *et al.*, 2019). Consequently, in recent years, they have gained traction as an appealing option for environmentally sustainable applications, including the development of functional components in electrochemical sensors, and are currently under active consideration as "nanoprobes" for utilization in

electrochemical biosensing applications (Ng *et al.*, 2019; Kumar *et al.*, 2023). Moreover, carbon nanomaterials are particularly intriguing due to their ability to exhibit various hybridization states of elemental carbon (Cui *et al.*, 2021), such as sp, sp^2, sp^3 and sp^2/sp^3. These remarkable properties led to L. Brus (Rossetti *et al.*, 1983), M. Bawendi (Bawendi *et al.*, 1989), and A. Ekimov (Ekimov, 1996) being awarded the Nobel Prize in Chemistry for their discovery of quantum dots, nanoscale materials that are revolutionating contemporary scientific research.

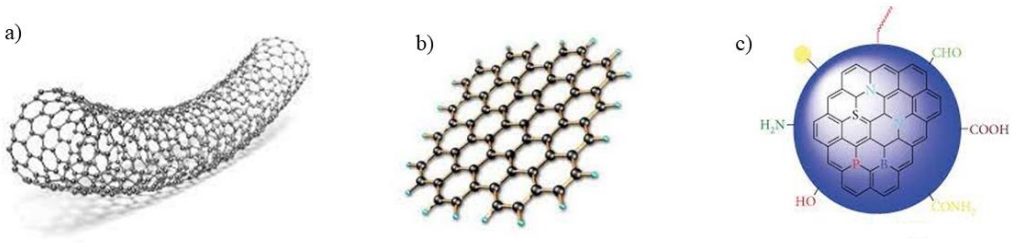

Figure 1.3. ***a) Carbon nanotubes*** *('Looking to the Future of Carbon Nanotube Transistors' 2023)*, ***b) graphene quantum dots*** *('Graphene Quantum Dots: Introduction and Market News | Graphene-Info', 2023)*, ***c) carbon nanodots*** *(Gayen, Palchoudhury, and Chowdhury 2019)*

The diverse morphologies of carbon nanomaterials, encompass carbon nanotubes (CNTs), graphene quantum dots (GQDs), carbon nanodots or carbon quantum dots (CNDs or CDs), and other carbon-based composite nanomaterials (**Figure 1.3**). The concept of CNTs initially emerged from the intersection of traditional carbon fibers and the innovative fullerene. CNTs are acknowledged as the most robust carbon fibers, distinguished by their extraordinary cylindrical structures composed of tightly coiled layers of graphene, which can either be single-walled (SWCNT) or multi-walled (MWCNT) (Zhang *et al.*, 2023). Their distinctive crystalline arrangement and exceptional electrical conductivity render them pivotal materials for applications in nanotechnology, advanced electronic devices, and engineered

composites. CNTs can exhibit either semiconductor or metallic properties, a versatility that underscores their fundamental role in numerous realms of research and technological advancement. Despite their intriguing properties, CNTs are less frequently employed in sensor applications compared to other carbon-based nanomaterials (Zhou *et al.*, 2022). This is primarily due to the complexity of their synthesis and functionalization, especially when aiming to produce CNTs with precise length and diameter specifications. Additionally, the variability in CNTs properties poses challenges for standardization in specific sensor applications. Furthermore, their relatively larger dimensions can be a drawback in terms of biocompatibility, particularly in comparison to smaller nanomaterials. The fundamental building block of carbon nanotubes is graphene, a two-dimensional layer material composed of carbon atoms arranged in hexagonal cells (Gerstner, 2010). Within the realm of graphene-derived nanomaterials, there exists a category known as Graphene Quantum Dots (GQDs). GQDs are disk of graphene that exhibit dimensions in the range of 2-20 nm and inherit their distinctive properties from both graphene and carbon dots. GQDs primarily consist of carbon atoms that are predominantly bonded in a sp^2 hybridized conFiguretion. These nanostructures exhibit a crystalline nature and display fluorescence as a result of quantum confinement of conjugated π-domains, the presence of surface defects, and the existence of zigzag edges (Zhu *et al.*, 2017). Their nanoscale dimensions, along with precisely defined edges, confer upon them unique optical, electronic, and chemical characteristics, making them invaluable in applications such as optoelectronic devices, advanced sensors, solar cells, and high-precision imaging (Bressi *et al.*, 2021; de Menezes *et al.*, 2019). GQDs are particularly noteworthy for their high surface area, abundant functional groups, and the ease of functionalization with organic, inorganic, or biological molecules (Zhou *et al.*, 2022; Barati *et al.*, 2023), leading to their utilization as electrode modifiers in electrochemical sensing (Bressi *et al.*, 2021). Additionally, GQDs boast

qualities of chemical stability, water solubility, robustness, inertness, and resistance to phenomena such as blinking and photobleaching (Wang *et al.*, 2016). Their water solubility has influenced their application in the fields of bio-imaging and targeted drug delivery (Kumar *et al.*, 2023; Mansuriya and Altintas, 2019; de Menezes *et al.*, 2019; Mehta *et al.*, 2017; Demirci *et al.*, 2020). GQDs serve as excellent sensing materials due to their high-mobility electrons, characterized by a rapid reaction rate, making them well-suited for sensing applications (Bressi *et al.*, 2021). Similarly, CNDs have intriguing features due to their nanoscale dimensions and well-defined architectures. Few materials have received as much attention as carbon nanodots, commonly regarded as the ultimate nanomaterial. Since their discovery in 2006 (Xu *et al.*, 2004), CNDs have collected an incredible amount of research, earning them a place of distinction in the scientific community (Banger *et al.*, 2023). Carbon nanodots, occasionally referred to as carbon quantum dots when describing the smallest particles, constitute a captivating group of carbon-based nanomaterials characterized by their spherical and polyhedral shapes, with dimensions typically less than 10 nm (Cui *et al.*, 2021; Bressi *et al.*, 2023), which were initially stumbled upon as contaminants during the production of single-walled carbon nanotubes performed by Xu et al (Xu *et al.*, 2004). Subsequently, Sun *et al.* identified and characterized these intriguing nanocarbons structures (Sun *et al.*, 2006). They are composed of sp^2/sp^3 hybridized carbon with a core-shell conFiguretion, usually amorphous and they can show in XRD the (100) plane of the basal planar of graphite (Mintz *et al.*, 2021). Because of their amorphous or semi-crystalline form, they are especially well-suited for a wide range of applications (Banger *et al.*, 2023; Kainth *et al.*, 2023). CNDs have become crucial tools in domains such as biomedical imaging (Kumar *et al.*, 2023), improved sensor technology (Yongli Liu *et al.*, 2016), and catalysis due to their customizable photoluminescent characteristics, biocompatibility, and variable surface chemistry.

1.2.1 Graphene Quantum Dots (GQDs) and Carbon Nanodots (CNDs)

One of the primary challenges on carbon-based nanomaterials development concerns their synthetic processes and the selection of precursor materials (Bressi *et al.*, 2023). . Depending on the raw materials used and the synthesis route, the resulting product will exhibit varying characteristics that influence its applicability. Moreover, the ability to ensure large-scale production hinges on the chosen synthetic process. Synthesis methods for both CNDs and GQDs are typically categorized into two groups, each based on the underlying reaction mechanism: *top-down* and *bottom-up* approaches (**Figure 1.4**). Following this step, the end product can undergo treatment processes such as electrophoresis, chromatography, centrifugation, dialysis, or other techniques to attain uniformity and eliminate any impurities (Banger *et al.*, 2023). The *top-down* approach involves the exfoliation and cutting of macroscopic carbon structures. In the case of GQDs, these structures encompass graphite powder, graphene sheets, (Lee *et al.*, 2023; Chen *et al.*, 2013) and CNTs, whereas for CNDs, they primarily consist of carbon black, coke, activated carbon, and carbon fibers (Banger *et al.*, 2023; Bressi *et al.*, 2023). As *top-down* processes entail the breakdown of macromolecules through chemical and physical forces, the primary reaction mechanism employed is oxidative cleavage. Additional *top-down* methodologies encompass electrochemical oxidation, chemical scission, and laser ablation (Bressi *et al.*, 2021). Top-down approaches are intricate processes that demand longer durations but offer the advantage of producing products with controllable dimensions and morphology (Cui *et al.*, 2021). Conversely, the *bottom-up* strategy utilizes small molecules as starting materials for nanomaterial production (Michenzi *et al.*, 2023). This approach relies on controlled synthesis techniques, including hydrothermal methods, microwave-assisted synthesis, and pyrolysis using organic molecules or

polymers as starting material. Polycyclic aromatic hydrocarbon molecules typically serve as dependable precursors for high-quality GQDs (Ding *et al.*, 2018), while organic molecules act as the precursors for CNDs. While a wide range of molecular precursors are accessible for bottom-up synthesis, non-toxic precursors are preferred to ensure that all synthetic products are biocompatible.

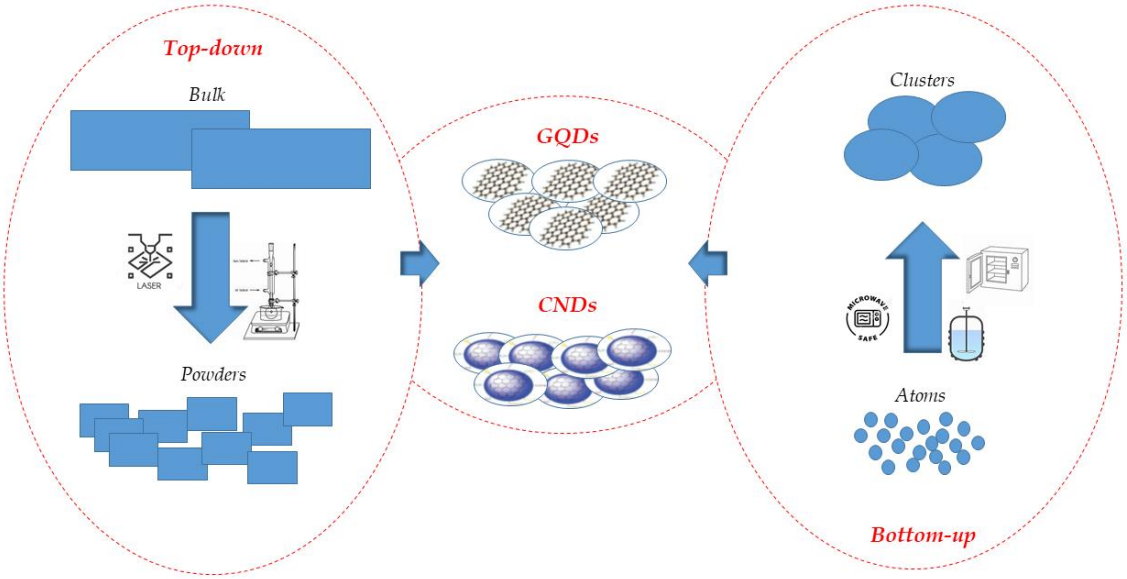

Figure 1.4. ***Top-down and bottom-up approaches for the synthesis of GQDs and CNDs***

However, a significant drawback associated with both top-down and bottom-up methods lies in the utilization of expensive, non-renewable raw materials such as petroleum coke, graphene oxide, coal or other graphene-based precursors (Zhou *et al.*, 2022) needing the use of toxic chemicals and strong acid treatments to fragment the robust and well-ordered structure into smaller carbon nanomaterials (Cui *et al.*, 2021). Additionally, high-pressure and high-temperature equipment are required, contributing to limited production scalability and lower yields (Bressi *et al.*, 2021). In response to these challenges, the adoption of green synthetic pathways is emerging as a promising area within the field of nanotechnology, offering economic and

environmental advantages as an alternative to conventional methods (Bressi *et al.*, 2023). Moreover, the utilization of eco-sustainable sources to produce high-quality carbon nanomaterials is an imperative concern. Renewable biomass, particularly waste biomass, stands out as a favourable option for large-scale nanomaterial synthesis (Zhou *et al.*, 2022). This approach not only enhances the material's exceptional properties but also offers a green solution that aligns waste management goals with the principles of a circular economy. The choice of biomass as the starting material is influenced by several factors, including local accessibility, sustainability, the chemical composition of the biomass itself, and the specific goals of the synthesis. Commonly utilized biomasses for carbon nanomaterial synthesis encompass agricultural waste, lignin-rich derivatives, coffee grounds, fruit waste, algae, and organic waste (Bressi *et al.*, 2023; Shivalkar *et al.*, 2021; Suresh *et al.*, 2023; Wang *et al.*, 2016). These materials contain a substantial carbon content and are converted into carbon nanomaterials through *bottom-up* processes such as pyrolysis, ultrasonication, microwave irradiation, or hydrothermal carbonizations (**Figure 1.5**). In some cases, it may be necessary to employ an integration of synthesis techniques to achieve the desired final characteristics, especially in terms of size. The choice of method hinges on the type of biomass being used: for instance, if dealing with a high-moisture biomass like fruit peels, a hydrothermal or microwave process might be more suitable than direct pyrolysis (Ababneh and Hameed, 2021; Tu *et al.*, 2021).

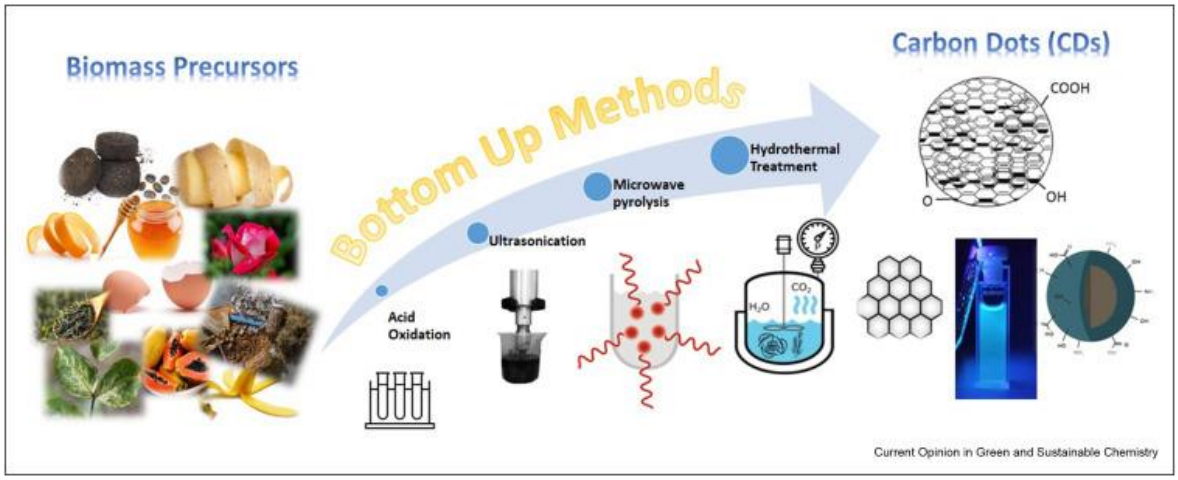

Figure 1.2. ***Synthesis of Carbon Dots via bottom-up approaches from biomass precursors***
(Bressi, Balu, et al. 2023)

Additionally, many biomasses possess intriguing chemical properties owing to their components. Therefore, when aiming to preserve the stability of these compounds, it is advisable to opt for mild processes conditions that do not degrade these constituents (Abid *et al.*, 2022). The biomass derived-carbon nanomaterials synthesis process involves a series of sequential reactions, constituting a multistep reaction mechanism (as depicted in **Figure 1.6**). Initially, condensation reactions take place, leading to the transformation of small molecules into polymeric intermediates. Subsequently, during the second phase, these intermediates undergo aggregation through the formation of both covalent and electrostatic bonds. Following this step, the polymers undergo carbonization resulting in the formation of carbon nanoparticles (Bressi *et al.*, 2023).

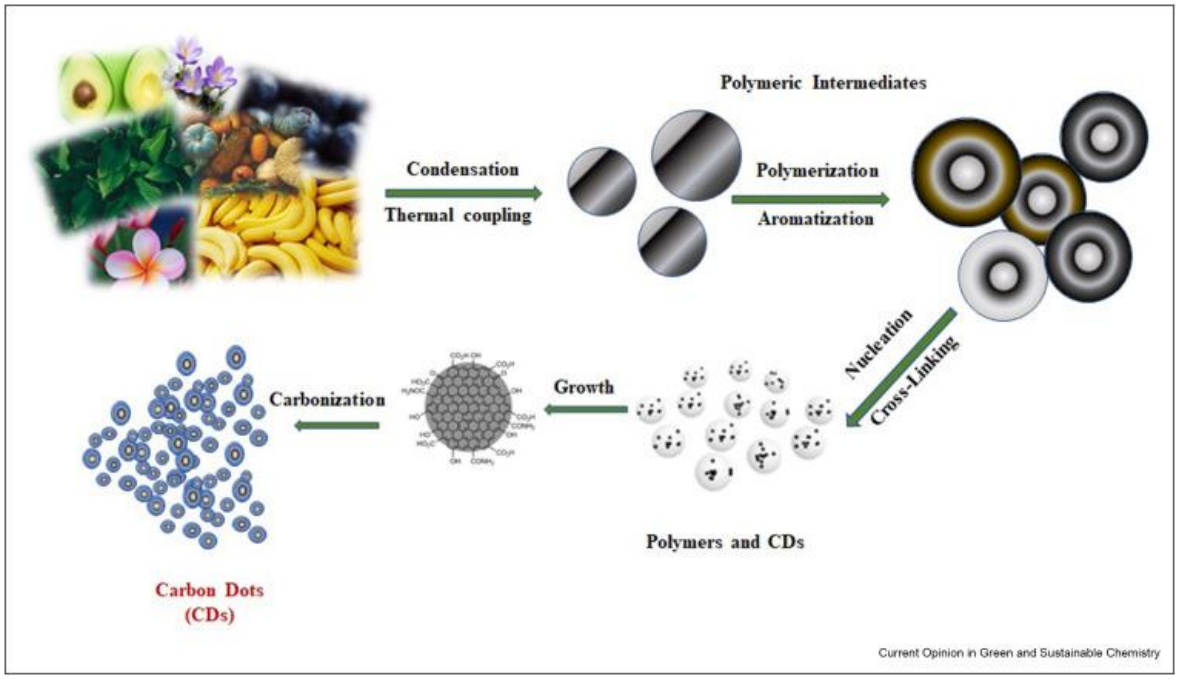

Figure 1.3. ***Formation Mechanism of Carbon Dots from Biomass Precursors during Bottom-up treatments***

If necessary, the surfaces of the nanomaterials can be further functionalized by using various surface passivating agents to enhance their properties (Tejwan *et al.*, 2021). In certain instances, natural sources containing Nitrogen and Sulfur can yield self-doped carbon dots or graphene quantum dots with N and S elements, exhibiting notably higher quantum yield (QY) when compared to undoped nanomaterials (Yinghui Liu *et al.*, 2020; Shuting Yang *et al.*, 2018). It is worth noting, however, that doping with additional elements is not always necessary, given that many components of biomass and thus related carbon nanomaterials contain functional groups such as carboxyl, amine, and hydroxyl, which are sufficient to establish interactions with ions or other molecules. On the contrary, doping can be strategically employed to enhance optical characteristics, such as fluorescence or magnetic properties (Li *et al.*, 2022). One way, for example, includes doping the CNDs with transition metal ions, which changes the band gap of the CNDs and provides new energy levels, ensuring their usage for photocatalytic purposes (Liu *et al.*, 2022).

1.2.2 Field of application of GQD and CNDs

As highlighted in the previous paragraph, carbon-based nanomaterials have received significant attention in scientific research and many technological applications due to their exceptional versatility and adaptability across a wide range of sectors, reaching from medicine and photocatalysis to electronics and bioimaging, have been investigated during recent years (**Figure 1.7**).

Figure 1.4. ***Initial Biomass Sources for Carbon Quantum Dot Synthesis and Potential Application Fields*** *(Wu et al. 2023)*

Due to their biocompatibility and low cytotoxicity, GQDs are emerging as drug carriers with applications in targeted drug delivery for anti-cancer therapy (Iannazzo *et al.*, 2019). Recently, biomass derived-CDs were used as carriers for the anticancer medication lycopodium, which targets hepatocyte cancer cells (Shao *et al.*, 2020). The loading of lycopodium onto carbon quantum dots is enabled by the creation of hydrogen bonds between functional groups on the CDs' surface, leading to accelerated endocytosis and enhanced uptake of the drug-loaded particles into cancer cells, ultimately boosting the overall efficacy of the anticancer treatment (Wu *et al.*, 2023). Notably, the survival of cancer cells exposed to lycopodium/CDs decreased significantly, showing the strong anticancer potential of these specific carbon quantum dots (Shao *et al.*, 2020). The pressing need to develop clean and sustainable energy sources has led to the use of nanomaterials derived from biomass in sustainable energy development. In 2020, Achilleos *et al.* (Achilleos *et al.*, 2020) conducted a study employing carbon quantum dots derived from lignin waste as photocatalytic agents for hydrogen production from sea and river water. This photocatalytic system, built for ecologically friendly hydrogen production, has proven to be extremely efficient for pollutant oxidation without the use of external electron donors. Carbon nanodots, owing to their good electrical conductivity, have also been extensively investigated for their potential as supercapacitors. Recently, Xu *et al.* (Xu *et al.*, 2021) utilized biomass-based carbon/graphene composite aerogels as electrode materials for supercapacitors, showing excellent cyclic stability and favourable conductivity-a promising prospect for energy storage applications.

Despite the captivating results achieved in medicine and energy fields, one of the most significant domains in which carbon nanomaterials are gaining importance is environmental and sensor applications for pollutant detection

(**Figure 1.8**). Within the environmental context, the properties of GQDs and CNDs, including their high specific surface area, sensitivity to chemical variations, and ease of surface functionalization, enable precise detection of a wide range of pollutants such as heavy metals, air pollutants, volatile organic compounds, and contaminants in water and soil. Such nanodots can be effectively integrated into advanced sensor devices that offer rapid and dependable responses, thus enhancing environmental monitoring and safeguarding human health.

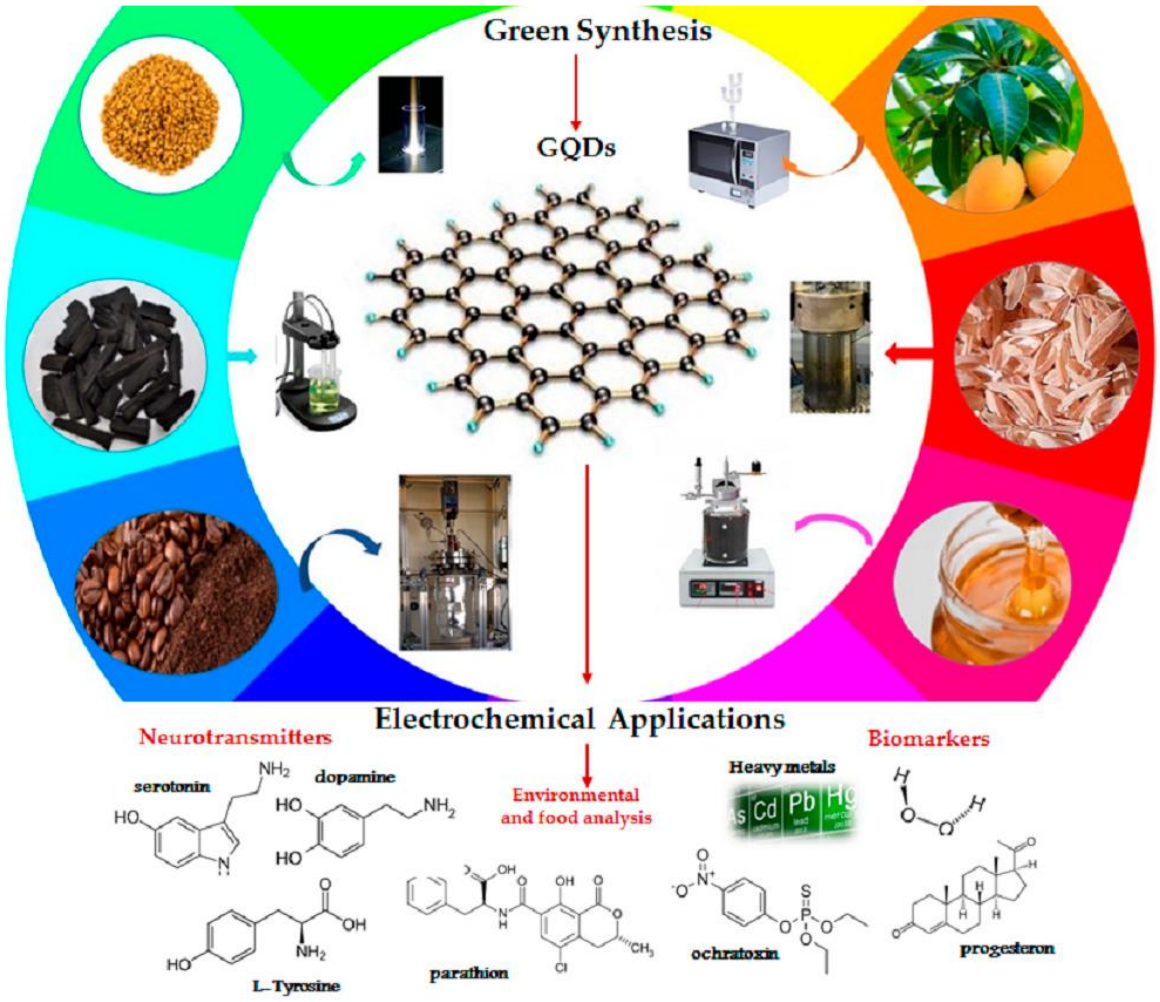

Figure 1.5. ***Green synthesis routes of GQDs and their applications in electrochemical sensing***
(Bressi et al. 2021)

Furthermore, GQDs and carbon quantum dots, characterized by their high photoluminescent properties, have been employed as real-time fluorescent probes for detecting several analytes (Abbas *et al.*, 2023; G. Li *et al.*, 2023; Mansuriya and Altintas, 2019). Photoluminescence emission behaviour differs between GQDs and CDs (**Figure 1.9**). Photoluminescence in GQDs is principally caused by the transition between the Highest Occupied Molecular Orbital (HOMO) and Lowest Unoccupied Molecular Orbital (LUMO) energy levels. Upon excitation of GQDs by an energy source, such as UV light, electrons residing in the HOMO band experience promotion to higher-energy LUMO bands, thereby generating an "excited" electron/electron pair. Subsequently, during the release of this excited energy, the electrons return to their original positions within the HOMO band, leading to the emission of visible light photons (Rossini *et al.*, 2019). Wang *et al.* were pioneers in introducing GQDs-based photoluminescent probes by demonstrating the selective quenching of GQDs photoluminescence by Fe^{3+} ions through a charge transfer mechanism (Wang *et al.*, 2012). More recent developments have further underscored the potential of these nanomaterials. Recently, Xiong *et al.* (Xiong *et al.*, 2022) demonstrated the efficacy of nitrogen-doped graphene quantum dots derived from biomass (N-GQDs) for highly selective and nanomolar-level fluorescent detection of mercury ions in solution. Ethylenediamine was used as a nitrogen dopant, and the formation of amine or amide groups had a discernible impact on the final fluorescent characteristics of the complex. This is likely attributed to the introduction of new energy levels by the nitrogen atoms within the electron band, thereby modifying the structure of the HOMO and LUMO levels of the undoped GQDs, resulting in a shift in the fluorescence emission wavelength (Sun *et al.*, 2015). In contrast, the fluorescence exhibited by CNDs frequently involves valence states that

encompass both HOMO and LUMO band electrons (Balakrishnan *et al.*, 2022), along with intermediate states, resulting in a more intricate fluorescence mechanism in CNDs than that observed in GQDs. This complexity derives from a multitude of factors influencing CNDs photoluminescence, such as the dimensions of the CDs, their chemical composition, and the environmental conditions. Recently, CNDs derived from biomass via hydrothermal processing have found application in the fluorescence detection of Fe^{3+} and Pd^{2+} ions in solutions (Kang *et al.*, 2023). Because of the different responses to these two cations, the chemical influence of the CDs on the ensuing fluorescence emission may be investigated. Specifically, in the presence of Fe^{3+}, a noticeable enhancement in fluorescence was observed. This increase was caused by the chelating effect of surface groups on CNDs, such as carboxyl groups, in their interaction with Fe^{3+}, because it reduced non-radiative energy transfer while increasing N-content and the abundance of nitrogen-containing groups, resulting in increased final fluorescence emission. Conversely, when exposed to Pd^{2+}, there was a significant reduction in fluorescence. This attenuation was due to a significant contact between the surface groups on the CNDs and Pd^{2+}, which resulted in a reduction of radiative transitions from the electron to the ground state. This interaction successfully quenched the electron-hole pairs,

contributing to the observed effect in photoluminescence behaviour (Kang *et al.*, 2023).

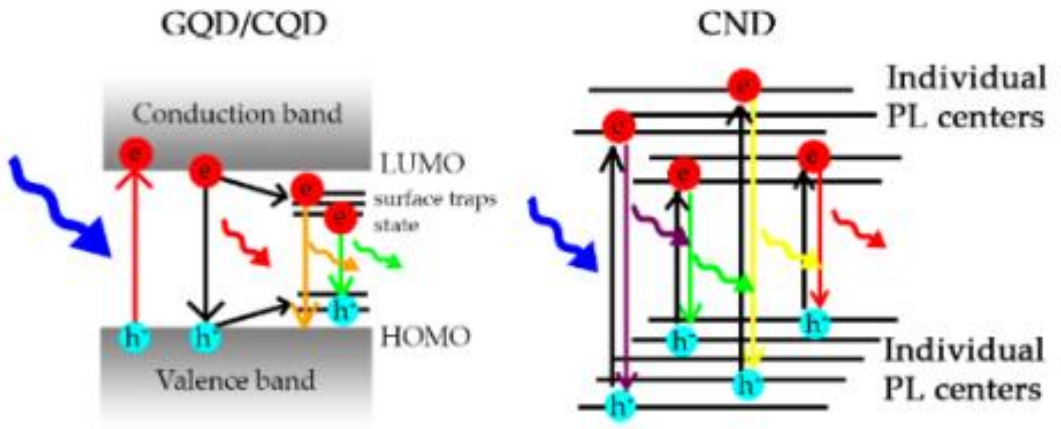

Figure 1.6. ***Photoluminescent mechanism of carbon-based nanomaterials***
(Suvarnaphaet and Pechprasarn 2017)

Water pollution has emerged as a global concern due to the grave risks posed by human activities, which can release hazardous and non-biodegradable substances such as heavy metals, posing a severe threat to both human health and the environment. Consequently, the detection of hazardous ions and molecules becomes a crucial safeguard for human well-being and environmental protection. Both CNDs and GQDs offer substantial advantages in the detection of environmental pollutants in water and soil. They exhibit sensitivity, selectivity, and the ability to achieve remarkably low detection limits. These features make them valuable tools for ensuring the safety of both human populations and ecosystems in the face of increasing water pollution challenges (Bressi *et al.*, 2021). Notably, carbon nanomaterials have been proven to expand the effective surface area of the electrode, enhance the rate of electron transfer between the electrode and analytes, and serve as efficient catalysts to heighten the efficacy of electrochemical reactions (Jose *et al.*, 2023). For example, carbon nanomaterials derived from algae were functionalized by Guan *et al.* and utilized as electrochemical sensors (Guan *et*

al., 2020). These sensors, employing square wave anodic stripping voltammetry (SWASV), demonstrated remarkable sensitivity in simultaneously detecting Pb^{2+} ions of 53.4 μA μM^{-1} and Cd^{2+} ions of 26.5 μA μM^{-1}. Recently, an enhanced electrochemical sensor, modified by drop-casted cellulose-derived CNDs, was evaluated for its capacity to detect Pb^{2+} ions in palm oil mill effluents by performing the same analytical technique (SWASV) (Ajab *et al.*, 2019). It exhibited excellent performance in a concentration range of 10-50 μg/L, showcasing a detection limit of 0.11 ± 0.37 μg/L and a quantification limit of 0.37 ± 0.37 μg/L, all achieved without the necessity for additional activation processes (Ajab *et al.*, 2019). There are numerous examples in the literature of GQDs or CDs being used as electrochemical sensors for the detection of heavy metals and other contaminants in water (Jose *et al.*, 2023; Yadav *et al.*, 2013). However, there are still knowledge gaps regarding the use of nanomaterials synthesized from natural resources, emphasizing the need for continued advancement in this field.

The environmental introduction of pesticide residues, originating from both agricultural and aquatic environments, presents another significant challenge related to the ecosystems and environmental health. In response, Ghiasi *et al.* developed an innovative green derived GQDs-based electrode designed for the detection of organophosphorus pesticides, such as diazinon. Utilizing differential pulse voltammetry (DPV) analysis, the electrochemical sensor showed strong selectivity and a linear detection factor ranging from 0.1 to 330 μM for diazinon. Unfortunately, the issue of environmental pollutants extends beyond water and soil, including the atmosphere as well. In this regard, carbon nanomaterials have demonstrated their remarkable efficiency (Crispi *et al.*, 2023). Recently, Sawalha *et al.* (Sawalha *et al.*, 2021) have developed a novel conductometric sensor for the detection of gas pollutants, based on CDs derived from olive solid waste characterized by a highly selective and sensitive

response to NO_2 at concentrations as low as below ppm levels, with a remarkable detection limit of 50 ppb.

In this context, the improper discharge of hazardous dyes, including methylene blue, methyl orange, Rhodamine B, and others frequently used in industrial processes, constitutes the primary contributor to water pollution (Rafiq *et al.*, 2021). To address this challenge, researchers have developed an advanced technology aimed at alleviating the impact of toxic dyes: the photocatalytic treatment of dye-contaminated wastewater utilizing carbon quantum dots derived from biomass (Wu *et al.*, 2023). Carbonaceous nanomaterials. (Supriya *et al.*, 2023) obtained from domestic organic waste, demonstrated notable effectiveness as catalysts for the reductive degradation of azo dyes, allowing a complete degradation within approximately 10 minutes of microwave irradiation, resulting in the creation of corresponding amines, which have been effectively utilized in the synthesis of novel azo compounds (Shetty *et al.*, 2023).

1.3 Environmental Pollutants

Environmental pollutants encompass a range of substances and agents, including chemicals and gases, released into the environment. They pose a threat to ecosystems, wildlife, and, in some instances, human health. Environmental pollutants can be classified in different ways, depending on their attributes and their effects on the environment as atmospheric, water, soil, and other pollutants.

Atmospheric pollutants like carbon dioxide (CO_2), nitrogen oxides (NO_x), sulfur dioxide (SO_2), and particulate matter, when inhaled, contribute to climate change, acid rain and respiratory diseases.

Water pollution results from impurities like heavy metal ions, sewage, pharmaceuticals, and industrial derivatives, disrupting aquatic ecosystems and risking safe drinking water sources.

Soil pollution arises from pesticides or improper waste disposal leading to soil contamination and the degradation of fertile land.

Additional forms of pollution encompass noise pollution, light pollution, thermal pollution, and contamination stemming from radioactive materials. Hazardous wastes, including industrial chemicals and radioactive materials, pose long-term risks to both the environment and human well-being. Since

fish, fruits, and agricultural supplies are key components of the food chain, soil and water pollution contaminates them, providing an indirect hazard to human health. Addressing these concerns necessitates a concentrated approach aimed at reducing emissions, fostering sustainable agricultural practices, advocating for environmental preservation, and establishing efficient, adaptable techniques for the early detection of harmful compounds.

1.3.1 Inorganic Pollutants

Inorganic pollutants constitute a category of substances that pose significant harm to both ecosystems and humans, even at minimal concentrations (Borah *et al.*, 2020). These pollutants can exist in solid, liquid, or gaseous states. A common way to categorize inorganic pollutants is as primary or secondary pollutants. Primary pollutants are chemical substances emitted directly from identifiable sources that already exist in nature, such as nitrogen dioxide. Secondary pollutants, on the other hand, are substances that result from the chemical transformation of primary pollutants (Tahir *et al.*, 2022). Generally, the negative effects of pollution are more commonly associated with secondary pollutants. Natural sources, such as volcanic eruptions, rock erosion, and forest fires, typically contribute to primary pollution. From these natural sources, secondary pollutants can develop, for instance, the oxidized derivatives of nitrogen oxides (NO_x) found in the soil or the oxidized forms of sulfur dioxide (SO_2) and hydrogen sulfide (H_2S) released by fires and volcanoes. Anthropogenic sources of primary pollutants include activities like the burning of fossil fuels, vehicle emissions from combustion engines, the release of volatile dust particles during industrial processes, and the wear and tear of tires and brakes. Secondary pollution, on the other hand, is primarily a result of processes

such as the oxidation of sulfur dioxide (SO_2), the oxidation of nitrogen oxides (NO_x), the release of ammonia (NH_3) from agricultural and livestock activities, the oxidation of hydrocarbons emitted by motor vehicles, and improper waste disposal leading to the release of heavy metal ions into water sources.

From a chemical point of view, inorganic pollutants can be broadly categorized into metallic and non-metallic compounds (Muthusaravanan *et al.*, 2018). Metallic compounds encompass metals and asbestos, whereas non-metallic compounds encompass nitrogen compounds, oxygen compounds, non-organic carbon compounds, and sulfur compounds. Atmospheric particulate matter, found in airborne dust, may contain a mixture of both organic and inorganic compounds.

Nitrogen compounds can be found in the atmosphere as molecular nitrogen (N_2), or radical species including nitrogen monoxide (NO), and nitrogen dioxide (NO_2), generally referred as NO_x. NO_x compounds are toxic to humans and, under the influence of solar radiation and other reactants, can lead to the formation of other toxic nitrogen derivatives (such as nitric acid and nitrous acid), resulting in the production of ozone and photochemical smog (Lamsal *et al.*, 2013). In water and soil (including sediments), inorganic nitrogen is found in the forms of nitrite ion (NO_2^-), nitrate ion (NO_3^-), and ammonium ion (NH_4^+). The primary sources of nitrogen oxides in the air are combustion processes (resulting from the combination of N_2 and O_2), natural sources (such as fires and volcanic emissions), anthropogenic emissions (from combustion engines, domestic heating, power plants, and industrial processes), and biological processes (J. Wang *et al.*, 2022). Nitrates in water sources originate from municipal sewage, waste, fertilizers, and combustion processes. Acidic compounds contribute to the formation of acid rain. Nitrogen oxides are primarily emitted as nitric

oxide (NO), which can rapidly convert to NO_2 by reacting with ozone and other oxidizing compounds. Among the various nitrogen oxides, NO_2 is particularly toxic, with severe oxidizing capabilities that predominantly impact mucous membranes, notably those in the eyes and respiratory tract, as well as cancerogenic effects (Ansari *et al.*, 2017). Nitrite ions can frequently be found in foods since they are employed as preservatives in meat and fish (Noor *et al.*, 2016). Moreover, this presence can be attributed to several factors, including indirect contamination stemming from the excessive use of fertilizers in soil, which subsequently leaches into water sources. Excessive consumption of nitrite-laden foods can result in the formation of intestinal tumors. This phenomenon occurs due to the conversion of nitrite into N-nitrosamines within the stomach (Cui *et al.*, 2012). Additionally, nitrites can bind with hemoglobin in the bloodstream, reducing its oxygen-carrying capability (Zhang *et al.*, 2023). Within the body, nitrogen oxides react with unsaturated lipids in cell membranes, forming peroxides, which disrupt biological processes. In the atmosphere, other pollutants are also formed, including nitrous acid (HNO_2), nitric acid (HNO_3), peroxyacetyl nitrate (PAN), and inorganic nitrates, which may exist as particulate matter (Bray, 2019).

Oxygen exists in the atmosphere, as well as in water, in various forms, including hydrogen peroxide (H_2O_2), molecular oxygen (O_2), ozone (O3), and radicals including hydroxyl radicals (OH^-) and perhydroxyl radicals (HOO^-). O_2 and O_3 species have the ability to absorb UV radiation, alongside nitrogen (N_2) (McKenzie *et al.*, 2011). Ozone is the primary oxidant present in photochemical smog, and exposure to ozone occurs primarily through inhalation, leading to noticeable adverse effects on mucous membranes upon contact. The depletion of ozone occurs due to

chemical reactions involving radical species (such as $Cl^{\cdot}$ or $NO^{\cdot}$) (McKenzie *et al.*, 2011).

Inorganic carbon is primarily found in the atmosphere as carbon monoxide and carbon dioxide. In aquatic environments and soils, it occurs in dissolved forms, including CO_2, H_2CO_3, HCO_3^-, and CO_3^{2-}. In soils, it is also present as carbonates and bicarbonates of various elements such as calcium (Ca), magnesium (Mg), aluminum (Al), and iron (Fe). Carbon dioxide plays a vital role in chlorophyll photosynthesis, where it is utilized to form organic compounds. CO primarily originates from sources like cigarette smoke, vehicle emissions, and polluted urban air. In the bloodstream, CO binds to the iron atom within hemoglobin's heme group, resulting in the formation of carboxyhemoglobin ("*Carbon Monoxide Poisoning-Symptoms and Causes*", 2023). Hemoglobin bound to CO loses its ability to effectively capture and transport oxygen, leading to the onset of anemic hypoxia.

Sulfur compounds can originate from natural processes such as volcanic eruptions or from the combustion of coal containing sulfur impurities in power plants and ores in smelters. Although traces of sulfur compounds may be present in automotive fuels, the primary sources of sulfur dioxide (SO_2) are biological processes, the paper industry, and vehicular traffic. Notably, hydrogen sulfide (H_2S) is a colorless gas at room temperature and is known for its distinct smell resembling rotten eggs. It is significantly more toxic than SO_2. Similar to nitrites, sulfites are present in numerous beverages and food items, potentially triggering various allergic reactions and health issues like nausea, asthma, headaches, and more (Pandi *et al.*, 2018; Silva *et al.*, 2015). To mitigate these risks, the Food and Drug Administration (FDA) recommends not exceeding a concentration of 50 mg/L in beer and 350 mg/L in wine ("*Health*", 2023). Sulfates in water can have various origins, including the dissolution of minerals like gypsum or anhydrite when in

contact with groundwater, the oxidation of sulfides such as pyrites, and contributions from marine aerosols in coastal regions. During the anaerobic decomposition of organic matter, H_2S, methanethiol (CH_3SH), and dimethyl disulfide ($CH_3S\text{-}SCH_3$), all of which emit unpleasant odors, can be generated. Dimethyl sulfide undergoes oxidation in the air to form carbonyl sulfide (COS), which subsequently converts to sulfate. Bacteria play a role in the oxidation of hydrogen sulfide: they first convert it to elemental sulfur (S) and then further to sulfate (SO_4^{2-}). Certain anaerobic bacteria can utilize sulfate as a source of oxygen to facilitate the oxidation of organic substances to carbon dioxide (CO_2) in the absence of oxygen, ultimately producing sulfur (especially in seawater).

Metallic compounds have significant biological functions in both plants and animals. In certain instances, their chemical coordination and oxidation-reduction properties empower them to effectively regulate vital processes like homeostasis, transport, compartmentalization, and interaction with essential cellular components (Muthusaravanan *et al.*, 2018; Naushad *et al.*, 2015).

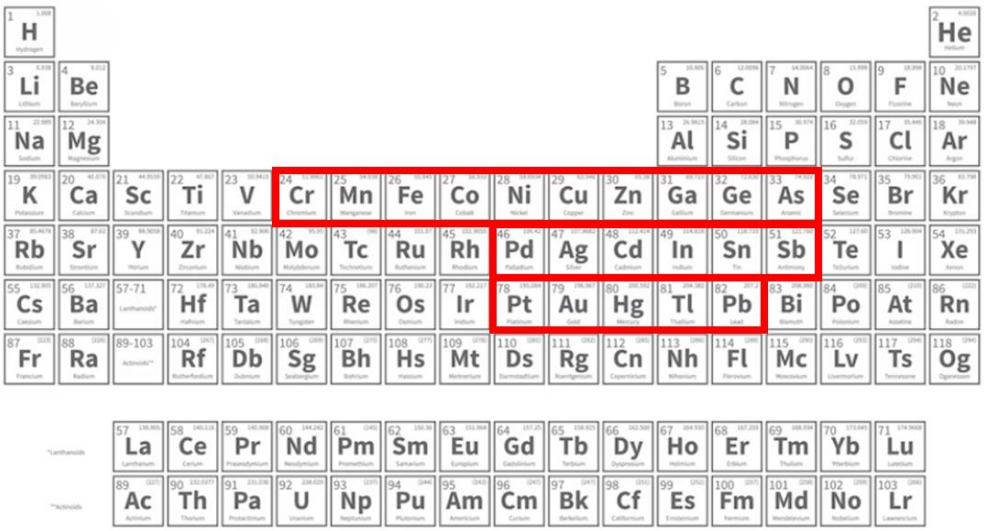

Figure 1.10. ***Heavy metals callout in Periodic Table*** *('Periodic Table - Heavy Metals Callout' n.d.)*

Specifically, when discussing inorganic pollution, heavy metal ions are the focus due to their potential to cause significant harm to human health, and marine and terrestrial ecosystems, even when present in exceedingly low concentrations.

This category encompasses metals that share specific chemical characteristics, including ductility, an atomic number greater than 20, a density exceeding 5.0 g/cm^3, and low solubility of hydrates (**Figure 1.10**). Heavy metal ions can generally classified as either essential or non-essential. Some heavy metals are essential micronutrients, playing vital roles in organic functions and the growth of plants and animals (e.g., Zn), and they only become harmful when their concentrations exceed specific thresholds, which vary depending on the element and the organism. Non-essential heavy metals, such as cadmium (Cd), mercury (Hg), arsenic (As), nickel (Ni), and lead (Pb), are highly toxic even in trace amounts (Maftouh *et al.* 2023; Moulaee *et al.* 2022). On the other hand, essential heavy metals like copper (Cu), zinc (Zn), iron (Fe), and cobalt (Co) are required in recommended threshold amounts to support metabolic processes. Still, they can be toxic when present in excess (Gedda *et al.* 2016). Heavy metals found in various environmental matrices can have natural origins, arising from soils and rocks with anomalous concentrations of these elements, atmospheric particulates from sources like volcanic emissions, geysers, and forest fires, or they can be of anthropogenic origin, originating from mining, industrial activities, and combustion plants (Bressi *et al.*, 2022). The toxicological behavior of an element can also vary significantly depending on its chemical form (e.g., Cr), representing an additional factor influencing its impact on human health ("Geochimica Ambientale. Metalli Potenzialmente Tossici", 2023).

Mercury

Mercury ions are released into the air in elemental and inorganic forms, which can be biologically converted into organic compounds. Methylmercury, in particular, raises significant concerns as it accumulates in the food chain, posing risks to humans. According to the European Union guidelines, the maximum allowable limit for mercury in drinking water is 1 μg L^{-1}, equivalent to 1 part per billion (ppb) ("*Water and Sanitation Are a Human Right!*", 2020). For certain foods, precisely some types of fish, the limit is set at 0.5 mg/kg (Francesconi, 2007).

Cadmium

Cadmium has been identified as a potential cause of lung cancer in humans, with specific population groups, including the elderly, diabetics, smokers, and pregnant women facing a higher risk. Exposure to cadmium ions primarily occurs through water and food for the general population (Y. Wang *et al.* 2022). Prolonged exposure to cadmium can lead to kidney and bone damage. One of the critical effects is an increase in the excretion of low molecular weight proteins in urine and a higher risk of osteoporosis (Satarug *et al.* 2023). European drinking water guidelines have set a maximum allowable concentration of 5 μg L^{-1} for cadmium ions in drinking water ("*Water and Sanitation Are a Human Right!*", 2020). Additionally, the WHO has established a maximum limit of 0.05 mg/kg in certain foods, such as shellfish, which can be a significant source of metal (Francesconi, 2007).

Lead

Lead is a potent neurotoxin; exposure to this heavy metal can adversely affect on the behavior and development of fetuses, infants, and children. It can also increase blood pressure in adults. Epidemiological studies imply that blood lead levels of around 5 μg/dL are related to health impacts in children, and new investigations reveal that one in every three children is expected to have blood lead levels in excess ("*WHO Guidance to Reduce Illness Due to Lead Exposure*", 2023). New European proposals have lowered the permissible concentration of lead ions (Pb^{2+}) in drinking water from 10 to 5 parts per billion (ppb) (Ferrari *et al.*, 2020).

Zinc

Zinc is recognized as an essential trace element for humans due to its pivotal role in insulin production (Dzianová *et al.*, 2020; Kambe *et al.*, 2017) and its regulatory function in numerous biological processes, playing a catalytic role in over 200 metalloenzymes (Kambe *et al.*, 2021). Moreover, zinc is naturally present in various foodstuffs, such as cereals, where the permissible upper limit for zinc content is 150 mg/kg (Szuba-Trznadel *et al.*, 2021). While Zn^{2+} ions are generally considered low toxic, elevated concentrations can lead to nausea, vomiting, lethargy, and fatigue (Lavado *et al.*, 2019). Recent research has indicated a potential correlation between alterations in serum Zn^{2+} levels and the onset of neurodegenerative disorders, notably Alzheimer's (Hsieh *et al.*, 2012). Additionally, this cation is prevalent in industrial waste streams from sectors such as paint, electroplating, pharmaceuticals, and fine chemical manufacturing. The European Union (EU) has established a typical maximum contamination threshold for zinc in drinking water at 25 μg/L ("*Progress on Household*

Drinking Water, Sanitation and Hygiene 2000-2020: Five Years into the SDGs", 2020).

Copper

Similar to zinc, copper is also a necessary element for human health, playing a crucial role in various biological functions, including the formation of connective tissue, energy production, and the body's immune response against pathogens (Rodríguez-Tomàs *et al.*, 2021). However, excessive exposure to copper can have adverse health effects, resulting in symptoms such as nausea, vomiting, diarrhea, and gastrointestinal diseases (Frydrych *et al.*, 2023). Moreover, the excessive buildup of copper in the body can lead to severe neurological and liver disorders. EU drinking water guidelines established a maximum concentration of 5 μg L^{-1} for copper ions in drinking water ("*Water and Sanitation Are a Human Right!*", 2020).

In conclusion, heavy metal ions and, in general, inorganic pollutants can have harmful effects on human health and the environment. Therefore, monitoring and control of these pollutants is essential for the protection of public health and environmental conservation.

1.3.2 Organic Molecules

Organic pollutants are organic-based compounds that exhibit resistance to biological and chemical degradation. They are semi-volatile, enabling them to disperse over long distances and possess the capacity to be absorbed by living organisms, thereby posing a significant threat to humans, animals,

and the environment at large. These pollutants are characterized by specific properties, including:

- accumulation and bioaccumulation: the ability to accumulate in the environment, water, and the adipose tissue of living organisms, including fish, predatory birds, mammals, and humans;
- persistence: the capacity to withstand biological, chemical, and photochemical degradation over time;
- toxicity: the potential to cause harm to both humans and the environment, often with long-term effects;
- volatility: the capability to be transported over considerable distances through atmospheric processes.

One prominent category is "Persistent Organic Pollutants" (POPs), encompassing synthetic organic compounds such as pesticides, herbicides, by-products of industrial processes (dioxins and furans), polychlorinated biphenyls (PCBs), and dichlorodiphenyltrichloroethane (DDT) (Alharbi *et al.*, 2018). POPs can bio-accumulate in the food chain, leading to enduring environmental consequences. The last property pertains to compounds that exhibit a pronounced inclination to transition into the vapor phase or change from liquid to gaseous.

These compounds are categorized as Volatile Organic Compounds (VOCs). VOCs, such as toluene, xylene, benzene, and formaldehyde, are often associated with industrial processes, vehicle emissions, and household products (Lim *et al*., 2014). VOCs contribute to air pollution and have adverse health effects. Polycyclic aromatic hydrocarbons (PAHs) are chemical compounds characterized by their multiple fused aromatic rings including anthracene, acenaphthene, and fluorene (Kocak *et al.*, 2023) and formed as byproducts of incomplete combustion of organic materials, as

well as in vehicle exhaust, cigarette smoke, and grilled meats (Liu *et al.*, 2018; Mosallaei *et al.*, 2023). Aromatic pollutants encompass isomers of dihydroxybenzene, like resorcinol, hydroquinone, and catechol. These compounds find extensive applications as intermediates in pharmaceutical synthesis, dyes, cosmetics, and pesticides (Viggiano *et al.*, 2023; Siyi Yang *et al.*, 2020). Despite their versatile utility, dihydroxybenzene isomers present substantial environmental and human health risks due to their elevated toxicity, carcinogenic properties, and resistance to degradation (Hu *et al.*, 2023). Consequently, they have become prominent subjects of environmental monitoring (Dong *et al.*, 2023; Meng *et al.*, 2017). Additionally, products such as cosmetics and pharmaceuticals can enter wastewater systems through improper disposal, contamining the water sources and persistent presence (Kaur *et al.*, 2023; Zha *et al.*, 2013). Moreover, as industrialization advances, another group of organic compounds that is steadily rising in prominence as organic pollutants is dyes. The dyes are extensively employed in various industries, including chemicals, paints, cement, etc. They are released into the water environment, either directly or indirectly, leading to environmental consequences or posing a severe health hazard if consumed by humans. Notably, Methylene blue and Rhodamine B have been categorized as potential human carcinogens by the International Agency for Research on Cancer (IARC) (Cheng and Tsai, 2017; Xiao *et al.*, 2023), as well as aniline, which is a precursor for the synthesis of multiple dyes (Thakur and Qanungo, 2021). Moreover, Rhodamine B is recognized as toxic to aquatic organisms, leading to environmental contamination and its detrimental consequences on aquatic species, thereby disrupting ecosystems (Bilgic, 2022).

Extensive efforts are undertaken to monitor and regulate the release of organic pollutants into the environment to mitigate their impact on ecosystems and human health.

1.4 Environmental monitoring techniques

Environmental monitoring is a crucial component of ecosystem management and human health protection, which involves observing, measuring, and collecting data on a given environment to detect changes in it. European Environment Agency (EEA) defined environmental monitoring as "the periodic and/or continuous measurement, assessment and determination of environmental parameters and/or pollution levels to prevent adverse and harmful effects on the environment" ("*European Environment Agency's*," 2023). Various environmental monitoring techniques have been developed, each tailored to detect specific pollutants or environmental parameters (**Figure 1.11**). These include advanced analytical methods such as mass spectrometry and liquid chromatography, which can precisely detect and quantify diverse chemical pollutants. While these methods are highly reliable, they require sophisticated instrumentation. Optical techniques, including fluorescence and UV-Vis spectroscopy, can be harnessed for detecting heavy metals and organic molecules or for analyzing photodegradation or adsorption. Biological indicators, commonly called bioindicators, are frequently employed in environmental monitoring. These indicators encompass species of animals, plants, or fungi known for their heightened sensitivity to alterations within their living ecosystems induced by various pollutants. A bioindicator possesses the capacity to gauge pollution levels within a specific area due to its capability to accumulate pollutants, which can subsequently be detected in laboratory analyses. For instance, lichens, recognized for their ability to get heavy metals,

are utilized in air quality assessments as bioindicators. Furthermore, electrochemical sensors have proven invaluable in environmental monitoring. They find application in air quality assessment, where they detect pollutants like nitrogen oxides (NOx), fine particulate matter (PM2.5), sulfur dioxide (SO_2), and volatile organic compounds (VOCs). They also monitor water bodies (seas, rivers, and wastewater), biological fluids, and soil. In electrochemistry, modified electrodes emerge as valuable tools for environmental monitoring. These electrodes exploit electrochemical reactions to detect pollutants, offering advantages such as high sensitivity, selectivity, and the ability to conduct simultaneous and real-time monitoring.

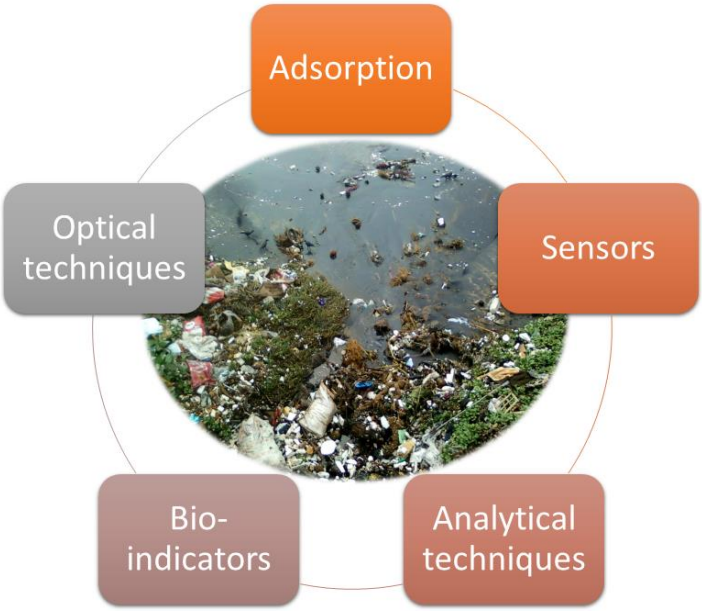

Figure 1.11. ***Environmental monitoring techniques***

1.4.1 Electrochemistry: Unlocking the Power of Electrochemical Sensors

Electrochemistry represents a specialized area of chemistry dedicated to studying and comprehending the processes governing the conversion of

electrical energy into chemical energy and vice versa ("*Elettrochimica nell'Enciclopedia Treccani*", 2023). Consequently, it is primarily concerned with chemical reactions that either induce the movement of electric charges or are catalyzed by such action. Electrochemistry has certainly assumed a pivotal role in bridging the domains of scientific inquiry and modern industrial applications, serving as the cornerstone for various contemporary disciplines, including theoretical chemistry, materials science, and medicine (Larios-Durán *et al.*, 2020). The invention of the voltaic pile, now known as the forerunner of the contemporary electric battery, by the Italian Alessandro Volta, who is most known for his pioneering work, is where electrochemistry first emerged (Breitkopf and Swider-Lyons, 2017). Humphry Davy made a significant discovery a few years after Volta's contributions when he discovered that the electricity generation by the voltaic pile depended on chemical reactions instead of just the juxtaposition of different metals, as Volta had proposed. According to Davy's postulation, since electric currents can overcome the usual forces holding together elements in compounds, they must inherently have an electrical nature, leading to the creation of metals through a process known as fusion electrolysis (Inzelt, 2020). Remarkably, despite the numerous following theoretical contributions, the fundamental theories behind the discoveries in the field of electrochemistry have mostly not changed since Volta's revolutionary work in 1800. However, throughout the past century, significant progress has been made in the areas of cell structure and electrode materials. A scientific renaissance occurred in the 20^{th} century, characterized by remarkable instrumentation advancements, most notably the development of sophisticated multi-channel potentiostats. These developments strengthened the science of electrochemistry and made it possible to use more complex scanning- and modulation-based electrochemical techniques. Electrochemistry's future terrain still offers a wide range of opportunities for research and growth. Notably, the sensor field has remarkable potential for new advancements and breakthroughs

and is continually growing. The word "*sensor*" derives from the Latin word "*sentire*", suggesting that the sensor is, by definition, a device sensitive to specific inputs and able to translate these into quantifiable data. The current produced during the oxidation and reduction events involving the recognition element and its intended target molecule can be measured using electrochemical sensors. They are fascinating for examining the content or concentration of biological or analytical substances due to their unique ability to directly convert biological processes into electrical signals.

Consequently, electrochemical sensors are practical analytical tools that may be used in many fields, including the biomedical industry, where they help detect neurotransmitters, hormones, and biomolecules. They are also relevant for forensic investigations, particularly when analyzing illegal substances, and for environmental monitoring when looking for contaminants.

Electrochemical sensors' most prevalent electrode systems are two-electrode (2E) and three-electrode (3E) devices. A 3E system cell has reference, counter, and working electrodes, whereas a 2E system cell only has reference and working electrodes. The electrolyte solution's state determines the choice of 2E and 3E systems, the amount of current passed via the electrode-solution interface, and the electrochemical technique used (Saputra, 2023). The assessment of an electrical property (such as resistance, current, potential, conductance, or impedance), which is evaluated through various electroanalytical methods, forms the basis of the operation of electrochemical sensors. The chemical potential of the analytes in the test solution, as measured concerning a reference electrode, is intrinsically linked to this electrical measurement. Based on the analytical method and the signal produced by the transducer, these sensors can essentially be divided into amperometric, potentiometric, voltammetric, or conductometric types (**Figure 1.12**, top). The sensors could also be divided into three categories, depending on the analytes

they are intended to detect (**Figure 1.12**, centrer): gas sensors, which are made to detect particular gases or volatile compounds; biosensors, which are sensors that have been modified to include biological recognition components (such as enzymes and antibodies) to detect biomolecules; and chemical sensors, which are the most common because they can detect a variety of chemical compounds. The composition of the sensitive layer, immobilization techniques on the transducer, analyte types that can be detected, general structural design, and signal processing methods vary among electrochemical sensors within each categorization. Numerous analytes are identified via well-known chemical processes, such as the creation of metal ion complexes or the catalytic oxidation of organic compounds by enzymes. Different methods can be used to immobilize the sensitive layer, such as chemical bonding with the transducer, electropolymerization, adsorption, vapor deposition, or inclusion into a membrane. These sensors can take various structural forms, such as screen-printed or microelectronic compact devices, or they can take the form of customarily functionalized electrodes (**Figure 1.12**, down).

They may be reusable or disposable, and can be used in fieldwork, lab settings, or remote measurement scenarios. They can provide qualitative, semi-quantitative, or quantitative analytical response. In the case of sensor arrays, multivariate statistical procedures may be used in place of more traditional statistical techniques for data analysis.

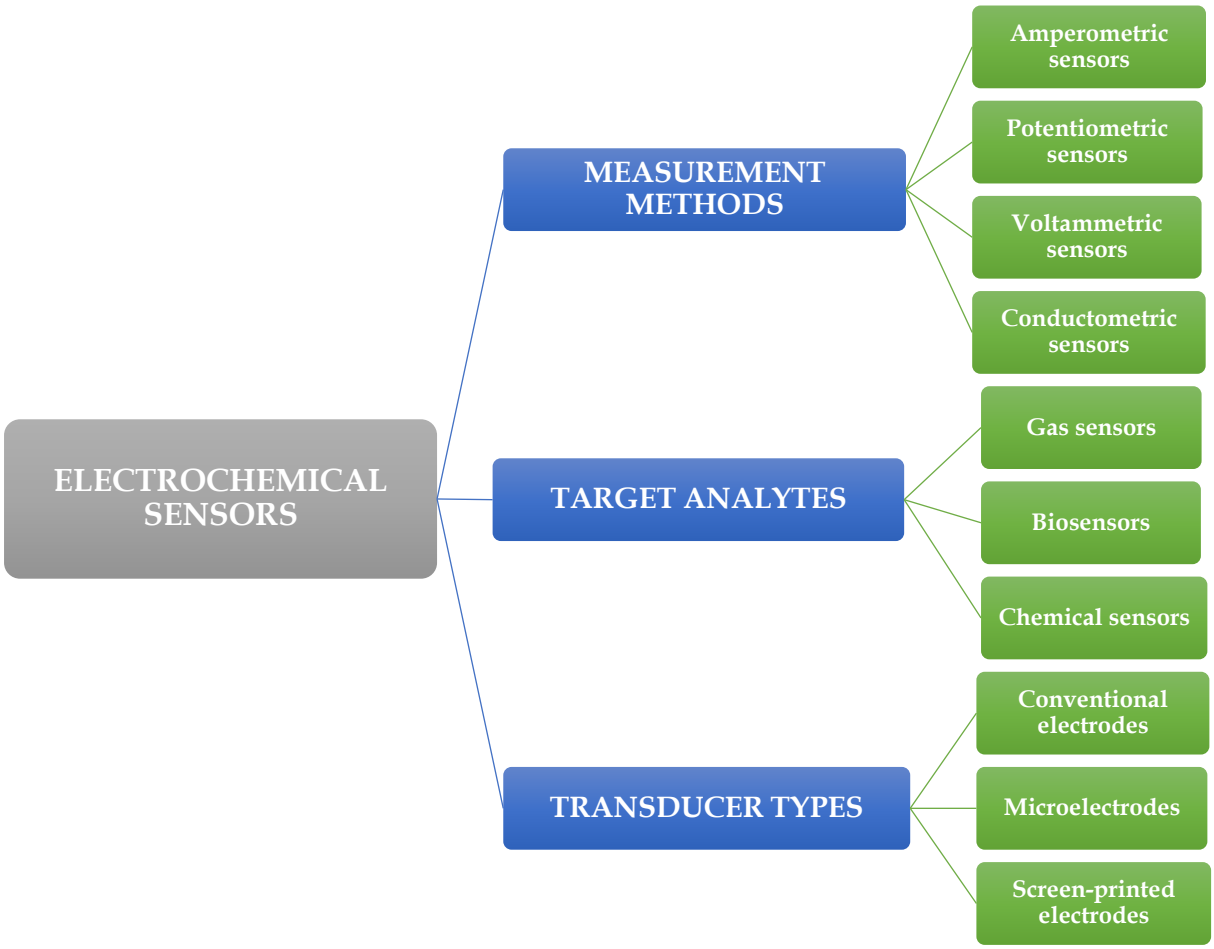

Figure 1.12. ***Classification of Electrochemical Sensors Based on 3 Criteria: Measurement Methods, Target Analytes, and Transducer Types***

To ensure the effectiveness of an electrochemical sensor, the device must meet strict criteria in terms of operating performance and manufacturing process. Any failure to achieve these standards can be a serious barrier, and the sensor can only be released to the market when these difficulties have been satisfactorily resolved. The subsections that follow will provide comprehensive descriptions of these fundamental characteristics.

1.4.1.1 Exploring Electroanalytical Methods

According to the above definition, electrochemical sensors are widely classed as amperometric, potentiometric, voltammetric, and conductometric sensors based on the measuring method performed. In each category, sensors exhibit variations in the composition of the sensing layer, the method of attachment to the transducer, the range of detectable analytes, the overall structural design, and how the signal is handled. The target analyte, sensitivity requirements, selectivity, and ambient variables all influence sensor type selection. Each category offers distinct advantages and is geared to specific analytical needs:

- Amperometric Sensors: measure the current produced by an electrochemical reaction at a constant applied voltage. This current is directly proportional to the concentration of the analyte. Commonly, amperometric sensors are used for the detection of gases (e.g., oxygen sensors), ions (e.g., nitrate sensors), and various biomolecules (e.g., glucose sensors).
- Potentiometric Sensors: measure the potential (voltage) difference between a reference electrode and a working electrode in a solution containing the analyte. This potential is related to the analyte concentration through Nernst's equation. Potentiometric sensors are widely employed in pH measurement, ion-selective electrodes (ISEs), and other environmental monitoring (e.g., pH meters and ion concentration sensors).
- Voltammetric Sensors: sweep the voltage applied to the working electrode across a range and measure the resulting current. This technique provides detailed information about the redox behavior of analytes. They are utilized to analyze heavy metals, organic compounds,

and complex analytes like neurotransmitters, heavy metal ions, and pharmaceuticals.

- Conductometric Sensors: measure changes in the electrical conductivity of a solution due to chemical reactions or the presence of specific ions. Typically, these sensors rely on interdigitated electrode structures and find applications in detecting gas concentrations (e.g., carbon monoxide and ammonia), ion-selective detection, and chemical monitoring.

As technology advances, electrochemical sensors are anticipated to play a prominent part in improving the ability to detect and analyze a wide range of analytes in various applications. This thesis focuced on using potentiometric and voltammetric sensors for electrochemical detection, particularly for heavy metal ions and organic molecules. These techniques were deemed more suitable for efficiency, time effectiveness, and selectivity.

1.4.1.1.1 Potentiometry

Potentiometry is an analytical technique based on measuring electrical potentials (**Figure 1.13**). This method, in particular, involves measuring the electrical potentials between a reference electrode and a working electrode immersed in a solution containing the target analyte (Zdrachek and Bakker, 2019). The reference electrode plays a crucial role by providing a steady and well-known reference potential, essential for estimating the working electrode's potential for the analyte. These potentials are measured in Volts (V) and can change according to chemical processes involving the analytes (Baranwal *et al.*, 2022).

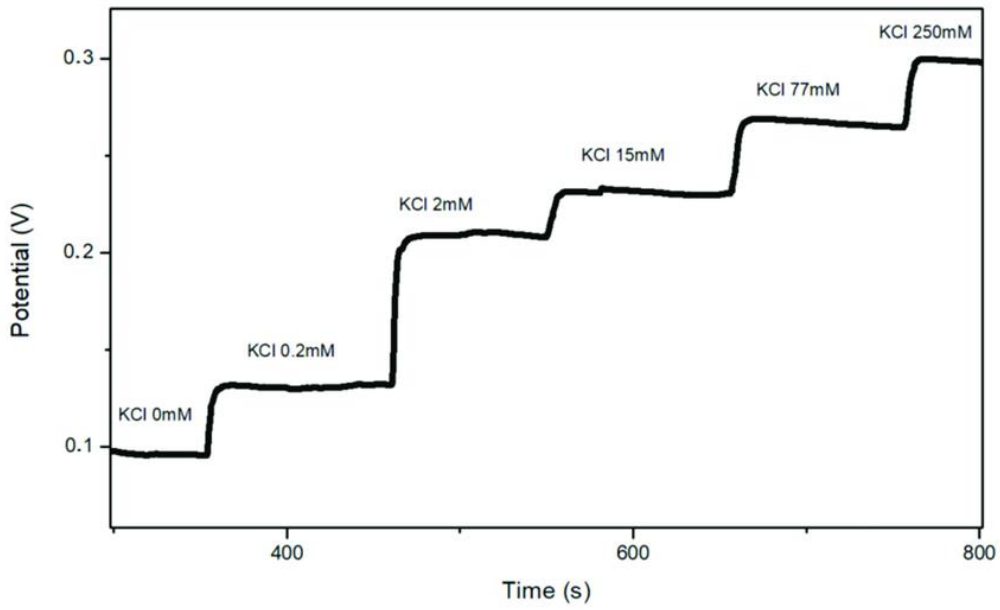

Figure 1.13. ***Potentiometric tests of SPCE modified sensor towards different concentrations of K^+ ions***
(Iannazzo et al. 2021)

One of the most commonly used reference electrodes in potentiometry is the silver/silver chloride electrode. It consists of an AgCl-coated silver electrode immersed in an aqueous solution enriched with concentrated KCl and saturated with AgCl. Measuring the potential difference generated within this cell can provide valuable insights into the concentration of the researched chemical species. The relationship between the estimated potential and the amount of analyte is delineated by the Nernst equation (Bakker and Pretsch, 2005).

$$EMF = E^0 + \frac{RT}{zF} ln(Q)$$

where *EMF* is the potential into the electrochemical cell, E^0 is the standard reduction potential of the species, *R* is the gas constant (8.314 J/(mol·K)), *T* is the absolute temperature (in kelvin), *z* is the number electrons transferred during the reaction (known as the stoichiometric coefficient), *F* is Faraday's constant (approximately 96485,34 C mol^{-1}), *ln* represents the natural logarithm,

and Q denotes the reaction quotient, which is the ratio of product to reactant concentrations raised to the power of their corresponding coefficients in the balanced chemical equation for the cell reaction. Notably, potentiometric sensors do not consume materials and are characterized by user-friendly operation, making them particularly suitable for routine analyses in fields such as examining natural and wastewater. Among potentiometric sensors, ion-selective electrodes (ISEs) are the most prevalent. These sensors can convert an ion-exchange event into a voltage signal that detects ions in a solution (Cuartero *et al.*, 2019). The pH meter is an excellent example because it catches the potential difference between two electrodes caused by changes in the concentration of H^+ ions in the solution. In the clinical fields, ISEs are employed for determining the levels of essential elements such as Na^+ and K^+ ions in blood samples. With the help of nanotechnologies, molecular potentiometric sensors have been developed to monitor glucose in blood or pharmaceutical compounds (Cuartero *et al.*, 2019).

1.4.1.1.2 Voltammetry

Voltammetry is an analytical technique that involves gradually increasing or decreasing the electrical potential provided to the working electrode and measuring the consequent current passing through the electrode (Saito and Kikuchi, 2014). This method is commonly performed within a three electrodes-electrochemical cell, and it allows for the collection of extensive information regarding the chemical reactivity and concentrations of the chemical species in question. The chemical species of interest may participate in redox processes that generate electrochemical current, with current intensity directly proportional to chemical species concentration. The potential is delivered incrementally or continuously throughout the measurement process, producing a voltammogram as a graphical output. During a voltammetric analysis, it is

essential to introduce an inert gas into the solution to remove atmospheric oxygen. Oxygen removal ensures that the electrochemical reaction only occurs between the chemical species of interest because dissolved oxygen can interfere with the current response and affect the results. Due to its high purity, availability, and low cost, nitrogen gas is commonly the best choice as an inert gas. Voltammetric analyses are typically conducted in a highly concentrated solution of a supporting electrolyte (Wang *et al.*, 2022). This supporting electrolyte serves a dual purpose: firstly, to reduce the resistance within the solution and diminish the contribution of analyte migration to the overall current. The supporting electrolyte must meet stringent purity criteria since it's added to the solution at a significantly higher concentration (often exceeding 0.1 M) than the analyte, and even trace impurities can wield significant influence (Arce-Castro *et al.*, 2022). Secondly, this supporting electrolyte should yield ions not readily subject to oxidation or reduction upon dissolution. This broadens the potential range for the analysis. After obtaining the related voltammograms, the graphs depicting the peak current intensity or peak area of these voltammograms as a function of the concentration of each analyzed ion will represent the calibration curves. This approach is referred to as “direct” because, for a given signal recorded in a specific artificial or real medium, the experimenter directly utilizes the corresponding calibration line(s) to determine the detection limit (as defined by IUPAC, International Union of Pure and Applied Chemistry). The detection limit (LOD) is the lowest concentration of an analyte that generates a detectable signal significantly different from the signal produced by a blank sample under identical conditions.

$$LOD = \frac{3.3\sigma}{p}$$

where σ denotes the standard deviation derived from a minimum of 10 measurements taken from the blank sample, and p means the slope of the

calibration line, which characterizes the sensitivity of the analytical method. The value 3.3 corresponds to the 90% confidence level for the difference between the observed signal and the response from the blank. Furthermore, the limit of quantification (LOQ) can be assessed based on the changes in concentration. This limit represents the smallest quantity of a substance in a sample that can be accurately determined using the experimental conditions described while maintaining an acceptable coefficient of variation for the response factor. It is calculated using Equation, with the terms having the same meanings as those in the detection limit expression.

$$LOQ = \frac{10\sigma}{p}$$

Additionally, sensitivity, accuracy, and precision parameters can be evaluated. The analyte concentration range in voltammetric methods is typically 0.1 to 5 mM because concentrations greater than 5 mM can cause increased currents and significant ohmic drop, a significant source of inaccuracy in voltammetric analyses. Concentrations below 0.1 mM, on the other hand, decrease the analyte's faradic current contribution relative to the background current, creating mistakes in concentration determinations. By increasing the ratio of Faradaic current to background current, specific voltammetric techniques, such as differential pulse or square wave voltammetry, can obtain detection limits as low as nanomolar or even lower. There are several variations of voltammetry, including:

- *Cyclic Voltammetry (CV):* this method allows for the investigation of reversible redox reactions and provides insights into the rate constants of these reactions. The potential undergoes cyclic variations, oscillating back and forth between two predefined limits (Venton and Di Scenza, 2020). This experimental approach is commonly employed to investigate specific chemicals' reduction and oxidation processes and the kinetics

associated with these reactions. **Figure 1.14** depicts a typical graph illustrating the variation in electrical potential overtime during a cyclic voltammetry experiment resulting from a single electron reduction and oxidation:

$$M^{+} + e^{-} \rightleftharpoons M$$

In the initial half-cycle, during which it is assumed that only substances conducive to oxidation are present in the environment, the experiment is initiated with a high electrical potential that is gradually decreased. As the potential approaches a specific value where reduction occurs, a surge in the electric current flowing through the electrode is observed. This escalation reaches its highpoint at a peak (cathodic peak), coinciding with the reduction potential (E_{pc}). The resulting current is called cathodic current (i_{pc}) ('*Cyclic Voltammetry*', 2013). Subsequently, the direction of the electric potential is reversed, moving in the opposite direction. In this phase of the experiment, the molecule that had undergone a reduction in the preceding half-cycle reverted to its initial state through oxidation. This oxidation process gives rise to another peak, called anodic peak (E_{pa}). In this case, the resulting current is called anodic current (i_{pa}).

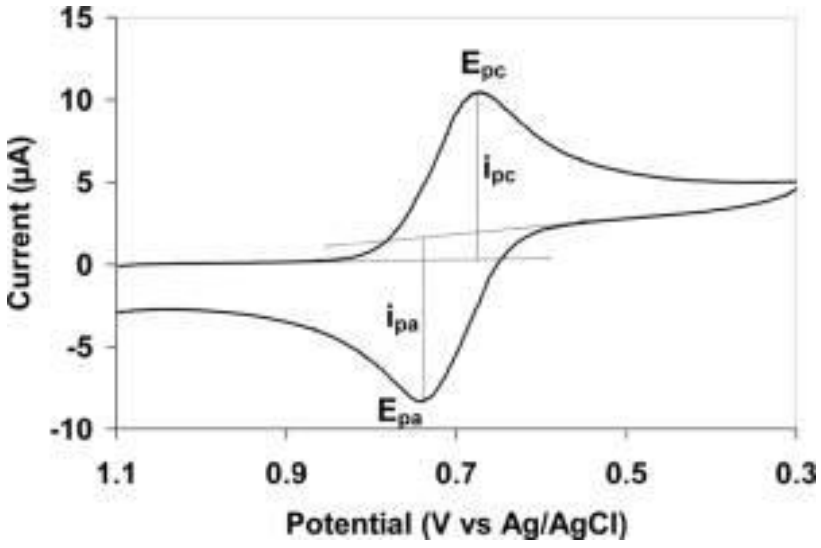

Figure 1.14. ***Cyclic voltammogram*** *('Ciclovoltammetria', 2023)*

- *Linear Sweep Voltammetry (LSV)*: in this technique, the potential applied to the working electrode is linearly altered concerning time or current. LSV is commonly employed to ascertain peak potentials and determine the concentrations of chemical species (Venton and Di Scenza, 2020). The equations governing the LSV responses acquired using this technique are identical to those used in CV. The fundamental difference between CV and LSV is that an "inverse" scan follows the "direct" linear potential scan in CV. Therefore, LSV is particularly beneficial for irreversible systems, where a reverse scan would yield no additional information. In both methods, the oxidation or reduction of species is registered as a peak or trough in the current signal at the potential where the species commences its oxidation or reduction.

- *Differential Pulse Voltammetry (DPV):* DPV is a technique that employs short, precisely defined pulses of potential, and with the current being measured after each pulse. This approach is renowned for its heightened sensitivity and is frequently used to analyze chemical species' trace quantities. In pulse voltammetry, potential pulses traverse a linear baseline, spanning from an initial potential to a final potential, while sampling the current at predetermined intervals (Simões and Xavier, 2017). The peak height, i.e., the amplitude, corresponds directly to the concentration of the redox chemical species present in the analyte. The time-potential curve depicted in **Figure 1.15a** provides the opportunity to subtract the current measured just before the pulses from the current recorded at the end of the pulse. This current difference, designated as

Δ_{ip}, is final reported current observed in the voltammogram shown in **Figure 1.15b**.

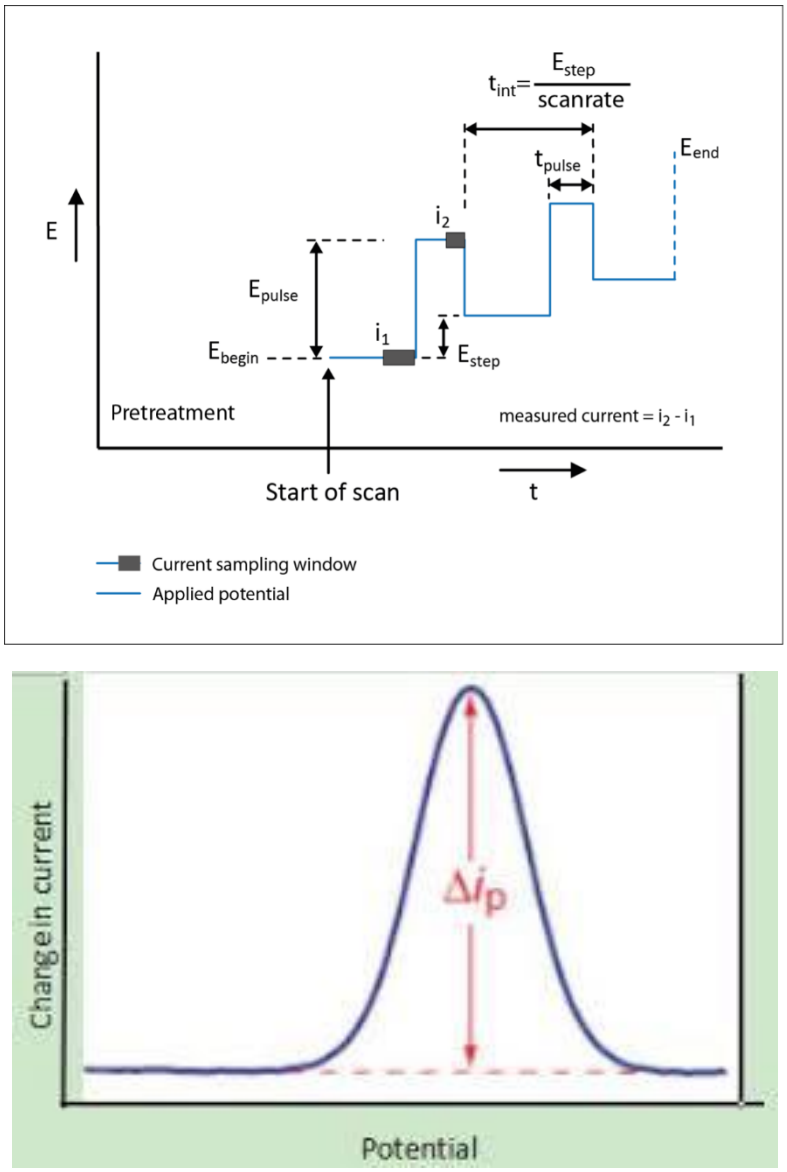

Figure 1.15. a) ***Potential applied during Differential Pulse Voltammetry*** *('Differential Pulse Voltammetry (DPV)')* ***and b)*** ***Differential Pulse Voltammetry voltammogram*** *(N.Z.N et al. 2018)*

- *Square Wave Voltammetry (SWV)* employs a square wave pattern to generate remarkably sharp current peaks, enabling superior resolution

and heightened sensitivity compared to other voltammetric techniques (Li *et al.*, 2016). SWV, unlike cyclic voltammetry, employs potential pulses with no intervals, comparable to differential pulse voltammetry but without the need for pre-electrolysis time. The pulse width (t_p), pulse height (ΔE_p), potential step height (ΔE_s), and frequency (f), which are inversely related to pulse width $\left(f = \frac{1}{2t_p}\right)$, are all critical parameters of this technique (**Figure 1.16**). The potential scan rate (W) is equal to $\frac{E_s}{2t_p}$. The current is sampled twice during each cycle: once at the end of the direct pulse, during which the electroactive species present near the electrode are discharged (reduction); and the second time at the end of the opposite pulse, in which the products that were formed during the forward pulse undergo the reverse reaction (oxidation). Compared to cyclic voltammetry, SWV eliminates background effects, making it helpful in evaluating low analyte concentrations (Maiocco *et al.*, 2018).

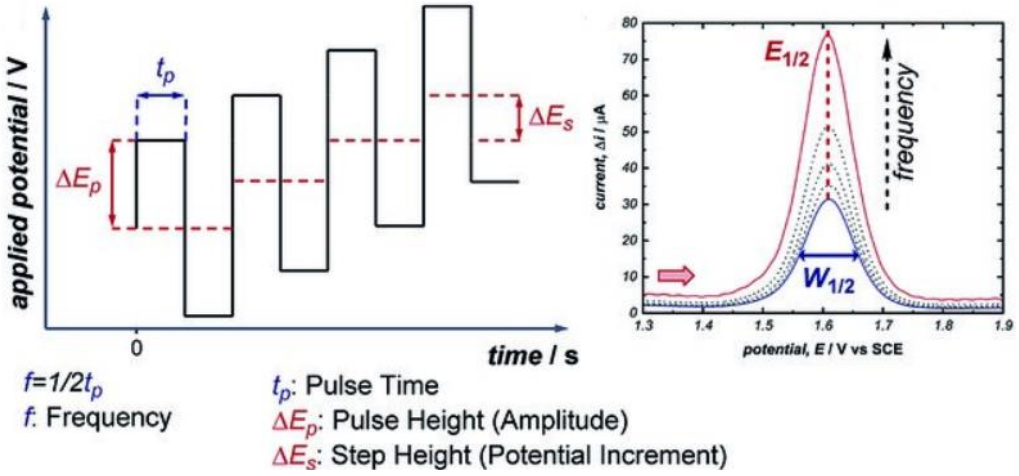

***Figure 1.16. left)** SVW staircase-shaped waveform and **right)** "bell-shaped" curve*
(Sandford et al. 2019)

In Square Wave Voltammetry, performing a pre-concentration of redox chemical species at the electrode is possible, followed by their swift

oxidation, enabling their detection as current peaks. This technique is precious for quantifying trace metals or other redox chemical species in dilute solutions (Barón-Jaimez *et al.*, 2013; Borrill *et al.*, 2019; Wang and Yue, 2017), and it's commonly called anodic or cathodic stripping (**Figure 1.17**). In stripping square wave voltammetry, the sample is initially concentrated or "pre-concentrated" at the working electrode by applying a sufficiently negative potential. The pre-concentration phase may last for a few seconds or minutes. This reduction step accumulates ions or electrons of the redox chemical species of interest at the electrode. Subsequently, the voltage is rapidly altered to initiate the reverse reaction, leading to the oxidation of the accumulated ions or electrons and generating a measurable current peak (Moulaee *et al.*, 2022). This peak, called the "stripping peak" (anodic or cathodic) is directly proportional to the concentration of the redox chemical species in the sample.

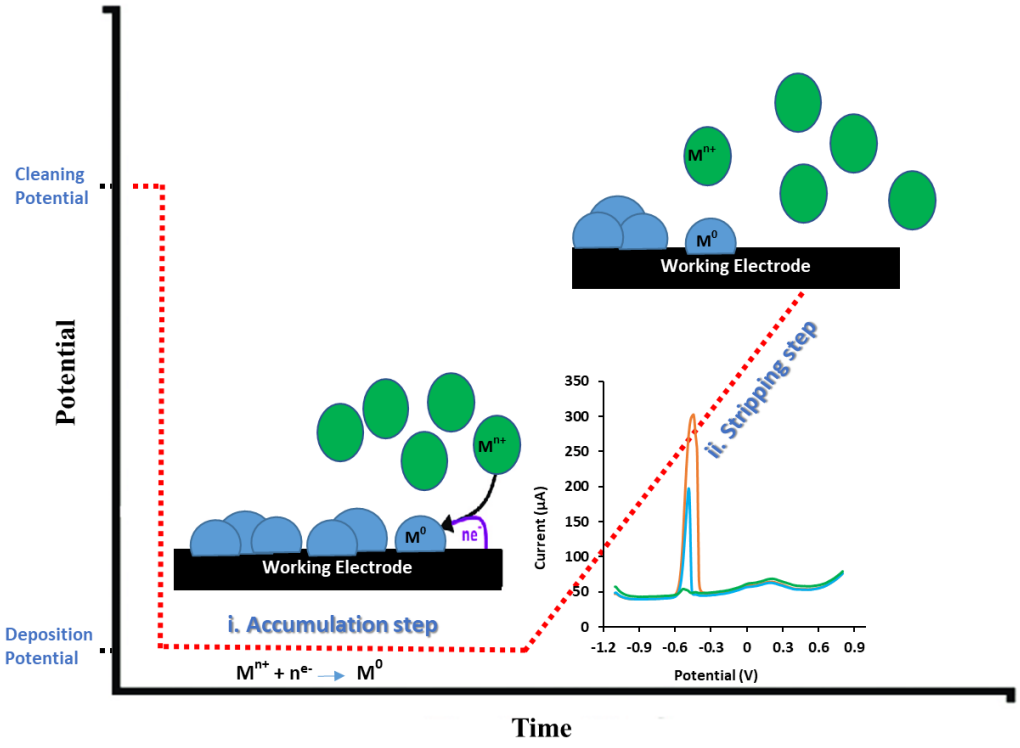

Figure 1.17. Square wave anodic stripping voltammetry steps: i) accumulation step and ii) stripping step

These measurement methods have found widespread applications in the analysis of several sample types, including clinical specimens (Amjadi *et al.*, 2023), pharmaceutical formulations (Barzani *et al.*, 2023), environmental pollutants (Illuminati *et al.*, 2016; Maciel *et al.*, 2023; Yadavalli *et al.*, 2023), and more.

1.4.2 Adsorption: Harnessing Surface Chemistry for Pollution Removal

In addition to advantages offered by electrochemical approaches, there has been a growing emphasis in recent decades on developing robust and efficient techniques for detecting contaminants and treating water contaminated with organic or inorganic pollutants. Current methods encompass several approaches, including oxidation, photodegradation, photocatalysis, coagulation, and adsorption (Cheng *et al.*, 2021; Rout *et al.*, 2023; Rout *et al.*, 2022; Spagnuolo *et al.*, 2023). Among these, adsorption stands out as a winning alternative due to its economic efficiency and superior effectiveness in removing even trace amounts of hazardous pollutants (Awad *et al.*, 2020; García *et al.*, 2021). In contrast, other methods face challenges such as high operational costs, substantial energy consumption, extended processing times, and the potential generation of undesired by-products (Mohammed *et al.*, 2014). Adsorption is a process where a substance (adsorbate) in a gaseous or liquid medium adheres to the surface of a solid material (adsorbent). Many factors influence adsorption processes involving both inorganic and organic pollutants. These factors encompass temperature, pH, salinity, additional dissolved substances, and the physicochemical properties inherent to the adsorbent materials (Ramanayaka *et al.*, 2020). It is noteworthy that temperature can accelerate the adsorption process, yet its influence varies depending on the specific chemical reactions, thus revealing temperature-dependent effects (El-Bery *et al.*, 2022). Moreover, the effect of pH on pollutant adsorption is linked to its capacity to induce structural alterations in the pollutants themselves, as well as in the properties of the surrounding water and the surface functional groups of the soil (Narváez Valderrama *et al.*, 2023). In more complex solutions, the coexistence of other substances may lead to competition for the available adsorption sites alongside the contaminant. This

competitive interaction can potentially impact the adsorption process's overall efficiency (Mejías *et al.*, 2023; Ramanayaka *et al.*, 2020).

Adsorption processes can be classified as either *physisorption* (physical adsorption) or *chemisorption* (chemical adsorption) (**Figure 1.18**). Physical adsorption, between the adsorbent and adsorbate, occurs through weak physical interactions, such as van der Waals forces. Molecules adsorbed via physisorption can be quickly released with changes in environmental conditions, such as alterations in temperature or pressure. Common materials used for physisorption include activated carbon (Cardenas *et al.*, 2023; EL Kassaoui *et al.*, 2023), zeolites (Hernández-Montoya *et al.*, 2013), and MOFs (Eltaweil *et al.*, 2020; Pi *et al.*, 2018). Conversely, chemisorption involves chemical reactions between the contaminant molecules and functional groups on the adsorbent's surface, leading to the formation of ionic or covalent bonds. Chemisorption becomes more selective and effective in removing specific pollutants as a result. Carbon-based nanomaterials (Awad *et al.*, 2020), iron oxide (Gutierrez *et al.*, 2017), and titanium dioxide (Youssef and Malhat, 2014) are commonly employed materials in chemical adsorption processes. Additionally, many adsorbents can be regenerated once they reach their adsorption capacity, extending their useful lifetime.

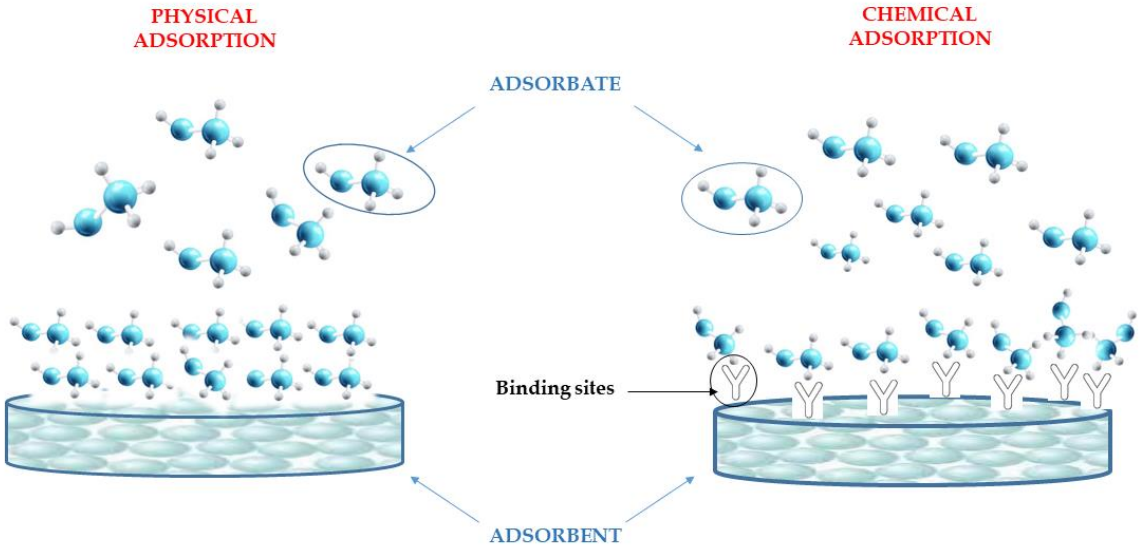

Figure 78. ***Physical and chemical adsorption***

The adsorption capacity at equilibrium of a material is typically evaluated using the equation (Yuan *et al.*, 2016):

$$q_e = \frac{(C_0 - C_e)}{m} \times V$$

where q_e (mol/g) represents the adsorption capacity at equilibrium (the amount of adsorbate adsorbed per unit mass of adsorbent at equilibrium); C_0 and C_e (mg/L) are the adsorbate concentrations at time 0 and at equilibrium, respectively; V (L) is the volume of solution, and m (g) is the weight of adsorbent. From a graphic point of view (**Figure 1.19**), the effectiveness of the adsorption process and therefore the adsorption capacity of the adsorbent as a function of the concentration of the adsorbate in the studied environment is described by the adsorption isotherms.

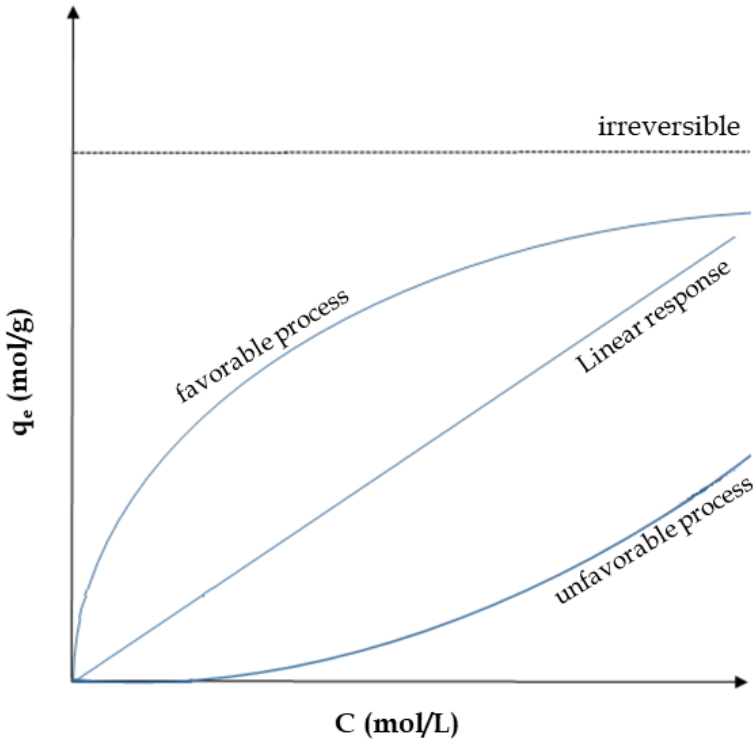

Figure 1.19. ***Adsorption isotherm models***

Adsorption isotherms illustrate the variation in adsorption capacity concerning the concentration (or partial pressure in the case of gases) of the adsorbate in the fluid undergoing treatment. There are different types of adsorption isotherms, the most common of which are:

- BET (Brunauer-Emmett-Teller), which studies adsorption on porous materials;
- Langmuir isotherm, which describes adsorption on a homogeneous surface and provides a theoretical insight into the formation of a monolayer of adsorbate on the surface of the adsorbent;
- Freundlich isotherm is used to describe adsorption on non-homogeneous or heterogeneous surfaces. It is often applied to systems where adsorption is more complex and varies with concentration.

Adsorption isotherms generallyaid in understanding how an adsorbent material responds to the presence of pollutants in the environment and serve as a foundation for constructing more effective adsorption procedures. In conclusion, adsorption is vital in addressing environmental concerns by efficiently removing pollutants from different ecosystems. Its versatility and capacity to target specific contaminants, combined with the selective properties of certain adsorbents, make it an economical, rapid, selective, and versatile approach.

References

Ababneh, H.; Hameed, B. H. Chitosan-Derived Hydrothermally Carbonized Materials and Its Applications: A Review of Recent Literature. *International Journal of Biological Macromolecules*, **2021**, 186, 314–27. https://doi.org/10.1016/j.ijbiomac.2021.06.161

Abbas, A.; Rubab, S.; Rehman, A.; Irfan, S.; Sharif, H.M.A.; Liang, Q.; Tabish, T.A. One-Step Green Synthesis of Biomass-Derived Graphene Quantum Dots as a Highly Selective Optical Sensing Probe. *Materials Today Chemistry*, **2023**, 101555. https://doi.org/10.1016/j.mtchem.2023.101555

Abid, N.; Khan, A.M.; Shujait, S.; Chaudhary, K.; Ikram, M.; Imran, M.; Haider, J.; Khan, M.; Khan, Q.; Maqbool, M. Synthesis of Nanomaterials Using Various Top-down and Bottom-up Approaches, Influencing Factors, Advantages, and Disadvantages: A Review. *Advances in Colloid and Interface Science*, **2022**, 102597. https://doi.org/10.1016/j.cis.2021.102597

Achilleos, D. S.; Kasap, H.; Reisner, E. Photocatalytic Hydrogen Generation Coupled to Pollutant Utilisation Using Carbon Dots Produced from Biomass. *Green Chemistry*, **2020**, 22 (9), 2831–39. https://doi.org/10.1039/D0GC00318B

Adams, P.; Bridgwater, T.; Lea-Langton, A.; Ross, A.; Watson, I. Chapter 8 - Biomass Conversion Technologies. In *Greenhouse Gas Balances of Bioenergy Systems*, edited by Patricia Thornley and Paul Adams, **2018**, 107–39. https://doi.org/10.1016/B978-0-08-101036-5.00008-2

Adeoye, A. O.; Lawal, O. S.; Quadri, R. O.; Malomo, D.; Aliyu, M. T.; Dang, G.E.; Emojevu, E. O.; Maikato, M. J.; Yahaya, M. G.; Omonije, O. O.; Edidem, V. G.; Abubakar, Y . K.; Offor, O. F.; Sochima, E. H.; Peter, B. E.; Hikon, B. N. Sustainable Energy via Thermochemical and Biochemical Conversion of Biomass Wastes for Biofuel Production'. In *Transportation Energy and Dynamics*, edited by Sunil Kumar Sharma, Ram Krishna Upadhyay, Vikram Kumar, and Hardikk Valera, **2023**, 245–306. Energy, Environment, and Sustainability. Singapore: Springer Nature. https://doi.org/10.1007/978-981-99-2150-8_11

Ajab, H.; Khan, A.A.A; Nazir, M. S.; Yaqub, A.; Abdullah, M. A. Cellulose-Hydroxyapatite Carbon Electrode Composite for Trace Plumbum Ions Detection in Aqueous and Palm Oil Mill Effluent: Interference, Optimization and Validation Studies. *Environmental Research*, **2019**, 176, 108563. https://doi.org/10.1016/j.envres.2019.108563

Alharbi, O. M. L.; Basheer, A. A.; Khattab, R.A.; Ali, I. Health and Environmental Effects of Persistent Organic Pollutants. *Journal of Molecular Liquids*, **2018**, 263 (August): 442–53. https://doi.org/10.1016/j.molliq.2018.05.029

Amjadi, S.; Akhoundian, S.; Alizadeh, T. A Simple Method for Melatonin Determination in the Presence of High Levels of Tryptophan Using an Unmodified Carbon Paste Electrode and Square Wave Anodic Stripping Voltammetry. *Electroanalysis*, **2023**, 35 (2), e202200210. https://doi.org/10.1002/elan.202200210

Ansari, F.A.; Ali, S.N.; Arif, H.; Khan, A.A.; Mahmood, R. Acute Oral Dose of Sodium Nitrite Induces Redox Imbalance, DNA Damage, Metabolic and Histological Changes in Rat Intestine. *PLoS ONE*, **2017**, 12 (4), e0175196. https://doi.org/10.1371/journal.pone.0175196

Antero Pacheco, V.R.; Fonseca Alves, A. C.; Botelho de Oliveira, S.; Anneli Ojala, S.; Silva Brum, S. Challenges and Alternatives for the Adequacy of Hydrothermal Carbonization of Lignocellulosic Biomass in Cleaner Production Systems: A Review. *Journal of Cleaner Production*, **2020**, 252, 119899. https://doi.org/10.1016/j.jclepro.2019.119899

Arce-Castro, J.; Vilasó-Cadre, J.E.; Benítez-Fernández, D.; Rodríguez-de la Rosa, H.; Arada-Pérez, M.A. Effect of Supporting Electrolytes on Voltammetry with Manual Staircase Voltage Scan. *The Journal of Engineering and Exact Sciences*, **2022**, 8 (3): 14235–01e. https://doi.org/10.18540/jcecvl8iss3pp14235-01e

Awad, A. M.; Jalab, R.; Benamor, A.; Nasser, M. S.; Ba-Abbad, M. M; El-Naas, M.; Mohammad, A. W. Adsorption of Organic Pollutants by Nanomaterial-Based Adsorbents: An Overview. *Journal of Molecular Liquids*, **2020**, 112335. https://doi.org/10.1016/j.molliq.2019.112335

Bakker, E.; Pretsch, E. Potentiometric Sensors for Trace-Level Analysis. *TrAC Trends in Analytical Chemistry*, Trace-metal analysis, **2005**, 24 (3), 199–207. https://doi.org/10.1016/j.trac.2005.01.003

Balakrishnan, T.; Ang, W.L.; Mahmoudi, E.; Mohammad, A. W.; Sambudi, N.S. Formation Mechanism and Application Potential of Carbon Dots Synthesized from Palm Kernel Shell via Microwave Assisted Method. *Carbon Resources Conversion*, **2022**, 5 (2): 150–66. https://doi.org/10.1016/j.crcon.2022.01.003

Banger, A.; Gautam, S.; Jadoun, S.; Jangid, N. K.; Srivastava, A.; Pulidindi, I. N.; Dwivedi, J.; Srivastava, M. Synthetic Methods and Applications of Carbon Nanodots. *Catalysts*, **2023**, 13 (5), 858. https://doi.org/10.3390/catal13050858

Baranwal, J.; Barse, B.; Gatto, G.; Broncova, G.; Kumar, A. Electrochemical Sensors and Their Applications: A Review. *Chemosensors*, **2022**, 10 (9), 363. https://doi.org/10.3390/chemosensors10090363

Barati, F.; Avatefi, M.; Moghadam, N. B.; Asghari, S.; Ekrami, E.; Mahmoudifard, M. A Review of Graphene Quantum Dots and Their Potential Biomedical Applications. *Journal of Biomaterials Applications*, **2023**, 37 (7), 1137–58. https://doi.org/10.1177/08853282221125311

Barón-Jaimez, J.; Joya, M. R.; Barba-Ortega, J. Anodic Stripping Voltammetry – ASV for Determination of Heavy Metals. *Journal of Physics: Conference Series*, **2013**, 466 (1), 012023. https://doi.org/10.1088/1742-6596/466/1/012023

Barzani, H. A. H.; Ali, H. S.; Yardım, Y. An Anodically Pretreated Boron-Doped Diamond Electrode Surface for Square-Wave Adsorptive Stripping Voltammetric Quantification of the Non-Absorbable Antibiotic Rifaximin in the Pharmaceutical Formulation. *Diamond and Related Materials*, **2023**, 132, 109647. https://doi.org/10.1016/j.diamond.2022.109647

Bawendi, M. G., A. R. K.; Steigerwald, M. L.; Brus., L.E. X-ray Structural Characterization of Larger CdSe Semiconductor Clusters. *The Journal of Chemical Physics*, **1989**, 91 (11), 7282–90. https://doi.org/10.1063/1.457295

Bilgic, A. Fabrication of monoBODIPY-Functionalized Fe3O4@SiO2@TiO2 Nanoparticles for the Photocatalytic Degradation of Rhodamine B under UV Irradiation and the Detection and Removal of Cu(II) Ions in Aqueous Solutions. *Journal of Alloys and Compounds*, **2022**, 899, 163360. https://doi.org/10.1016/j.jallcom.2021.163360

Borah, P.; Kumar, M.; Devi, P. Chapter 2 - Types of Inorganic Pollutants: Metals/Metalloids, Acids, and Organic Forms. In *Inorganic Pollutants in Water*, edited by Pooja Devi, Pardeep Singh, and Sushil Kumar Kansal, **2020**, 17–31. Elsevier. https://doi.org/10.1016/B978-0-12-818965-8.00002-0

Bray, C. Reactive Nitrogen Emissions from Biomass Burning and the Impact of Climate Change. *Environmental Science*, **2019**, Ph.D., Ann Arbor, United States. https://www.proquest.com/docview/2295446266/abstract/CD96C70E3298485DPQ/1

Breitkopf, C.; Swider-Lyons, K. Electrochemical Science — Historical Review'. In *Springer Handbook of Electrochemical Energy*, edited by Cornelia Breitkopf and Karen Swider-Lyons, **2017**, 1–9. Springer Handbooks. Berlin, Heidelberg: Springer. https://doi.org/10.1007/978-3-662-46657-5_1

Bressi, V.; Akbari, Z.; Montazerozohori, M.; Ferlazzo, A.; Iannazzo, D.; Espro, C.; Neri, G. On the Electroanalytical Detection of Zn Ions by a Novel Schiff Base Ligand-SPCE Sensor. *Sensors*, **2022**, 22 (3), 900. https://doi.org/10.3390/s22030900

Bressi, V.; Balu, A.M.; Iannazzo, D.; Espro, C. Recent Advances in the Synthesis of Carbon Dots from Renewable Biomass by High-Efficient Hydrothermal and Microwave Green Approaches. *Current Opinion in Green and Sustainable Chemistry*, **2023**, 40, 100742. https://doi.org/10.1016/j.cogsc.2022.100742

Bressi, V.; Chiarotto, I.; Ferlazzo, A.; Celesti, C.; Michenzi, C.; Len, T.; Iannazzo, D.; Neri, G.; Espro, C. Voltammetric Sensor Based on Waste-Derived Carbon Nanodots for Enhanced Detection of Nitrobenzene. *ChemElectroChem*, **2023**, e202300004. https://doi.org/10.1002/celc.202300004

Bressi, V.; Ferlazzo, A.; Iannazzo, D.; Espro, C. Graphene Quantum Dots by Eco-Friendly Green Synthesis for Electrochemical Sensing: Recent Advances and Future Perspectives. *Nanomaterials*, **2021**, 11 (5), 1120. https://doi.org/10.3390/nano11051120

Burguete, P.; Corma, A.; Hitzl, M.; Modrego, R.; Ponce, E.; Renz, M. Fuel and Chemicals from Wet Lignocellulosic Biomass Waste Streams by Hydrothermal Carbonization. *Green Chemistry*, **2016**, 18 (4), 1051–60. https://doi.org/10.1039/C5GC02296G

C60: Buckminsterfullerene | Nature, (accessed 27 September 2023). https://www.nature.com/articles/318162a0

Carbon Monoxide Poisoning-Symptoms and Causes. Mayo Clinic, (accessed 4 October 2023). https://www.mayoclinic.org/diseases-conditions/carbon-monoxide/symptoms-causes/syc-20370642

Cardenas, C. ; Sigot, L. ; Vallières, C. ; Marsteau, S. ; Marchal, M. ; Latifi, A.M. Ammonia Capture by Adsorption on Doped and Undoped Activated Carbon: Isotherm and Breakthrough Curve Measurements. *Separation and Purification Technology*, **2023**, 313, 123454. https://doi.org/10.1016/j.seppur.2023.123454

Chen, J.; Yao, B.; Li, C.; Shi, G. An Improved Hummers Method for Eco-Friendly Synthesis of Graphene Oxide. *Carbon*, **2013**, 64, 225–29. https://doi.org/10.1016/j.carbon.2013.07.055

Cheng, S. Y.; Show, P-L.; Juan, J.C.; Chang, J-S.; Lau, B. F.; Lai, S. H.; Ng, E. P.; Yian, H. C.; Ling, T.C. Landfill Leachate Wastewater Treatment to Facilitate Resource Recovery by a Coagulation-Flocculation Process via Hydrogen Bond. *Chemosphere*, **2021**, 262, 127829. https://doi.org/10.1016/j.chemosphere.2020.127829

Cheng, Y-Y.; Tsai, T-H. Pharmacokinetics and Biodistribution of the Illegal Food Colorant Rhodamine B in Rats. *Journal of Agricultural and Food Chemistry*, **2017**, 65 (5), 1078–85. https://doi.org/10.1021/acs.jafc.6b04975

'Ciclovoltammetria' in *Wikipedia*, accessed August **2023**. https://it.wikipedia.org/w/index.php?title=Ciclovoltammetria&oldid=132995460

Crispi, S.; Nocito, G.; Nastasi, F.; Condorelli, G.; Ricciardulli, A. G.; Samorì, P.; Conoci, S.; Neri, G. Development of a Novel C-Dots Conductometric Sensor for NO Sensing. *Sensors and Actuators B: Chemical*, **2023**, 390, 133957. https://doi.org/10.1016/j.snb.2023.133957

Cuartero, M.; Parrilla, M.; Crespo, G.A. Wearable Potentiometric Sensors for Medical Applications. *Sensors*, **2019**, 19 (2), 363. https://doi.org/10.3390/s19020363

Cui, L.; Ren, X.; Sun, M.; Liu, H.; Xia, L. Carbon Dots: Synthesis, Properties and Applications. *Nanomaterials*, **2021**, 11 (12), 3419. https://doi.org/10.3390/nano11123419

Cui, L.; Zhu, J.; Meng, X.; Yin, H.; Pan, X.; Ai, S. Controlled Chitosan Coated Prussian Blue Nanoparticles with the Mixture of Graphene Nanosheets and Carbon Nanoshperes as a Redox Mediator for the Electrochemical Oxidation of Nitrite. *Sensors and Actuators B: Chemical*, **2012**, 161 (1), 641–47. https://doi.org/10.1016/j.snb.2011.10.083

'Cyclic Voltammetry'. Chemistry LibreTexts, **2013**. https://chem.libretexts.org/Bookshelves/Analytical_Chemistry/Supplemental_Modules_(Analytical_Chemistry)/Instrumentation_and_Analysis/Cyclic_Voltammetry

Demirci, S.; McNally, A.B.; Ayyala, R. S.; Lawson, L. B.; Sahiner, N. Synthesis and Characterization of Nitrogen-Doped Carbon Dots as Fluorescent Nanoprobes with Antimicrobial Properties and Skin Permeability'. *Journal of Drug Delivery Science and Technology*, **2020**, 59, 101889. https://doi.org/10.1016/j.jddst.2020.101889

'Differential Pulse Voltammetry (DPV)'. PalmSens, (accessed 2 October **2023**). https://www.palmsens.com/knowledgebase-article/differential-pulse-voltammetry-dpv/

Ding, Z.; Li, F.; Wen, J.; Wang, X.; Sun, R. Gram-Scale Synthesis of Single-Crystalline Graphene Quantum Dots Derived from Lignin Biomass. *Green Chemistry*, **2018**, 20 (6), 1383–90. https://doi.org/10.1039/C7GC03218H

Dong, J.; Wen, L.; Liu, H.; Yang, H.; Zhao, J.; Luo, X.; Hou, C.; Huo, D. Simultaneous Detection of Dihydroxybenzene Isomers in the Environment by a Free-Standing Flexible $ZnCo_2O_4$ Nanoplate Arrays/Carbon Fiber Cloth Electrode. *Science of The Total Environment*, **2023**, 855, 158878. https://doi.org/10.1016/j.scitotenv.2022.158878

Dzianová, P.; Asai, S.; Chrudinová, M.; Kosinová, L.; Potalitsyn, P.; Šácha, P.; Hadravová, R.; Selicharova, I.; Kriz, J.; Turkenburg, J. P.; Brzozowski, A.M.; Jirácek, J.; Zakova, L. The Efficiency of Insulin Production and Its Content in Insulin-Expressing Model β-Cells Correlate with Their Zn^{2+} Levels. *Open Biology*, **2020**, 10 (10): 200137. https://doi.org/10.1098/rsob.200137

Ebbesen, T. W. Carbon Nanotubes. *Annual Review of Materials Science*, **1994**, 24 (1), 235–64. https://doi.org/10.1146/annurev.ms.24.080194.001315

Ekimov, A. Growth and Optical Properties of Semiconductor Nanocrystals in a Glass Matrix. *Journal of Luminescence*, **1996**, Spectroscopy of Isolated and Assembled Semiconductor Nanocrystals, 70 (1), 1–20. https://doi.org/10.1016/0022-2313(96)00040-3

EL Kassaoui, M.; Loulidi, M.; Benyoussef, A.; El Kenz, A.; Mounkachi, O. Tuning Hydrogen Storage Properties of Li- and Na-Decorated 3D Carbon-Honeycomb through a Physisorption Process. *Energy & Fuels*, **2023**, 37 (12), 8689–98. https://doi.org/10.1021/acs.energyfuels.3c00708

El-Bery, H. M.; Saleh, M.; El-Gendy, R. A.; Saleh, M. R.; Thabet, S. M. High Adsorption Capacity of Phenol and Methylene Blue Using Activated Carbon Derived from Lignocellulosic Agriculture Wastes. *Scientific Reports*, **2022**, 12 (1), 5499. https://doi.org/10.1038/s41598-022-09475-4

'Elettrochimica nell'Enciclopedia Treccani', *Treccani*, accessed 7 September 2023. https://www.treccani.it/enciclopedia/elettrochimica

Eltaweil, A.; El-Monaem, E.; Omer, A.; Khalifa, R.; El-Latif, M. A.; El-Subruiti, G.; Omer, A. Efficient Removal of Toxic Methylene Blue (MB) Dye from Aqueous Solution Using a Metal-Organic Framework (MOF) MIL-101(Fe): Isotherms, Kinetics, and

Thermodynamic Studies. *Desalination and Water Treatment*, **2020**, 189, 395–407. https://doi.org/10.5004/dwt.2020.25599

Espro, C.; Satira, A.; Mauriello, F.; Anajafi, Z.; Moulaee, K.; Iannazzo, D.; Neri, G. Orange Peels-Derived Hydrochar for Chemical Sensing Applications. *Sensors and Actuators B: Chemical*, **2021**, 341, 130016. https://doi.org/10.1016/j.snb.2021.130016

'*European Environment Agency's* Home Page', (accessed 6 June 2023). https://www.eea.europa.eu/en

Fang, J.; Zhan, L.; Ok, Y. S.; Gao, B. Minireview of Potential Applications of Hydrochar Derived from Hydrothermal Carbonization of Biomass. *Journal of Industrial and Engineering Chemistry*, **2018**, 57, 15–21. https://doi.org/10.1016/j.jiec.2017.08.026

Ferlazzo, A.; Bressi, V.; Espro, C.; Iannazzo, D.; Piperopoulos, E.; Neri, G. Electrochemical Determination of Nitrites and Sulfites by Using Waste-Derived Nanobiochar. *Journal of Electroanalytical Chemistry*, **2023**, 928, 117071. https://doi.org/10.1016/j.jelechem.2022.117071

Ferrari, A. G.-M.; Carrington, P.; Rowley-Neale, S. J.; Banks, C. E. Recent Advances in Portable Heavy Metal Electrochemical Sensing Platforms. *Environmental Science: Water Research & Technology*, **2020**, 6 (10), 2676–90. https://doi.org/10.1039/D0EW00407C

Francesconi, A. K. Toxic Metal Species and Food Regulations—Making a Healthy Choice'. *Analyst*, **2007**, 132 (1), 17–20. https://doi.org/10.1039/B610544K

Frydrych, A.; Krośniak, M.; Jurowski, K. The Role of Chosen Essential Elements (Zn, Cu, Se, Fe, Mn) in Food for Special Medical Purposes (FSMPs) Dedicated to Oncology Patients—Critical Review: State-of-the-Art. *Nutrients*, **2023**, 15 (4), 1012. https://doi.org/10.3390/nu15041012

Futura, Elettricità. 'Pubblicazioni | Studi e Approfondimenti | Biomass Supply Report 2021'. Elettricità Futura, (accessed 3 October 2023). https://www.elettricitafutura.it/Pubblicazioni/Studi-e-Approfondimenti/Biomass-Supply-Report-2021_3920.html

García, L.; Leyva-Díaz, J. C.; Díaz, E.; Ordóñez, S. A Review of the Adsorption-Biological Hybrid Processes for the Abatement of Emerging Pollutants: Removal Efficiencies, Physicochemical Analysis, and Economic Evaluation. *Science of The Total Environment*, **2021**, 780, 146554. https://doi.org/10.1016/j.scitotenv.2021.146554

Gayen, B.; Palchoudhury, S.; Chowdhury, J. Carbon Dots: A Mystic Star in the World of Nanoscience. *Journal of Nanomaterials*, **2019**, e3451307. https://doi.org/10.1155/2019/3451307

Gedda, G.; Lee, C-Y.; Lin, Y-.C.; Wu, H. Green Synthesis of Carbon Dots from Prawn Shells for Highly Selective and Sensitive Detection of Copper Ions. *Sensors and Actuators B: Chemical*, **2016**, 224, 396–403. https://doi.org/10.1016/j.snb.2015.09.065

'Geochimica Ambientale. Metalli Potenzialmente Tossici', (accessed 4 October 2023). https://www.iris.unina.it/handle/11588/304102

Gerstner, Ed. Nobel Prize 2010: Andre Geim & Konstantin Novoselov. *Nature Physics* , **2010**, 6 (11), 836–836. https://doi.org/10.1038/nphys1836

'Graphene Quantum Dots: Introduction and Market News | Graphene-Info', (accessed 27 September 2023). https://www.graphene-info.com/graphene-quantum-dots

'Green Chemistry', (accessed 3 October 2023). https://www.organic-chemistry.org/topics/green-chemistry.shtm

'Green Deal europeo: la chiave per un'UE sostenibile e climaticamente neutrale | Attualità | Parlamento europeo', **2020**, accessed 25 July 2020. https://www.europarl.europa.eu/news/it/headlines/society/20200618STO81513/green-deal-europeo-la-chiave-per-un-ue-sostenibile-e-climaticamente-neutrale

Guan, J.; Fang, Y.; Zhang, T.; Wang, L.; Zhu, H.; Du, M.; Zhang, M. Kelp-Derived Activated Porous Carbon for the Detection of Heavy Metal Ions via Square Wave Anodic Stripping Voltammetry. *Electrocatalysis*, **2020**, 11 (1), 59–67. https://doi.org/10.1007/s12678-019-00568-9

Gutierrez, A. M.; Dziubla, T. D.; Hilt, T. J. Recent Advances on Iron Oxide Magnetic Nanoparticles as Sorbents of Organic Pollutants in Water and Wastewater Treatment.

Reviews on Environmental Health, **2017**, 32 (1–2), 111–17. https://doi.org/10.1515/reveh-2016-0063

Health, Center for Devices and Radiological. 'Code of Federal Regulations - Title 21 - Food and Drugs'. *FDA*, August 2023. https://www.fda.gov/medical-devices/medical-device-databases/code-federal-regulations-title-21-food-and-drugs

Hernández-Montoya, V., M. A. P-C.; Mendoza-Castillo, D.I.; Moreno-Virgen, M. R.; Bonilla-Petriciolet, A. Competitive Adsorption of Dyes and Heavy Metals on Zeolitic Structures. *Journal of Environmental Management*, **2013**, 116, 213–21. https://doi.org/10.1016/j.jenvman.2012.12.010

Hsieh, W. H.; Wan, C-F.; Liao, D.-J.; Wu, A-T. A Turn-on Schiff Base Fluorescence Sensor for Zinc Ion. *Tetrahedron Letters*, **2012**, 53 (44), 5848–51. https://doi.org/10.1016/j.tetlet.2012.08.058

Hu, G. X.; Rao, Q.; Li, G.; Zheng, Y.; Liu, Y.; Guo, C.; Li, F.; Hu, F-X.; Yang, H. B.; Chen, F. A Single-Atom Cobalt Integrated Flexible Sensor for Simultaneous Detection of Dihydroxybenzene Isomers. *Nanoscale*, **2023**, 15 (21), 9484–95. https://doi.org/10.1039/D2NR06293C

Hussin, F.; Hazani, N. N.; Khalil, M.; Kheireddine Aroua, M. Environmental Life Cycle Assessment of Biomass Conversion Using Hydrothermal Technology: A Review. *Fuel Processing Technology*, **2023**, 246, 107747. https://doi.org/10.1016/j.fuproc.2023.107747

Iannazzo, D.; Espro, C.; Ferlazzo, A.; Celesti, C.; Branca, C.; Neri, G. Electrochemical and Fluorescent Properties of Crown Ether Functionalized Graphene Quantum Dots for Potassium and Sodium Ions Detection. *Nanomaterials*, **2021**, 11, 2897. https://doi.org/10.3390/nano11112897

Iannazzo, D.; Pistone, A.; Celesti, C.; Triolo, C.; Patané, S.; Giofré, S.V.; Romeo, R.; Ziccarelli, I.; Mancuso, R.; Gabriele, B.; Visalli, G.; Facciolà, A.; Di Pietro, A. A Smart Nanovector for Cancer Targeted Drug Delivery Based on Graphene Quantum Dots. *Nanomaterials (Basel, Switzerland)*, **2019**, 9 (2), 282. https://doi.org/10.3390/nano9020282

‘IEA Bioenergy Countries’ Report – Update 2021 | Bioenergy’. 18 November 2021. https://www.ieabioenergy.com/blog/publications/iea-bioenergy-countries-report-update-2021/

Illuminati, S.; Annibaldi, A.; Truzzi, C.; Scarponi, G. Heavy Metal Distribution in Organic and Siliceous Marine Sponge Tissues Measured by Square Wave Anodic Stripping Voltammetry. *Marine Pollution Bulletin*, **2016**, 111 (1), 476–82. https://doi.org/10.1016/j.marpolbul.2016.06.098

‘International Union of Pure and Applied Chemistry’, (accessed 6 June 2023). https://publications.iupac.org/compendium/index.html

Inzelt, G. ‘Future of Electrochemistry in Light of History and the Present Conditions’. *Journal of Solid State Electrochemistry*, **2020**, 24 (9), 2089–92. https://doi.org/10.1007/s10008-020-04585-3

‘Italy: biomass & waste energy production 2011-2022’. *Statista*, (accessed 3 October 2023). https://www.statista.com/statistics/753717/gross-energy-production-from-biomass-and-waste-sources-in-italy/

Borrill, J. A.; Reily, N.E.; Macpherson, J. V. Addressing the Practicalities of Anodic Stripping Voltammetry for Heavy Metal Detection: A Tutorial Review. *Analyst*, **2019**, 144 (23), 6834–49. https://doi.org/10.1039/C9AN01437C

Jose, J.; Prakash, P.; Jeyaprabha, B.; Abraham, R.; Mathew, R. M.; Zacharia, E. S.; Thomas, V.; Thomas, J. Principle, Design, Strategies, and Future Perspectives of Heavy Metal Ion Detection Using Carbon Nanomaterial-Based Electrochemical Sensors: A Review. *Journal of the Iranian Chemical Society*, **2023**, 20 (4), 775–91. https://doi.org/10.1007/s13738-022-02730-5

Kainth, S.; Maity, B.; Shetti, N. P.; Basu, S.; Kakarla, R. R. Dual Emissive Carbon Dots: Synthesis Strategies, Properties and Its Ratiometric Sensing Applications. *Nano-Structures & Nano-Objects*, **2023**, 33, 100931. https://doi.org/10.1016/j.nanoso.2022.100931

Kambe, T.; Matsunaga, M.; Takeda, T. Understanding the Contribution of Zinc Transporters in the Function of the Early Secretory Pathway. *International Journal of Molecular Sciences*, **2017**, 18 (10), 2179. https://doi.org/10.3390/ijms18102179

Kambe, T.; Taylor, K. M.; Fu, D. Zinc Transporters and Their Functional Integration in Mammalian Cells. *Journal of Biological Chemistry*, **2021**, 296 (January). https://doi.org/10.1016/j.jbc.2021.100320

Kang, K.; Liu, B.; Yue, G.; Ren, H.; Zheng, K.; Wang, L.; Wang, Z. Preparation of Carbon Quantum Dots from Ionic Liquid Modified Biomass for the Detection of Fe^{3+} and Pd^{2+} in Environmental Water. *Ecotoxicology and Environmental Safety*, **2023**, 255, 114795. https://doi.org/10.1016/j.ecoenv.2023.114795

Kaur, I.; Batra, V.; Kumar Reddy Bogireddy, N.; Torres Landa, S.D.; Agarwal, V. Detection of Organic Pollutants, Food Additives and Antibiotics Using Sustainable Carbon Dots. *Food Chemistry*, **2023**, 406, 135029. https://doi.org/10.1016/j.foodchem.2022.135029

Kocak, T. K.; Kocak, G. O.; Stuart, A M. Polycyclic Aromatic Hydrocarbons in Aquatic Media of Turkey: A Systematic Review of Cancer and Ecological Risk. *Marine Pollution Bulletin*, **2023**, 188, 114671. https://doi.org/10.1016/j.marpolbul.2023.114671

Kumar, V.; Bhatt, D.; Saruchi; Pandey, S. Luminescence Nanomaterials for Biosensing Applications. *Luminescence*, 2023, 38 (7), 1011–25. https://doi.org/10.1002/bio.4373

Lamsal, L. N.; Martin, R.V.; Parrish, D.D.; Krotkov, N.A. Scaling Relationship for NO2 Pollution and Urban Population Size: A Satellite Perspective. *Environmental Science & Technology*, **2013**, 47 (14), 7855–61. https://doi.org/10.1021/es400744g

Larios-Durán, E. R.; Casillas, N.; Bárcena-Soto, M. A Brief Summary of Electrochemistry: From Its Beginnings to Its Present Challenges. *Journal of Solid State Electrochemistry*, **2020**, 24 (9), 2033–34. https://doi.org/10.1007/s10008-020-04692-1

Lavado, L. K.; Zhang, M. H.; Patel, K.; Khan, S.; Patel, U. K.; Lavado, L. K.; Zhang, M. K.; Patel, K.; Khan, S.; Patel, U. K. Biometals as Potential Predictors of the Neurodegenerative Decline in Alzheimer's Disease. *Cureus*, **2019**, 11 (9). https://doi.org/10.7759/cureus.5573

Lee, B.; Stokes, G. A.; Valimukhametova, A.; Nguyen, S.; Gonzalez-Rodriguez, R.; Bhaloo, A.; Coffer, J.; Naumov, A. V. Automated Approach to In Vitro Image-Guided Photothermal Therapy with Top-Down and Bottom-Up-Synthesized Graphene Quantum Dots. *Nanomaterials*, **2023**, 13 (5), 805. https://doi.org/10.3390/nano13050805

Len, T.; Bressi, V.; Balu, A. M.; Kulik, T.; Korchuganova, O.; Palianytsia, B.; Espro, C.; Luque, R. Thermokinetics of Production of Biochar from Crop Residues: An Overview. *Green Chemistry*, **2022**, 24 (20), 7801–17. https://doi.org/10.1039/D2GC02631G

Li, G.; Liu, Z.; Gao, W.; Tang, B. Recent Advancement in Graphene Quantum Dots Based Fluorescent Sensor: Design, Construction and Bio-Medical Applications. *Coordination Chemistry Reviews*, **2023**, 478, 214966. https://doi.org/10.1016/j.ccr.2022.214966

Li, X.; Fu, Y.; Zhao, S.; Xiao, J. F.; Lan, M.; Wang, B.; Zhang, K.; Song, X.; Zeng, L. Metal Ions-Doped Carbon Dots: Synthesis, Properties, and Applications. *Chemical Engineering Journal*, **2022**, 430, 133101. https://doi.org/10.1016/j.cej.2021.133101

Li, X.; Zhou, H.; Fu, C.; Wang, F.; Ding, Y.; Kuang, Y. A Novel Design of Engineered Multi-Walled Carbon Nanotubes Material and Its Improved Performance in Simultaneous Detection of Cd(II) and Pb(II) by Square Wave Anodic Stripping Voltammetry. *Sensors and Actuators B: Chemical*, **2016**, 236, 144–52. https://doi.org/10.1016/j.snb.2016.05.149

Lim, S. K.; Shin, H. S.; Yoon, K. S.; Kwack, S. J.; Um, Y. S.; Hyeon, J. H.; Kwak, H. M.; Kim, J.Y.; Kim, T.Y.; Kim, Y.J.; Roh, T.H.; Lim, D.S.; Shin, M.K.; Choi, S.M.; Kim, H.S.; Lee, B.M. Risk Assessment of Volatile Organic Compounds Benzene, Toluene, Ethylbenzene, and Xylene (BTEX) in Consumer Products. *Journal of*

Toxicology and Environmental Health, Part A, **2014**, 77 (22–24), 1502–21. https://doi.org/10.1080/15287394.2014.955905

Liu, G.; Zheng, H.; Zhixiang Jiang, Jian Zhao, Zhenyu Wang, Bo Pan, and Baoshan Xing. 'Formation and Physicochemical Characteristics of Nano Biochar: Insight into Chemical and Colloidal Stability'. *Environmental Science & Technology*, **2018**, 52 (18): 10369–79. https://doi.org/10.1021/acs.est.8b01481

Liu, P.; Huang, Z.; Gao, X.; Hong, X.; Zhu, J.; Wang, G.; Wu, Y.; Zeng, J.; Zheng, X. Synergy between Palladium Single Atoms and Nanoparticles via Hydrogen Spillover for Enhancing CO_2 Photoreduction to CH_4. *Advanced Materials*, **2022**, 34 (16), 2200057. https://doi.org/10.1002/adma.202200057

Liu, R.; He, R.; Cui, X.; Ma, L. Q. Impact of Particle Size on Distribution, Bioaccessibility, and Cytotoxicity of Polycyclic Aromatic Hydrocarbons in Indoor Dust. *Journal of Hazardous Materials*, **2018**, 357, 341–47. https://doi.org/10.1016/j.jhazmat.2018.05.058

Liu, Y.; Zhu, C.; Gao, Y.; Yang, L.; Xu, J.; Zhang, X.; Lu, C.; Wang, Y.; Zhu, Y. Biomass-Derived Nitrogen Self-Doped Carbon Dots via a Simple One-Pot Method: Physicochemical, Structural, and Luminescence Properties. *Applied Surface Science*, **2020**, 510, 145437. https://doi.org/10.1016/j.apsusc.2020.145437

Liu, Y.; Zhou, Q.; Li, M. L.; Yan, X. Selective and Sensitive Chemosensor for Lead Ions Using Fluorescent Carbon Dots Prepared from Chocolate by One-Step Hydrothermal Method'. *Sensors and Actuators B: Chemical*, **2016**, 237, 597–604. https://doi.org/10.1016/j.snb.2016.06.092

'Looking to the Future of Carbon Nanotube Transistors', Northwestern Engineering, (accessed 27 September 2023). https://www.mccormick.northwestern.edu/news/articles/2022/11/looking-to-the-future-of-carbon-nanotube-transistors/

Maciel, C.C.; de Barros, A.; Mazali, I. O.; Ferreira, M. Flexible Biodegradable Electrochemical Sensor of PBAT and CNDs Composite for the Detection of

Emerging Pollutants. *Journal of Electroanalytical Chemistry*, **2023**, 940, 117491. https://doi.org/10.1016/j.jelechem.2023.117491

Maftouh, A.; El Fatni, O.; El Hajjaji, S.; Jawish, W.; Sillanpää, M. Comparative Review of Different Adsorption Techniques Used in Heavy Metals Removal in Water. *Biointerface Research in Applied Chemistry*, **2023**, 13, 397. https://doi.org/10.33263/BRIAC134.397

Maiocco, S. J.; Walker, L.M.; Elliott, S. J. Chapter Eleven - Determining Redox Potentials of the Iron–Sulfur Clusters of the AdoMet Radical Enzyme Superfamily. In *Methods in Enzymology*, edited by Vahe Bandarian, **2018**, 606, 319–39. Radical SAM Enzymes. Academic Press. https://doi.org/10.1016/bs.mie.2018.06.002

Mansuriya, B. D.; Altintas, Z. Graphene Quantum Dot-Based Electrochemical Immunosensors for Biomedical Applications. *Materials (Basel, Switzerland)*, **2019**, 13 (1), 96. https://doi.org/10.3390/ma13010096

Masoumi, S.; Dalai, A. K. Optimized Production and Characterization of Highly Porous Activated Carbon from Algal-Derived Hydrochar. *Journal of Cleaner Production*, **2020**, 263, 121427. https://doi.org/10.1016/j.jclepro.2020.121427

McKenzie, R. L.; Aucamp, P. J.; Bais, A. F.; Björn, L. O.; Ilyas, M.; Madronich, S. Ozone Depletion and Climate Change: Impacts on UV Radiation. *Photochemical & Photobiological Sciences*, **2011**, 10 (2), 182–98. https://doi.org/10.1039/C0PP90034F

Mehta, J.; Bhardwaj, N.; Bhardwaj, S. K.; Tuteja, S. K.; Vinayak, P.; Paul, A. K.; Kim, K-H; Deep, A. Graphene Quantum Dot Modified Screen Printed Immunosensor for the Determination of Parathion. *Analytical Biochemistry*, **2017**, 523, 1–9. https://doi.org/10.1016/j.ab.2017.01.026

Mejías, C.J.M.; Santos, J. L.; Aparicio, I.; Alonso, E. Adsorption of Perfluoroalkyl Substances on Polyamide Microplastics: Effect of Sorbent and Influence of Environmental Factors. *Environmental Research*, **2023,** 216, 114834. https://doi.org/10.1016/j.envres.2022.114834

Menezes, F. D.; Rezende dos Reis, S. R.; Pinto, S. R.; Portilho, F. L.; Mello, F.d C.; Helal-Neto, E.; Oliveira da Silva de Barros, A.; Graphene Quantum Dots Unraveling: Green Synthesis, Characterization, Radiolabeling with 99mTc, in Vivo Behavior and Mutagenicity. *Materials Science and Engineering: C*, **2019**, 102, 405–14. https://doi.org/10.1016/j.msec.2019.04.058

Meng, S.; Hong, Y.; Dai, Z.; Huang, W.; Dong, X. Simultaneous Detection of Dihydroxybenzene Isomers with ZnO Nanorod/Carbon Cloth Electrodes. *ACS Applied Materials & Interfaces*, **2017**, 9 (14), 12453–60. https://doi.org/10.1021/acsami.7b00546

Michenzi, C.; Espro, C.; Bressi, V.; Celesti, C.; Vetica, F.; Salvitti, C.; Chiarotto, I. Electrochemical Bottom-up Synthesis of Biomass-Derived Carbon Dots for Promoting Knoevenagel Condensation. *Molecular Catalysis*, **2023**, 544, 113182. https://doi.org/10.1016/j.mcat.2023.113182

Mintz, K. J.; Bartoli, M.; Rovere, M.; Zhou, R.; Hettiarachchi, S. D.; Paudyal, S.; Chen, J.; Domena, J. B; Liyanage, P. Y.; Sampson, R.; Khadka, D.; Pandey, R. R.; Huang, S.; Chusuei, C. C.; Tagliaferro, A.; Leblanc, R. A Deep Investigation into the Structure of Carbon Dots. *Carbon*, **2021**, 173 (March): 433–47. https://doi.org/10.1016/j.carbon.2020.11.017

Mohammed, M.A.; Shitu, A.; Ibrahim, A. Removal of Methylene Blue Using Low Cost Adsorbent: A Review. *Research Journal of Chemical Sciences*, **2014**, 4, 91–102

Mosallaei, S.; Hashemi, H.; Hoseini, M.; Dehghani, M.; Naz, A. Polycyclic Aromatic Hydrocarbons (PAHs) in Household Dust: The Association between PAHs, Cancer Risk and Sick Building Syndrome. *Building and Environment*, **2023**, 229, 109966. https://doi.org/10.1016/j.buildenv.2022.109966

Moulaee, K.; Bressi, V.; Ferlazzo, A.; Iannazzo, D.; Espro, C.; Neri, G. Electrochemical Stripping Determination of Trace Heavy Metals Using Screen-Printed Electrodes as a Versatile Approach toward a Mobile Sensing Platform. In *2022 IEEE International Workshop on Metrology for the Sea; Learning to Measure Sea Health Parameters (MetroSea)*, **2022**, 164–67. https://doi.org/10.1109/MetroSea55331.2022.9950951

Muthusaravanan, S.; Sivarajasekar, N.; Vivek, J. S.; Paramasivan, T.; Naushad, M.; Prakashmaran, J.; Gayathri, V.; Al-Duaij, O. K. Phytoremediation of Heavy Metals: Mechanisms, Methods and Enhancements. *Environmental Chemistry Letters*, **2018**, 16 (4), 1339–59. https://doi.org/10.1007/s10311-018-0762-3

Narváez Valderrama, J. F.; García, J. J.; Gil R, D. H.; Ríos S, R.; Gonzalez, J. D.; Porras, J.; Agudelo E, D. M. Adsorption of the Emerging Pollutants on Buena Vista Landfill Cover Material and Implications on Regional Aquatic Pollution. *Groundwater for Sustainable Development*, **2023**, 20, 100885. https://doi.org/10.1016/j.gsd.2022.100885

Naushad, M.; ALOthman, Z. A.; Inamuddin; Javadian, H. Removal of Pb(II) from Aqueous Solution Using Ethylene Diamine Tetra Acetic Acid-Zr(IV) Iodate Composite Cation Exchanger: Kinetics, Isotherms and Thermodynamic Studies. *Journal of Industrial and Engineering Chemistry*, **2015**, 25, 35–41. https://doi.org/10.1016/j.jiec.2014.10.010

Ng, S. M. 12 - Carbon Dots as Optical Nanoprobes for Biosensors'. In *Nanobiosensors for Biomolecular Targeting*, edited by Subash C. B. Gopinath and Thangavel Lakshmipriya, **2019**, 269–300. Micro and Nano Technologies. Elsevier. https://doi.org/10.1016/B978-0-12-813900-4.00012-9

Noor, N. S. M., Tan, L. L.; Heng, L. Y.; Chong, K. F.; Tajuddin, S. N. Acrylic Microspheres-Based Optosensor for Visual Detection of Nitrite. *Food Chemistry*, **2016**, 207, 132–38. https://doi.org/10.1016/j.foodchem.2016.03.088

N.Z.N, A.; Abdullah, W. F. H.; Zain, Z. M.; Rani, S. Embedded 32-Bit Differential Pulse Voltammetry (DPV) Technique for 3-Electrode Cell Sensing. *IOP Conference Series: Materials Science and Engineering*, **2018**, 340 (1), 012016. https://doi.org/10.1088/1757-899X/340/1/012016

Pagés-Díaz, J.; Huiliñir, C. Valorization of the Liquid Fraction of Co-Hydrothermal Carbonization of Mixed Biomass by Anaerobic Digestion: Effect of the Substrate to Inoculum Ratio and Hydrochar Addition. *Bioresource Technology*, **2020**, 317, 123989. https://doi.org/10.1016/j.biortech.2020.123989

Pandi, K.; Sivakumar, M.; Chen, S.-M.; Sakthivel, M.; Raghavi, G.; Chen, T.-W; Liu, Y-C.; Madhu, R. Electrochemical Synthesis of Lutetium (III) Hexacyanoferrate/Poly(Taurine) Modified Glassy Carbon Electrode for the Sensitive Detection of Sulfite in Tap Water. *Journal of The Electrochemical Society*, **2018**, 165 (10), B469. https://doi.org/10.1149/2.1171810jes

Pauline, A. L.; Joseph, K. Hydrothermal Carbonization of Organic Wastes to Carbonaceous Solid Fuel – A Review of Mechanisms and Process Parameters. *Fuel*, **2020**, 279 118472. https://doi.org/10.1016/j.fuel.2020.118472

'Periodic Table - Heavy Metals Callout'. *Homeopathic Associates* (blog), (accessed 4 October 2023). https://secureservercdn.net/166.62.108.229/egw.dab.myftpupload.com/wp-content/uploads/2017/09/Periodic-Table-Heavy-Metals-Callout.gif?time=1640136335

Pi, Y.; Li, X.; Xia, Q.; Wu, J.; Li, Y.; Xiao, J.; Li, Z. Adsorptive and Photocatalytic Removal of Persistent Organic Pollutants (POPs) in Water by Metal-Organic Frameworks (MOFs). *Chemical Engineering Journal*, **2018**, 337, 351–71. https://doi.org/10.1016/j.cej.2017.12.092

Picone, A.; Volpe, M.; Messineo, A. Process Water Recirculation during Hydrothermal Carbonization of Waste Biomass: Current Knowledge and Challenges. *Energies*, **2021**, 14 (10), 2962. https://doi.org/10.3390/en14102962

'*Progress on Household Drinking Water, Sanitation and Hygiene 2000-2020: Five Years into the SDGs*', (accessed 6 June 2023). https://apps.who.int/iris/handle/10665/345081

Rafiq, A.; Ikram, M.; Ali, S.; Niaz, F.; Khan, M.; Khan, Q.; Maqbool, M. Photocatalytic Degradation of Dyes Using Semiconductor Photocatalysts to Clean Industrial Water Pollution. *Journal of Industrial and Engineering Chemistry*, **2021**, 97, 111–28. https://doi.org/10.1016/j.jiec.2021.02.017

Ramanayaka, S.; Hettithanthri, O.; Sandanayake, S.; Vithanage, M. Ecological Effects of Chemical Contaminants Adsorbed to Microplastics. In *Handbook of Microplastics in the Environment*, **2020**, 1–31. https://doi.org/10.1007/978-3-030-10618-8_50-1

Ramanayaka, S.; Vithanage, M.; Alessi, D. S.; Liu, W-S.; Jayasundera, A.C.A.; Ok, Y. S. Nanobiochar: Production, Properties, and Multifunctional Applications. *Environmental Science: Nano*, **2020**, 7 (11), 3279–3302. https://doi.org/10.1039/D0EN00486C

'Renewable Energy Statistics' (accessed 3 October 2023). https://ec.europa.eu/eurostat/statistics-explained/index.php?title=Renewable_energy_statistics

Rodríguez-Tomàs, E.; Baiges-Gaya, G.; Castañé, H.; Arenas, M.; Camps, J.; Joven, J. Trace Elements under the Spotlight: A Powerful Nutritional Tool in Cancer. *Journal of Trace Elements in Medicine and Biology*, **2021**, 68, 126858. https://doi.org/10.1016/j.jtemb.2021.126858

Rossetti, R., S. N.; Brus, L.E. Quantum Size Effects in the Redox Potentials, Resonance Raman Spectra, and Electronic Spectra of CdS Crystallites in Aqueous Solution. *The Journal of Chemical Physics*, **1983**, 79 (2), 1086–88. https://doi.org/10.1063/1.445834

Rossini, E.L.; Milani, M. I.; Redigolo Pezza, H. Green Synthesis of Fluorescent Carbon Dots for Determination of Glucose in Biofluids Using a Paper Platform. *Talanta*, **2019**, 201, 503–10. https://doi.org/10.1016/j.talanta.2019.04.045

Rout, D.R.; Chaurasia, S.; Jena, H. M. Enhanced Photocatalytic Degradation of Malachite Green Using Manganese Oxide Doped Graphene Oxide/Zinc Oxide (GO-ZnO/Mn2O3) Ternary Composite under Sunlight Irradiation. *Journal of Environmental Management*, **2022**, 318, 115449. https://doi.org/10.1016/j.jenvman.2022.115449

Rout, D.R.; Jena, H. M.; Baigenzhenov, O.; Hosseini-Bandegharaei, A. Graphene-Based Materials for Effective Adsorption of Organic and Inorganic Pollutants: A Critical

and Comprehensive Review. *Science of The Total Environment*, **2023**, 863, 160871. https://doi.org/10.1016/j.scitotenv.2022.160871

Saito, Y.; Kikuchi, T. Voltammetry: Theory, Types and Applications-Chemical Engineering Methods and Technology, *Nova Publishers*, **2014**.

Sandford, C.; Edwards, M. A.; Klunder, K.J.; Hickey, D. P.; Li, M.; Barman, K.; Sigman, M. S.; White, H. S.; Minteer, D. S. A Synthetic Chemist's Guide to Electroanalytical Tools for Studying Reaction Mechanisms. *Chemical Science*, **2019**, 10 (26), 6404–22. https://doi.org/10.1039/C9SC01545K

Saputra, H.A. Electrochemical Sensors: Basic Principles, Engineering, and State of the Art. *Monatshefte Für Chemie - Chemical Monthly*, **2023**, 154 (10), 1083–1100. https://doi.org/10.1007/s00706-023-03113-z

Satarug, S.; Vesey, D. A.; Gobe, G. C.; Phelps, K. R. Estimation of Health Risks Associated with Dietary Cadmium Exposure. *Archives of Toxicology*, **2023**, 97 (2), 329–58. https://doi.org/10.1007/s00204-022-03432-w

Satira, A.; Paone, E.; Bressi, V.; Iannazzo, D.; Marra, F.; Calabrò, P. S.; Mauriello, F.; Espro, C. Hydrothermal Carbonization as Sustainable Process for the Complete Upgrading of Orange Peel Waste into Value-Added Chemicals and Bio-Carbon Materials. *Applied Sciences*, **2021**, 11 (22), 10983. https://doi.org/10.3390/app112210983

Sawalha, S.; Moulaee, K.; Nocito, G.; Silvestri, A.; Petralia, S.; Prato, M.; Bettini, S.; Valli, L.; Conoci, S.; Neri, G. Carbon-Dots Conductometric Sensor for High Performance Gas Sensing. *Carbon Trends*, **2021**, 5, 100105. https://doi.org/10.1016/j.cartre.2021.100105

Schnepf, R. Agriculture-Based Biofuels: Overview and Emerging Issues. *Congressional Research Service Reports. Paper*, **2010**, 17.

Shao, Y.; Zhu, C.; Fu, Z.; Lin, K.; Wang, Y.; Chang, Y.; Han, L.; Yu, H.; Tian, F. Green Synthesis of Multifunctional Fluorescent Carbon Dots from Mulberry Leaves (Morus Alba L.) Residues for Simultaneous Intracellular Imaging and Drug

Delivery. *Journal of Nanoparticle Research*, **2020**, 22 (8), 229. https://doi.org/10.1007/s11051-020-04917-4

Sharma, S.; Meena, R.; Sharma, A.; Goyal, P. Biomass Conversion Technologies for Renewable Energy and Fuels: A Review Note. *IOSR Journal of Mechanical and Civil Engineering*, **2014**, 11, 28–35. https://doi.org/10.9790/1684-11232835

Shen, Y. A Review on Hydrothermal Carbonization of Biomass and Plastic Wastes to Energy Products. *Biomass and Bioenergy*, **2020**, 134, 105479. https://doi.org/10.1016/j.biombioe.2020.105479

Shetty, A.; Molahalli, V.; Sharma, A.; Hegde, G. Biomass-Derived Carbon Materials in Heterogeneous Catalysis: A Step towards Sustainable Future. *Catalysts*, **2023**, 13 (1), 20. https://doi.org/10.3390/catal13010020

Shivalkar, S.; Gautam, P. K.; Verma, A.; Maurya, K.; Palashuddin Sk, Md.; Samanta, S. K.; Sahoo, A. K. Autonomous Magnetic Microbots for Environmental Remediation Developed by Organic Waste Derived Carbon Dots. *Journal of Environmental Management*, **2021**, 297, 113322. https://doi.org/10.1016/j.jenvman.2021.113322

Silva, E. M.; Takeuchi, R. M.; Santos, A. L. Carbon Nanotubes for Voltammetric Determination of Sulphite in Some Beverages. *Food Chemistry*, **2015**, 173, 763–69. https://doi.org/10.1016/j.foodchem.2014.10.106

Simões, F. R.; Xavier, M. G. '6 - Electrochemical Sensors'. In *Nanoscience and Its Applications*, edited by Alessandra L. Da Róz, Marystela Ferreira, Fábio de Lima Leite, and Osvaldo N. Oliveira, **2016**, 155–78. Micro and Nano Technologies. William Andrew Publishing. https://doi.org/10.1016/B978-0-323-49780-0.00006-5

Singh, M.; Pandey, N.; Dwivedi, P.; Kumar, V.; Bhuwan B. Mishra, B. Production of Xylose, Levulinic Acid, and Lignin from Spent Aromatic Biomass with a Recyclable Brønsted Acid Synthesized from d-Limonene as Renewable Feedstock from Citrus Waste. *Bioresource Technology*, **2019**, 293, 122105. https://doi.org/10.1016/j.biortech.2019.122105

Spagnuolo, D.; Iannazzo, D.; Len, T.; Balu, A. M.; Morabito, M.; Genovese, G.; Espro, C.; Bressi, V. Hydrochar from Sargassum Muticum: A Sustainable Approach for High-Capacity Removal of Rhodamine B Dye. *RSC Sustainability*, **2023**. https://doi.org/10.1039/D3SU00134B

'Statistical Review of World Energy | Energy Economics | Home'. Bp Global (accessed 3 October 2023). https://www.bp.com/en/global/corporate/energy-economics/statistical-review-of-world-energy.html

Sun, J.; Yang, S.; Wang, Z.; Shen, H.; Xu, T.; Sun, L.; Li, H.; Chen, W.; Jiang, X.; Ding, G.; Kang, Z.; Xie, X.; Jiang, M. Ultra-High Quantum Yield of Graphene Quantum Dots: Aromatic-Nitrogen Doping and Photoluminescence Mechanism. *Particle & Particle Systems Characterization*, 2015, 32 (4), 434–40. https://doi.org/10.1002/ppsc.201400189

Sun, Y-P; Zhou, B.; Lin, Y.; Wang, W.; Shiral Fernando, K.A.; Pathak, P.; Meziani, M. J. Harruff, B. A.; Wang, X.; Wang, H.; Luo, P. G.; Yang, H.; Kose, M. E.; Chen, B.; Veca, L. M.; Xie, S. Quantum-Sized Carbon Dots for Bright and Colorful Photoluminescence. *Journal of the American Chemical Society*, **2006**, 128 (24), 7756–57. https://doi.org/10.1021/ja062677d

Supriya, S.; Ananthnag, G. S.; Maiyalagan, T.; Hegde, G. Kitchen Waste Derived Porous Nanocarbon Spheres for Metal Free Degradation of Azo Dyes: An Environmental Friendly, Cost Effective Method. *Journal of Cluster Science*, **2023**, 34 (1), 243–54. https://doi.org/10.1007/s10876-021-02208-z

Suresh, U.; Subhadra, S.; Sivaramakrishnan, S. Green Hydrothermal Synthesis of Carbon Dot-Silver Nanocomposite from Chondrococcus Hornemanni (Marine Algae): An Application of Mosquitocidal, Anti-Bacterial, and Anti-Cancer (MDA-MB-231 Cells). *Biomass Conversion and Biorefinery*, **2023**. https://doi.org/10.1007/s13399-023-04214-9

Suvarnaphaet, P.; Pechprasarn, S. Graphene-Based Materials for Biosensors: A Review. *Sensors*, **2017**, 17 (10), 2161. https://doi.org/10.3390/s17102161

Szuba-Trznadel, A.; Rząsa, A.; Hikawczuk, T.; Fuchs, B. Effect of Zinc Source and Level on Growth Performance and Zinc Status of Weaned Piglets'. *Animals*, **2021**, 11 (7), 2030. https://doi.org/10.3390/ani11072030

Tahir, M.B.; Nawaz, T.; Nabi, G.; Sagir, M.; Khan, M. I.; Malik, N. Role of Nanophotocatalysts for the Treatment of Hazardous Organic and Inorganic Pollutants in Wastewater. *International Journal of Environmental Analytical Chemistry*, **2022**, 102 (2), 491–515. https://doi.org/10.1080/03067319.2020.1723570

Tasca, A.L.; Puccini, M.; Gori, R.; Corsi, I.; Raspolli Galletti, A. M.; Vitolo, S. Hydrothermal Carbonization of Sewage Sludge: A Critical Analysis of Process Severity, Hydrochar Properties and Environmental Implications. *Waste Management*, **2019**, 93, 1–13. https://doi.org/10.1016/j.wasman.2019.05.027

Tejwan, N.; Saini, A. K.; Sharma, A.; Singh, T. A.; Kumar, N.; Das, J. Metal-Doped and Hybrid Carbon Dots: A Comprehensive Review on Their Synthesis and Biomedical Applications. *Journal of Controlled Release*, **2021**, 330, 132–50. https://doi.org/10.1016/j.jconrel.2020.12.023

Thakur, S.; Qanungo, K. Removal of Aniline Blue from Aqueous Solution Using Adsorption: A Mini Review. *Materials Today: Proceedings*, International Conference on Newer Trends and Innovation in Mechanical Engineering: Materials Science, **2021**, 37, 2290–93. https://doi.org/10.1016/j.matpr.2020.07.725

'THE 17 GOALS | Sustainable Development'. Accessed 30 July 2023. https://sdgs.un.org/goals

Tu, W.; Liu, Y.; Xie, Z.; Chen, M.; Ma, L.; Du, G.; Zhu, M. A Novel Activation-Hydrochar via Hydrothermal Carbonization and KOH Activation of Sewage Sludge and Coconut Shell for Biomass Wastes: Preparation, Characterization and Adsorption Properties. *Journal of Colloid and Interface Science*, **2021**, 593, 390–407. https://doi.org/10.1016/j.jcis.2021.02.133

Usman, M.; Chen, H.; Chen, K.; Ren, S.; Clark, J. H.; Fan, J.; Luo, G.; Zhang, S. Characterization and Utilization of Aqueous Products from Hydrothermal

Conversion of Biomass for Bio-Oil and Hydro-Char Production: A Review. *Green Chemistry*, **2019**, 21 (7), 1553–72. https://doi.org/10.1039/C8GC03957G

Venton, B. J.; DiScenza, D. J. 'Chapter 3 - Voltammetry'. In *Electrochemistry for Bioanalysis*, edited by Bhavik Patel, **2020**, 27–50. Elsevier. https://doi.org/10.1016/B978-0-12-821203-5.00004-X

Viggiano, S.; Panzella, L.; Reichenbach, M.; Hans, J.; Napolitano, A. The Effect of Cosmetic Ingredients of Phenol Type on Immediate Pigment Darkening and Their (Photo) Protective Action in Association with Melanin Pigmentation: A Model In Vitro Study. *Cosmetics*, **2023**, 10 (1), 22. https://doi.org/10.3390/cosmetics10010022

Wang, D.; Wang, L.; Dong, X.; Shi, Z.; Jin, J. Chemically Tailoring Graphene Oxides into Fluorescent Nanosheets for Fe^{3+} Ion Detection. *Carbon*, **2012**, 50 (6), 2147–54. https://doi.org/10.1016/j.carbon.2012.01.021

Wang, J.; Alli, A. S.; Clark, S.; Hughes, A.; Ezzati, M.; Beddows, A.; Vallarino, J.; Nimo, J.; Bedford-Moses, J.; Baah, S.; Owusu, G.; Agyemang, E.; Kelly, F.; Barratt, B.; Beevers, S.; Agyei-Mensah, S.; Baumgartner, J.; Brauer, M.; Arku, R. E. Nitrogen Oxides (NO and NO_2) Pollution in the Accra Metropolis: Spatiotemporal Patterns and the Role of Meteorology. *Science of The Total Environment*, **2022**, 803,149931. https://doi.org/10.1016/j.scitotenv.2021.149931

Wang, L.; Li, W.; Wu, B.; Li, Z.; Wang, S.; Liu, Y.; Pan, D.; Wu, M. Facile Synthesis of Fluorescent Graphene Quantum Dots from Coffee Grounds for Bioimaging and Sensing. *Chemical Engineering Journal*, **2016**, 300, 75–82. https://doi.org/10.1016/j.cej.2016.04.123

Wang, S.; Cole, I. S.; Li., Q. The Toxicity of Graphene Quantum Dots. *RSC Advances*, **2016**, 6, (92): 89867–78. https://doi.org/10.1039/C6RA16516H

Wang, T.; Yue, W. Carbon Nanotubes Heavy Metal Detection with Stripping Voltammetry: A Review Paper. *Electroanalysis*, **2017**, 29 (10), 2178–89. https://doi.org/10.1002/elan.201700276

Wang, Y.; Wu, X.; Sun, J.; Wang, C.; Zhu, G.; Bai, L-P.; Jiang, Z-H.; Zhang, W. Stripping Voltammetric Determination of Cadmium and Lead Ions Based on a Bismuth Oxide Surface-Decorated Nanoporous Bismuth Electrode. *Electrochemistry Communications*, **2022**, 136, 107233. https://doi.org/10.1016/j.elecom.2022.107233

'*Water and Sanitation Are a Human Right!*' 2020. Right to Water. 22 March 2020. https://www.right2water.eu/

Wernberg, T.; Thomsen, M. D.; Baum, J. K.; Bishop, M. J.; Bruno, J. F.; Coleman, M. A.; Filbee-Dexter, K.; Gagnon, K.; He, Q.; Murdiyarso, D.; Rogers, K.; R Silliman, B.; Smale, A. D.; Starko, S. A.; Vanderklift, M. Impacts of Climate Change on Marine Foundation Species. *Annual Review of Marine Science*, **2024**, 16 (1). https://doi.org/10.1146/annurev-marine-042023-093037

'*WHO Guidance to Reduce Illness Due to Lead Exposure*', (accessed 4 October 2023). https://www.who.int/news/item/27-10-2021-who-guidance-to-reduce-illness-due-to-lead-exposure

Wu, J.; Chen, T.; Ge, S.; Fan, W.; Wang, H.; Zhang, Z.; Lichtfouse, E.; Van Tran, T.; Liew, R. K.; Rezakazemi, M.; Huang, R. Synthesis and Applications of Carbon Quantum Dots Derived from Biomass Waste: A Review. *Environmental Chemistry Letters*, **2023**, 21 (6), 3393–3424. https://doi.org/10.1007/s10311-023-01636-9

Xiao, J.; Shen, Y.; Yang, X.; Wei, M.; Meng, W.; Wang, Z. Methylene Blue Can Increase the Number of Lymph Nodes Harvested in Colorectal Cancer: A Meta-Analysis. *International Journal of Colorectal Disease*, **2023**, 38 (1), 50. https://doi.org/10.1007/s00384-023-04312-0

Xiong, Z-H.; Zou, Y-N.; Cao, X-C.; Lin, Z-H. Color-Tunable Fluorescent Nitrogen-Doped Graphene Quantum Dots Derived from Pineapple Leaf Fiber Biomass to Detect Hg^{2+}. *Chinese Journal of Analytical Chemistry*, **2022**, 50 (2), 69–76. https://doi.org/10.1016/j.cjac.2021.10.003

Xu, M.; Wang, A.; Xiang, Y.; Niu, J. Biomass-Based Porous Carbon/Graphene Self-Assembled Composite Aerogels for High-Rate Performance Supercapacitor. *Journal*

of Cleaner Production, **2021**, 315, 128110. https://doi.org/10.1016/j.jclepro.2021.128110

Xu, X.; Ray, R.; Gu, Y.; Ploehn, H.J.; Gearheart, L.; Raker, K.; Scrivens, W.A. Electrophoretic Analysis and Purification of Fluorescent Single-Walled Carbon Nanotube Fragments. *Journal of the American Chemical Society*, **2004**, 126 (40), 12736–37. https://doi.org/10.1021/ja040082h

Yadav, V.; Baruah, B.P.; Khare, P. Comparative Study of Thermal Properties of Bio-Coal from Aromatic Spent with Low Rank Sub-Bituminous Coals. *BIORESOURCE TECHNOLOGY*, **2013**, 137, 376–85. https://doi.org/10.1016/j.biortech.2013.03.131

Yadavalli, S.S.; Sen, B.; Acharyya, S. G. Simultaneous Detection of Cd^{2+}, Pb^{2+}, and As^{3+} Ions in Water Using Green-Synthesized Gold Nanoparticles by Square Wave Anodic Stripping Voltammetry. *IEEE Sensors Journal*, **2023**, 23 (6), 5569–76. https://doi.org/10.1109/JSEN.2023.3241158

Yang, S.; Mao, X.; Cao, Z.; Yin, Y.; Wang, Z.; Shi, M.; Dong, H. Onion-Derived N, S Self-Doped Carbon Materials as Highly Efficient Metal-Free Electrocatalysts for the Oxygen Reduction Reaction. *Applied Surface Science*, **2018**, 427, 626–34. https://doi.org/10.1016/j.apsusc.2017.08.222

Yang, S.; Yang, M.; Yao, X.; Fa, H.; Wang, Y.; Hou, C. A Zeolitic Imidazolate Framework/Carbon Nanofiber Nanocomposite Based Electrochemical Sensor for Simultaneous Detection of Co-Existing Dihydroxybenzene Isomers. *Sensors and Actuators B: Chemical*, **2020**, 320, 128294. https://doi.org/10.1016/j.snb.2020.128294

Youssef, A. M.; Malhat, F. M. Selective Removal of Heavy Metals from Drinking Water Using Titanium Dioxide Nanowire. *Macromolecular Symposia*, **2014**, 337 (1), 96–101. https://doi.org/10.1002/masy.201450311

Yuan, X.; Wu, Z.; Zhong, H.; Wang, H.; Chen, X.; Leng, L.; Jiang, L.; Xiao, Z.; Zeng, G. Fast Removal of Tetracycline from Wastewater by Reduced Graphene Oxide Prepared via Microwave-Assisted Ethylenediamine–N,N'–Disuccinic Acid

Induction Method. *Environmental Science and Pollution Research*, **2016**, 23 (18), 18657–71. https://doi.org/10.1007/s11356-016-6892-x

Zdrachek, E.; Bakker, E. 'Potentiometric Sensing'. *Analytical Chemistry*, **2019**, 91 (1), 2–26. https://doi.org/10.1021/acs.analchem.8b04681

Zha, S.X.; Zhou, Y.; Jin, X.; Chen, Z. The Removal of Amoxicillin from Wastewater Using Organobentonite. *Journal of Environmental Management*, **2013**, 129, 569–76. https://doi.org/10.1016/j.jenvman.2013.08.032

Zhang, J.; Chen, H.; Liu, J.; Gui, J.; Liu, M.; Zhang, Y.; Yao, S. The Target-Induced Redox and Diazotized Reaction for Colorimetric Ratio Detection of Nitrite Using CoOOH Nanosheets as Mimetic Oxidase. *Talanta*, **2023**, 258, 124458. https://doi.org/10.1016/j.talanta.2023.124458

Zhang, P.; Su, J.; Guo, J.; Hu, S. Influence of Carbon Nanotube on Properties of Concrete: A Review. *Construction and Building Materials*, **2023**, 369, 130388. https://doi.org/10.1016/j.conbuildmat.2023.130388

Zhang, Y.; Niu, Q.; Gu, X.; Yang, N.; Zhao, G. Recent Progress on Carbon Nanomaterials for the Electrochemical Detection and Removal of Environmental Pollutants. *Nanoscale*, **2019**, 11 (25), 11992–14. https://doi.org/10.1039/C9NR02935D

Zhou, Y.; He, J.; Chen, R.; Li, X. Recent Advances in Biomass-Derived Graphene and Carbon Nanotubes. *Materials Today Sustainability*, **2022**, 18, 100138. https://doi.org/10.1016/j.mtsust.2022.100138

Zhu, S.; Song, Y.; Wang, J.; Wan, H.; Zhang, Y.; Ning, Y.; Yang, B. Photoluminescence Mechanism in Graphene Quantum Dots: Quantum Confinement Effect and Surface/Edge State. *Nano Today*, **2017**, 13, 10–14. https://doi.org/10.1016/j.nantod.2016.12.006.

Chapter 2. Materials and Methods

The materials employed, the associated synthetic procedures, and application strategies will all be thoroughly examined in this section, outlining the rationale for selecting these particular resources and methods. Both biomass and non-biomass materials were used in this PhD thesis to evaluate different aspects of their environmentally friendly utilization. This chapter will also provide a brief overview of the various characterization techniques used to assess the optical and electrical properties of the resultant materials. The technique for environmental application and sensor setup will then be described, and a whole discussion of the recognized electrochemical and non-electrochemical tests will follow.

2.1 Materials

Hydrothermal treatment (HTC) was applied to various biomass sources, and the resulting products were subjected to comprehensive characterization before being utilized for environmental applications. The primary product of the HTC process is a carbonaceous solid referred to as hydrochar. Hydrochar is pivotal in mitigating carbon dioxide (CO_2) production and reducing greenhouse gas emissions (Sri Shalini S. *et al.*, 2021). Notably, during its production from lignocellulosic and vegetative biomass, approximately 90% of the carbon becomes sequestered within the char in a stable form, capable of enduring in the soil for over a century Furthermore, using hydrochar in agricultural and animal practices helps lower nitrous oxide (NO_2) emissions and sequester pure CO_2 in the soil. Consequently, producing and applying hydrochar to the environment is a sustainable strategy, garnering global attention. The best biomass sources for producing hydrochar are thought to be wood and

lignocellulosic wastes (such as cereal straw, fruit peels, and seeds) (Len *et al.*, 2022). Another benefit of the hydrothermal method is that it produces a liquid phase that is abundant in bioactive chemicals and can be easily extracted, thereby eliminating lipophilic components from the organic matrix and making quick extraction operations possible. The preference for the hydrothermal process over alternative biomass conversion methods arises from its mild operating conditions and the feasibility of employing materials with high water content, such as algae or orange peels. As described in more detail in the previous chapter, HTC entails adding fresh biomass and water to an autogenous pressure autoclave for reactions that can take minutes to days and have a maximum temperature of 400 °C. A list of the analyzed biomass sources is provided in the following section. . The final products were also thoroughly characterized before being used in environmental fields.

Brewing waste and other biomass-derived materials were chosen for their environmentally friendly and sustainable properties, which aligns the Green Chemistry principles. However, non-biomass materials, such as the Schiff base, were included in these studies because of their distinctive qualities and functions. The Schiff base's versatile coordination chemistry and capacity to interact with divalent metals made it an essential part of the research aimed at improving the fundamental understanding of electrochemical detection of heavy metals. This approach facilitated bridging the gap between conventional chemical synthesis and sustainable, biomass-based methods, thereby playing a role in the progress of environmentally conscious processes within the domains of electrochemical sensing and environmental pollutant detection.

2.1.1 Orange peels waste

During food production, industries frequently need to dispose of specific resources (Espro *et al.*, 2021). This is the situation with citrus peels, which have various purposes despite being unable to be used directly to make juice. In the world of citrus fruits, oranges are highly valued, boasting a remarkable yearly production rate of almost 2 million tons (iSTAT, 2023) in Italy ("*Coltivazioni : Coltivazioni legnose fruttifere*," 2023). Their popularity is due to their delicious taste and rich nutritional value. Vitamins, as well as different mineral salts like calcium, phosphorus, and potassium, dietary fiber, and a wide range of phytochemical components that are good for human health, are all abundant in oranges. The citrus industries produce about 170.000 tons of citrus peels per day ("*Progetto C.L.I.M.A., economia circolare. Visita alla multinazionale CARGILL PEC ITALY*," 2023), which results in a significant amount of waste that, despite being biodegradable, requires careful and expensive disposal. The "pastazzo", which makes up about 60% of the weight of the fruit and is the primary by-product of the industrial transformation of citrus (Sorrenti *et al.*, 2023), results in an annual waste output of around 700.000 tonnes.

According to a chemical-physical point of view, pastazzo (**Figure 2.1**) is composed primarily of peels (60–75%), pulp (30–35%), and seeds (0–9% on average, depending on the grade of the oranges and lemons that were transformed) (Tittarelli *et al.*, 2002). It can be used for a number of purposes, the most well-known of which are the organic fertilization of soil, the

Figure 2.1. ***Pastazzo***

feeding of cattle, and the extraction of pectin, a naturally occurring polysaccharide that thickens fruit and is commonly utilized in the making of jams. Citrus pulp is used as biomass, in part due to scientific advancements, for the production of electricity, biogas, and bioethanol, as well as for the extraction of chemicals with high added values such as pectins, lactic acid, furfural, and levulinic acid (**Table 2.1**). When used directly on fresh orange peels with an 80% moisture content or above, the hydrothermal method presents a highly effective alternative. In this thesis work, the orange peel waste was put in an autoclave with various solid/liquid ratios of deionized water. The reaction mixture was heated under autogenous pressure for various residence times (30 min, 60 min, 180 min, and 300 min) until it reached the reaction temperature (150-300 °C). Since the orange peels are abundant in alcohols, phenols, and furan compounds, commonly used in the literature for carbon nanomaterial synthesis, the liquid phase generated through hydrothermal carbonization (HTC) of orange peel waste was employed as the primary feedstock for an innovative carbon nanomaterial synthesis method by developing a novel approach, integrating HTC with the electrochemical treatment (EC).

Table 2.1. *Major chemical components of organic phase obtained from HTC of orange peels waste detected by GC-MS analysis*[a]

	Compound Name	**Peak area %**
Furans	Furfural (FU)	16.69
	5-Methylfurfural	7.88
	5-Hydroxymethylfurfural (5-HMF)	61.82
Phenols	Phenol	0.1
	Catechol	0.29
	1,2-Benzenediol, 3-methyl	0.11
Acids	Benzoic acid	0.61
Ketones	2-Pentanone, 4-hydroxy-4-methyl	0.68

	Ethanone, 1-(2-furanyl)	0.46
	1,2-Cyclopentanedione, 3-methyl	0.81
Aldehydes	1H-Pyrrole-2-carboxaldehyde	0.41
	Benzaldehyde, 3-hydroxy	0.17
Alcohols	α-Terpineol	0.24
Alkenes	1-Nonadecene	0.33
	1-Pentadecene	0.59

[a] Chromatogram has been reported in ref. (Satira *et al.*, 2021)

2.1.2 Bagasse beer waste

One of the biggest and oldest industries in the food industry is the beer industry. Beer is an ancient beverage that dates back at least 7000 years. In reality, historical records from the ancient Egyptians to the Greeks, the inhabitants of Mesopotamia, and the Romans all witness the beer consumption. The Hymn to Ninkasi, a Sumerian hymn composed 3900 years ago and addressed explicitly to this patron deity of brewing beer, has our oldest beer recipe. Beer is currently one of the most popular alcoholic beverages in the world. It requires several steps, including the fermentation of essential materials such as barley malt, hops, water, and yeast. Waste and derivatives can be produced during brewing, often used as energy sources and as animal feed. The majority of the organic waste among these products is made up of beer bagasse (**Figure 2.2**), estimating that for every hectoliter of beer, 20 kg of bagasse beer is produced (Castro-Criado *et al.*, 2023; Ferrari *et al.*, 2016), which is commonly dismissed as basic brewing waste. The issue of waste management has become more critical in our quickly

Figure 2.2. ***Bagasse beer***

evolving world since many different types of materials are being thrown daily. Bagasse is a by-product of the beer industry created during the pressing and filtration of the wort after cereal malt has been saccharified (Castro-Criado *et al.*, 2023) and represents a widely accessible, simple-to-process, and logistically advantageous agro-industrial bio-waste. Researchers have studied the use of these organic by-products from brewing and agriculture to disinfest the soil, preserve healthy soil microorganisms, and increase yields in recent years to try to reduce waste from the agricultural industry and the amounts of harmful chemicals used (Cechinel *et al.*, 2022; Gokulakrishnan *et al.*, 2023; Magar *et al.*, 2023). Beer bagasse's dry basis composition is high in proteins (15–25%) and lignocellulosic matter (70%) and presents itself as an ideal starting material for several applications (Castro-Criado *et al.*, 2023). An industry collected the bagasse beer used in this thesis in Seville. It was initially sieved to eliminate any grinding by ball-milling at 450 rpm for 10 minutes to reduce the initial size and make the powder uniform. In order to convert the biomass into hydrochar, which was employed as a substrate for catalysts for environmentally friendly conversions and/or the synthesis of carbonaceous nanomaterials used in sensor systems, the powder thus obtained was put through a hydrothermal procedure.

2.1.3 Algae *Sargassum Muticum*

Without a strict taxonomic categorization, algae are an artificial group of aquatic plants, which include a variety of photosynthetic organisms, from simple single cells to intricate multicellular thalli (Wehr, 2007). The multicellular forms of algae, or macroalgae, stand out within this diverse group as fascinating natural sources of chemical compounds with anti-inflammatory, antibacterial, anti-inflammatory, antioxidant, and anticancer activities (Bilal and Iqbal, 2020; Marino *et al.*, 2016). Nevertheless, macroalgae, particularly those that live in transitional ecosystems like artificial coastal areas, greatly contribute to the production of garbage, needing ongoing clearance efforts (Zammuto *et al.*, 2022).

Figure 2.3. ***Algae Sargassum Muticum in Venice Lagoon***

The Lagoon of Venice is one such coastal region dealing with these difficulties. Its shallow coastal waters and many human-induced conditions may encourage the introduction and spread of non-native species, which can outcompete local flora. Among these alien species, the brown macroalgae *Sargassum muticum* (Phaeophyceae) has made a name for itself in the Venice Lagoon by primarily colonizing the docks in the old centre (**Figure 2.3**). *Sargassum muticum*'s uncontrolled development can have negative effects on the environment; hence, it is urgent to dispose of them (Louime *et al.*, 2017). A potential strategy to fix this issue is to collect invasive algae species and convert them into valuable bioactive substances (Kandasamy *et al.*, 2023). This strategy shows promise for reducing the harmful effects on the environment caused by the unchecked

proliferation of algae. These algae's extracts have demonstrated biological activity including bactericidal and fungicidal effects. Despite having valuable properties, algae can sometimes grow out of control and cause environmental problems, making it difficult to dispose of them. Therefore, HTC approach was performed to convert algae. In order to characterize the solid products and determine how the factors affected their final qualities, the temperature and reaction time of the hydrothermal method used to treat the algae were varied. In particular, a set solid/liquid ratio (5 gr/100 mL) was used to transfer a mixture of algae and deionized water to a stainless steel autoclave. At three different reaction temperatures of 180, 240, and 300 °C, the reaction mixture was heated for 60, 180, and 300 minutes, respectively. The hydrochars collected were used as adsorption materials for the removal of organic contaminants from water.

2.1.4 Other materials not derived from biomass

Schiff base ligands have been known for a very long time and are simple to make through the condensation of primary amines and carbonyl compounds, which results in the formation of the distinctive azomethine link (Fabbrizzi, 2020). Due to their distinctive characteristics, such as high stability and selectivity to metal coordination, good reproducibility, more active sites, and good homogeneity, Schiff bases have played a crucial role in the development of coordination chemistry (Anbu Durai *et al.*, 2020; Kaur *et al.*, 2020). This makes them particularly appealing in the field of metal ion recognition, especially by means of optical techniques. Due to their excellent adaptability in the chemical analysis of heavy metal ions, electrochemical sensors have drawn a lot of attention in recent years. Innovative electrodes for the electrochemical detection of heavy metal ions in water have been developed using a variety of Schiff bases (Forzani *et al.*, 2005; Ghosh *et al.*, 2021; Mohammed *et al.*, 2022).

A research team from Yasouj University synthesized the Shiff base that was utilized in this project, and investigations on its electrochemical and optical characteristics were done. This base was chosen because of its structure, shown in **Figure 2.4**, which enables the coordination of divalent metals due to its appearance as a bidentate structure and the placement of the two central imine N atoms.

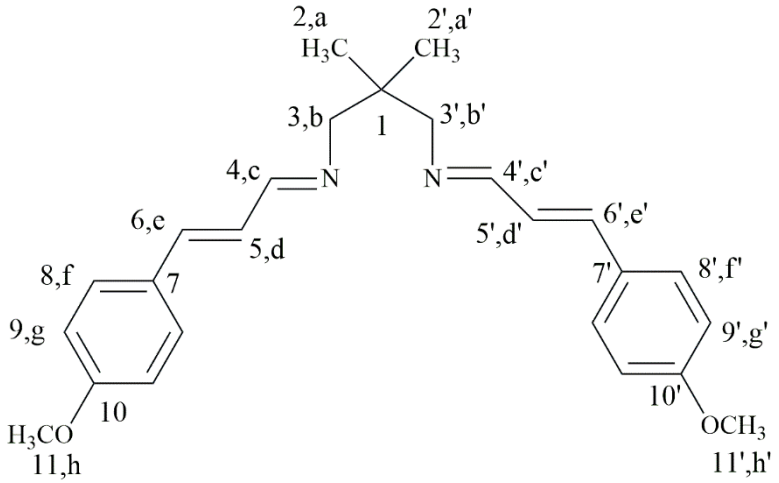

Figure 2.4. Shiff base ligand structure (L2)

2.2 Materials Characterization and Electrical Behavior Analysis: Equipment and Techniques

Several characterization methods have been developed to explore and investigate the morphological, chemical-physical, and optical properties of the reported materials. Specifically, various methods falling into the following categories have been employed:

- **Structural Analysis Techniques:** Scanning Electron Microscopy (SEM), Transmission Electron Microscopy (TEM), X-ray Diffraction (XRD).
- **Particle Size and Distribution Analysis Techniques:** Dynamic Light Scattering (DLS).
- **Chemical Analysis Techniques:** Fourier-Transform Infrared Spectroscopy (FTIR), and Brunauer–Emmett–Teller (BET) Surface Area Analysis.
- **Optical Analysis Techniques:** UV-Visible Spectroscopy (UV-Vis), and Fluorescence Spectroscopy.

Besides material comprehension, it is crucial to grasp the electrochemical behavior that underlies the employment of these materials in the sensing field. In this context, electrical studies have been conducted on the modified sensors by performing Electrochemical Impedance Spectroscopy (EIS).

2.2.1 Structural Analysis Techniques

The morphological and physical architecture of various materials can be explored and studied using several structural analysis techniques. From macroscale structures to nanoscale conFiguretions, these analytical tools offer useful information on the arrangement, morphology, composition, and shape of materials from various sources. Structural analysis techniques are noteworthy in many scientific fields, such as chemistry, materials science, and engineering, because they let researchers learn crucial information about the characteristics and behavior of substances. In this context, many important morpho-structural analysis methods are thoroughly examined. These methods serve as essential

tools in the search for greater comprehension and innovation across various scientific and technical domains.

2.2.1.1 Scanning Electron Microscopy (SEM)

The human eye can detect objects just under a millimeter in size. In order to observe objects at the micrometer scale, such as bacteria or certain human cells, an optical microscope is necessary. However, electron microscopy becomes essential for viewing materials and objects that are considerably smaller, at the nanometer or even low level. Electron microscopy is a technique that exploits on the interaction between an electron beam and the atoms constituting the sample under examination. It enables the generation of images at exceptionally high magnifications, surpassing the limits of optical microscopy represented by the light. The scanning electron microscope (SEM) possesses a significantly higher resolution limit, typically in the nanometer range, owing to the utilization of electrons whose wavelength is three orders of magnitude shorter than that of photons. Moreover, SEM provides images with a greater depth of field and, if equipped with an EDX detector, the capability to analyze the sample's composition (elemental analysis). The instrument involves an electron emitter, typically represented by a tungsten filament, which is heated to high temperatures, generating electrons through the thermionic effect. A potential difference then accelerates the resulting electron beam. It first passes through several electromagnetic lens to undergo deflection for scanning purposes. Ultimately, it impacts the sample’s surface, which is positioned on a holder at the instrument’s base. When the electrons strike the sample surface, some electrons may experience elastic scattering, while others may become captured, releasing energy at the energy levels of the surface atoms. This interaction can induce the emission of various signal types, captured by specialized detectors

ensuring information regarding the sample's morphology, chemical composition, and other characteristics.

As illustrated in **Figure 2.5**, scanning electron microscope consists of several key components:

a) electron source that emits the electron beam;
b) anode which serves as the positive electrode and to control the energy and intensity of the electron beam;
c) a column comprising various electromagnetic lenses and slits, that control the electron beam by decreasing its diameter;
d) sample holder;
e) a vacuum system, typically consisting of a pre-vacuum pump and a turbomolecular pump. This system is responsible for maintaining a high vacuum level to prevent the electron beam and generated signals from colliding with gas molecules, ensuring more accurate imaging results;
f) a set of detectors that record signals generated during the interaction between the electron beam and the sample. These signals are employed in the reconstruction of the images or the gathering of compositional data.

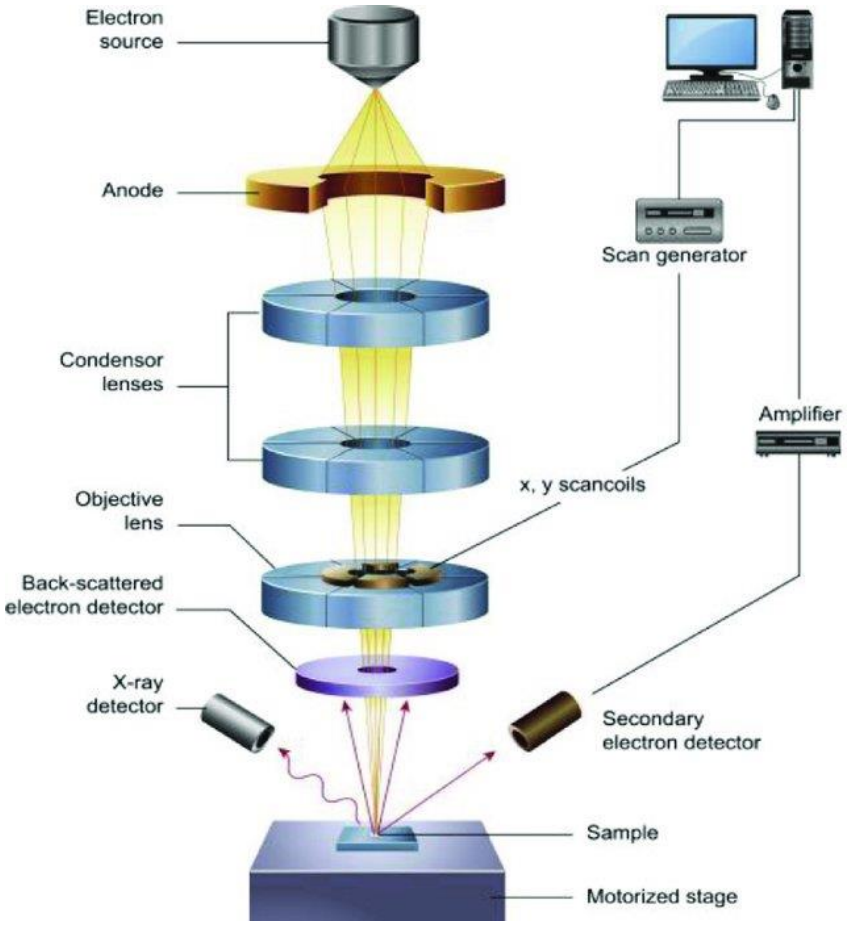

Figure 2.5. ***Diagram of SEM Components*** *(Ali S., 2020)*

EDX spectroscopy (Energy Dispersive X-ray Analysis) or EDS spectroscopy (energy-dispersive electron microscopy with EDX probe) is an instrumental analytical technique that exploits the emission of X-rays generated by an accelerated electron beam incident onto the sample surface. It is an integral detection system associated with SEM, which not only enables "morphological" analysis, allowing for the observation of samples at much higher magnifications but also facilitates the analysis of the chemical elements (atomic number $Z \geq 3$) present at every point within the observed sample performing a chemical element "mapping" over more or less extensive areas of the sample (Gupta *et al.*, 2022). Consequently, SEM-EDX proves to be a powerful instrument for material assessment, defect localization, and the

investigation of surface attributes. It enables the creation of high-resolution images, offering intricate visualizations of surface features at the nanoscale and determines the elemental composition.

2.2.1.2 Transmission Electron Microscopy (TEM)

Louis de Broglie's discovery of cathode rays as electrons in the early 1920s cleared the door for creating of an electron microscope that used a stream of electrons to produce a wave motion. The electrons were focused using magnetic fields as lenses. With the help of these discoveries, Ernst Ruska and Max Knolls created the first electron microscope in 1931, which they later upgraded into a transmission electron microscope (TEM) in collaboration with the Siemens business in 1933 (Robinson, 1986). This advanced electron microscope employs an electron beam to concentrate on a sample, creating a greatly enlarged and intricately detailed representation of the sample. Its magnification capabilities far exceed those of a standard light microscope (more than 2.000.000 times), providing a highly detailed portrayal of the specimen that facilitates the comprehensive analysis of its morphological characteristics, composition, and crystalline properties (Mokobi, 2022). With a few exceptions, the TEM's components are similar to the SEM's. The electron beam, however, penetrates the sample rather than just affecting its surface, giving researchers precise information about the shape and internal structure of the object (Madsen and Susi, 2021). Therefore, the main advantage of transmission electron microscopy TEM over SEM is that, the electron beam penetrates the sample in TEM, whereas in SEM, it impacts the sample's surface. Consequently, while TEM is an invasive and sample-altering technique, it offers superior insights into size distribution and the true population mean. Higher resolution electron microscopes, like the STEM (Scanning Transmission Electron Microscope) and HRTEM (High Resolution Transmission Electron Microscope), are also

available. These microscopes can examine materials at the atomic and subatomic levels and produce images with exceptional resolution.

2.2.1.3 X-ray Diffraction (XRD)

X-ray diffraction (XRD) is an analytical method for examining the crystal structure of materials. The interaction of X-rays with crystals is the basis of the basic X-ray diffractometry principle: the regular arrangement of atoms in the crystal lattice causes the X-rays to be deflected (or diffracted) in different directions when they impact crystalline samples (Sharma, 1981). This X-ray diffraction results in a diffraction pattern called “diffractogram” which indicates the material’s crystalline or amorphous structure. The sample generates strong reflected X-rays through a constructive interference, which occurs when specific conditions align with Bragg’s Law. This law delineates the correlation between the incident X-ray wavelength, the angle at which the beam strikes the sample, and the separation between the crystal lattice planes of atoms (Chauhan, 2014), displayed in **Figure 2.6**. Constructive interference arises when the discrepancies in the X-rays’ paths correspond to whole-number multiples of the wavelength. The result is a diffraction pattern where the peak position depends on the wavelength and graphs intensity versus detector angle (2 theta).

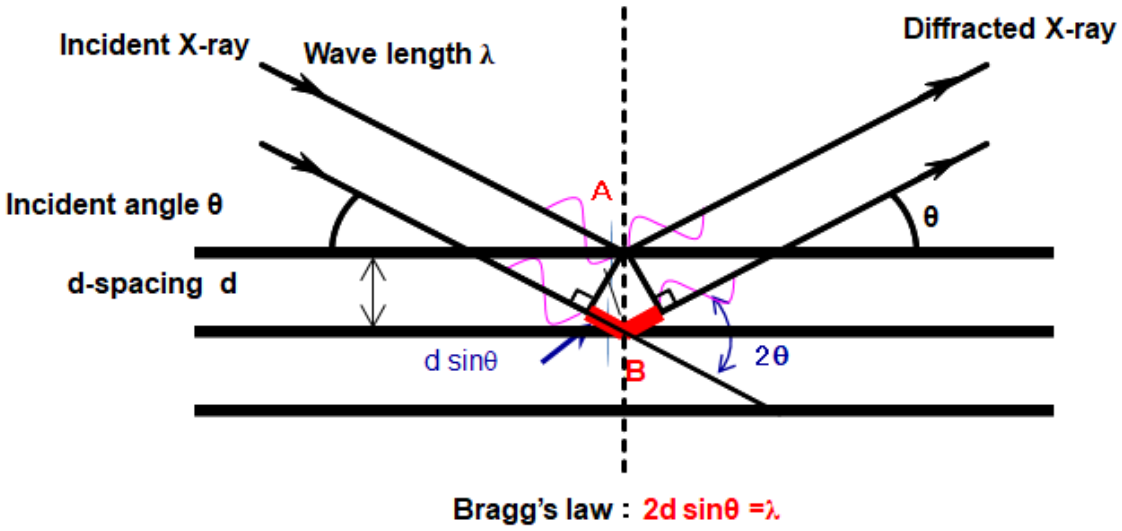

Figure 2.6. ***Principles of X-Ray Diffraction*** (“*X-ray Diffraction : XRD | Techniques | Fields | Toray Research Center | TORAY*”)

Once the diffractogram has been obtained, it’s possible to calculate the sample's degree of crystallinity by using the following formula:

$$x = \frac{A_c}{A_t} \times 100$$

where A_c represents the area below the diffraction peak attributed to the sample's crystalline component; A_t stands for the whole region that includes the crystalline and amorphous components underneath the diffraction peak. A higher value of x indicates a greater degree of crystallinity within the sample. A value of 100% would indicate complete crystallinity, while a lower value suggests the presence of an amorphous or disordered component. Two examples of XRD spectra that illustrate a pattern where a crystalline component predominates (**Figure 2.7a**) and a pattern where the amorphous component predominates (**Figure 2.7b**) are shown below.

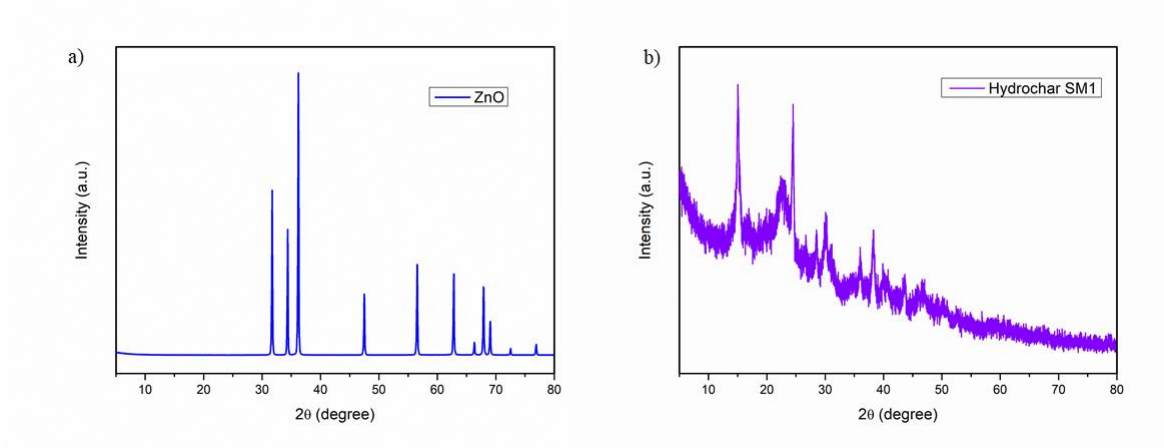

Figure 2.7. ***XRD patterns of a) crystalline ZnO powder, and b) amorphous hydrochar SM1 obtained through HTC of algae Sargassum Muticum after 60 min at 180 °C*** *(Spagnuolo et al., 2023)*

2.2.2 Particle Size and Distribution Analysis Techniques

As previously mentioned, microscopic analysis enables the observation and measurement of even the smallest size of nanomaterials. However, it frequently requires sample preparation, which may result in material damage, involve material removal, or necessitate the application of conductive coatings. Moreover, materials exist in suspension form in numerous instances, requiring direct observation of particles within their respective solvents. Given that the dimensions of materials, particularly nanoscale materials, significantly affect their final properties, the development of advanced, non-destructive techniques for sizing materials becomes crucial. Dynamic light scattering (DLS) analysis, also known as photon correlation spectroscopy (PCS), is non-destructive method involves measuring scattered light to determine the size distribution of particles in a sample (**Figure 2.8**) (Tscharnuter, 2006). In a DLS analysis, a laser beam impacts the sample, and a detector measures the variations in the intensity of the light dispersed by the sample over time. The intensity variations are generated by the Brownian motion of the suspended particles at the origin

of the scattering which is the basis of the Dynamic Light Scattering technique (Choudhary *et al.*, 2019).

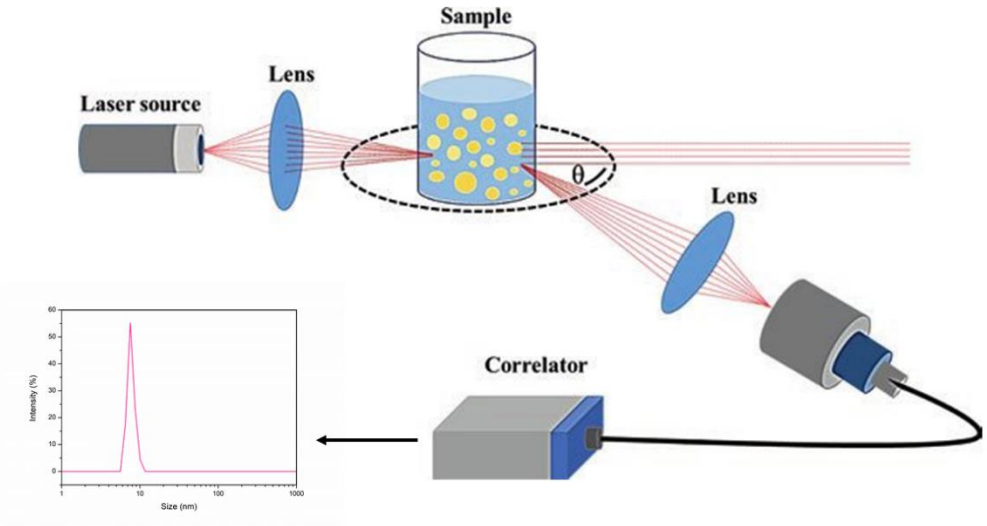

Figure 2.8. ***Representation of dynamic light scattering principle*** *(Choudhary et al., 2019)*

According to the Stokes-Einstein equation, the diffusion coefficients (D) of the particles are inversely proportional to the size (d_p, hydrodynamic diameter) of the particles:

$$D = \frac{kT}{3\pi\eta d_p}$$

where k is the Boltzmann constant, T is the temperature in Kelvin, and η is the viscosity of the liquid. Therefore, to accurately determine particle size, it is crucial to have precise values for the parameters T (temperature) and η (viscosity) of the solvent. Under identical temperature and viscosity conditions, smaller particles exhibit faster motion, resulting in rapid fluctuations in scattering intensity, while larger particles move more slowly, leading to slower intensity variations. When the light beam interacts with the suspension, the scattered light contains data about the diffusion rates and, consequently, the

size distribution of these particles. Analyzing the fluctuations in intensity over time allows for the extraction of information regarding the size and size distribution of the particles within the sample. DLS analysis thus provides the advantage of studying the size distribution of samples directly in solution. However, because the surfactant interferes with the hydrodynamic diameter, median DLS values have a tendency to be a little bit higher than TEM values (Bressi *et al.*, 2023).

2.2.3 Chemical Analysis Techniques

Chemical studies, which include both spectroscopic and non-spectroscopic techniques, are essential in chemical-pharmaceutical manufacturing to confirm that final products, intermediate molecules, and raw materials follow predetermined standard properties. It is feasible to get a thorough understanding of the chemical and physical properties of individual molecules or mixtures by using these analysis approaches, separately or together. These studies cover surface areas, functional chemical groups, and the arrangement of and bindings among individual atoms or molecules. The main chemical methods used in this thesis were Fourier-Transform Infrared (FTIR) Spectroscopy, and Brunauer–Emmett–Teller (BET) Surface Area Analysis.

2.2.3.1 Fourier-Transform Infrared (FTIR) Spectroscopy

Fourier-Transform Infrared (FTIR) Spectroscopy is a non-destructive analytical technique widely applied in both industrial fields and academic research laboratories. Its primary utility lies in elucidating the chemical structural characteristics of individual molecules or the composition of compounds through the examination of chemical bond vibrations. In this

method, infrared light (λ between 780 nm and 1 mm) is absorbed at precise frequencies directly aligned with the vibrational energy levels of the bonds between atoms within a molecule. Bonds with matching vibrational and infrared energy levels absorb this energy. As different bonds within a molecule vibrate at distinct energy levels, they absorb varying wavelengths of infrared radiation. The position (frequency) and intensity of these absorption bands collectively form the overall spectrum, essentially creating a fingerprint of those molecules (**Figure 2.9**). The FTIR spectrometer is the device that FTIR spectroscopy employs, and it is essentially equipped with an infrared light lamp, frequently a broadband infrared ray sent through an optical divider to the sample holder system (Patrizi *et al.*, 2019); the light will thus pass through and interact with the sample, which will be able to absorb some specific frequencies of infrared light. Each type of chemical bond has a certain vibration frequency that corresponds to the frequencies of infrared light that it can absorb. This absorption is caused by chemical vibrations that take place between the vibrational layers of individual atoms. Following its passage through the sample, infrared light is divided into two paths: one that leads directly to a detector and the other that is sent to an interferometer, a moving mirror used to create an optical path difference between the two paths of light by combining its own reflection with that of the detector (Butterfly, 2019). The detector measures the interference between the two light waves caused by this combination (Fourier transform). The chemical composition and structural details of the molecules in the sample are revealed by a spectrum that identifies absorption peaks, or "bands", that correspond to the vibrations of chemical bonds inside the sample. To determine the components contained in the sample, FTIR spectra can be compared to reference spectra. Additionally, it is possible to do a quantitative analysis by measuring the concentration of specific chemical components using the bands' intensity.

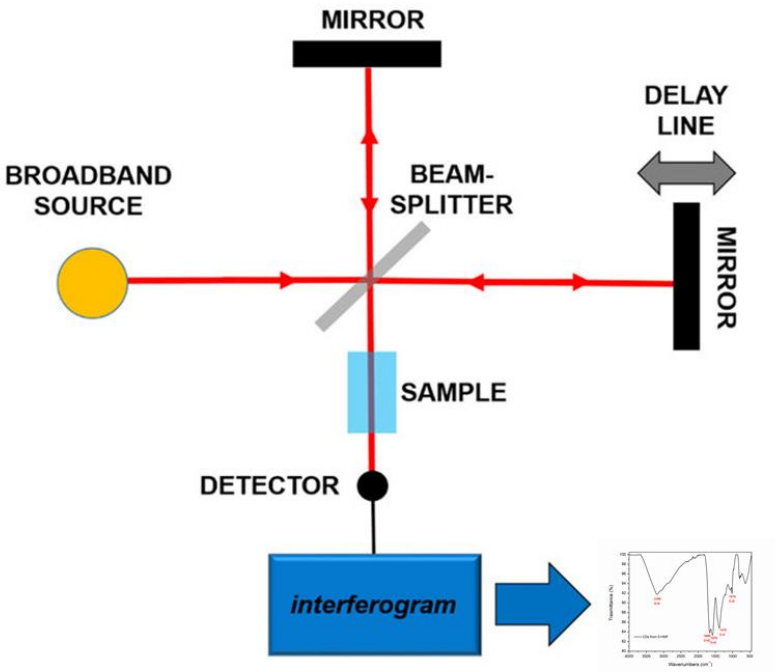

Figure 2.9. ***Principles of the Fourier-Transform Infrared (FT-IR) Spectroscopy*** *(Patrizi et al., 2019).* ***The spectrum presented is reported in*** *Michenzi et al., 2023* ***work***

FTIR spectroscopy helps in understanding the molecular architecture of materials and finds applications in catalytic processes. Moreover, FTIR spectroscopy serves as a process analytical technology, ensuring process stability, control, and the attainment of desired final product specifications. One notable advantage is the shallow penetration depth of infrared energy into the sample, enabling high-quality FTIR spectra even in heavily absorbing reaction mixtures. This facilitates clear determination of the solution-phase aspects of chemical reactions without interference from bubbles, particles, catalysts, biological solids, or water. FTIR analysis is also possible for a real-time determination of chemical reactions that necessitate the transmission of modulated infrared rays into a reactor or continuous flow chemistry setup, with the unabsorbed energy subsequently returned to the spectrophotometer. For this purpose, it employs an internal reflection sensor, often referred to as attenuated

total reflectance (ATR), fixed at the end of a tubular optical probe. This probe can be inserted into the chemical reaction vessel or integrated into a cell for continuous monitoring. ATR is a valuable complement to FTIR instruments for the analysis of chemical reactions reagents and products. ATR sensors suitable for chemical reaction analysis possess a compatible refractive index for internal reflection and might be resilient in harsh chemical environments.

2.2.3.2 Brunauer–Emmett–Teller (BET) Surface Area Analysis

The BET analysis enables the determination of both the external and internal specific surface areas of compounds, including dispersed materials like nanopowders or porous solids (Alothman, 2012). This is achieved by quantifying the physical adsorption of gas, following the principles of the Brunauer, Emmett, and Teller (BET) method, from which it derives its name. These three scientists developed a mathematical approach for calculating the specific surface area of the materials, taking into account pore size distribution through gas adsorption. Indeed, during this process, a gas, typically nitrogen, is introduced and adsorbed onto the surface of the particles at its boiling point (−196°C for nitrogen). At this low temperature, nitrogen gas condenses on the particle surfaces. Since the size of the gas atom or molecule is known, it is assumed that the gas condenses into a monolayer on the surface, and the amount of gas adsorbed (condensed) coincides with the total surface area of the particles, including the surface area within the pores. This correlation, specifically the relationship between adsorbed volume and surface area, yields the final BET value. It's important to note that inaccessible pores are not accounted for in this calculation. The BET analysis procedure comprises sequential steps ("*BET surface area – Andy Connelly*"), as illustrated in the following **Figure 2.10**:

1. Degassing: prior to determining an adsorption isotherm within the BET region, the sample undergoes degassing to prevent irreversible surface alterations. Typically, this is achieved using a vacuum system or by purging the sample with a gas, often nitrogen (N_2), at elevated temperatures. The choice of temperature depends on the sample's stability.
2. Evacuation of Sample Tubes: The sample tubes are evacuated (a), followed by the introduction of an inert gas such as helium to measure the dead volume (b), and another evacuation step is performed (c).
3. Nitrogen (N_2) Adsorption: During this phase, nitrogen gas is adsorbed onto the surface of the porous sample. The sample is exposed to nitrogen gas at a controlled temperature and incremental pressure. Nitrogen molecules adhere to the internal surfaces of the sample, filling the void spaces (pores) within the material. Concurrently, the adsorption curve is generated by recording the quantity of adsorbed nitrogen as a function of pressure.
4. Nitrogen (N_2) Desorption: Following the adsorption phase, the process transitions to desorption. Pressure is gradually reduced, enabling nitrogen gas to desorb from the sample's surface. This phase is also closely monitored, with the relationship between the amount of desorbed gas and the pressure recorded as a desorption curve.

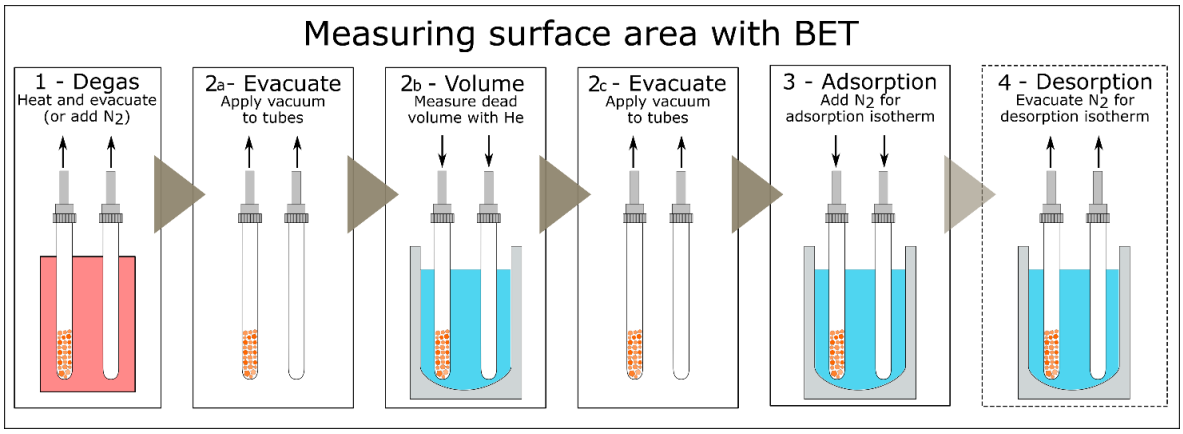

Figure 2.10. ***Principles of Principles of the BET method*** *("BET surface area – Andy Connelly")*

The quantitative description of gas adsorption on a porous material is provided by an adsorption isotherm. According to the IUPAC classification, the six isotherm types shown in **Figure 2.11** are indicative of adsorbents that can denote various porosity loops. Specifically, type I describes microporous materials, types II, III, and VI are typical of non-porous or macroporous materials, and mesoporous materials give types IV and V.

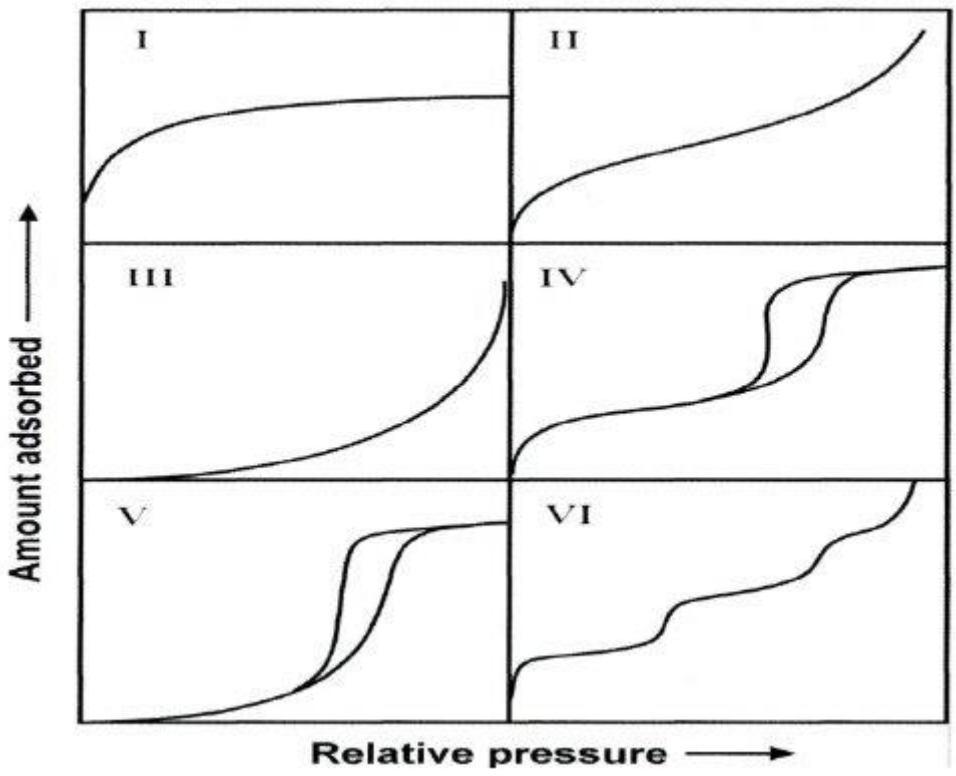

Figure 2.11. ***The IUPAC classification of adsorption isotherms showing both the adsorption and desorption trails*** *(Alothman, 2012)*

In addition to employing the BET method for surface area analysis, the N_2 adsorption/desorption system frequently incorporates the BJH (Barrett-Joyner-Halenda) method. The BJH method is utilized to gather data concerning the distribution of pore sizes within the material (Bardestani *et al.*, 2019). By utilizing both methods, it becomes feasible to achieve a comprehensive and complete characterization of the material's porosity. When capillary condensation takes place within mesopores, the desorption route differs from the adsorption path, resulting in a hysteresis loop (**Figure 2.12**) (Bardestani *et al.*, 2019). H1-type hysteresis is commonly linked to porous materials comprising spherical and/or cylindrical mesoporous channels. H2-type hysteresis is often observed in materials with disordered interconnect pore structures (Afshar Taromi and Kaliaguine, 2017). H3-type hysteresis is characteristic of solids composed of aggregates of sheet-like particles. On the

other hand, materials featuring narrow slot-like pores typically exhibit H4-type hysteresis (Alothman, 2012).

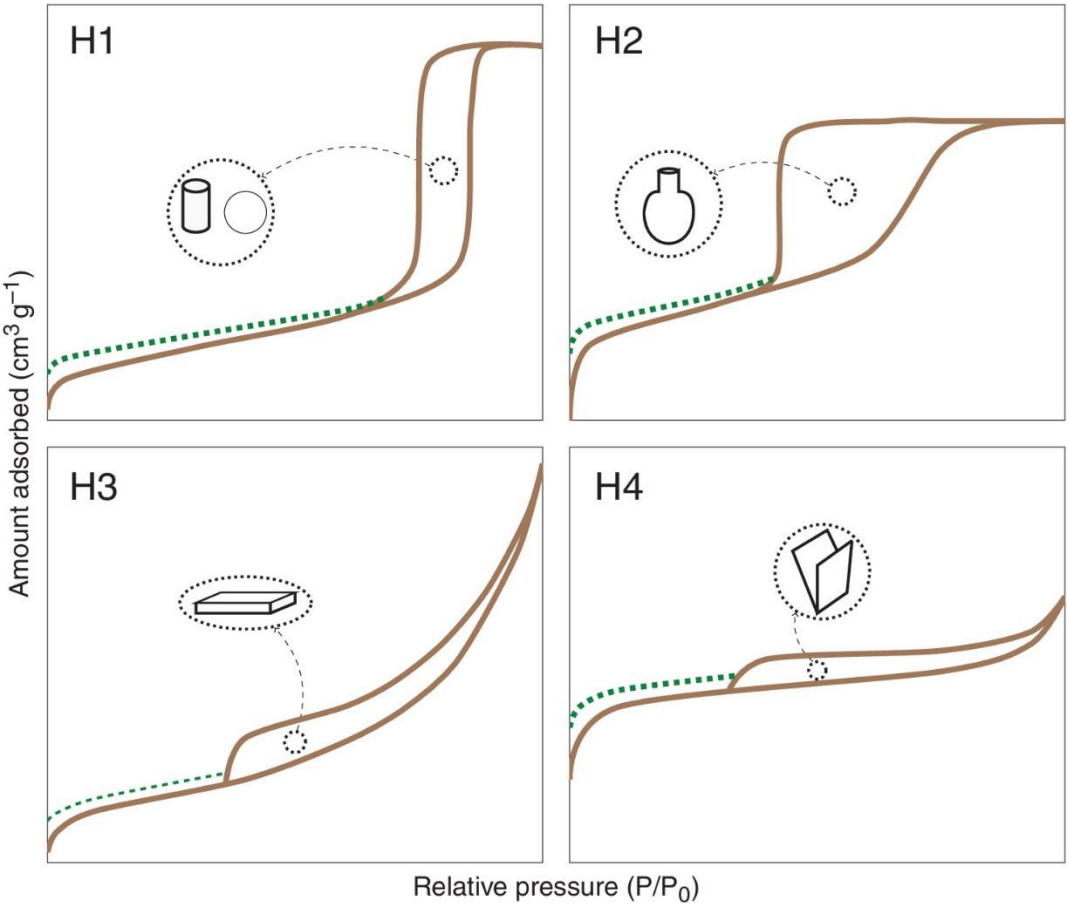

Figure 2.12. ***Types of hysteresis loops obtained by N_2 adsorption/desorption isotherms*** *(Bardestani et al., 2019)*

Hence, the BET analysis enables the determination of the size and distribution of the pores within a porous material and the evaluation of the effectiveness of the catalysts since, in catalysis, the specific surface plays a crucial role since the more surface is available, the greater the effectiveness of the catalyst, and also, characterize the adsorbent materials, such as zeolites or activated carbons.

2.2.4 Optical Analysis Techniques

Optical analyses are a class of analytical techniques that exploit the interaction of light (often in visible light or ultraviolet light) with matter to reveal details about the properties of samples, including chemical composition, luminescence, molecular structure, chemical concentration, and more (Walt, 2013). Optical analysis techniques are useful tools in many scientific and industrial areas because they shed light on the electrical, structural, and application-related characteristics of materials. Due to advantages including speed of analysis and accessibility to a variety of materials, UV-Vis spectroscopy and photoluminescence spectroscopy were the two optical approaches that were most frequently exploited in this PhD thesis work. Furthermore, both techniques have not only been employed for characterizing the obtained materials but also for investigating the adsorption phenomena of organic pollutants (UV-Vis analysis) and the detection of heavy metals (photoluminescence analysis).

2.2.4.1 Ultraviolet-Visible Spectroscopy (UV-Vis) Analysis and Photoluminescence Spectroscopy (PL) Analysis

UV-Vis spectroscopy and photoluminescence spectroscopy are fundamental optical analysis techniques employed to explore the absorption and emission properties of substances, delivering invaluable insights essential for various scientific applications like photocatalysis, photodegradation, and fluorescent sensors. A UV-Vis spectrophotometer typically comprises a light source (usually a xenon or tungsten lamp), a monochromator for selecting specific wavelengths, a sample holder (either a cuvette or solid sample holder), and a detector, which can be an array of photodiodes or a photomultiplier tube. A schematic diagram of a UV-Vis spectrometer is shown in **Figure 2.13**. This instrument emits radiation within the UV and visible spectrum. This emitted light passes through the sample, and the detector measures the intensity of the

transmitted or absorbed light. The resulting spectrum displays wavelength on the x-axis and absorbance on the y-axis, revealing peaks and troughs corresponding to absorption bands in the UV and visible regions if the material isn't entirely transparent. These absorptions arise from electronic energy level transitions, and the absorbance value is directly proportional to the concentration of the sample under examination, in accordance with the Lambert-Beer law:

$$A = \varepsilon \cdot C \cdot l$$

where A is the absorbance, ε is the molar absorptivity or molar extinction coefficient, C is the concentration of the samples, and l is the path length of the sample holder. This law establishes the quantitative relationship between absorbance and concentration, enabling the determination of analyte concentrations in solution. UV-Vis spectroscopy can be employed to investigate the kinetics of substance adsorption in solution, specifically how the adsorption rate changes over time (Spagnuolo *et al.*, 2023), biosorption (Hannachi and Hafidh, 2020), photodegradation phenomena (Yi *et al.*, 2023) and photocatalysis studies (Mehdizadeh *et al.*, 2023).

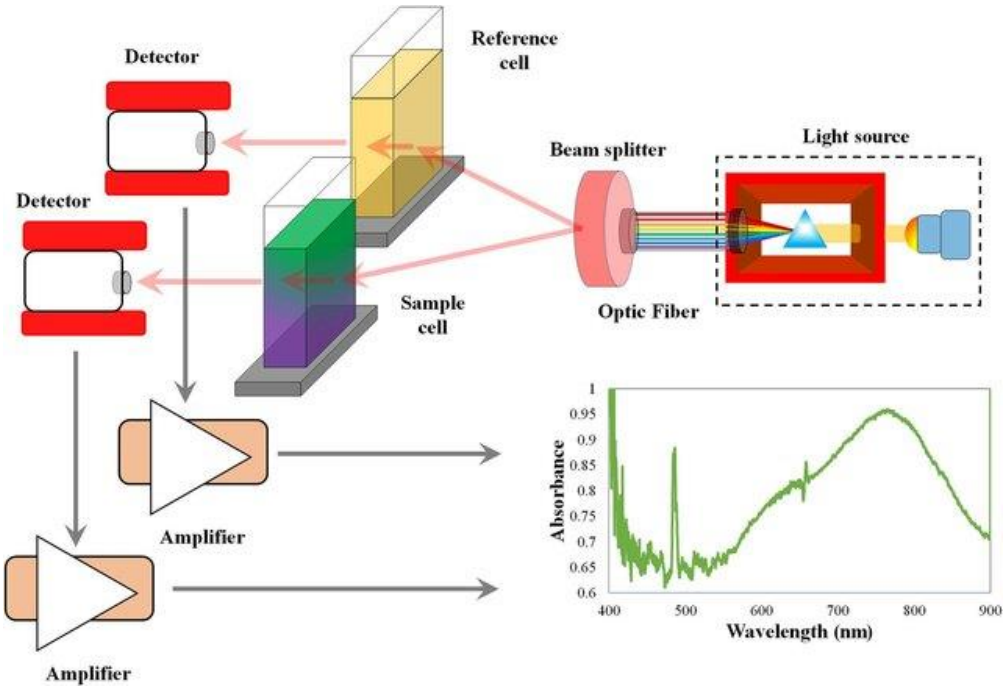

Figure 2.13. ***Schematic of UV-Vis setup*** *(Ashraf Gandomi et al., 2018)*

The components of a fluorescence spectrophotometer are similar to those of a UV-Vis instrument, but it contains extra features such as a monochromator for the excitation and emission wavelengths, and the filters to stop scattered excitation light from reaching the detector. In contrast to UV-Vis, the sample is activated by a specific wavelength of light in fluorescence spectroscopy, and the equipment detects the fluorescence that is emitted, typically at longer wavelengths (Stokes-shift). This happens because electrons have the ability to transition from a lower energy state to a higher energy state when they sufficiently absorb photons of energy (Kogure *et al.*, 2008). When the electron returns to its lower energy state, this energy is subsequently released as light (**Figure 2.14**). The wavelength of these photons (and hence the color of the fluorescence) is directly related to the band gap energy of the fluorescent material (Elson *et al.*, 1974). A material with a larger band gap will emit photons with higher energy, resulting in shorter wavelengths and distinct visible colors (Maddalena *et al.*, 2023). Since a compound's spectrum would

be straight if it cannot emit fluorescence, this technique can be used to analyze the emission characteristics of fluorescent substances. Fluorescence can also be used as an analytical application technique, as has been seen with UV-Vis analysis. For instance, the phenomenon known as "quenching" can be studied when the fluorescence intensity of a sample decreases or switch-off as a result of collisions with nearby molecules or the formation of complexes between the fluorescent molecule and a chemical substance present in the solution (Zu *et al.*, 2017). These interactions can be utilized to detect compounds and to explain the chemical-physical bindings between the components under study (Al-Maskari *et al.*, 2023).

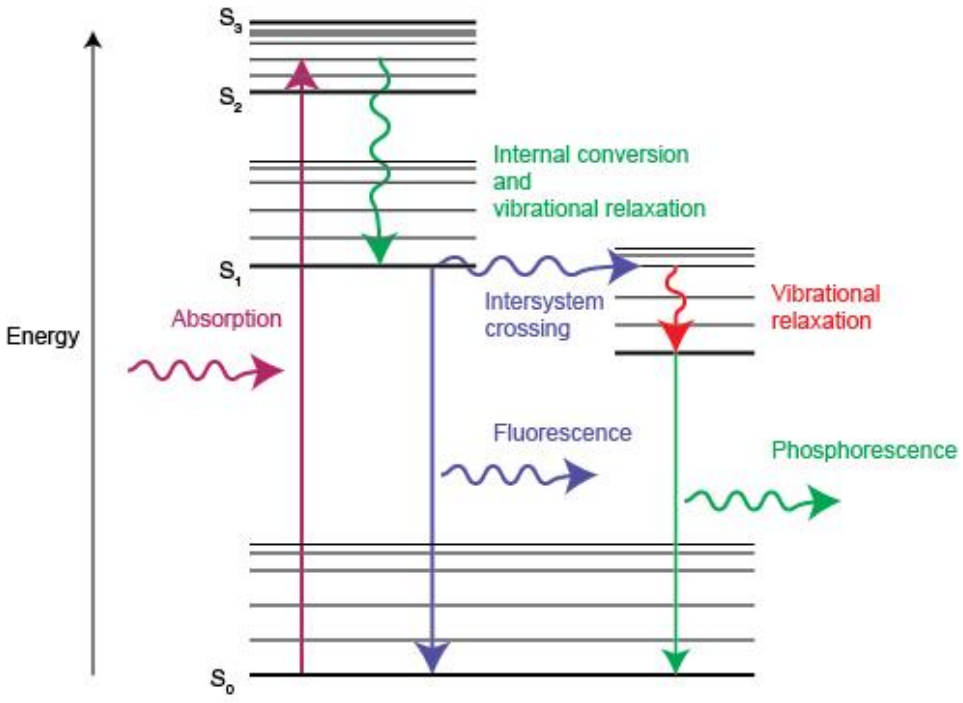

Figure 2.14. ***Energy diagram illustrating light absorption and emission processes: fluorescence (and phosphorescence)*** *(plc, n.d.)*

2.2.5 Electrochemical Analysis Techniques: Electrochemical Impedance Spectroscopy

Electrochemical impedance spectroscopy (EIS) is an experimental technique used to study the electrical properties of materials, electrical systems, circuits, and corrosion phenomena. It is also employed for characterizing batteries, sensors, electrochemical cells, polymers, and conducting materials in general (Fernández-Sánchez *et al.*, 2005). EIS possesses the capability to investigate any intrinsic electrical or interfacial property of a specific substance or process that might influence the conductivity of an electrochemical system (Suni, 2008).

This method investigates electrical impedance (Z), which represents a system's resistance and reactance (inductive or capacitive) in response to alternating current as a function of the frequency of an electrical signal. When applied to electrochemical systems, this signal typically consists of a low-amplitude (AC) voltage (around 5-10 mV peak-to-peak), and the response is a current that varies in both amplitude and phase relative to the applied voltage (Han *et al.*, 2015). Consequently, the system's impedance, easily calculable over a wide range of frequencies, is determined as the ratio between the applied voltage and the measured current (Z = E/I). This yields a spectrum in which processes with various kinetics are present and dominant in different frequency ranges, reflecting the occurrences within the system under investigation. The impedance of an equivalent circuit primarily composed of resistors and capacitors can be easily matched to experimental data regarding the impedance of an electrochemical cell. In these circuits, capacitance typically accounts for regions of space charge polarization within the system as well as modifications to an electrode's surface due to adsorption or deposition processes. On the other hand, resistance ideally describes a conductive pathway, such as that formed

by the overall conductivity of the system or the charge transfer step associated with an electrode reaction.

The simplest equivalent circuit is the Randles circuit (see **Figure 2.15**), which combines four elements to describe an electrochemical cell: the double-layer capacitance (CPE) representing the contact resistance between electrode and current collector; R_s denoting the resistance of the solution phase which is relevant analytically mostly in conductivity sensors (Suni, 2008); the impedance faradaic (Z_f) resulting from the charge transfer process, and the charge transfer resistance (R_{ct}). The Warburg impedance (W), representing the influence of mass transport of electroactive species on the overall impedance of the electrochemical cell due to mass transfer restrictions, is part of Z_f, which is typically separated into W and R_{ct}. Consequently, W becomes dominant for diffusion-limited processes, whereas Z_f essentially equals R_{ct} for processes under charge transfer control (Han *et al.*, 2015). Analytical applications rarely employ Warburg impedance, which can be used to measure effective diffusion coefficients. By analyzing the impedance variation of an electrochemical cell across a broad frequency range (typically 100 kHz to 0.1 Hz), all these components can be determined.

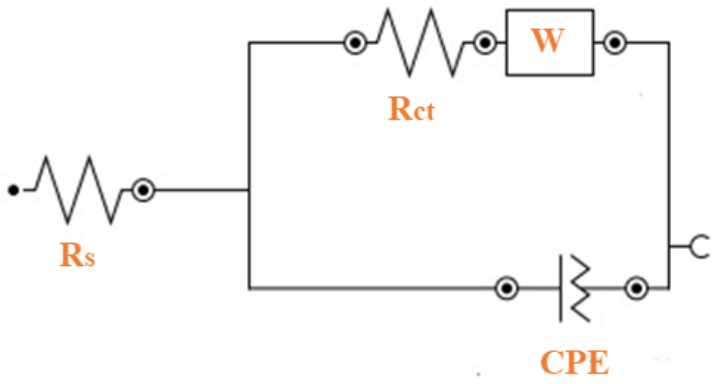

Figure 2.15. Electrical equivalent circuit

One of the most interesting aspects of Electrochemical Impedance Spectroscopy lies in the marked correlation observed between the behavior of a real system and an idealized model circuit composed of discrete electrical components. In the Nyquist spectrum generated from the equivalent Randles circuit, the real (Z') and imaginary (−Z'') components of the impedance, respectively, represent resistance and reactance. The Nyquist plot, as illustrated in **Figure 2.16**, provides a graphical representation of the system's dynamics. Within this plot, the CPE describes the diameter of the semicircle, which arises from the resistance to charge transfer and exhibits an inverse proportional relationship with the electron transfer rate.

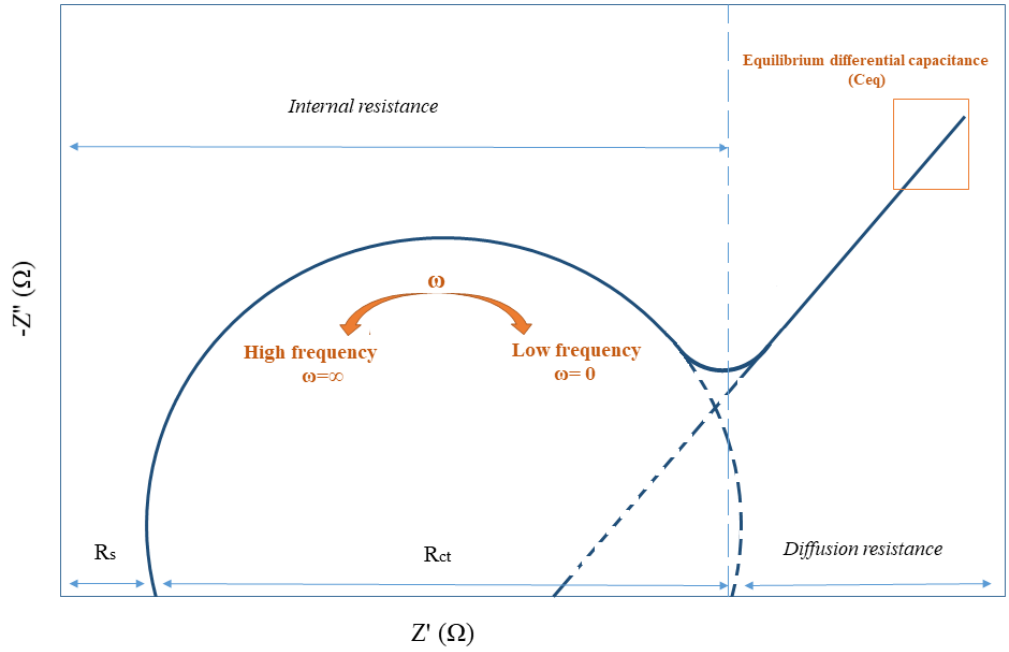

Figure 2.16. ***Nyquist diagram***

Impedance methods can be employed for analyte detection if an analyte changes one or more of these equivalent circuit characteristics, and these parameters are unaffected by the interfering species. The measured capacitance usually results from the series combination of several elements, including those

associated with the analyte, such as analyte binding (C_a) to a sensing layer (C_s) on a carbon or gold electrode (C_x) (Suni, 2008). In this case, the measured capacitance for a continuous system of sensing layer and analyte layer results as:

$$\frac{1}{CPE} = \frac{1}{C_a} + \frac{1}{C_s} + \frac{1}{C_x}$$

The capacitance at the interface between the electrode (especially in the case of the gold electrode) and the sensing layer is frequently significant (Suni, 2008). However, in many cases, it is omitted because its contribution may not significantly influence the overall measurement. Therefore, impedance techniques can be used to detect analytes in electrochemical systems, offering an equation to determine the total capacitance and highlighting the significance of stable circuit properties.

2.3 Sensor Preparation and Modification Procedures

Electrochemical sensors played a central role in most of the applications aimed at detecting pollutant ions or molecules developed in this thesis. In particular, Screen-printed sensors were employed. Screen-printing is a technique that offers the advantage of material flexibility, enabling the creation of customized sensors tailored to specific application requirements (Kadara *et al.*, 2009). These advantages render them an appealing choice across various industries, including automotive, consumer electronics, electrochemistry, and more (Medina-Plaza *et al.*, 2015). Because electrochemical reactions take place on the working electrode surface, this electrode plays an important function in the sensor system. The working electrode is typically changed with chemically stable substrates, such as nanomaterials, polymers, or composite materials, to

increase sensor performance, particularly selectivity and sensitivity (Saputra, 2023). The sensors utilized in this study were purchased from Metrohm DropSens Company (Spain), specifically the C110 and the 110 models. This sensor comprises a ceramic platform measuring approximately 3.4 cm × 1.0 cm × 0.05 cm, housing an electrochemical cell consisting of a carbon-working electrode, a silver pseudo-reference electrode, and a carbon counter electrode. **Figure 2.17** displays an image of the basic C110 screen-printed carbon electrode (SPCE) platform along with its specifications.

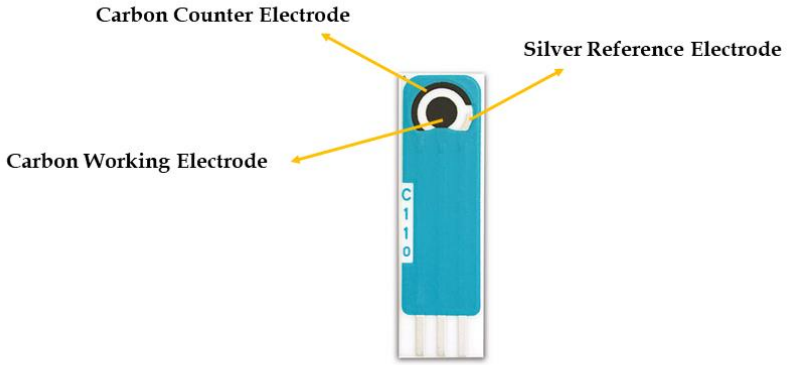

Figure 2.17. ***Metrohm DropSens Screen-Printed Carbon Electrodes mod. C110*** *("Metrohm DropSens: Your electrochemical sensor")*

To modify the bare working electrode surface of SPCEs, a straightforward process involved adding the desired solution drop by drop, allowing the electrode to dry after each drop. In the case of the sensor modified with the Schiff base, 1.0 mg of Schiff base was dissolved ultrasonically in 0.5 mL of DMSO. Subsequently, 2 µL of the solution was directly applied to the surface of the carbon working electrode and allowed to air-dry at room temperature or in a well-ventilated oven at a maximum temperature of 50 °C overnight. Furthermore, a membrane was prepared by mixing 0.5 mg of sodium tetraphenyl borate (NaTBP), 33 mg of polyvinyl chloride (PVC), 65.71 mg of

2-nitrophenyl octyl ether (2-NPOE), and 1 mg of Schiff base in 1.0 mL of THF. Then, 2 μL of this mixture were deposited onto the sensor, and the solvent was left to evaporate overnight at room temperature, resulting in the formation of a transparent membrane. The membrane's use helped to eliminate interferences, stabilize the interface between the sensor and the sample solution, and increase the sensitivity of the modified sensor.

Regarding carbon nanodots derived from orange peels, modified sensors were fabricated by ultrasonically dispersing 1 mg of carbon nanodots in 1 mL of distilled water. Then, 10 μL of each suspension was drop-cast onto the working carbon electrode surface. After each application, the electrode was allowed to dry before the subsequent drop. The modified sensors were left to dry at room temperature overnight. As far as carbon nanodots obtained from beer bagasse, since they were already in aqueous suspension, they were applied onto the working electrode surface through drop-casting (four additions of 5 μL) and allowed to dry at room temperature. In the case of carbon nanodots, there was no need for the addition of membranes.

References

Metrohm DropSens : Your electrochemical sensor https://www.dropsens.com/en/your_electrochemical_sensor.html (accessed September 2023)

Afshar Taromi, A.; Kaliaguine, S. Synthesis of ordered mesoporous γ-alumina – Effects of calcination conditions and polymeric template concentration. *Microporous and Mesoporous Materials*, **2017**, 248, 179–191. https://doi.org/10.1016/j.micromeso.2017.04.040

Ali, S. A. Application of Nanomaterials in Environmental Improvement. *Nanotechnology and the Environment*, **2020** https://doi.org/10.5772/intechopen.91438

Al-Maskari, S.; Issac, A.; Rao Varanasi, S.; Hildner, R.; Sumesh Sofin, R.G.; Ramadan Ibrahim, A., K.; Abou-Zied, O. Dye-induced photoluminescence quenching of quantum dots: role of excited state lifetime and confinement of charge carriers. *Physical Chemistry Chemical Physics*, **2023**, 25, 14126–14137. https://doi.org/10.1039/D3CP00715D

Alothman, Z. A Review: Fundamental Aspects of Silicate Mesoporous Materials. *Materials*, **2012**, 5, 2874–2902. https://doi.org/10.3390/ma5122874

Anbu Durai, W.; Ramu, A.; Dhakshinamoorthy, A. A chromogenic and fluorescence turn-on sensor for the selective and sensitive recognition of Al^{3+} ions – A new approach by Schiff base derivative as probe. *Inorganic Chemistry Communications*, **2020**, 121, 108191. https://doi.org/10.1016/j.inoche.2020.108191

Ashraf Gandomi, Y.; Aaron, D.; Houser, J.; Daugherty, M.; Clement, J.; Pezeshki, A.; Ertuğrul, T.; Moseley, D.; Mench, M.M. Critical Review—Experimental Diagnostics and Material Characterization Techniques Used on Redox Flow Batteries. *Journal of The Electrochemical Society*, **2018**, 165, A970–A1010. https://doi.org/10.1149/2.0601805jes

Bardestani, R.; Patience, G.S.; Kaliaguine, S. Experimental methods in chemical engineering: specific surface area and pore size distribution measurements—BET,

BJH, and DFT. *The Canadian Journal of Chemical Engineering*, **2019**, 97, 2781–2791. https://doi.org/10.1002/cjce.23632

BET surface area – Andy Connelly, https://andyjconnelly.wordpress.com/2017/03/13/bet-surface-area/ (accessed September 2023)

Bilal, M.; Iqbal, H.M.N. Marine seaweed polysaccharides-based engineered cues for the modern biomedical sector. *Marine Drugs*, **2020**, 18. https://doi.org/10.3390/md18010007

Bressi, V.; Chiarotto, I.; Ferlazzo, A.; Celesti, C.; Michenzi, C.; Len, T.; Iannazzo, D.; Neri, G.; Espro, C. Voltammetric Sensor Based on Waste-Derived Carbon Nanodots for Enhanced Detection of Nitrobenzene. *ChemElectroChem*, **2023**, e202300004. https://doi.org/10.1002/celc.202300004

Butterfly, B. FTIR: Fourier-Transform Infrared Spectroscopy Principles and Applications. FindLight Blog, **2019**. https://www.findlight.net/blog/ftir-principles-applications/ (accessed September 2023)

Castro-Criado, D.; Abdullah, J.A.A.; Romero, A.; Jiménez-Rosado, M. Stabilization and Valorization of Beer Bagasse to Obtain Bioplastics. *Polymers*, **2023**, 15, 1877. https://doi.org/10.3390/polym15081877

Cechinel, M.A.P.; dos Santos, K.M.; Rostirolla, A.C.; Junca, E. Synthesis of biochar using brewery waste for efficient adsorption of ionic iron species. *Biomass Conversion and Biorefinery*, **2022.** https://doi.org/10.1007/s13399-022-03495-w

Chauhan, A. Powder XRD Technique and its Applications in Science and Technology. *Journal of Analytical and Bioanalytical Techniques*, **2014**, 5. https://doi.org/10.4172/2155-9872.1000212

Choudhary, R.C.; Kumari, S.; Kumaraswamy, R. V.; Pal, A.; Raliya, R.; Biswas, P.; Saharan, V. Characterization Methods for Chitosan-Based Nanomaterials. *Nanotechnology in the Life Sciences*, **2019**. https://doi.org/10.1007/978-3-030-12496-0_5

Coltivazioni :Coltivazioni legnose fruttifere (accessed August 2023) http://dati.istat.it/Index.aspx?QueryId=33705

Elson, E.L.; Magde, D. Fluorescence correlation spectroscopy. I. Conceptual basis and theory. *Biopolymers*, **1974**, 13, 1–27. https://doi.org/10.1002/bip.1974.360130102

Espro, C.; Satira, A.; Mauriello, F.; Anajafi, Z.; Moulaee, K.; Iannazzo, D.; Neri, G. Orange Peels-Derived Hydrochar for Chemical Sensing Applications. *Sensors and Actuators B: Chemical*, **2021**, 341, 130016. https://doi.org/10.1016/j.snb.2021.130016

Fabbrizzi, L. Beauty in Chemistry: Making Artistic Molecules with Schiff Bases. *Journal of Organic Chemistry*, **2020**, 85, 12212–12226. https://doi.org/10.1021/acs.joc.0c01420

Fernández-Sánchez, C.; McNeil, C.J.; Rawson, K. Electrochemical impedance spectroscopy studies of polymer degradation: application to biosensor development. *TrAC Trends in Analytical Chemistry*, **2005,** 24, 37–48. https://doi.org/10.1016/j.trac.2004.08.010

Ferrari, J.; Villagra, E.; Claps, L.; Tittonel, P. REUTILIzACIÓN DE BAGAzO DE CEBADA CERVECERA POR SECADO y PELLETIzACIÓN COMO SUPLEMENTO FORRAJERO. *Presencia*, **2017**, 67. https://www.researchgate.net/publication/332332753

Forzani, E.S.; Zhang, H.; Chen, W.; Tao, N. Detection of Heavy Metal Ions in Drinking Water Using a High-Resolution Differential Surface Plasmon Resonance Sensor. *Environmental Science Technology*, **2005**, 39, 1257–1262. https://doi.org/10.1021/es049234z

Ghosh, S.; Singharoy, D.; Konar, S.; Naskar, J.P.; Bhattacharya, S.C. Solvatochromic behavior of a pyrene-pyrimidine-based Schiff base and detection of heavy metal ions in aqueous media. *Journal of Coordination Chemistry*, **2021**, 74, 1272–1283. https://doi.org/10.1080/00958972.2021.1897980

Gokulakrishnan, M.; Kumar, R.; Ferosekhan, S.; Siddaiah, G.M.; Nanda, S.; Pillai, B.R.; Swain, S.K. Bio-utilization of brewery waste (Brewer's spent yeast) in global aquafeed production and its efficiency in replacing fishmeal: From a sustainability

viewpoint. *Aquaculture*, **2023**, 565, 739161. https://doi.org/10.1016/j.aquaculture.2022.739161

Gupta, S.; Omar, T.; Muzzio, F.J. SEM/EDX and Raman chemical imaging of pharmaceutical tablets: A comparison of tablet surface preparation and analysis methods. *International Journal of Pharmaceutics*, **2022**, 611, 121331. https://doi.org/10.1016/j.ijpharm.2021.121331

Han, P.; Zhang, Y.; Chen, F.Y.; Bai, X. Interpretation of electrochemical impedance spectroscopy (EIS) circuit model for soils. *Journal of Central South University*, **2015**, 22, 4318–4328. https://doi.org/10.1007/s11771-015-2980-1

Hannachi, Y.; Hafidh, A. Biosorption potential of Sargassum muticum algal biomass for methylene blue and lead removal from aqueous medium. *International Journal of Environmental Science and Technology*, **2020**, 17, 3875–3890. https://doi.org/10.1007/s13762-020-02742-9

Kadara, R.O.; Jenkinson, N.; Banks, C.E. Characterization and fabrication of disposable screen printed microelectrodes. *Electrochemistry Communications*, **2009**, 11, 1377–1380. https://doi.org/10.1016/j.elecom.2009.05.010

Kandasamy, S.; Narayanan, M.; Raja, R.; Devarayan, K.; Kavitha, R. The current state of algae in wastewater treatment and energy conversion: a critical review. *Current Opinion in Environmental Science & Health*, **2023**, 33, 100469. https://doi.org/10.1016/j.coesh.2023.100469

Kaur, N.; Kaur, B. Colorimetric and fluorescent multi-ion recognition by Anthracene appended di-Schiff base chemosensor. *Inorganic Chemistry Communications*, **2020**, 121, 108239. https://doi.org/10.1016/j.inoche.2020.108239

Kogure, T.; Kawano, H.; Abe, Y.; Miyawaki, A. Fluorescence imaging using a fluorescent protein with a large Stokes shift. *Methods*, **2008**, 45, 223–226. https://doi.org/10.1016/j.ymeth.2008.06.009

Len, T.; Bressi, V.; Balu, A. M.; Kulik, T.; Korchuganova, O.; Palianytsia, B.; Espro, C.; Luque, R. Thermokinetics of Production of Biochar from Crop Residues: An

Overview. *Green Chemistry*, **2022**, 24 (20), 7801–17. https://doi.org/10.1039/D2GC02631G

Louime, C.; Fortune, J.; Gervais, G. Sargassum Invasion of Coastal Environments: A Growing Concern. *American Journal of Environmental Sciences*, **2017**, 13, 58–64. https://doi.org/10.3844/ajessp.2017.58.64

Maddalena, F.; Mahyuddin, M.H.; Kowal, D.; Witkowski, M.E.; Makowski, M.; Kuddus Sheikh, M.A.; Mahato, S.; Jędrzejewski, R.; Drozdowski, W.; Dujardin, C.; Dang, C.; Birowosuto, M.D. Lattice Expansion in Rb-Doped Hybrid Organic–Inorganic Perovskite Crystals Resulting in Smaller Band-Gap and Higher Light-Yield Scintillators. *Inorganic Chemistry*, **2023**, 62, 8892–8902. https://doi.org/10.1021/acs.inorgchem.3c00270

Madsen, J.; Susi, T. The abTEM code: transmission electron microscopy from first principles. *Open Research Europe*, **2021**, 24. https://doi.org/10.12688/openreseurope.13015.1

Magar, S.D.; Leibing, C.; Gómez-Urbano, J.L.; Cid, R.; Carriazo, D.; Balducci, A. Brewery waste derived activated carbon for high performance electrochemical capacitors and lithium-ion capacitors. *Electrochimica Acta*, **2023**, 446, 142104. https://doi.org/10.1016/j.electacta.2023.142104

Marino, F.; Di Caro, G.; Gugliandolo, C.; Spanò, A.; Faggio, C.; Genovese, G.; Morabito, M.; Russo, A.; Barreca, D.; Fazio, F.; Santulli, A. Preliminary Study on the In vitro and In vivo Effects of Asparagopsis taxiformis Bioactive Phycoderivates on Teleosts. *Frontiers in Physiology*, **2016**, 7. https://doi.org/10.3389/fphys.2016.00459

Medina-Plaza, C.; García-Hernández, C.; de Saja, J.A.; Fernández-Escudero, J.A.; Barajas, E.; Medrano, G.; García-Cabezón, C.; Martin-Pedrosa, F.; Rodriguez-Mendez, M.L. The advantages of disposable screen-printed biosensors in a bioelectronic tongue for the analysis of grapes. LWT- *Food Science and Technology*, **2015**, 62, 940–947. https://doi.org/10.1016/j.lwt.2015.02.027

Mehdizadeh, P.; Jamdar, M.; Mahdi, M.A.; Abdulsahib, W.K.; Jasim, L.S.; Raheleh Yousefi, S.; Salavati-Niasari, M. Rapid microwave fabrication of new nanocomposites based on Tb-Co-O nanostructures and their application as photocatalysts under UV/Visible light for removal of organic pollutants in water. *Arabian Journal of Chemistry*, **2023**, 16, 104579. https://doi.org/10.1016/j.arabjc.2023.104579

Michenzi, C.; Espro, C.; Bressi, V.; Celesti, C.; Vetica, F.; Salvitti, C.; Chiarotto, I. Electrochemical bottom-up synthesis of biomass-derived carbon dots for promoting Knoevenagel condensation. *Molecular Catalysis*, **2023**, 544, 113182. https://doi.org/10.1016/j.mcat.2023.113182

Mohammed, M.Q.; Ismail, H.K.; Alesary, H.F.; Barton, S. Use of a Schiff base-modified conducting polymer electrode for electrochemical assay of Cd(II) and Pb(II) ions by square wave voltammetry. *Chemical Papers*, **2022**, 76, 715–729. https://doi.org/10.1007/s11696-021-01882-7

Mokobi, F. Transmission Electron Microscope (TEM)-Definition, Principle, Images **2022** (accessed September 23) https://microbenotes.com/transmission-electron-microscope-tem/

Patrizi, B.; Cumis, S.; Viciani, D'Amato. Dioxin and Related Compound Detection: Perspectives for Optical Monitoring. *International Journal of Molecular Sciences*, **2019**, 20, 2671. https://doi.org/10.3390/ijms20112671

Plc, R. Renishaw: Photoluminescence (accessed September 23) http://www.renishaw.com.tw/tw/photoluminescence-explained--25809

Progetto C.L.I.M.A., economia circolare. Visita alla multinazionale CARGILL PEC ITALY: 120 tonnellate giornaliere di pastazzo de-pectinizzato di bucce fresche di agrumi vanno alle aziende che producono alimentazione per animali. Distretto Produttivo Agrumi di Sicilia, **2023**. https://www.distrettoagrumidisicilia.it/progetto-c-l-i-m-a-economia-circolare-visita-alla-multinazionale-cargill-pec-italy-120-tonnellate-giornaliere-di-pastazzo-de-pectinizzato-di-bucce-fresche-di-agrumi-vanno-alle-aziende-che-producon/ (accessed September 23)

Robinson, A.L. Electron Microscope Inventors Share Nobel Physics Prize. *Science*, **1986**, 234, 821–822. https://doi.org/10.1126/science.234.4778.821

Saputra, H.A. Electrochemical Sensors: Basic Principles, Engineering, and State of the Art. *Monatshefte Für Chemie - Chemical Monthly*, **2023**, 154 (10), 1083–1100. https://doi.org/10.1007/s00706-023-03113-z

Satira, A.; Paone, E.; Bressi, V.; Iannazzo, D.; Marra, F.; Calabrò, P.S.; Mauriello, F.; Espro, C. Hydrothermal Carbonization as Sustainable Process for the Complete Upgrading of Orange Peel Waste into Value-Added Chemicals and Bio-Carbon Materials. *Applied Sciences*, **2021**, 11, 10983. https://doi.org/10.3390/app112210983

Sharma, D.B.K. Instrumental Methods of Chemical Analysis. *Krishna Prakashan Media*, **1981**. https://link.springer.com/book/10.1007/978-3-031-38355-7

Sorrenti, V.; Burò, I.; Consoli, V.; Vanella, L. Recent Advances in Health Benefits of Bioactive Compounds from Food Wastes and By-Products: Biochemical Aspects. *International Journal of Molecular Sciences*, **2023**, 24, 2019. https://doi.org/10.3390/ijms24032019

Spagnuolo, D.; Iannazzo, D.; Len, T.; Balu, A. M.; Morabito, M.; Genovese, G.; Espro, C.; Bressi, V. Hydrochar from Sargassum Muticum: A Sustainable Approach for High-Capacity Removal of Rhodamine B Dye. *RSC Sustainability*, **2023**. https://doi.org/10.1039/D3SU00134B

Sri Shalini, S.; Palanivelu, K.; Ramachandran, A.; Raghavan, V. Biochar from biomass waste as a renewable carbon material for climate change mitigation in reducing greenhouse gas emissions—a review. *Biomass Conversion and Biorefinery*, **2021**, 11, 2247–2267. https://doi.org/10.1007/s13399-020-00604-5

Suni, I.I. Impedance methods for electrochemical sensors using nanomaterials. *TrAC Trends in Analytical Chemistry, Electroanalysis Based on Nanomaterials*, **2008,** 27, 604–611. https://doi.org/10.1016/j.trac.2008.03.012

Tittarelli, F.; Trinchera, A.; Intrigliolo, F.; Benedetti, A. Evaluation of Organic Matter Stability During the Composting Process of Agroindustrial Wastes. *Environmental*

Science, Agricultural and Food Sciences, **2002**. https://doi.org/10.1007/978-3-662-08724-4_33

Tscharnuter, W. Photon Correlation Spectroscopy in Particle Sizing, in: Encyclopedia of Analytical Chemistry. John Wiley & Sons, Ltd., **2006** https://doi.org/10.1002/9780470027318.a1512

Walt, D.R. Optical Methods for Single Molecule Detection and Analysis. *Analytical Chemistry*, **2013**, 85, 1258–1263. https://doi.org/10.1021/ac3027178

Wehr, J. Algae: Anatomy, Biochemistry, and Biotechnology by Barsanti, L. & Gualtieri, P. *Journal of Phycology*, **2007**, 43. https://doi.org/10.1111/j.1529-8817.2007.00335.x

X-ray Diffraction : XRD | Techniques | Fields | Toray Research Center | TORAY [WWW Document], (accessed September 2023). https://www.toray-research.co.jp/en/technicaldata/techniques/XRD.html

Yi, J.; Wan, J.; Ye, G.; Wang, Y.; Ma, Y.; Yan, Z.; Zeng, C. Targeted degradation of refractory organic pollutants in wastewater based on molecularly imprinted catalytic materials: Adsorption process and degradation mechanism. *Separation and Purification Technology*, **2023**, 311, 123244. https://doi.org/10.1016/j.seppur.2023.123244

Zammuto, V.; Rizzo, M.G.; Spanò, A.; Spagnuolo, D.; Di Martino, A.; Morabito, M.; Manghisi, A.; Genovese, G.; Guglielmino, S.; Calabrese, G.; Capparucci, F.; Gervasi, C.; Nicolò, M.S.; Gugliandolo, C. Effects of crude polysaccharides from marine macroalgae on the adhesion and biofilm formation of Pseudomonas aeruginosa and Staphylococcus aureus. *Algal Research*, **2022**, 63, 102646. https://doi.org/10.1016/j.algal.2022.102646

Zu, F.; Yan, F.; Bai, Z.; Xu, J.; Wang, Y.; Huang, Y.; Zhou, X. The quenching of the fluorescence of carbon dots: A review on mechanisms and applications. *Microchimica Acta*, **2017**, 184, 1899–1914. https://doi.org/10.1007/s00604-017-2318-9

Chapter 3. Experimental Endeavors, Outcomes, and Discussion

3.1 Voltammetric Sensor Based on Waste-Derived Carbon Nanodots for Enhanced Detection of Nitrobenzene

*Published: ChemElectroChem **2023***

Carbon dots (CDs) samples were synthesized from orange peel waste (OPW) via a simple and eco-friendly hydrothermal carbonization (HTC) and electrochemical (EC) bottom-up synthesis integrated approach. The comprehensive chemical-physical characterization of CDs samples, carried out by various techniques such as TEM, EDX, XRD, FT-IR, underlined their morphological and microstructural features. The CDs exhibited attractive electrochemical properties, and thus an electrochemical sensor by modifying a

screen-printed carbon electrode (CDs/SPCE) for the detection of nitrobenzene (NB) in water was developed. Electroanalytical performances of CDs/SPCE sensor using differential pulse voltammetry (DPV) demonstrated its high sensitivity (9.36 $\mu A \mu M^{-1} cm^{-2}$) towards NB in a wide linear dynamic range (0.1—2000 μM) and a low limit of detection (LOD=13 nM). The electrochemical sensor also shows high selectivity, long-term stability, and repeatability. This paper might open the way to a new synergistic HTC-EC approach for the synthesis of CDs from waste biomass material and their advanced application in highly efficient electrochemical sensors.

Experimental

CDs Synthesis process

The HTC experiments were performed following the procedure previously reported by our research group (Espro *et al.*, 2021). Based on the results obtained in the previous work (Satira *et al.*, 2021), the residence time, after reaching the reaction temperature, was set at 60 minutes, at a stirring speed of 750 rpm. Then, the solid and liquid products were separated by vacuum filtration with a Buchner funnel and filter paper. The obtained liquid aqueous sample, hereafter named $LHTC_{180\text{-}60}$, was employed as a raw material for the subsequent electrochemical bottom-up procedure. In a typical electrochemical synthesis of CDs, a solution 1:1 (V/V) of $LHTC_{180\text{-}60}$ (0.121 g mL^{-1}) and NH_3 30 % was put in a glass sample vial. Two Pt wire spirals used as both cathode and anode electrodes (apparent area 1.0 cm^2) were immersed into the alkaline solution (see Figure S1 in Supporting Information for details about the experimental apparatus). A direct current stabilized power supply was used to apply a static potential (8-12 V) between the two electrodes, and the treatment was carried out at room temperature (25 °C) for 2.5 h. The obtained dark brown aqueous solution was centrifuged in order to remove large or aggregated -

particles and to separate the dark solid from the supernatant. To further remove the matrix, the material was washed with ethanol and centrifuged three more times. Finally, pure, dark brown powder CDs were obtained after complete evaporation of the solvent. The mY of CDs was calculated using the following equation (Eq. 1):

$$\text{mY, wt \%} = \frac{m_{CDs,\ g}}{m_{feedstock,\ g}} \times 100 \quad (1)$$

where m_{CDs} is the mass of CDs, $m_{feedstock}$ is the dry mass of OPW.

Modified electrode fabrication

SPCEs mod C110, were purchased from DropSens (Methrom). The sensor platform consists of a ceramic substrate with a length of about 3.5 cm and a diameter of 4.0 mm, on which the electrochemical cell consists of three components: the carbon working electrode, the silver pseudo reference electrode, and the carbon counter electrode. The modified CDs/SPCE sensors were fabricated by dispersing, using ultrasound, 1 mg of CDs in 1 mL of distilled water. Then, 10μL of each suspension was drop cast on the surface of the working carbon electrode. After any dropping, the electrode was permitted to dry before the successive dropping. The sensors thus modified were allowed to dry at room temperature overnight.

Results and Discussion

The aim of this work is the use of the liquid phase deriving from the HTC treatment of OPW, generally considered a non-exploitable waste (Erdogan *et al.*, 2015). Based on the results of our previous studies (Satira *et al.*, 2021), which evidenced that the optimal reaction conditions to obtain an aqueous

phase rich in organic compounds, useful as raw materials for further EC treatment, the HTC experiments were performed at 180 °C for 60 minutes. The general chemical composition of the obtained liquid aqueous sample $LHTC_{180\text{-}60,}$ shows that the main compounds are furan derivatives, especially furfural (16.69%) and 5-hydroxymethylfurfural (61.82%), evidencing that, at low HTC temperatures (180°C), one of the main compounds obtained in the liquid phase is 5-hydroxymethylfurfural (5-HMF) (Satira *et al.*, 2021). The electrocatalytic conversion of 5-HMF has been widely demonstrated, and this area of research is in the growth phase. Accordingly, the use of raw materials containing 5-HMF is of great importance for recovery, recycling, and circular chemistry. Based on our continuous efforts and experience in both biomass valorization (Espro *et al.*, 2021) and the development of sustainable electrochemical methods, (Chiarotto *et al.*, 2019; Pandolfi *et al.*, 2019) an electrochemical process for producing carbon dots using the liquid phase from HTC, which is rich in 5-HMF, has been developed. In the field of carbon dots production from biomass waste, the use of the EC method represents a highly innovative application. The chosen electrochemical setup, consisting of an undivided cell employing two Pt spirals as electrodes and a potentiostat device, is cheap and easily available compared to other electro-synthesis techniques, and guarantees ease of operation and precise control over the amount of current flowing through the system. Under these conditions, the resulting mass yield (mY) of CDs was 37% (see Eq. 1). Indeed, further increase of the applied potential from 8 V to 12 V results in low amounts of CDs performing with the same reaction time of 2.5 h. **Figure 3.1.1** shows the effect of applied voltage (8-12 V) on mY of CDs.

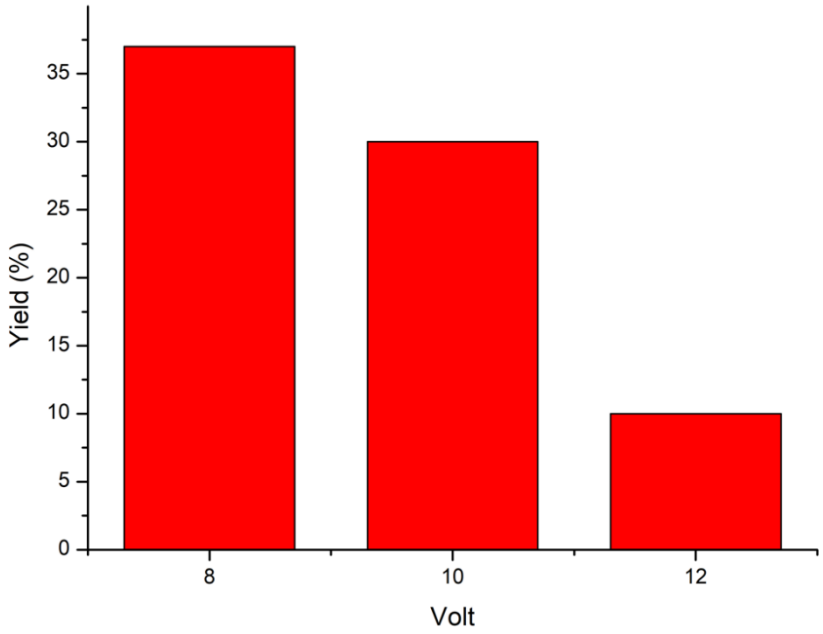

Figure 3.1.1. The effect of applied voltage (8-12 V) on the mY of CDs

CDs morphology was investigated by Transmission Electron Microscopy (TEM). The representative images of CDs (**Figure 3.1.2**) confirmed the presence of monodispersed small circular nanoparticles and crystalline cores. Synthesized CDs exhibited an average diameter in the range of 1.47 nm to 6.67 nm.

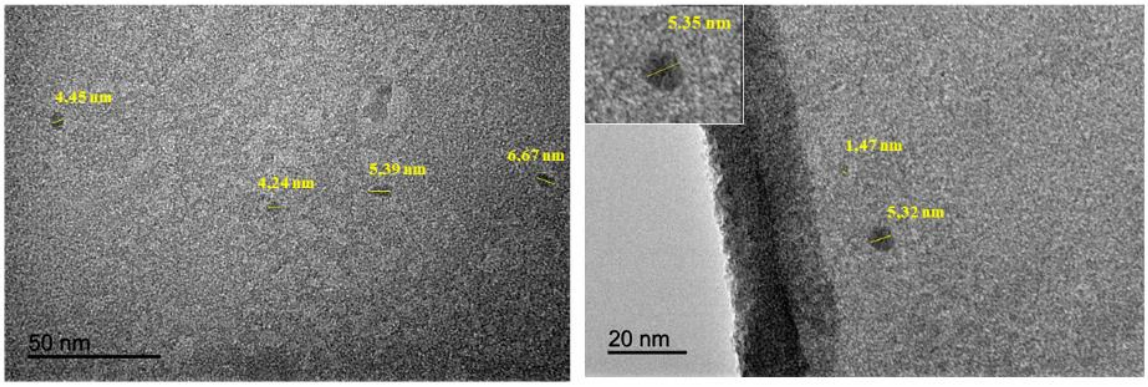

Figure 3.1.2. Representative TEM images of the CDs

The energy-dispersive X-ray spectroscopy (EDX) results (see **Figure 3.1.3**) indicate that the CDs contain mainly carbon, nitrogen, and oxygen, and no observable impurities were detected. EDX spectra of the CDs showed a high content of O due to many residual oxygen groups remaining on the surface.

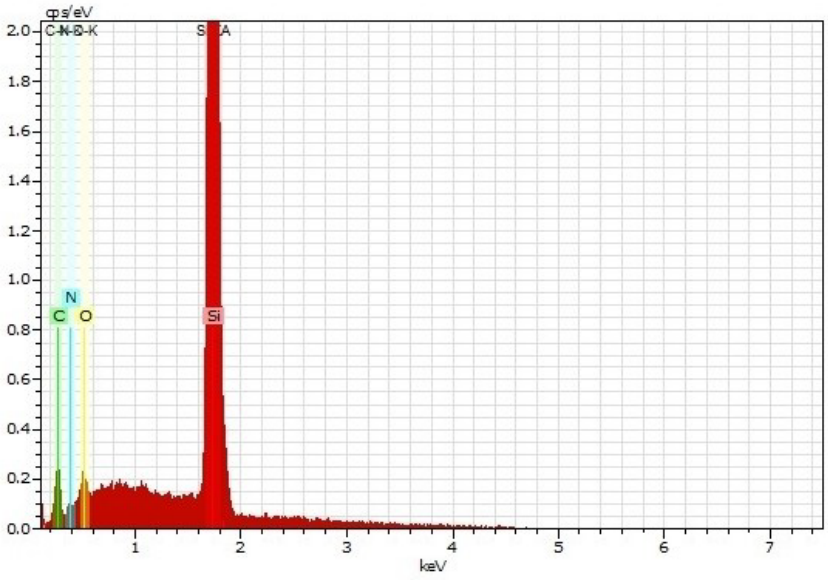

Figure 3.1.3. EDX spectrum

Nitrogen can derive from other water-soluble components present in the starting biomass (orange peels). Moreover, the dynamic light scattering (DLS) measurement, reported in **Figure 3.1.4a**, confirmed the small size of the synthesized CDs and their dispersibility in water. Volume-weighted DLS measurements revealed a population centered at 10.1 nm, a value slightly higher than that obtained by TEM, and a polydispersity index (PDI) of 0.425, further confirming the tight particle size distribution.

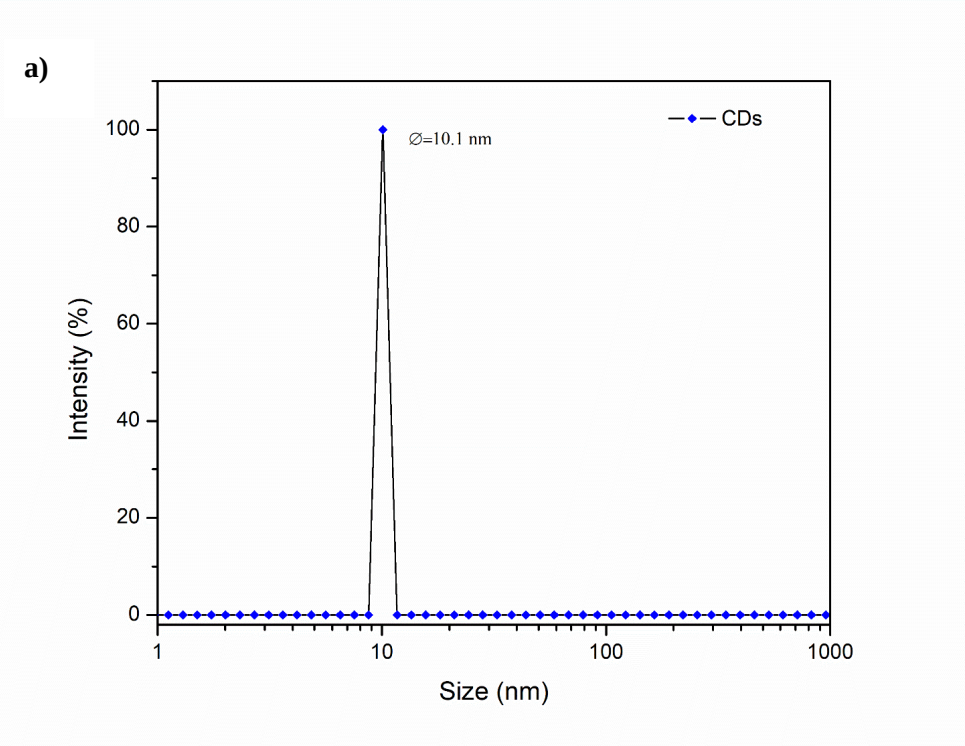

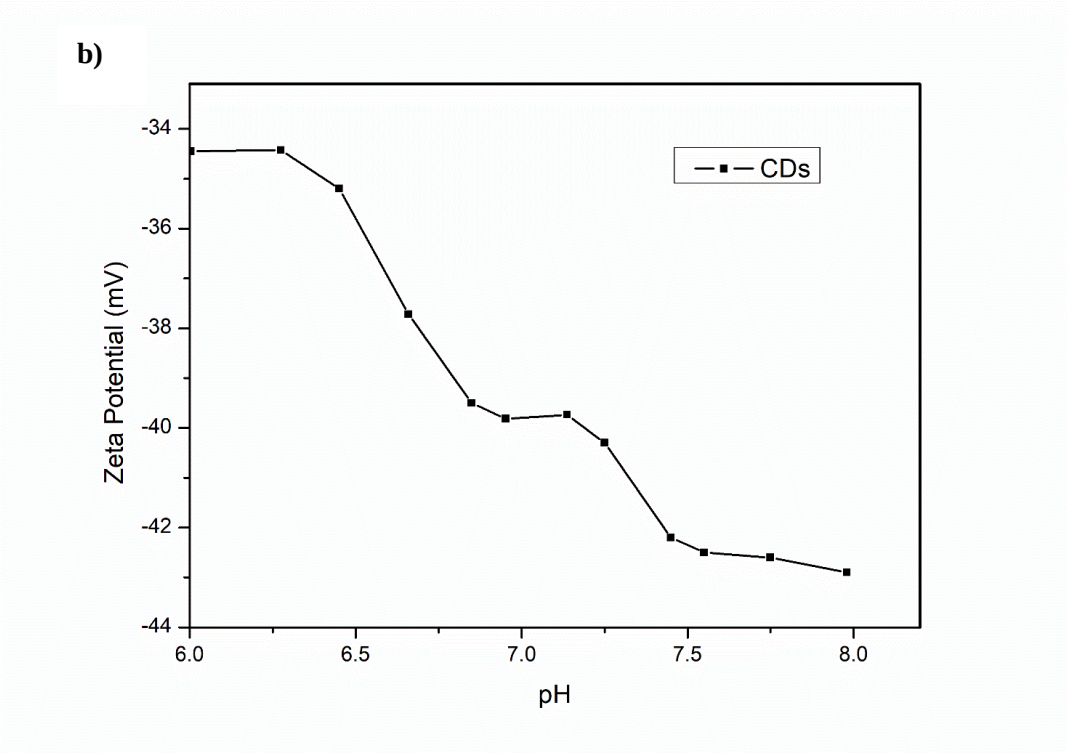

Figure 3.1.4. a) DLS size distribution and **b)** zeta potential at different pH values of CDs

Further confirmation of the electrical charges on the surface of nanoparticles and their colloidal stability was given by the zeta potential (**Figure 3.1.4 b**), evaluated in the pH range of 6.0 to 8.0. Zeta potential is a level of degree of electrostatic repulsion between contiguous similar charged particles in dispersed CDs. The negative value of zeta potential indicates that the electrostatic forces are repulsive between the molecules. In the investigated pH range, the CDs surfaces were always negatively charged, consistent with the Fourier-transform infrared spectroscopy (FTIR) results (**Figure 3.1.5b**), suggesting the presence of negatively charged hydroxyl (−OH) and carboxyl (−COOH) functional groups on their surface. The oxygen-rich and anionic functional groups present on CDs surfaces improved their hydrophilicity and stabilities in aqueous systems, which would be promising for sensing applications in aqueous media.

To acquire deeper information regarding the evolution of the microstructure and evidence about the surface groups present, CDs samples were investigated by X-ray diffraction spectroscopy (XRD) and FTIR (**Figure 3.1.5 a** and **b**, respectively). The XRD diffraction spectrum shows a diffraction peak centered at 2θ=27° and 2θ=35° corresponding relatively to the (002) graphitic plane and the turbostratic structure of disordered carbon coming from the (100) plane of graphite (Mewada *et al.*, 2013). The presence of different functional groups on CDs surface was confirmed by FTIR studies (**Figure 3.1.5b**). The FTIR spectrum of CDs shows the presence of oxygenated groups on the surface of the nanomaterial. The strong, broad stretching band at 3200 cm^{-1} in the IR spectrum, indicates the presence of an O−H alcohol group stretching by an intermolecular bonded functional group on prepared CDs while the peak at 1390 cm^{-1} could be assigned to the O−H bending of the alcoholic groups (Majumdar *et al.*, 2017). Moreover, the adsorption bands at 1655 cm^{-1} and 1590 cm^{-1} correspond to the C=O vibrations and the C=C band, respectively, indicating the asymmetric stretching of aromatic rings, esters, amides or carboxylic groups, revealing the aromatization and decarboxylation reaction of the OPW during the hydrothermal process (Singh *et al.*, 2022). As will be discussed later, the presence of these functional groups plays a crucial role in the selective interaction between the CDs and nitrobenzene (NB). As evidenced, the FTIR results indicate that the surface of CDs is rich in hydroxyl and carboxylic groups. As previously reported, it is probable that these hydrophilic groups may be due to the oxidation of the obtained carbon nanoparticles under electrochemical oxidation.

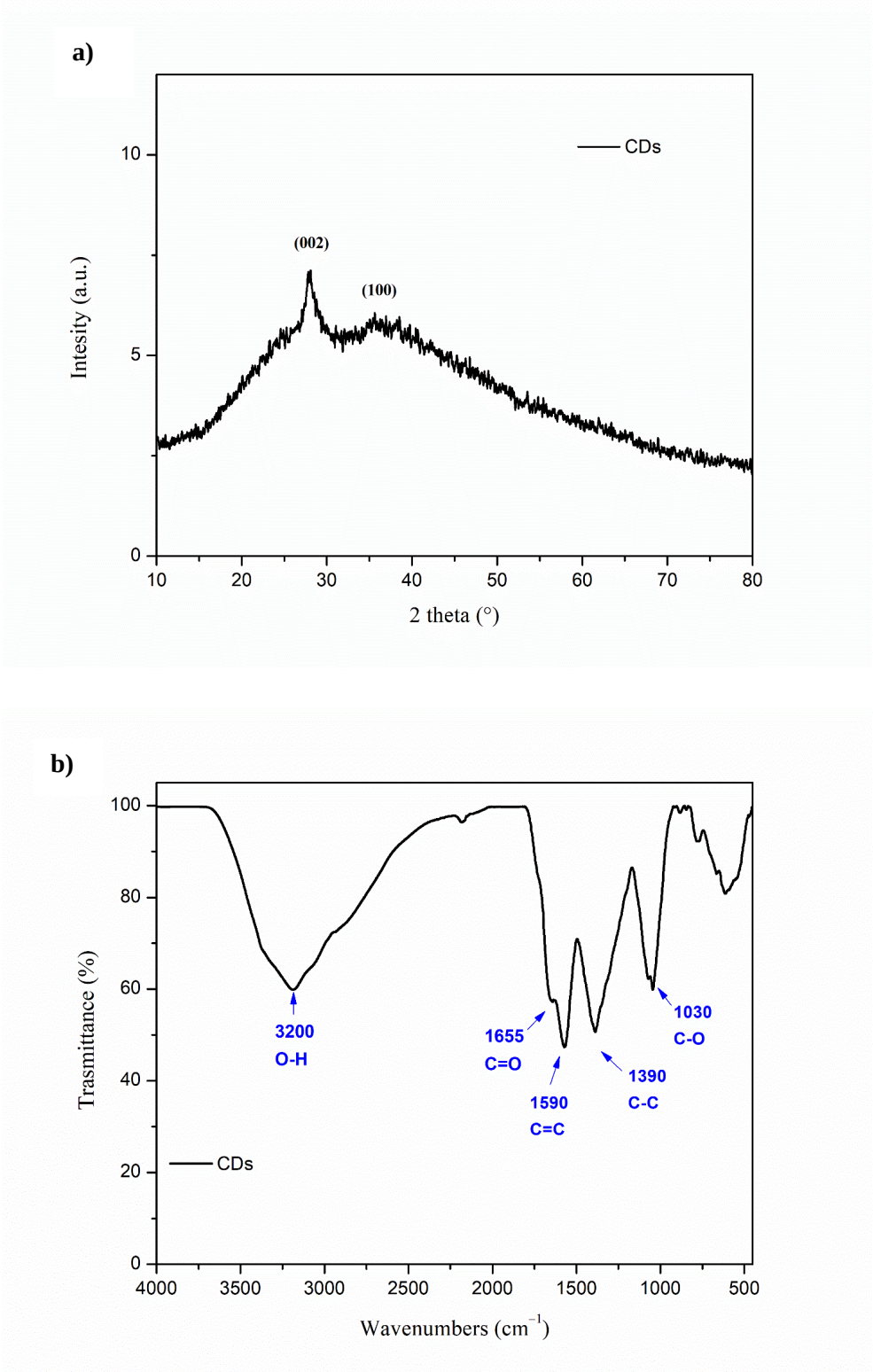

Figure 3.1.5. Compositional analysis of CDs: **a)** XRD spectrum; **b)** FTIR spectrum

An electrochemical study of the CDs deposited on the SPCE platform (CDs/SPCE) was first performed. The study of Nyquist diagrams in electrical

impedance spectroscopy (EIS) analysis shows the transfer capacity of the electron on the bare and modified sensor. The analysis was conducted in the presence of 10 mM $[Fe(CN)_6]^{3-/4-}$ and 0.1 M KCl, in the frequency range from 0.1 Hz to 105 Hz (amplitude 5 mV) and with an applied potential of 0.25 V. The size of the semicircle that can be observed at high frequencies indicates the resistance of the sensor to the charge transfer that takes place on its surface, while the linear portion is attributed to the diffusion process that takes place on the sensor and can be observed at low frequencies (Sarat *et al.*, 2006). **Figure 3.1.6a** shows the results obtained. The sensor modified with the CDs shows a very small semicircle diameter in the Nyquist plots (as reported in the inset in **Figure 3.1.6a**) compared to the bare SPCE. This indicates the ability of the new sensor functionalized with CDs to promote the transfer of electrons by improving the ability to start redox processes necessary for the detection of NB. **Figure 3.1.6b** shows the modeling of the electrical equivalent circuit obtained from the collected data, which combines four components: the electrolytic resistance between the working and reference electrodes (R_s), the double layer capacitance (CPE), the charge transfer resistance (R_p) and the Warburg impedance (W).

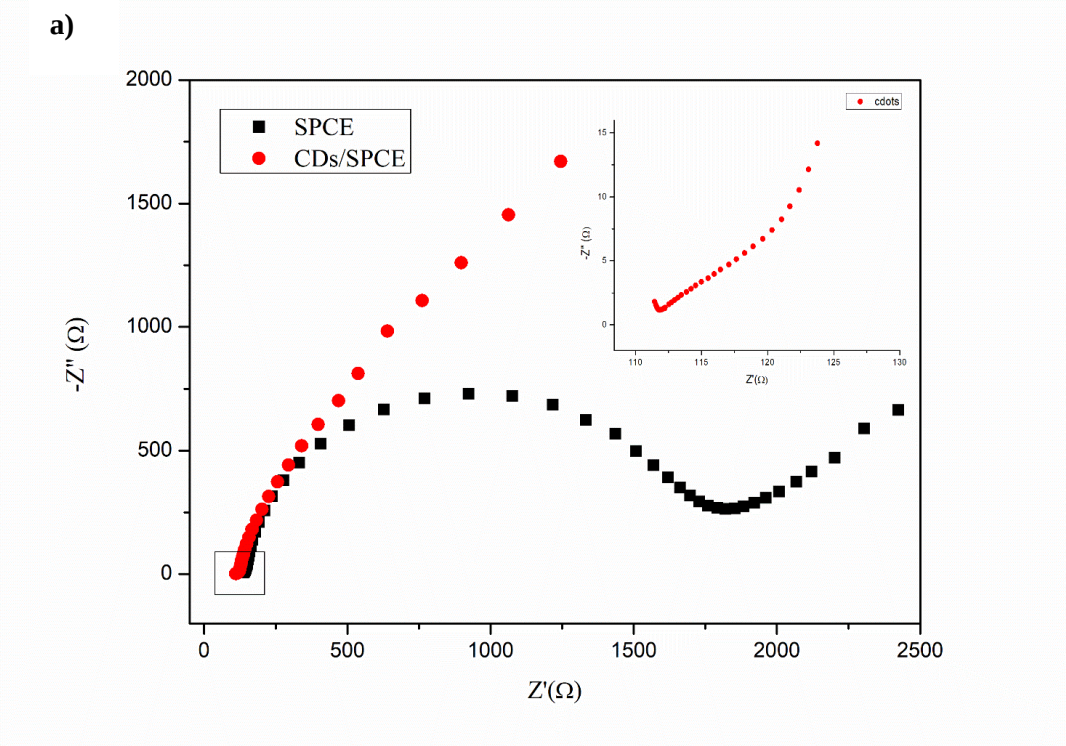

Figure 3.1.6. a) EIS of SPCE and CDs/SPCE in a solution containing 10 mM $[Fe(CN)_6]^{3-/4-}$ and 0.1 M KCl with a frequency range from 0.1 Hz to 105 Hz and amplitude 5 mV; **b)** electrical equivalent circuit

The modified sensor CDs/SPCE has also been characterized through cyclic voltammetry (CV) analysis using 10 mM $K_3[Fe(CN)_6]$ solution with a scanning speed of 50 mV s^{-1} (**Figure 3.1.7**). The recorded electrochemical behavior shows a modified sensor with a higher peak current than the bare (202.56 µA versus 112.67 µA respectively) and a peak-to-peak separation (ΔEp) lower in CDs/SPCE than SPCE with 120 mV and 230 mV respectively. All this confirms the great ability of the modified sensor to promote the

oxidation/reduction reaction by increasing the charge transfer compared to the bare, demonstrating better sensitivity.

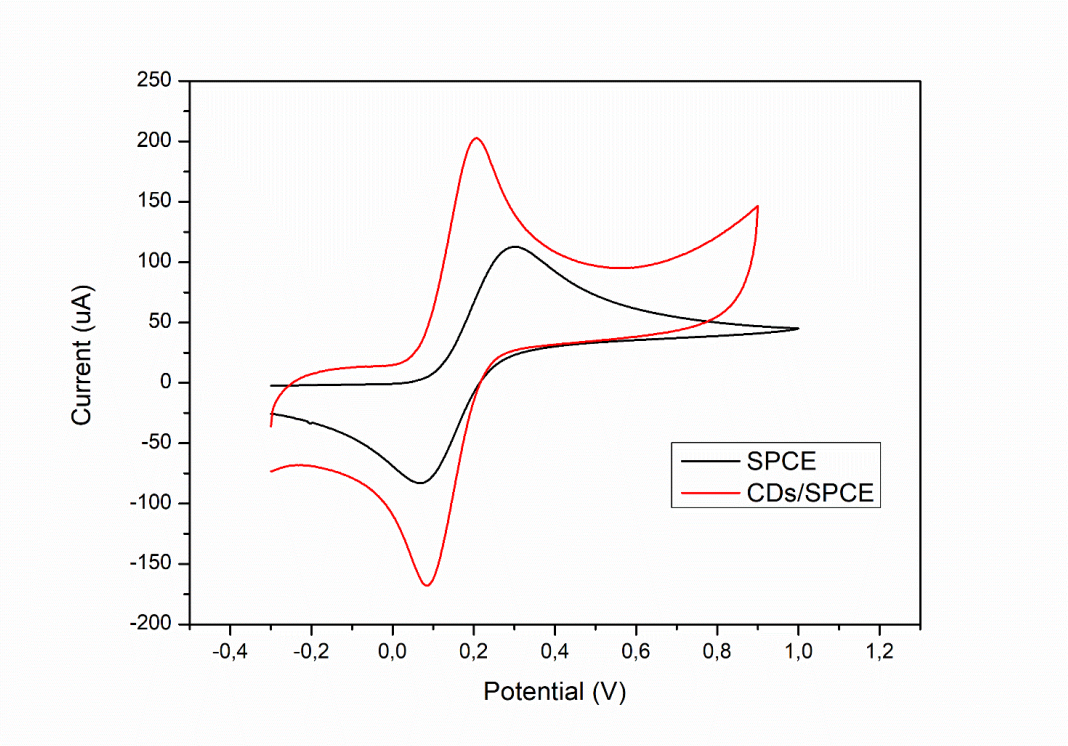

Figure 3.1.7. Cyclic voltammogram of SPCE and CDs/SPCE in presence of 10 mM $K_3[Fe(CN)_6]$ at a scan rate of 50 mVs^{-1}, in the potential range from −0.3 V to 0.9 V

The scan rate was obtained between 10 to 400mV s^{-1}, studying the oxidation/reduction phenomenon affected on the sensor surface. The results shown in **Figure 3.1.8a** demonstrate an increase in oxidation peak and a shift in work potential with increasing scanning speed. Relating the maximum current peak to the square root of the scanning speed shows a linear trend (**Figure3.1.8b**), which proves the capability of the CDs/SPCE sensor to promote the electrochemical process under diffusion control. The standard deviation (sd) was calculated on three repetitions for each measurement, resulting in equal/less than 3 (**Figure 3.1.8c**).

a)

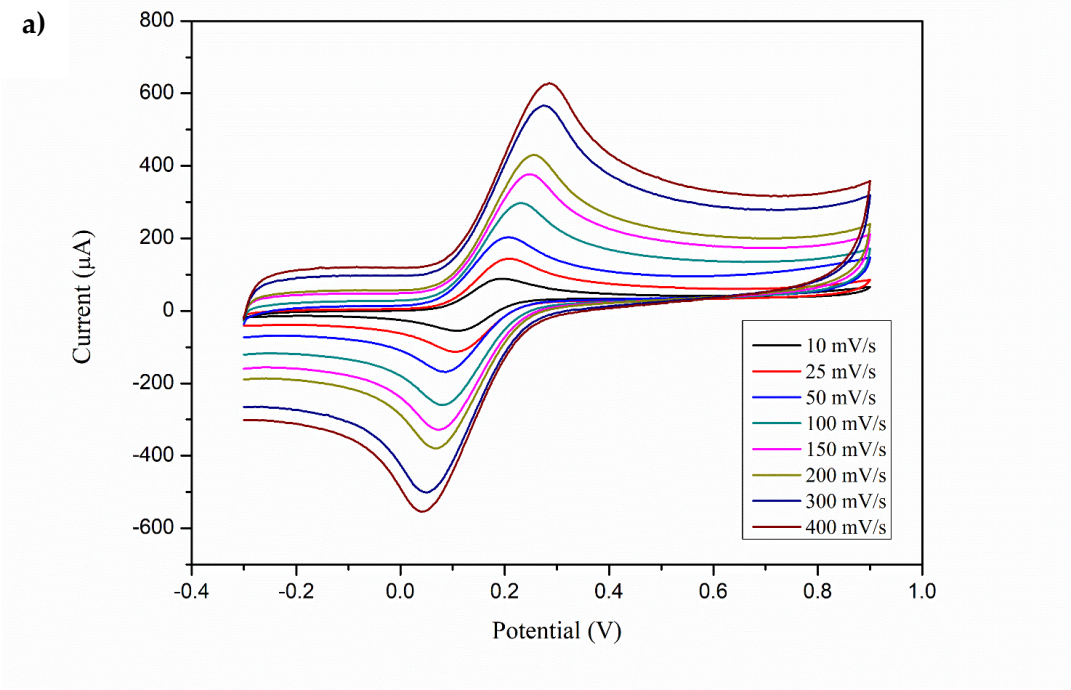
Current (µA)
Potential (V)
10 mV/s
25 mV/s
50 mV/s
100 mV/s
150 mV/s
200 mV/s
300 mV/s
400 mV/s

b)

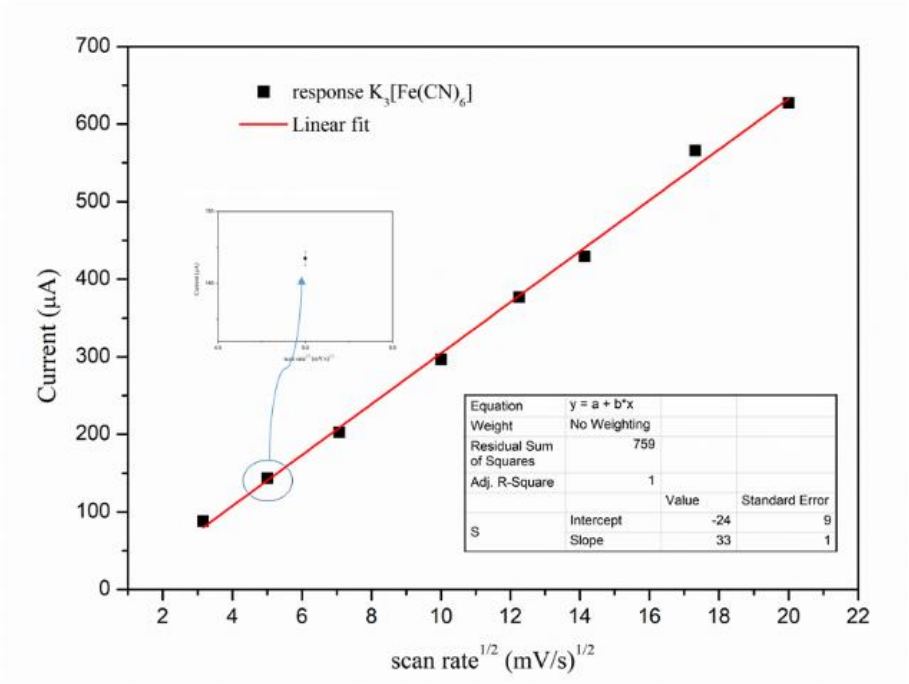
response K3[Fe(CN)6]
Linear fit
Current (µA)
scan rate1/2 (mV/s)1/2
Equation y = a + b*x
Weight No Weighting
Residual Sum of Squares 759
Adj. R-Square 1
Value Standard Error
Intercept -24 9
Slope 33 1

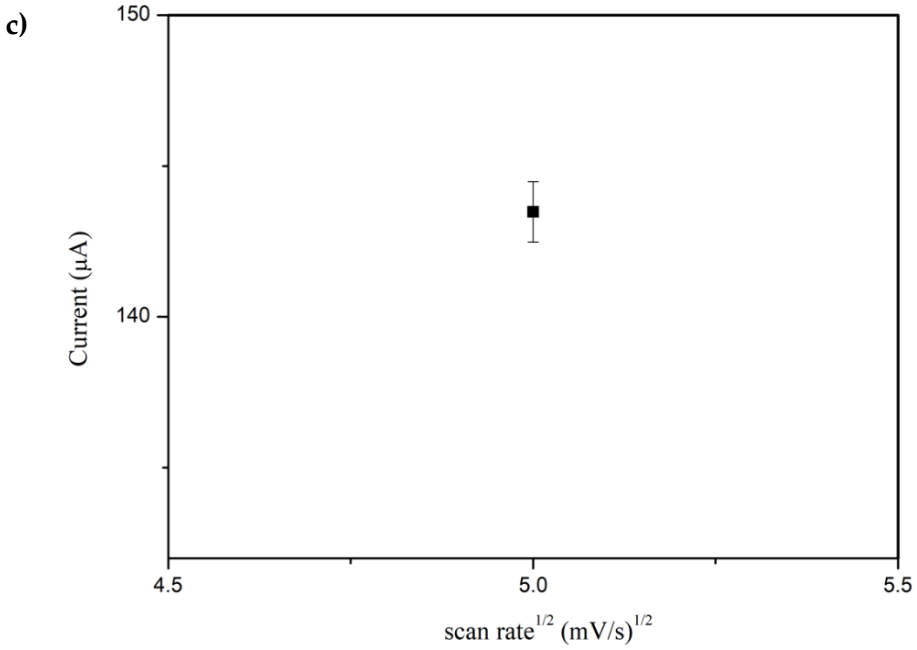

Figure 3.1.8. a) Cyclic voltammogram of SPCE and CDs/SPCE in presence of 10 mM $K_3[Fe(CN)_6]$ at different scan rates between 10 and 400 mVs^{-1}, in 0.01 M PBS (pH 7.4), in the potential range from −0.3 V to 0.9 V ; **b)** plot of Ip vs υ ½, **c)** detail, sd ≤ 3

The effective electrochemical active surface area of the prepared electrode was also determined from these data based on the Randles-Ševčik equation (Eq. 2). The effective electrochemical active surface area of CDs/SPCE was about 55 % more compared to the bare. The formula was employed to determine the active surface area of the SPCE and CDs/SPCE using ferro/ferrocyanide as the redox probe (Bressi *et al.*, 2022):

(2)

$$Ip = \pm 0{,}4463nFAC\sqrt{\frac{nFvD}{RT}}$$

where *Ip* is the voltammetric current (A) using the forward peak of the electrochemical process; *n* is the number of electrons transferred in the electrochemical reaction (*n*=1); *F* is the Faraday constant (F = 96485.3365 C/mol); *A* is the electrode surface area (cm^2); *C* is the concentration of the redox probe (C=10 mM); *v* is the applied voltammetric scan rate (v = 0.05 V/s); *D* is

the analytic diffusion coefficient (D = 7.6×10^{-6} cm^2/s); R is the universal gas constant (R = 8.314 J/mol); *T* is the Kelvin temperature (T = 298.15 K).

CV of the SPCE and CDs/SPCE was performed in the potential range of −1.4 to 0.9 V in 0.01 M phosphate buffer solution (PBS) at pH 7.4. In the absence of NB, no faradaic peak was observed (**Figure 3.1.9**).

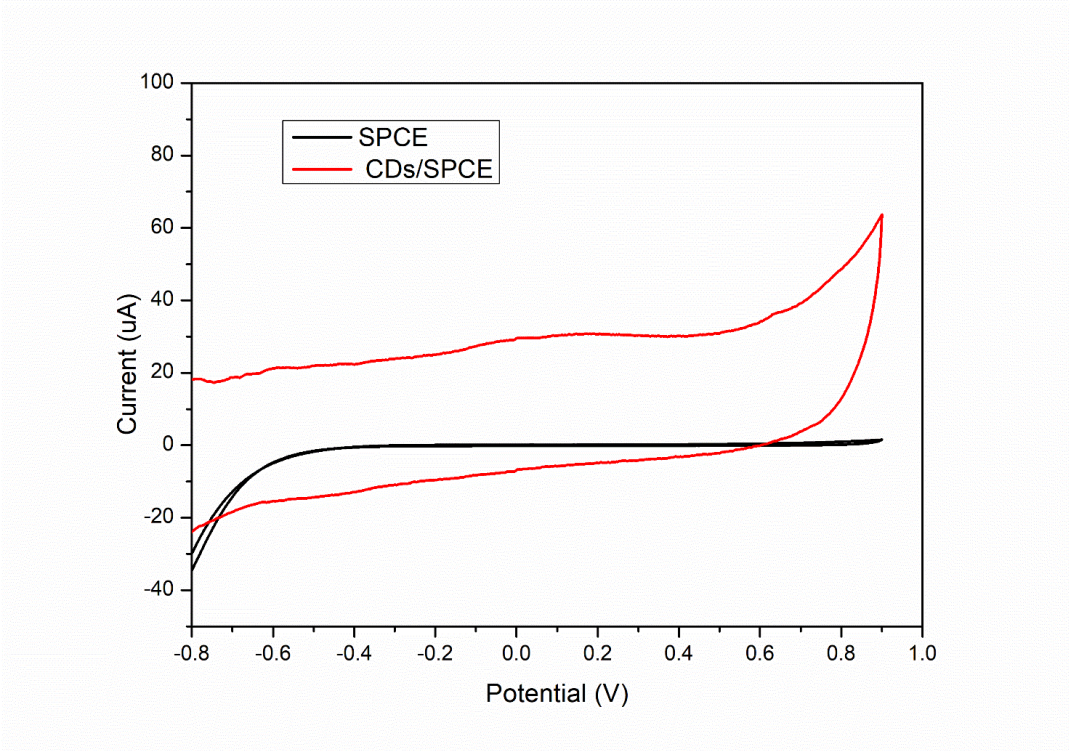

Figure 3.1.9. Electrochemical behaviour of the SPCE and CDs/SPCE in 0.01 M PBS, in the –0.8, +0.9 V potential window at a scan rate of 50 mV/s

The modified sensor exhibits a larger CV cycle than the SPCE one. This result indicates that the presence of CDs increases the active surface area of the electrode by increasing the available active sites. Further, in the presence of NB, the CDs/SPCE sensor shows two very intense oxidation peaks (O1 and O2) at −0.15 and 0.01 V and three reduction peaks (R1, R2, and R3) at −1.23 V, −0.9 V, and −0.31 V, respectively (**Figure 3.1.10a**). Literature data show that the R1 peak is due to the irreversible reduction of NB to

phenylhydroxylamine with subsequent reversible oxidation to nitrous benzene and reduction again to phenylhydroxylamine (Kokulnathan *et al.*, 2021; Thirumalraj *et al.*, 2016). Therefore, the R1 peak observed with the CDs/SPCE cycle is generated by the four-electron reduction of NB to phenylhydroxylamine, and then the phenylhydroxylamine continued to reduce to aniline through a two-electron process, namely the R2 peak. In the forward cycle, the phenylhydroxylamine produced through the reduction of NB was oxidized to nitrous benzene. Then, the produced nitrous benzene was reduced to phenylhydroxylamine, generating the R3 peak (Li *et al.*, 2007). Therefore, it is demonstrated that R1 and R3 reduction peaks are a redox couple of nitrous benzene and phenylhydroxylamine, and the R2 reduction peak could be due to the direct formation of aniline from nitrobenzene (Kariuki *et al.*, 2016). Based on these data, it is possible to speculate that the oxidation peaks observed in this work may result not only from the reversible oxidation-reduction reaction of hydroxylamine to nitrous benzene, but also from the oxidation of aniline formed during the redox process, as summarized in **Figure 3.1.10b**.

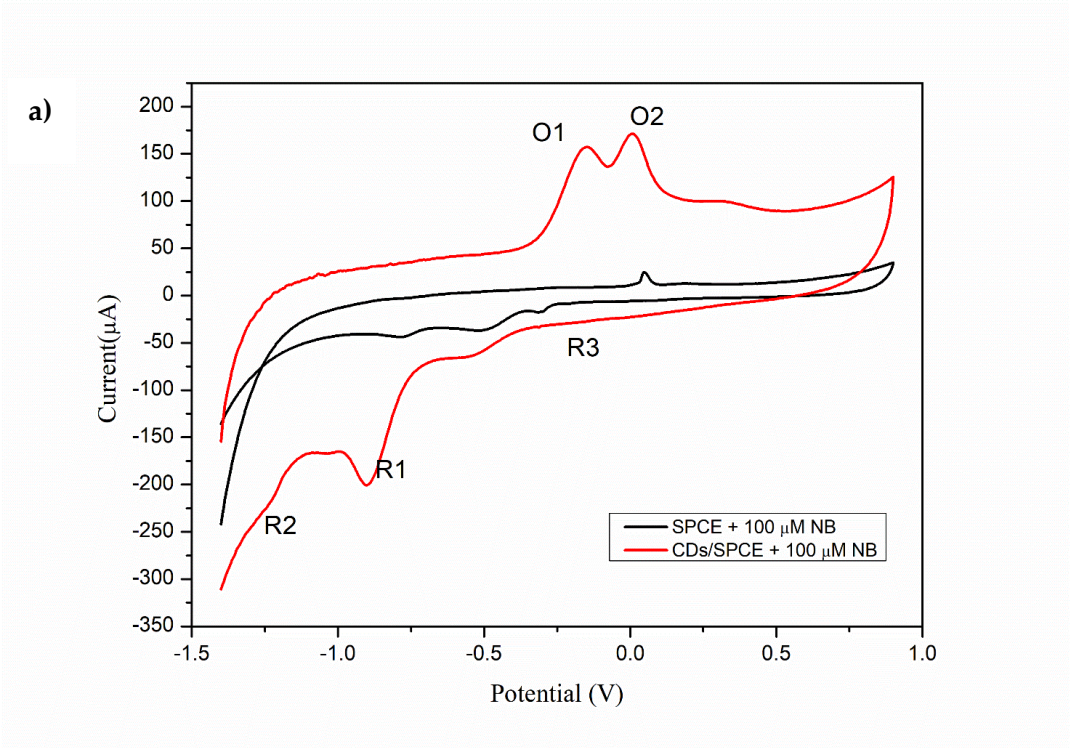

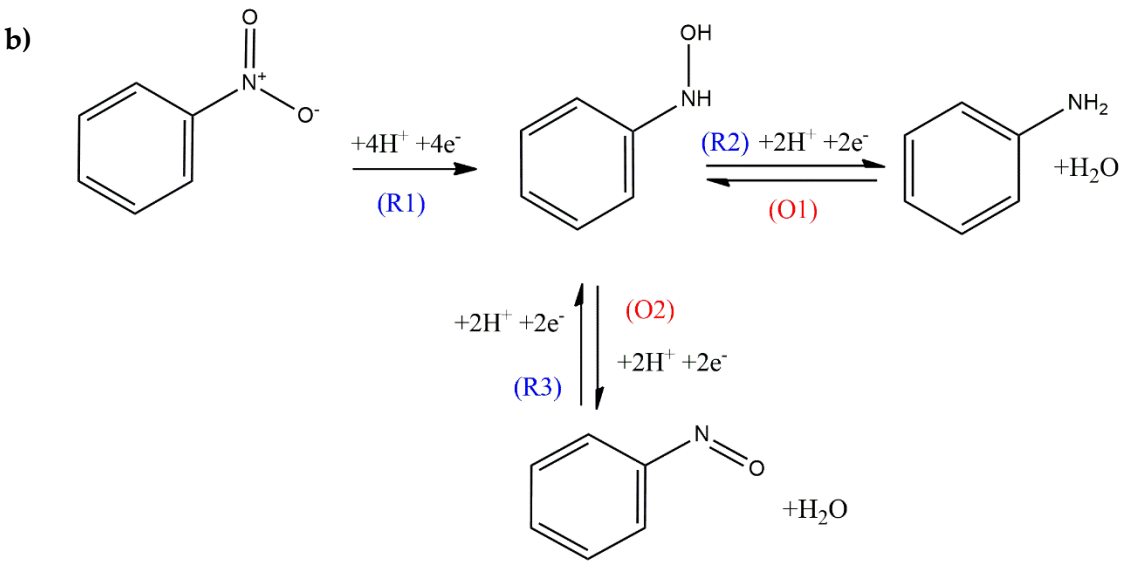

Figure 3.1.10. a) Electrochemical behavior of SPCE and CDs/SPCE with 100 µM NB in 0.01 M PBS at a scan rate of 50 mV/s from −1.4 to 0.9 V potential window; **b)** chemical transformations of NB

Figure 3.1.11a reports the linear sweep voltammetry (LSV) curves obtained at the different scan rates investigated, showing an increase in oxidation peak and a slight shift in potential with increasing scanning rate. Relating the maximum current peak (Ipa) to the scan rate shows a linear trend (**Figure 3.1.11b**) with an R^2 of 0.997. The sd was calculated on three repetitions for each measurement, resulting in equal/less than 1.6 (**Figure 3.1.11c**).

a)

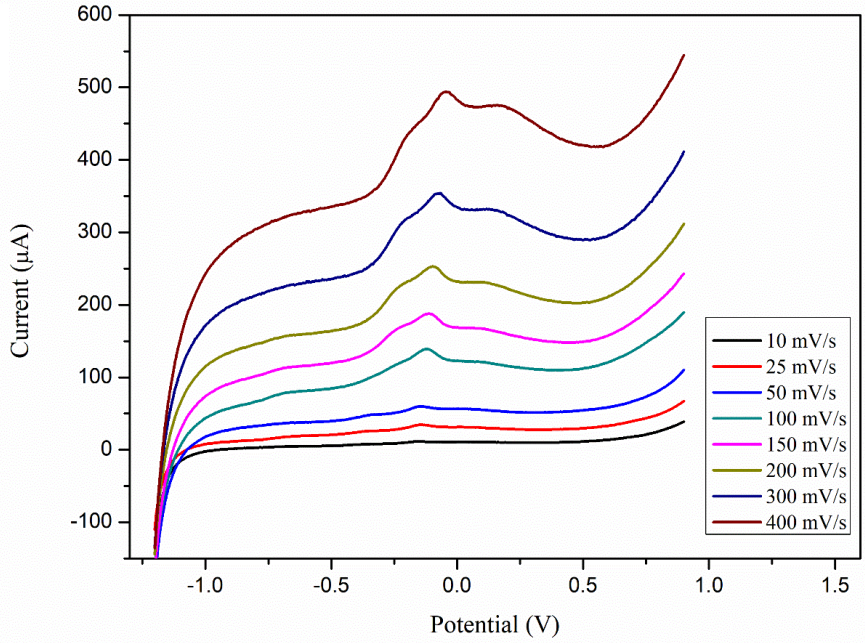
Current (µA)
Potential (V)
10 mV/s
25 mV/s
50 mV/s
100 mV/s
150 mV/s
200 mV/s
300 mV/s
400 mV/s

b)

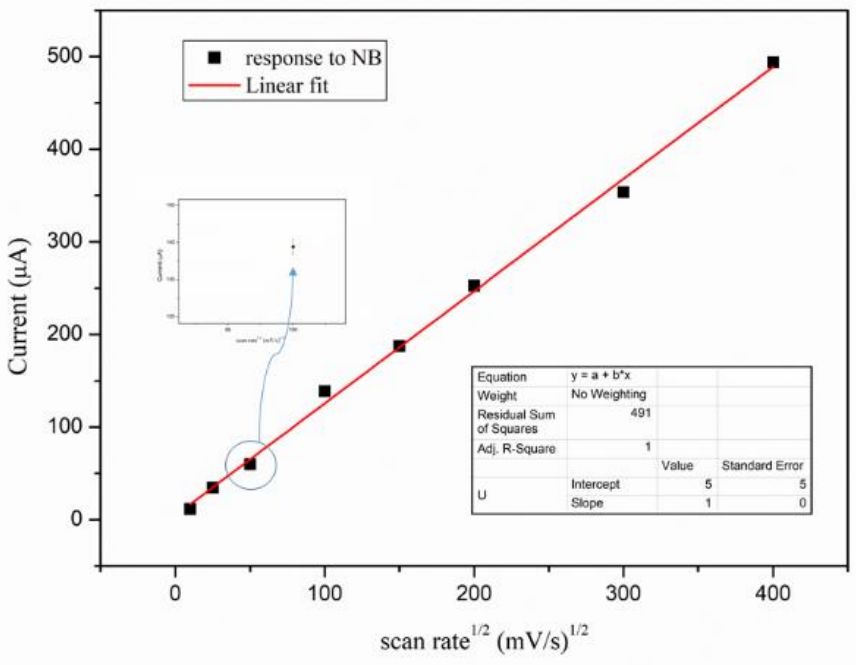
response to NB
Linear fit
Current (µA)
scan rate$^{1/2}$ (mV/s)$^{1/2}$
Equation y = a + b*x
Weight No Weighting
Residual Sum of Squares 491
Adj. R-Square 1
Value Standard Error
U Intercept 5 5
U Slope 1 0

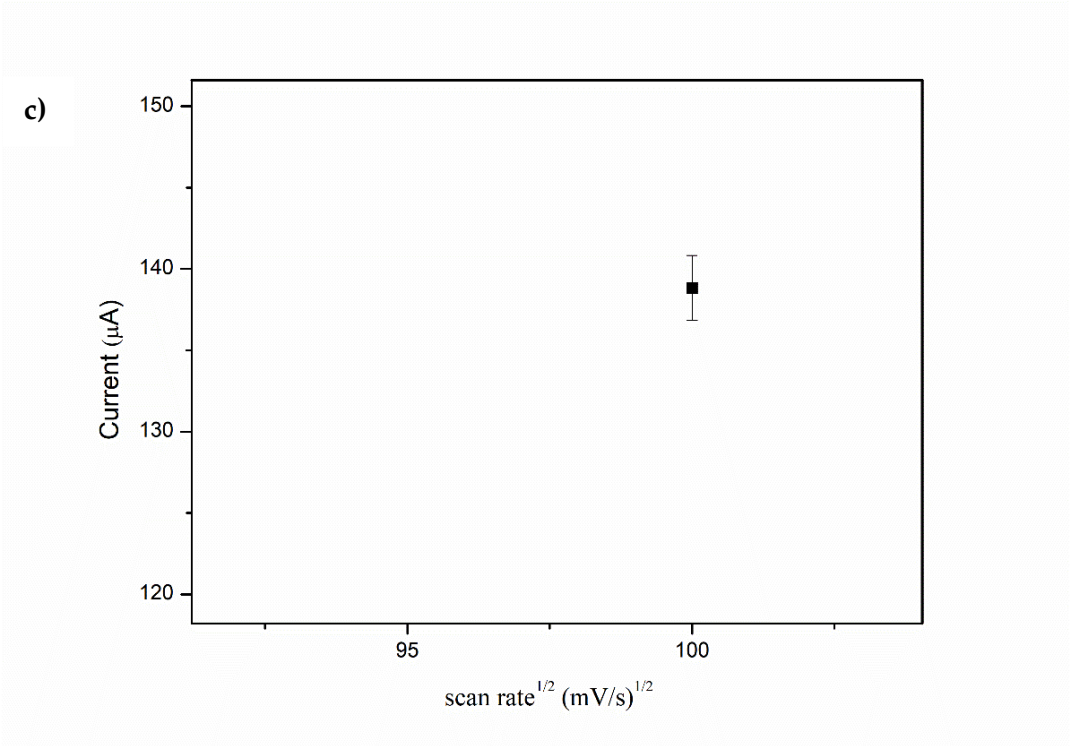

Figure 3.1.11. a) Linear sweep voltammogram of CDs/SPCE with 100 μM NB at different scan rates in 0.01 M PBs (pH 7.4); **b)** plot of Ip vs $v^{1/2}$; **c)** detail sd≤1.6

The effect of pH (**Figure 3.1.12**) on the reduction of NB (100 μM) was investigated by using a standard buffer solution in PBS (0.01 M) in the range between 2.3 to 13.0 at a scan rate of 50 mV s^{-1}. The sensor response was enhanced as the pH increased from 2.3 to 7.4, but it decreased at pH values greater than 8.0. The corresponding curves obtained by differential pulse voltammetry (DPV) at different pH values showed that the reduction of the NB has improved at pH=7.4.

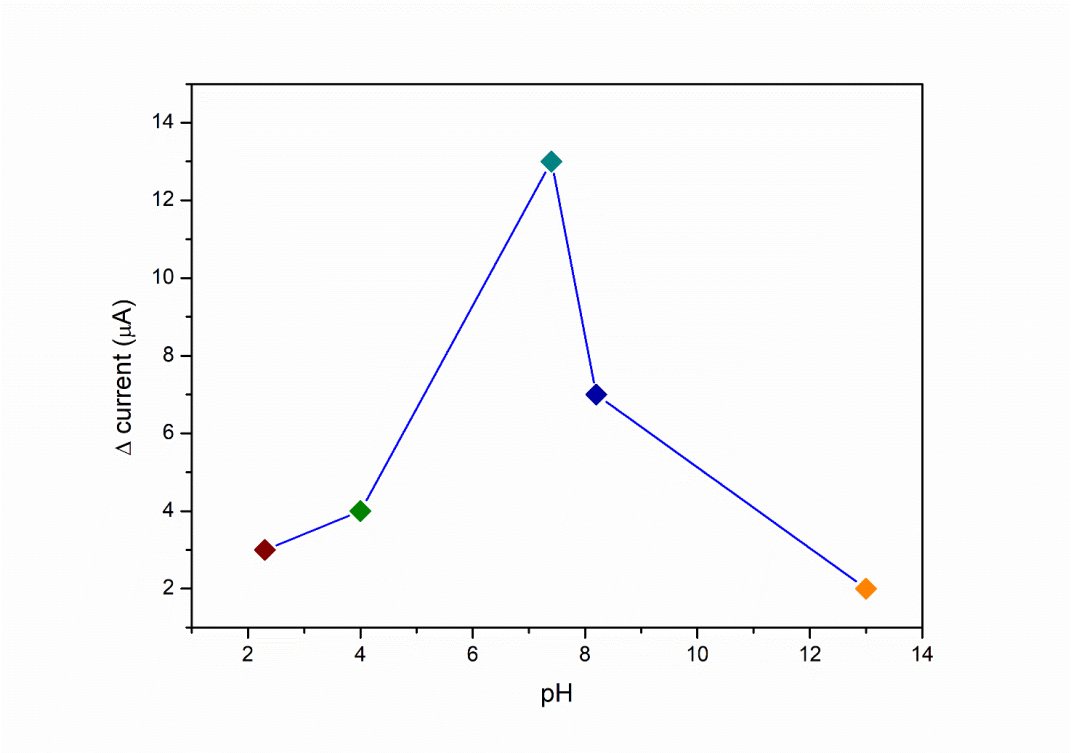

Figure 3.1.12. The pH effect on the reduction of NB

As reported in the literature (Kariuki *et al.*, 2016; Kokulnathan *et al.*, 2021), the increase in reduction peak current at neutral pH is attributed to the influence of the hydrogen ion on the reduction of NB. Thus, the value of 7.4 was chosen as the optimum pH for further experiments. The electroanalytical performances of the CDs/SPCE sensor were preliminarily assessed by studying its behavior for successive NB additions. NB is a compound rich in π-electrons and, therefore, interacts with CDs through the π–π interaction. Furthermore, the presence of weak bonds (such as hydrogen bonds) stabilizes the interaction between the CDs and the NO_2 group of the NB. As discussed in the characterization section, the presence of aromatic rings substituted by carboxyl and amide groups leads to interactions with nitrobenzene with a donor-acceptor electron transfer mechanism involving the NO_2 group. These interactions would attract more NB molecules onto the electrode surface, and therefore, the amplitude of the signal referred to the reduction is greater on the modified

electrode than on the bare one. Furthermore, recent studies have shown that the pore structure and the small size of CDs (~less than 10 nm) promote interaction as they increase the contact surface area, showing higher detection activity (Kariuki *et al.*, 2016; Mohd Rosli *et al.*, 2021).

From the CV analysis, there is an increase in peak current as the NB concentration increases for the two oxidation peaks (O1 and O2) and the reduction peak (R1) (**Figure 3.1.13a**). However, at low concentrations of NB, only one oxidation peak can be observed due to the formation of nitrous benzene. An increase in the NB concentration generates a signal shift to more positive potentials and, by 10 μM, highlights the presence of the second oxidation peak. For the reasons explained, only the O2 oxidation peak, relating Ipa to NB concentration, was considered. Two linear trends can be seen, one at low concentrations (0.1 to 0.6 μM) and another linear trend for concentrations between 10 and 100 μM (**Figure 3.1.13b**). The sensitivity of the sensor for NB is 768.54 $\mu A\ \mu M^{-1}\ cm^{-2}$ for concentrations between 0-0.6 μM, while for concentrations between 10–100 μM the sensitivity is 4.86 $\mu A\ \mu M^{-1}\ cm^{-2}$. The sensor denotes high sensitivity at low concentrations that decreases at concentrations above 10 μM, most likely due to saturation of the active sites that promote the oxidation-reduction reaction.

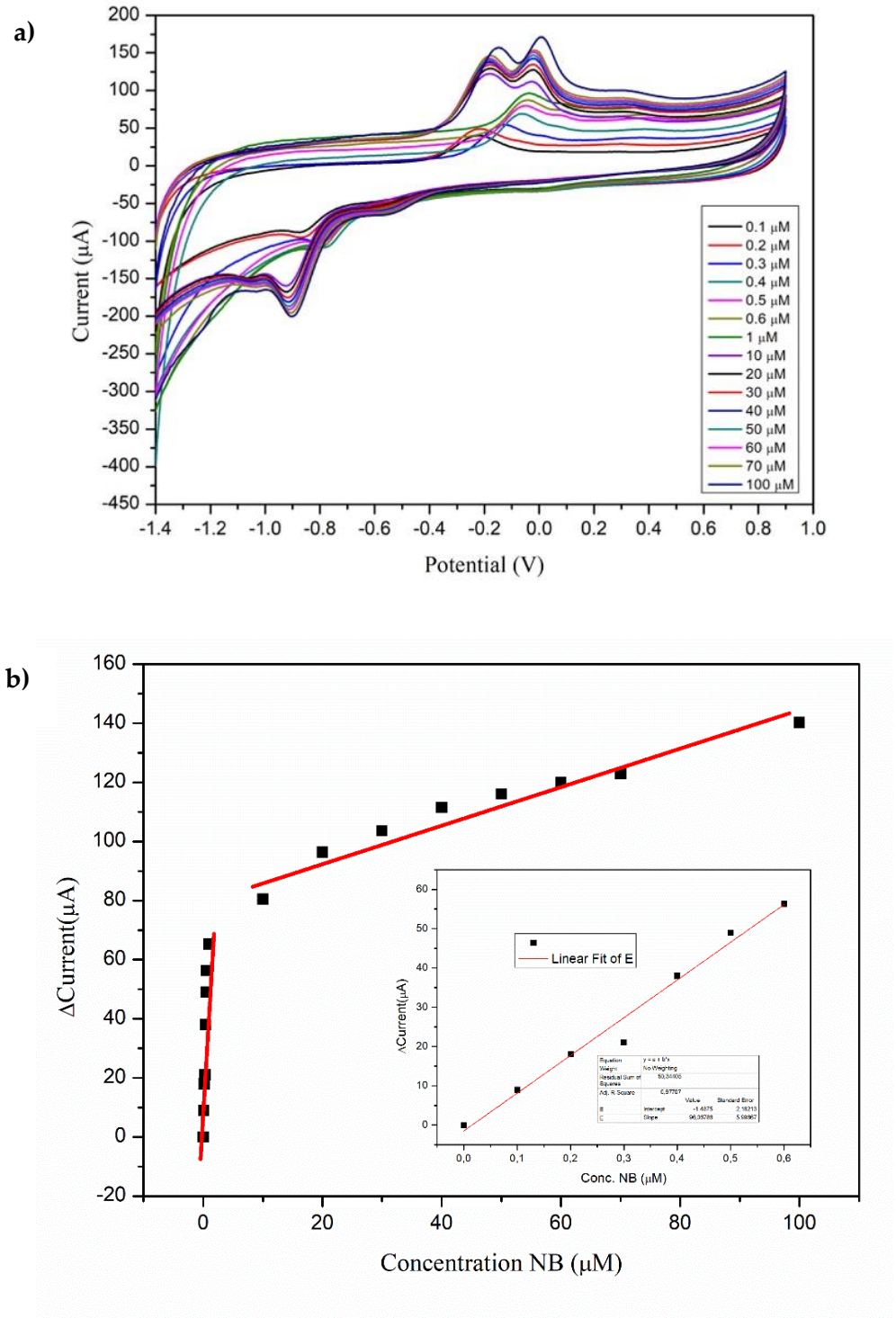

Figure 3.1.13. a) CV of CDs/SPCE in 0.01 PBS electrolyte and in the presence of different concentrations (0–100 µM) of NB; **b)** calibration curves for peak currents (baseline corrected) as a function of analyte concentrations with insert graph that shows calibration plots for peak currents (baseline corrected) as a function of analyte low concentrations (from 0 to 0.6 µM)

DPV test was carried out at different NB concentrations (**Figure 3.1.14a**), analyzing the reduction peak R1 because it appears to be the most sensitive in detecting changes in NB concentrations. To calculate the sensitivity and limit of detection (LOD) to NB of the CDs/SPCE sensor and obtain its calibration curve, NB additions were made in the range of 0.1 µM and 2 mM in 0.01 M buffer (PBS) solution at pH 7.4. The reduction current (Ip) showed a greater linear decrease with the change in NB concentration in CDs/SPCE (**Figure 3.1.14b**). The sensitivity was found to be 9.36 $\mu A\ \mu M^{-1}\ cm^{-2}$, and the calculated LOD is 13 nM. LOD is the limit of detection, and it represents the lowest concentration of the analyte that can be detected. It was calculated according to the IUPAC definition: 3.3 standard error/slope ("International Union of Pure and Applied Chemistry," n.d.; Mohd Rosli *et al.*, 2021).

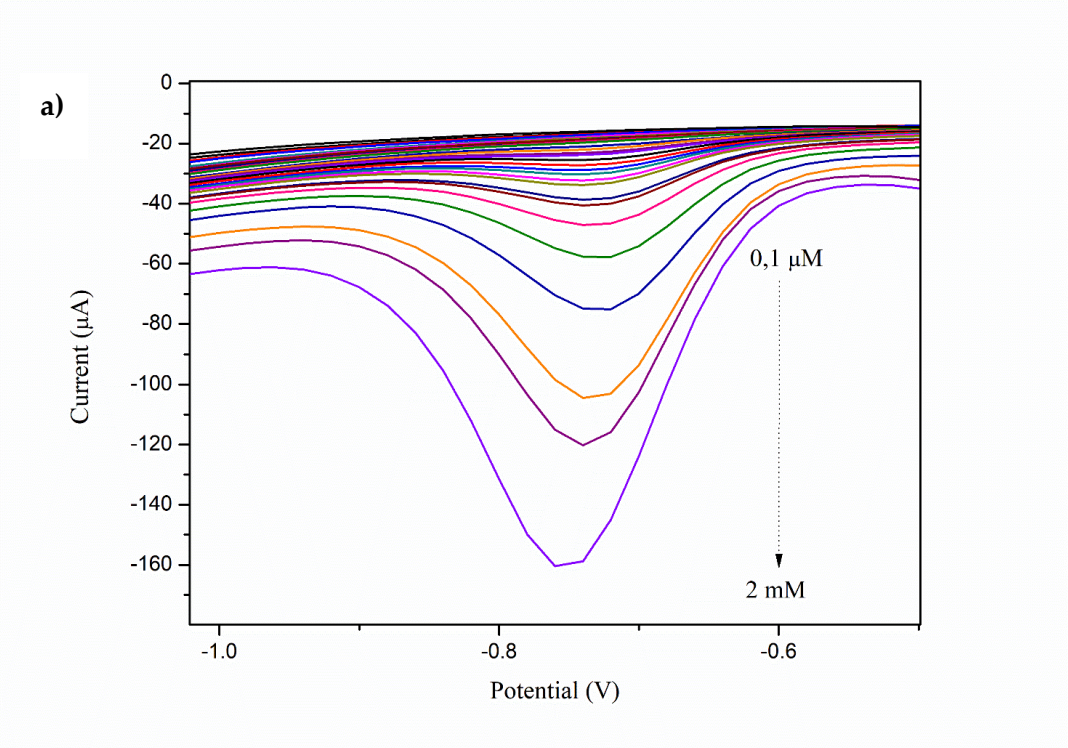

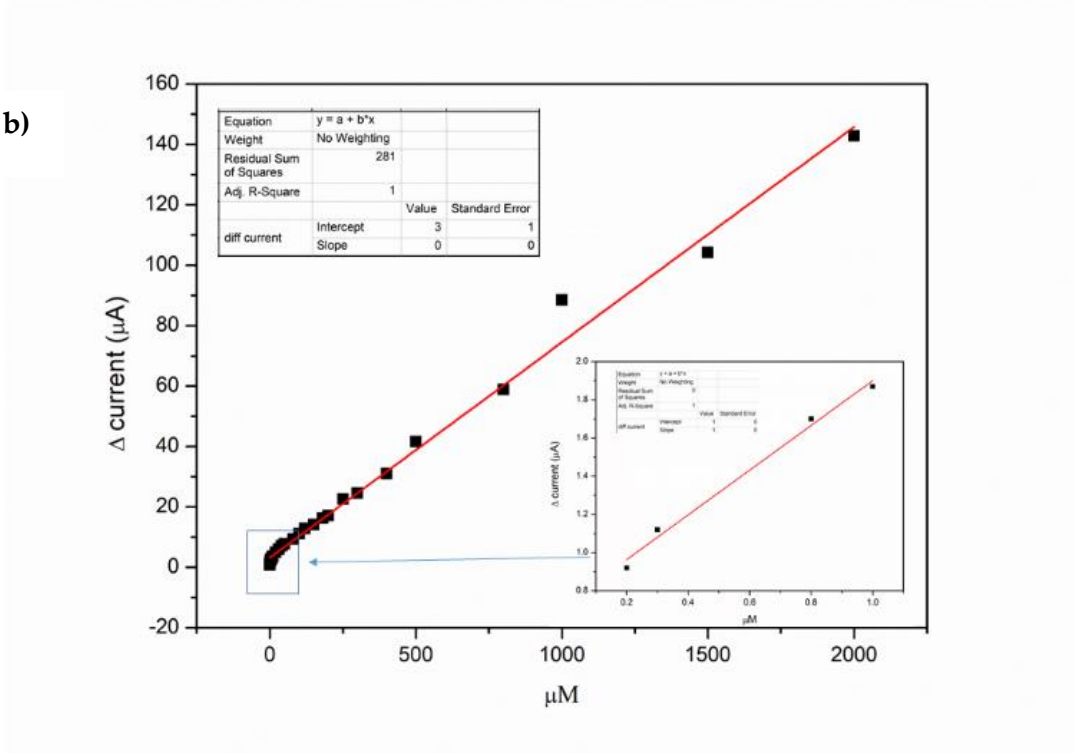

Figure 3.1.14. a) DPV of CDs/SPCE in 0.01 M PBS electrolyte and at different concentrations (0.1–2000 μM) of NB; **b)** calibration graphs for peak reduction currents, sd≤2.

To determine the selectivity of the sensor, DPV tests were performed at a fixed concentration [100 μM] of different inorganic and organic pollutants. All measurements were made in 0.01 M PBS at pH 7.4 with a scan rate of 50 mV s^{-1}. The tested interfering substances are phenyl pyruvic acid, toluene, aniline, heavy metal ions (Cd^{2+}, Pb^{2+}, and Ni^{2+}), nitrates, K^+, Cl^-, NH_4Br, picric acid, and *p*-nitrotoluene. The addition of these compounds did not result in any change in the intensity of the detected current in the presence of 100 μM of NB, and therefore the modified sensor exhibited high selectivity over the reference analyte (**Figure 3.1.15**). The selective response to NB may further confirm that a response to this analyte is due to the bonds with the functional groups of the CDs and to the entrapment of the analyte's pores in the molecular cavities, which, according to a recent study, allows stronger interactions between NB and the structure of CDs framework (Lin *et al.*, 2016).

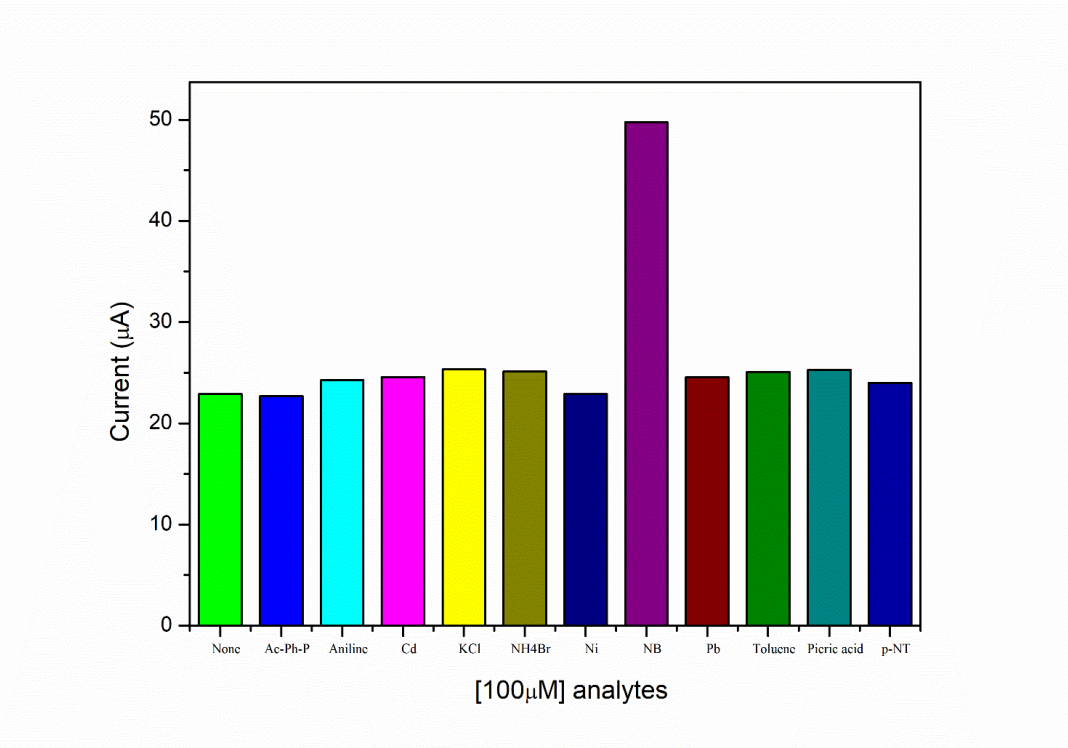

Figure 3.1.15. Histogram response of the CDs/SPCE at the addition of organic and inorganic interferents in solution (0.01M PBS at pH 7.4) at a concentration of 100 μM each (scan rate of 200mV/s)

Furthermore, this selective behavior can be attributed to the fact that under optimized electrochemical conditions, the NB reduction current is significantly greater than the similar molecules, and therefore, the modified sensor is able to detect the analyte selectively. Five tests were performed to check the repeatability and stability of the sensor by comparing the response of the sensor to the addition of NB in solution at the final concentration of 100 μM. The tests were carried out by monitoring the repeatability of the modified sensor during the analysis and over time. **Figure 3.1.16a** shows the results obtained after five repeated measurements. The average standard deviation (RSD) of the reduction peak determined by DPV was 1.02 %, which shows that the modified electrochemical sensor has good repeatability. The modified electrochemical sensor was tested for the detection of NB, at the same concentration, during different times to verify its stability: measurements were made after 24 hours

and after 7, 15 and 30 days. **Figure 3.1.16b** showed satisfactory stability with an RSD of 1.22 %.

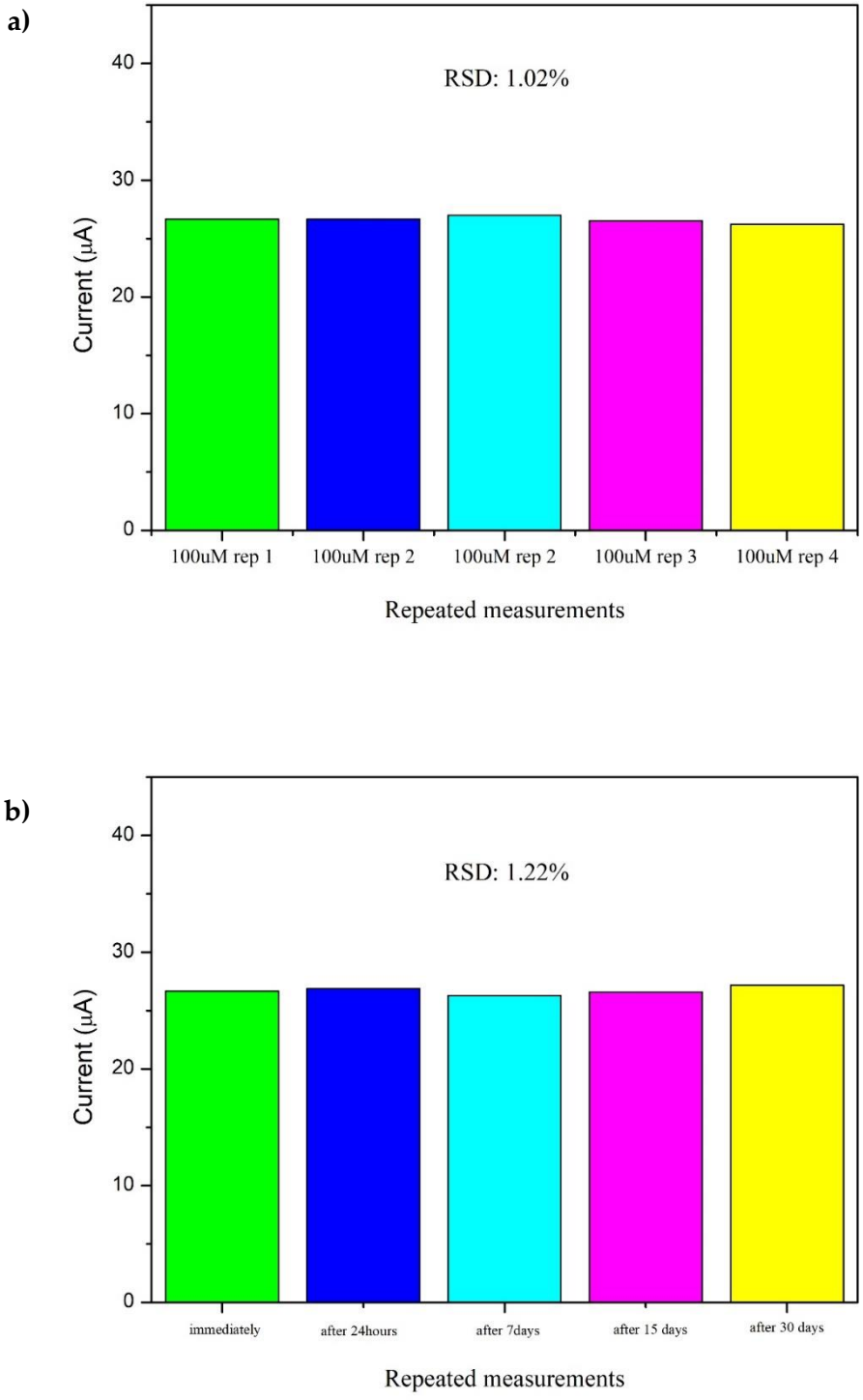

Figure 3.1.16. a) Repeatability test of CDs/SPCE performed by DPV in 0.01 M PBS electrolyte with 100 µM of NB; **b)** stability test of CDs/SPCE performed by DPV in 0.01 M PBS electrolyte with 100 µM of NB

To investigate the application of the CDs/SPCE in real samples, DPV was performed to detect the NB in wastewater collected by industry in Milazzo (Sicily, Italy). No voltammetric signal was noticed for the wastewater sample, indicating that NB was absent in the sample. Different concentrations of NB were added to the real sample after dilution with 0.01 M PBS (wastewater: PBS ratio 1:9) using standard addition methodology to investigate the spiked recovery rate. **Table 3.1.1** shows the percentage recovery of NB in a real sample performed by CDs/SPCE and compares it with literature data, highlighting that the obtained result exhibits similar or higher behavior. Therefore, the technology proposed in this study is satisfactory and has great prospects for the practical analysis of NB in wastewater.

Real sample	**Recovery (%)**	**Sensitivity ($\mu A \mu M^{-1} cm^{-2}$)**	**LOD (nM)**	**Ref.**
Wastewater	93	1.27	150	(Thirumalraj *et al.*, 2016)
Wastewater	99.35	-	10	(Kokulnathan *et al.*, 2021)
Lake water	102.26	0.35	86	(An *et al.*, 2022)
Tap water	99.7	-	7.3	(Ajith and John, 2022)
River water	105	-	9	(Kingsford *et al.*, 2018)
Tap water	101.36	-	1.56	(Zhou *et al.*, 2022)
Lake water	99.54	-	1.56	(Zhou *et al.*, 2022)
Wastewater	98	9.36	13	Present work

Table 3.1.1. NB detection in real samples

Conclusions

To sum up, the CDs were synthesized starting from a green source, deriving from the hydrothermal carbonization treatment of orange peel waste, generally considered a non-exploitable waste, by a bottom-up electrochemical synthesis, and then used to create an excellent electrochemical sensor for the detection of NB. OPW is a valuable and economical raw material, but it is very abundant and requires careful disposal. This work pursued a new synthetic approach through the electrochemical treatment of the liquid phase obtained by HTC of OPW. This liquid fraction, which is still rich in small organic molecules, was valorized instead of the solid carbonaceous residue mainly used to synthesize carbonaceous nanomaterials. The synthesized CDs exhibited interesting physicochemical and optical properties, allowing their use as an electrochemical sensor. The sensor showed excellent redox activity for the detecting NB with a linear response range of 0.1–2000 μM and a detection limit of 0.013 μM. Moreover, the sensor exhibited satisfactory stability, high repeatability, and high selectivity for determining of NB in the presence of interfering compounds. The sensing performance of the modified sensor was investigated in a real sample (wastewater), and the recoveries were 98 %, indicating that the technique proposed in this study can be very effective in practical analysis in the environment field and could be used as a new device for the rapid determination of NB in the environmental matrix.

References

Ajith, A.; John, S.A. Performance of graphitic carbon nitride nanosheets derived from liquid and thermal exfoliations towards the electrochemical reduction of nitrobenzene. *New Journal of Chemistry*, **2022**, 46, 6446–6452. https://doi.org/10.1039/D1NJ06209C

An, S.; Shang, N.; Zhang, J.; Nsabimana, A.; Su, M.; Zhang, S.; Zhang, Y. Fabrication of electrocatalytically active, cobalt-embedded nitrogen-doped ordered macroporous carbon for sensitive detection of nitrobenzene. *Colloids and Surfaces A: Physicochemical and Engineering Aspects*, **2022**, 653, 130078. https://doi.org/10.1016/j.colsurfa.2022.130078

Bressi, V.; Akbari, Z.; Montazerozohori, M.; Ferlazzo, A.; Iannazzo, D.; Espro, C.; Neri, G. On the Electroanalytical Detection of Zn Ions by a Novel Schiff Base Ligand-SPCE Sensor. *Sensors*, **2022**, 22 (3), 900. https://doi.org/10.3390/s22030900

Chiarotto, I.; Mattiello, L.; Pandolfi, F.; Rocco, D.; Feroci, M.; Petrucci, R. Electrochemical Oxidation of Theophylline in Organic Solvents: HPLC-PDA-ESI-MS/MS Analysis of the Oxidation Products. *ChemElectroChem*, **2019**, 6, 4511–4521. https://doi.org/10.1002/celc.201901071

Erdogan, E.; Atila, B.; Mumme, J.; Reza, M.T.; Toptas, A.; Elibol, M.; Yanik, J. Characterization of products from hydrothermal carbonization of orange pomace including anaerobic digestibility of process liquor. *Bioresource technology*, **2015**, 196, 35–42. https://doi.org/10.1016/j.biortech.2015.06.115

Espro, C.; Satira, A.; Mauriello, F.; Anajafi, Z.; Moulaee, K.; Iannazzo, D.; Neri, G. Orange Peels-Derived Hydrochar for Chemical Sensing Applications. *Sensors and Actuators B: Chemical*, **2021**, 341, 130016. https://doi.org/10.1016/j.snb.2021.130016

International Union of Pure and Applied Chemistry, (accessed June 2023). https://publications.iupac.org/compendium/index.html

Kariuki, V.M.; Fasih-Ahmad, S.A.; Osonga, F.J.; Sadik, O.A. An electrochemical sensor for nitrobenzene using π-conjugated polymer-embedded nanosilver. *Analyst*, **2016**, 141, 2259–2269. https://doi.org/10.1039/C6AN00029K

Kingsford, O.J.; Qian, J.; Zhang, D.; Yi, Y.; Zhu, G. Electrochemical sensing for 1-chloro-4-nitrobenzene based on β-cyclodextrin/carbon nanohorn nanohybrids. *Analytical Methods*, **2018**, 10, 5372–5379. https://doi.org/10.1039/C8AY01892H

Kokulnathan, T.; Jothi, A.I.; Chen, S.-M.; Almutairi, G.; Ahmed, F.; Arshi, N.; AlOtaibi, B. Integrating graphene oxide with magnesium oxide nanoparticles for electrochemical detection of nitrobenzene. *Journal of Environmental Chemical Engineering*, **2021**, 9, 106310. https://doi.org/10.1016/j.jece.2021.106310

Li, Y.-P.; Cao, H.-B.; Liu, C.-M.; Zhang, Y. Electrochemical reduction of nitrobenzene at carbon nanotube electrode. *Journal of Hazardous Materials*, **2007**, 148, 158–163. https://doi.org/10.1016/j.jhazmat.2007.02.021

Lin, R.-B.; Liu, S.-Y.; Ye, J.-W.; Li, X.-Y.; Zhang, J.-P. Photoluminescent Metal–Organic Frameworks for Gas Sensing. *Advanced Science*, **2016**, 3, 1500434. https://doi.org/10.1002/advs.201500434

Majumdar, B.; Mandani, S.; Bhattacharya, T.; Sarma, D.; Sarma, T.K. Probing Carbocatalytic Activity of Carbon Nanodots for the Synthesis of Biologically Active Dihydro/Spiro/Glyco Quinazolinones and Aza-Michael Adducts. *Journal of Organic Chemistry*, **2017**, 82, 2097–2106. https://doi.org/10.1021/acs.joc.6b02914

Mewada, A.; Pandey, S.; Shinde, S.; Mishra, N.; Oza, G.; Thakur, M.; Sharon, M.; Sharon, M. Green synthesis of biocompatible carbon dots using aqueous extract of Trapa bispinosa peel. *Materials Science and Engineering: C Materials for Biological Applications*, **2013**, 33, 2914–2917. https://doi.org/10.1016/j.msec.2013.03.018

Mohd Rosli, A.R.; Yusoff, F.; Hong Loh, S.; Mohd Yusoff, H.; Abdul Jamil, M.M.; Shamsudin, S.H. SIMULTANEOUS ELECTROCHEMICAL DETECTION OF ASCORBIC ACID, DOPAMINE, AND URIC ACID AT MAGNETIC NANOPARTICLES/REDUCED GRAPHENE OXIDE MODIFIED ELECTRODE. *Jurnal Teknologi*, 2021, 83, 85–92. https://doi.org/10.11113/jurnalteknologi.v83.15161

Pandolfi, F.; Chiarotto, I.; Mattiello, L.; Rocco, D.; Feroci, M. Cathodic Reduction of Caffeine: Synthesis of an Amino-Functionalized Imidazole from a Biobased Reagent. *Synlett*, **2019**, 30, 1215–1218. https://doi.org/10.1055/s-0037-1611483

Sarat, S. ; Sammes, N. ; Smirnova, A. Bismuth oxide doped scandia-stabilized zirconia electrolyte for the intermediate temperature solid oxide fuel cells. *Journal of Power Sources*, Special issue including selected papers presented at the International Workshop on Molten Carbonate Fuel Cells and Related Science and Technology **2006** together with regular papers 160, 892–896. https://doi.org/10.1016/j.jpowsour.2006.02.007

Satira, A.; Paone, E.; Bressi, V.; Iannazzo, D.; Marra, F.; Calabrò, P.S.; Mauriello, F.; Espro, C. Hydrothermal Carbonization as Sustainable Process for the Complete Upgrading of Orange Peel Waste into Value-Added Chemicals and Bio-Carbon Materials. *Applied Sciences*, **2021**, 11, 10983. https://doi.org/10.3390/app112210983

Singh, S.K.; Mishra, N.; Kumar, S.; Jaiswal, M.K.; Tiwari, V.K. Growing Impact of Carbohydrate-Based Organocatalysts. *ChemistrySelect*, **2022**, 7, e202201314. https://doi.org/10.1002/slct.202201314

Thirumalraj, B.; Palanisamy, S.; Chen, S.-M.; Thangavelu, K.; Periakaruppan, P.; Liu, X.-H. A simple electrochemical platform for detection of nitrobenzene in water samples using an alumina polished glassy carbon electrode. *Journal of Colloid and Interface Science*, **2016**, 475, 154–160. https://doi.org/10.1016/j.jcis.2016.04.042

Zhou, C.; Xie, J.; Zheng, S.; Chen, Y.; Gao, W. A sensitive and selective fluorescent probe for nitrobenzene based on Europium(III) post-functionalized Al(III)-based MOF. *Inorganic Chemistry Communications*, **2022**, 143, 109789. https://doi.org/10.1016/j.inoche.2022.109789

3.2 Waste-derived Carbon Nanodots for Fluorimetric and Simultaneous Electrochemical Detection of Heavy Metal Ions in Water

Submitted: Environmental Science: Nano

In this study, a simple and efficient synthesis of carbon nanodots (CNDs) was proposed by using hydrochar obtained through hydrothermal carbonization of beer bagasse (BB), a by-product of the beer industry that possesses several appealing advantages as a lignocellulosic source for carbon material synthesis. The raw materials and the produced CNDs were characterized by techniques such as TEM, XRD, FT-IR, DLS, and Zeta potential, and the optical properties were studied by spectrofluorophotometry (PL) and UV-Vis absorption spectroscopy. The synthesized CNDs exhibited small dimensions, interesting fluorescence behavior, high stability and remarkable water solubility due to the hydroxyl and carboxyl functional groups. CNDs were employed in developing highly sensitive fluorimetric and electrochemical probes for heavy metal ions, greatly concern for human health, aquatic life, and environmental sustainability. Hg^{2+} and Pb^{2+} were detected by the fluorimetric probe with a limit of detection of 11.3 nM and 78.8 nM, respectively, while the electrochemical platform allowed the selective and simultaneous detection of heavy metal ions, reaching a detection limit of 124 ng/L and 551 ng/L, respectively for mercury and lead ions with high sensitivity fo all the analysed metal ions, in the range between 11.4 and 34.1 $\mu A n M^{-1} cm^{-2}$.

Experimental

Carbon nanodots (CNDs) preparation

Carbon nanodots were obtained by beer bagasse-hydrochar as follows: 6 g of bagasse beer were grounded in a ball mill at 450 rpm for 10 minutes to reduce

the initial size and uniform the powder. Afterward, the powder was suspended in 50 mL of water and hydrothermally treated in an autoclave (series 4540 Parr Instrument Company, IL, USA). The hydrothermal process was performed at three different reaction times (60, 90, and 120 min) and three different temperatures (180, 210, and 240 °C) under autogenous pressure. As shown in **Table 3.2.1**, in the above reaction conditions, the maximum hydrochar yield was obtained at 240 °C for 90 min (**scheme 3.2.1a**). Therefore this sample was employed as starting material for the synthesis of the CNDs.

Sample (time-Temperature)	**Hydrochar yields* (wt%)**
Hydrochar (60–180)	15.35
Hydrochar (60–210)	18.27
Hydrochar (60–240)	24.27
Hydrochar (90–180)	22.51
Hydrochar (90–210)	31.09
Hydrochar (90–240)	38.55
Hydrochar (120–180)	18.05
Hydrochar (120–210)	23.52
Hydrochar (120–240)	27.10

*hydrochar yield was calculated as follow (Spagnuolo *et al.* 2023): $yield\ (wt\%) = \frac{g\ of\ product}{initial\ g\ of\ dry\ BB} \times 100$

Table 3.2.1. BB-hydrochar yields

The obtained solid fraction was separated from the liquid component through filtration (**Scheme 3.2.1b**) and subsequently dried in a ventilated oven at 95 °C for 24 hours (**Scheme 3.2.1c**). 4 g of obtained hydrochar$_{(90\text{-}240)}$ was crushed in a ball-milling for 20 minutes at 250 rpm. The obtained char was placed in an acid mixture (HNO_3/H_2SO_4, ratio 1:3) in a reaction flask equipped with a

condenser; the suspension was refluxed and sonicated in an ultrasonic water bath at 60 °C for 6 hours (Scheme 3.2.1d). The acid treatment allows the reduction of the dimensions of the carbon and the activation of the carboxyl and hydroxyl groups. The mixture was then neutralized with NaOH and diluted with deionized water. After, it was filtered under vacuum using a 0.1 µm Millipore membrane. The filtrate was placed in dialysis bags for 8 days (Scheme 3.2.1e). The resulting concentration of CNDs is 0.9 mg/mL. Pathways involved in the preparation of CNDs from BB are shown in the following scheme.

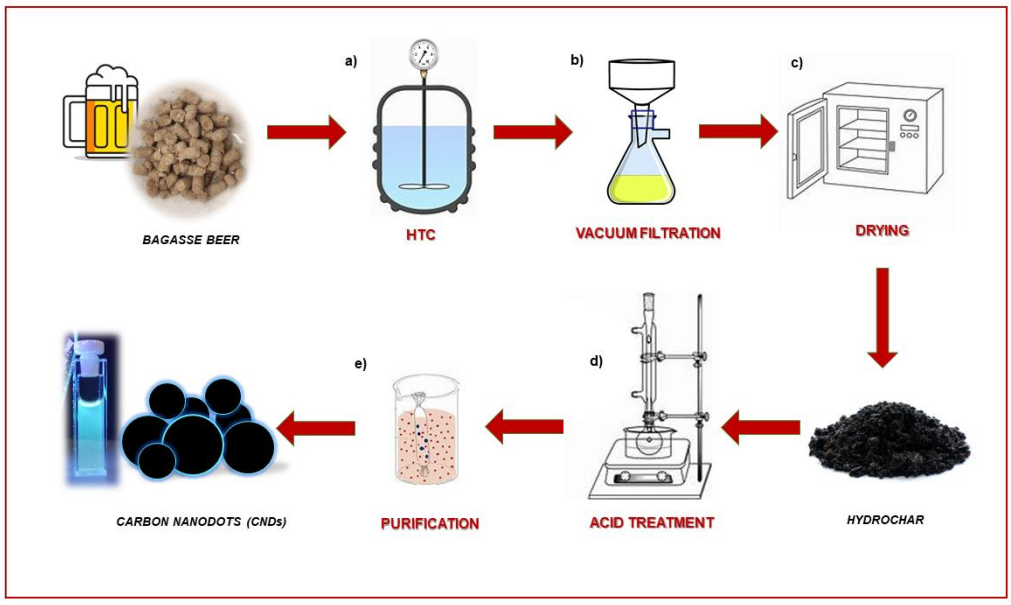

Scheme 3.2.1. Pathways involved in the preparation of CNDs from BB

Fabrication of CNDs-modified electrodes and electrochemical studies

The working electrode surface of SPCEs was modified by drop casting of 20 µL of CNDs solution. After any dropping (4 additions of 5 µL), the electrode was let dry before the successive dropping. The sensors, thus modified (henceforth called CNDs/SPCE), were allowed to dry at room temperature overnight. In order to characterize the modified sensor, Cyclic Voltammetry

(CV) and Electrical impedance spectroscopy (EIS) analyses were performed by using a potentiostat Galvanostat by Metrohom autolab. Electrochemical studies were developed by Square Wave Anodic Stripping Voltammetry (SWASV) performed using DropSens µStat 400 Potentiostat at a scan rate of 50 mV/s, in the potential range from −1.2 to 0.6 V by varying the concentration of the investigated analytes. Briefly, the different heavy metals were deposited onto the surface of the modified sensor at the optimized conditions (by applying a potential of −1 V vs Ag/AgCl electrode for 240 s). Then, they were stripped using anodic oxidation by cycling in the potential window between −1.2 and 0.6 V. Subsequently, the electrode was left at 0.6V for 60 s to remove all the metals absorbed in the surface. All the electrochemical measurements were carried out in acetate buffer (pH: 4.5), and the dissolved oxygen content in the electrolyte was removed by purging pure nitrogen gas for 20 min before each measurement to avoid interference. The calibration curves were obtained by plotting the current vs. analyte's concentration. The sensitivity was computed using the slope of the obtained calibration curve ($y = mx + b$). Thelimit of detection (LOD) was calculated, according to the IUPAC definition ("International Union of Pure and Applied Chemistry", 2023), 3.3 σ /slope, where σ is the standard deviation of analytical blank measurement ($n = 20$).

Results and discussion

Characterization data of raw materials

The raw BB composition was achieved by an organosolv treatment as follows: to recovery fats and oil, 30 g of BB were placed in n-Hexane for 24h at 50 °C. Lipids-free BB was placed overnight in NaOH (pH: 10) to recover proteins, and the surfactant was then ultracentrifuged 3 times. 6 g of bagasse beer (lipids and protein - free) was put in an autoclave in 50mL of EtOH-H_2O (50-50 wt%) for 90 min at 210 °C and then filtered. The solid part is represented by cellulose

and the liquid part is put in an acid solution to separate lignin (solid part) from hemicellulose (liquid part). (All the separated components were kept for further applications). The obtained results are reported in the dedicated section. As reported in the literature (Bressi *et al.*, 2023; Wareing *et al.*, 2021) the starting natural sources play an essential role in the final characteristics of the derived carbon nanomaterials. Indeed, the physicochemical properties represent the basis for the fundamental principles to understand the mechanisms involved in applying these nanomaterials (Liu *et al.*, 2019). **Table 3.2.2** shows the percentages of the lignocellulosic bio-components in beer bagasse obtained by the previously described organosolv treatment. As evident, cellulose is the predominant polymer, and the characterizations of the raw materials and the synthesized CNDs confirm the substantial presence of this polysaccharide.

Table 3.2.2. BB lignocellulose bio-components percentages.

Bio-components	**Value %**
Cellulose	56.8 ± 4.46
Hemicellulose	23.6 ± 1.18
Lignin	10.7 ± 2.98

Few characterizations were performed to compare the synthesized CNDs' properties with the starting materials' micro and macro-structural data. The FTIR spectra of the feedstock and its hydrochar showed absorption peaks characteristic of lignocellulosic biomasses (**Figure 3.2.1**) (Pang *et al.*, 2018). A strong broad band observed at 3300 cm^{-1} is attributed to the cellulose hydroxyl groups' O–H stretching. The weak absorption peaks among 2900-2850 cm^{-1} were due to the C–H stretching of the methylene groups (Saha *et al.*, 2020). The peak at 1640 cm^{-1} suggests the presence of amino groups, and the

band between 1500 cm^{-1} and 1160 cm^{-1} correspond to the vibrations of C–O–C and C–N (Saha *et al.*, 2020). The strong peak observed at 1030 cm^{-1} was attributed to C–O stretching. The absorption peak detected at 550 cm^{-1} was due to β-glycosidic bond between sugar monomers (Pang *et al.*2018).

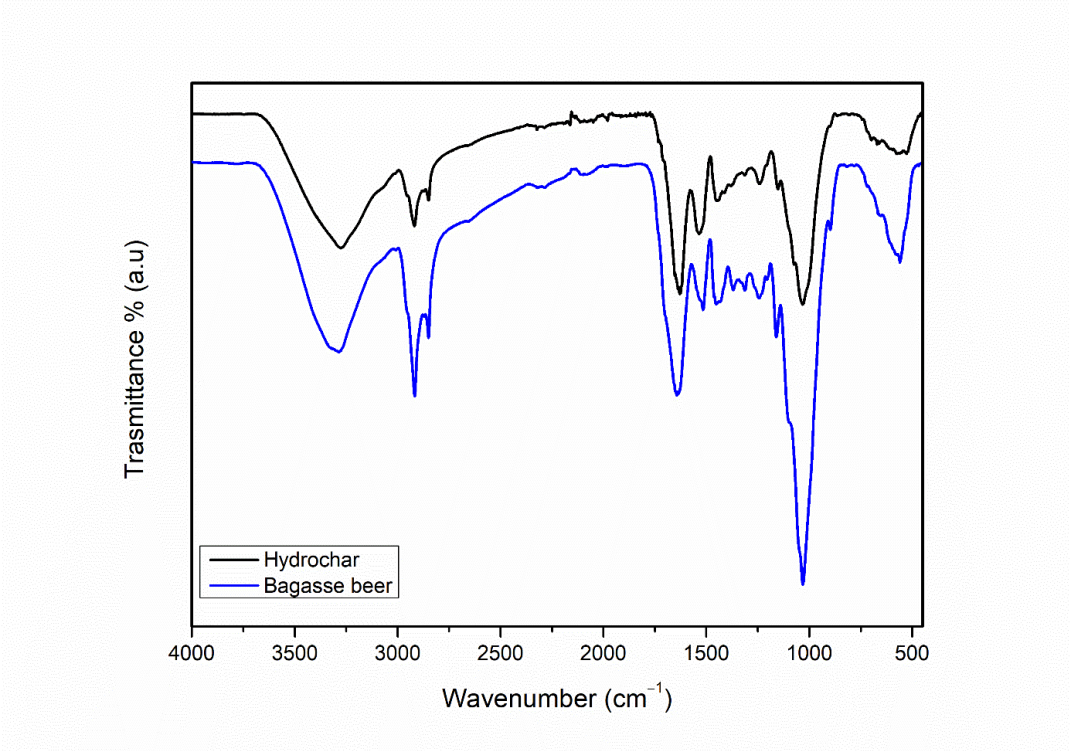

Figure 3.2.1. FTIR spectra of Bagasse beer (blue) and Hydrochar (black)

The DLS measurements were carried out to verify the size distribution profile and the presence of small particles in the raw materials. The DLS data (**Figure 3.2.2**) showed single size population centered at 615 nm for the BB, and two populations around 100 nm and 500 nm were observed for the hydrochar. These results suggest that the hydrothermal process helps to obtain nanomaterials but not smaller than 10 nm. Therefore, subsequent treatments and purification processes were necessary to reduce the size and minimize the formation of these agglomerated clusters.

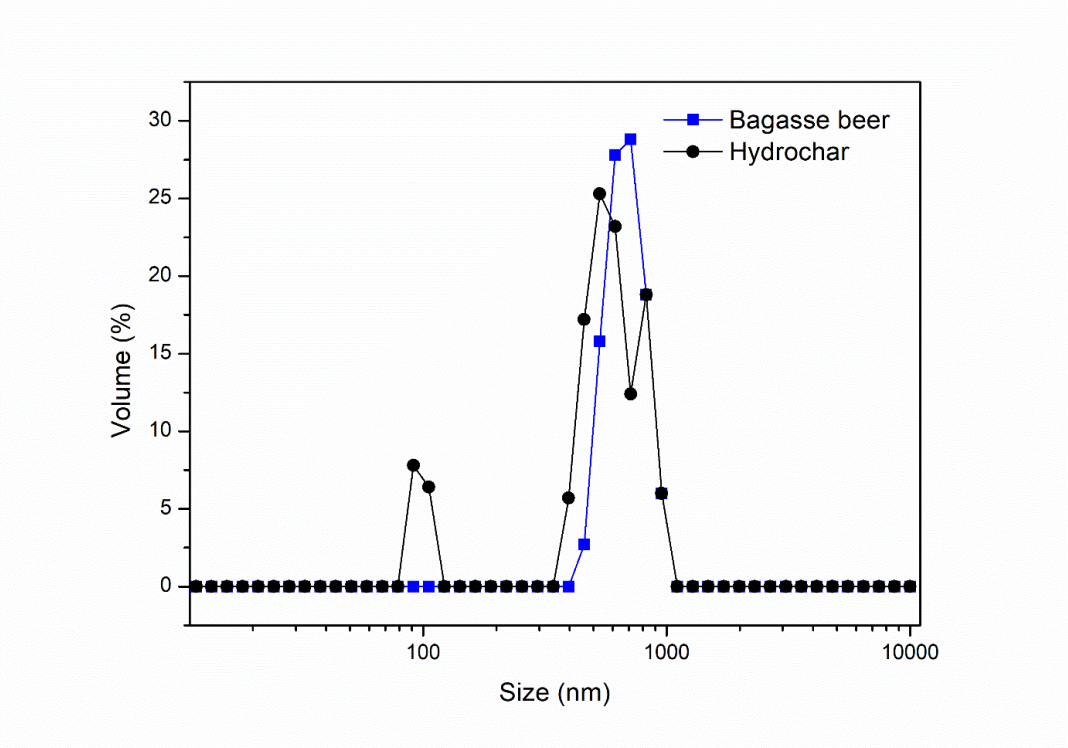

Figure 3.2.2. DLS distribution dimensions particles of bagasse beer (blue) and hydrochar (black)

The XRD spectra (**Figure 3.2.3**) show the crystalline cellulose peaks at 16 (101), 22.3 (002), and 35 (040) 2θ degrees, which are more pronounced in the starting material than in the hydrochar. This indicates that the hydrothermal treatment leads to a complete transformation of the "crystalline phase" to the "amorphous phase", considering the disappearance of the peak at 16 2θ (degree) (Satira *et al.*, 2021). This phenomenon can also be attributed to the BB's well-packed long chains of lignocellulose components, characterized by strong hydrogen bonds. These hydrogen bonds facilitate the preservation of the sugar rings, further promoted by the depolymerisation and hydrolysis reactions occurring during hydrothermal carbonization (Saha *et al.*, 2020).

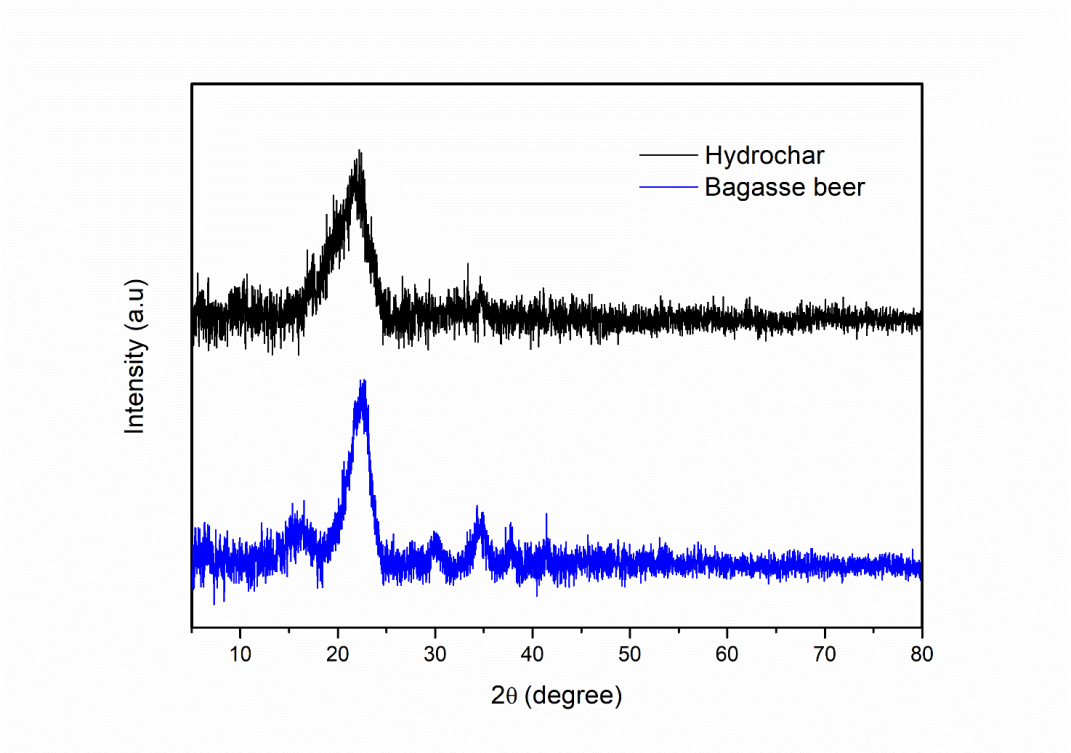

Figure 3.2.3. XRD spectra of bagasse beer (blue) and hydrochar (black) after background removal

Characterization data of CNDs

TEM investigated the morphology and the particle size of CNDs. **Figure 3.2.4** shows the representative TEM images obtained at different magnification (100 nm, 50 nm, 20 nm, and 2 nm). The results confirmed the presence of monodispersed circular small nanoparticles (from 3.30 nm to 8.06 nm) with an average diameter of around 6.01 nm. The TEM images also suggested that the CNDs are amorphous carbon nanoparticles since they lack a crystal core and lattices (confirmed by the following XRD pattern).

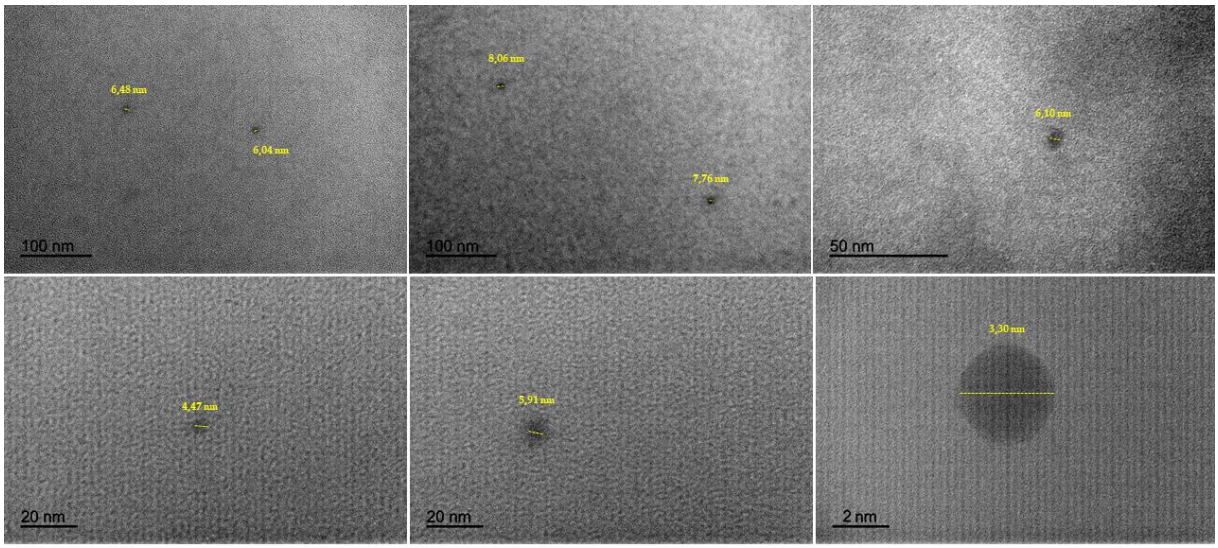

Figure 3.2.4. TEM images of the CNDs along with the corresponding calculated diameter values of the nanoparticles

Dynamic light scattering (DLS) measurements defined also the particle sizes to define their hydrodynamic diameter. **Figure 3.2.5a** depicts the size distribution obtained by the DLS test: the graph shows a population centered at around 7.66 nm (100 percent) with a polydispersity index (PDI) value of 0.375, confirming that no particle aggregation occurred between CNDs and the fitted particle size distribution. According to TEM results, the DLS experiment confirmed that the synthetic procedure reduced the sizes of the particles, but as expected and observed in other works (Bressi *et al.*, 2023; Souza *et al.*, 2016), the recorded DLS average diameter is slightly higher than the diameter size obtained by TEM and this is due to the interference of the dispersant into the hydrodynamic diameter (Bressi *et al.*, 2023). **Figure 3.2.5b** shows the Zeta potential of CNDs investigated in a pH range from 6 to 8. Zeta potential is an essential value of particle dispersion stability and an index of the electrical charges on the nanoparticles' surface. The degree of zeta potential indicates the magnitude of electrostatic repulsion between contiguous similar charged particles. The Zeta potential resulting from the analysis of the CNDs solution is −43 mV,

confirming the low particles' aggregation because the negative value of zeta potential indicates that the electrostatic forces between the particles are repulsive. Furthermore, this potential value also confirmed the stability of the nanoparticles because when the potential is low, attractive forces may exceed this repulsion, and the dispersion may flocculate. The negative value at pH 7 shows a negatively charged CNDs surface, according to the following FTIR spectrum (**Figure 3.2.7**) suggesting the presence of polar functional groups on their surface that enhance hydrophilicity and stability in aqueous systems, which would be promising for sensing applications in aqueous environments.

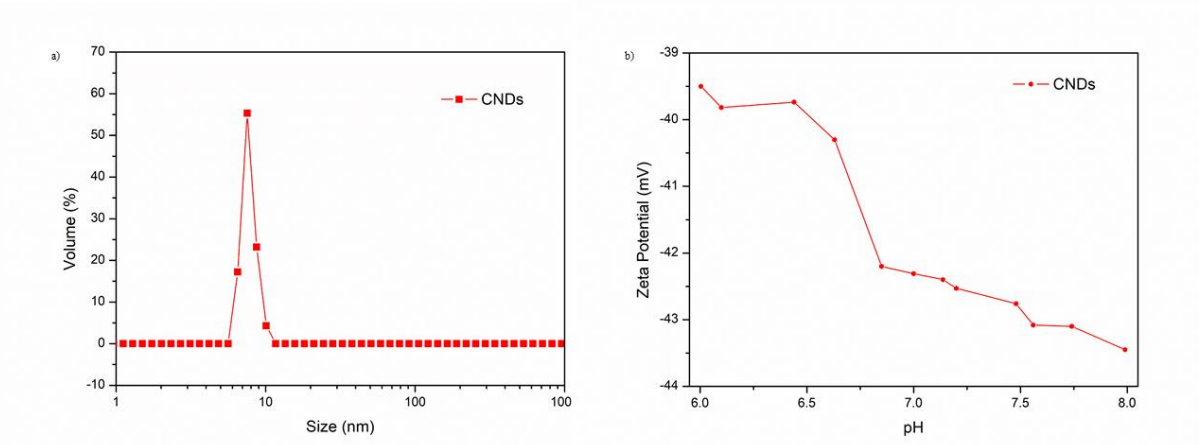

Figure 3.2.5. a) CNDs average DLS distribution, **b)** Zeta Potential investigated in pH range from 6 to 8

Figure 3.2.6 shows the X-ray diffraction spectrum (XRD) of CNDs. As observed for the hydrochar (see **Figure 3.2.3**), the diffraction peak around 22.3 2θ degrees derives from the ordered structure of the cellulose. The narrowing of the C (002) peak indicates the formation of a more ordered carbon lattice structure of the graphite, which arises from hydrothermal carbonization (Lin *et*

al., 2018). However, diffraction peaks of CNDs show low intensity and low signal-to-noise ratio compared with the raw materials, suggesting CNDs are amorphous. The weak peak centered around 35 (*) 2θ degrees is typically observed in the XRD pattern of cellulose. However it is hardly visible in the XRD spectrum of hydrochar and completely disappears in the spectrum of CNDs. The XRD analysis agrees with previously observed for CNDs obtained from cellulosic biomasses (Saha*et al.*, 2020).

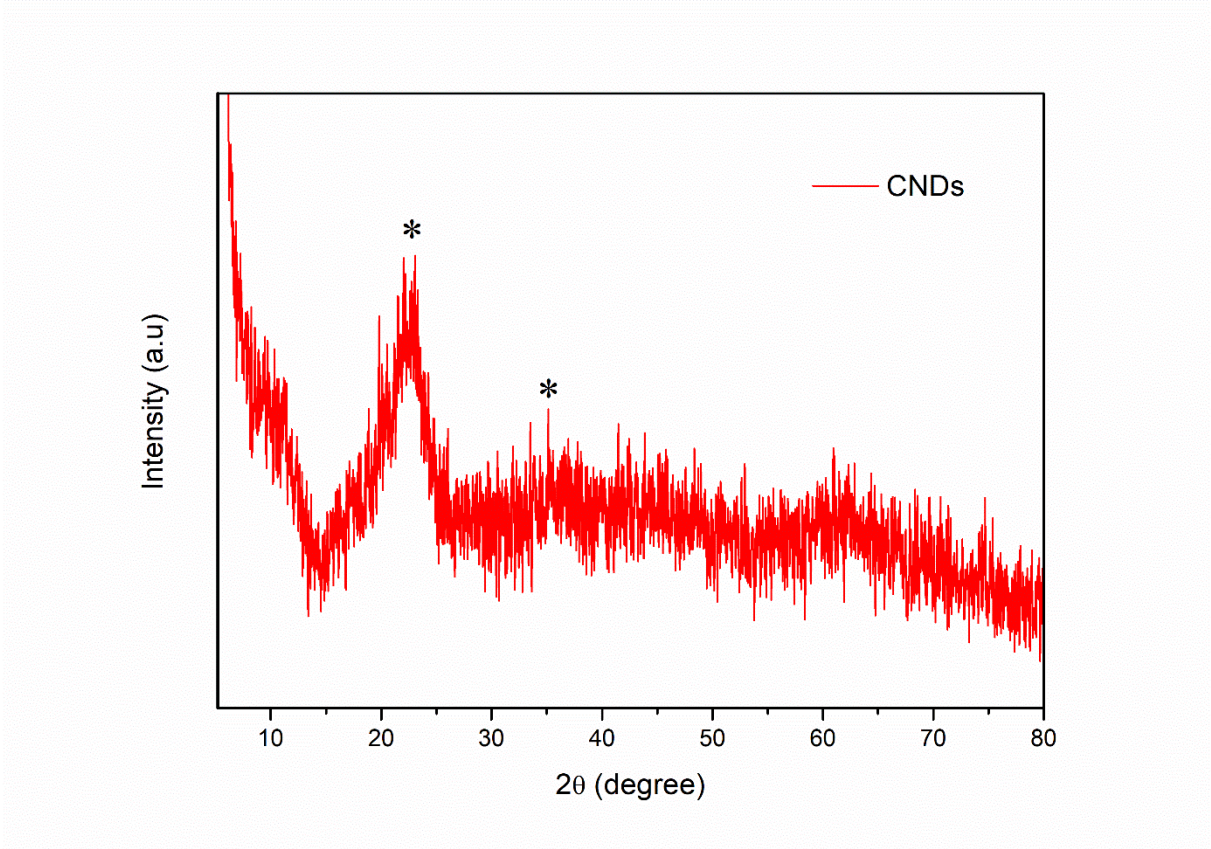

Figure 3.2.6. Fitted XRD spectrum of CNDs

Figure 3.2.7 displays the infrared spectrum obtained with the CNDs. The wide band at 3300 cm^{-1} is associated with the stretching vibration of the hydroxyl groups. The bands located at 2925 cm^{-1} and 2850 cm^{-1} are associated with stretching vibrations of the aromatic and aliphatic C–H groups (Pourmahdi *et al.*, 2019). The peak at 1630 cm^{-1} could be responsible for the stretching of C =

C and C = O. The intense signal at 1350 cm^{-1} could be related to the stretching vibration of the aromatic ring, which is in agreement with the XRD spectra showing the amorphous structure and the band at 1370 cm^{-1} is related to bending vibration peak of the aminic group derived probably from the protein components or to the vibrations of C–O–C (Kalpana *et al.*, 2023). The small band at 1240 cm^{-1} corresponds to sp^3 hybridized carbon atoms. According to literature (Demirci *et al.*, 2020; Varsha *et al.*, 2022), the strong band around 1060 cm^{-1} can be associated with the β-glycosidic bond of cellulose and hemicellulose, which is much more intense in hydrochar as the subsequent treatments with the acid cause the hydrolysis of the polysaccharides (Pang *et al.*, 2018). The medium band at 790 cm^{-1} can be associated with the bending C=C. Therefore, the resulting spectrum of CNDs revealed the presence of interesting functional groups on the carbon nanodots surfaces, including aminic, hydroxyl, and carbonyl groups, which contribute to the excellent water solubility of CNDs and their promising potential for many applications.

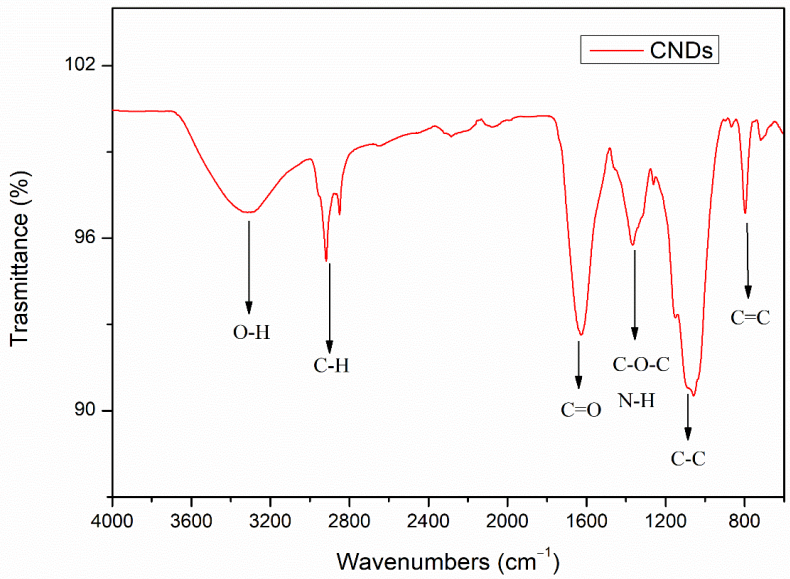

Figure 3.2.7. FTIR spectrum of CNDs

Optical and electrochemical properties of CNDs

Fluorescence and UV-Vis analysis are the preliminary and most straightforward steps for identifying the properties of novel nano-compounds. The photoluminescence behavior of carbon nanodots is one of the most extensively studied properties (Bressi*et al.*, 2023; Balakrishnan *et al.*, 2022). Fluorescence active carbon nanomaterials have been used to rapid detect several analytes due to their high accuracy, excellent water solubility and photostability (Kainth *et al.*, 2023). Moreover, photoluminescence carbon nanodots have oxygen and nitrogen functional groups which that bind carbon nanodots with metal ions (Wu *et al.*, 2017). In visible light, the synthesized CNDs appear as a clear yellow solution. However, under ultraviolet radiation (λ=365 nm) the CNDs emit strong blue luminescence without any treatment, such as surface passivation (see **Figure 3.2.8d**).

The best excitation wavelength was selected after mapping studies: 3D patterns (**Figure 3.2.8a**) resulting in a collection of emission spectra measurements at different excitation wavelengths with a constant step; consequently, the resulted graph shows three dimensions: excitation wavelengths (Z), emission wavelengths (X) and Intensity of emission (Y) (Locquet *et al.*, 2018). The maximum emission intensity of the CNDs is around 520 nm when the solution was excited at 420 nm. However, the 3D mapping also shows that probably the CNDs have two fluorophore groups and at the wavelength of 420 nm the fluorophore with the lowest photoluminescence emission disappears; instead, it maintained its maximum emission peak when excited at 370nm (**Figure 3.2.8b**). At the excitation wavelength of 370 nm, CNDs showed a photoluminescence emission behaviour with a well-defined band around 450 nm (**Figure 3.2.8c**). Typically, the strong emission band in the blue region matches the n–π transition excitation absorption peak, while the excitation absorption peak for the π–π transition (i.e., far UV) shows a weak

emission band (Carbonaro *et al.* 2018). This distinctive property of the CNDs is called the excitation-dependent emission experiencing the bathochromic shift (Sekar *et al.*, 2021). Also, the corresponding weak intensity is due to the low absorption in the visible region. In UV-Vis spectrum (**Figure 3.2.8c**, red line) CNDs exhibited a maximum optical absorption peak at 212 nm with a slight extension towards the visible region which is in good agreement with the literature (Sekar *et al.*, 2021). The existence of the peak can be labeled to be sp^2 C-atoms (π-conjugated system) and, therefore, ascribed due to the π-π* transition of doubly bonded carbon (i.e in the aromatic bond C=C). The low strength absorption portion, i.e., the long tail that extends towards the visible region, is credited to the lower energy sub-bands associated with the functional groups.

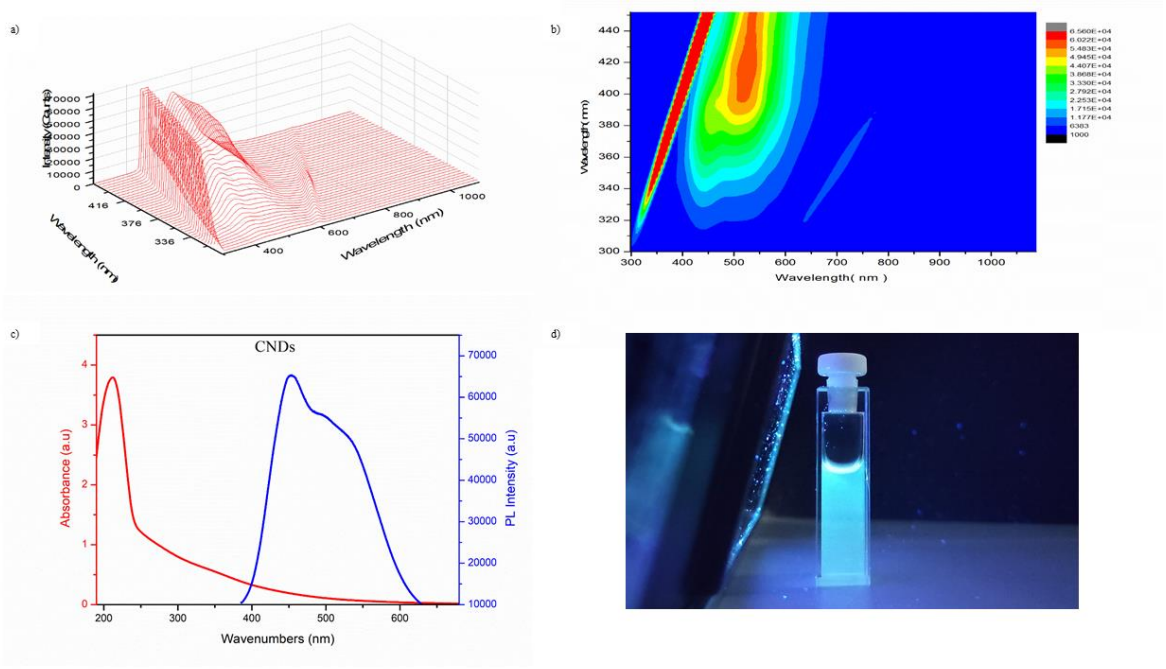

Figure 3.2.8. a) 3D front-face fluorescence spectra CNDs (3D view), **b)** 3D fluorescence spectra CNDs (contour map), **c)** CNDs UV-Vis and PL spectra, **d)** CNDs luminescence emission under ultraviolet radiation (λ=365 nm)

The photo-stability of carbon nanomaterials is a crucial issue for their usefulness as fluorescent probes (Balakrishnan *et al.*, 2022). In this study, we assessed the photo-stability of CNDs by exposing them continuously to UV radiation for 120 minutes, and collecting 2.5 mL of CNDs solution every 20 minutes to measure any variations in photoluminescence (PL) intensity. As illustrated in **Figure 3.2.9**, CNDs exhibited excellent photo-stability, maintaining a PL intensity of approximately 98.75% even after 120 minutes of UV exposure.

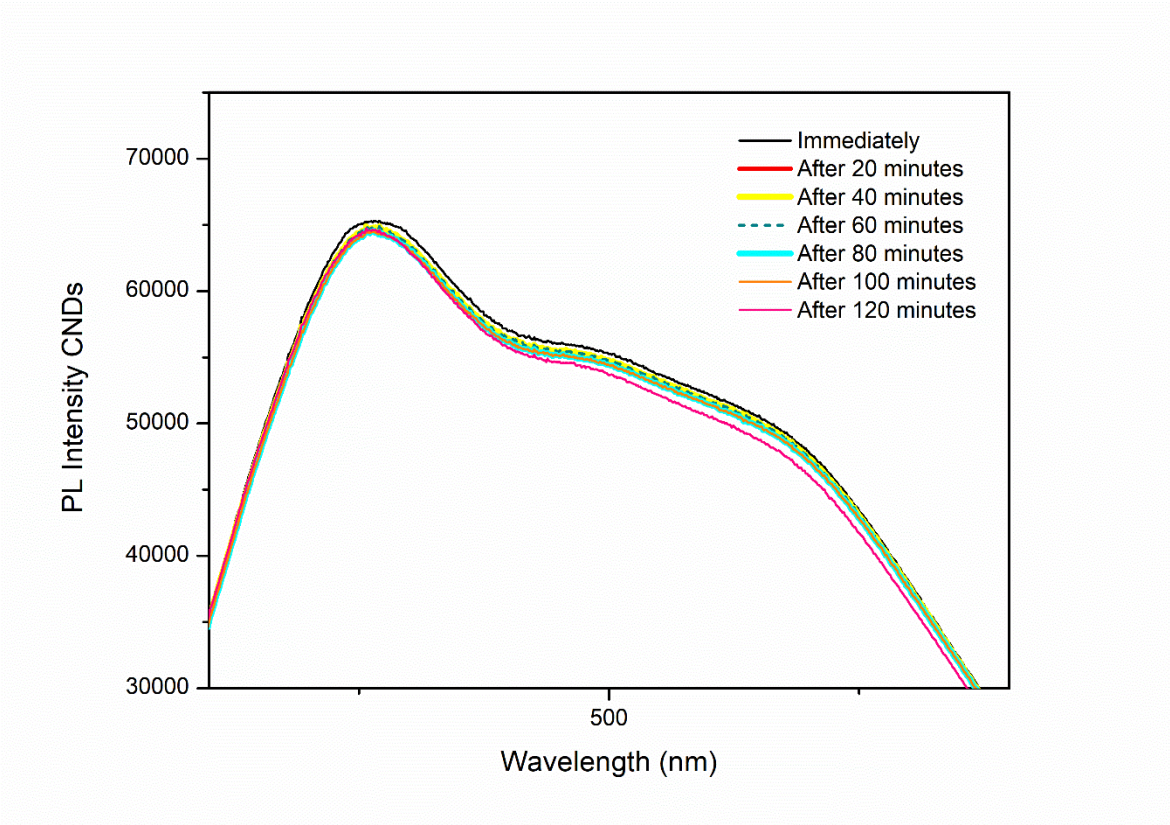

Figure 3.2.9. Photostability of CNDs

Furthermore, by changing the solutions several times and repeating the measurements under the same conditions, the repeatability of the CNDs probe was evaluated: six samples of CNDs solutions were exposed to an excitation wavelength of 370 nm, and the results were recorded. As shown in **Figure**

3.2.10, the calculated relative standard deviation (RSD) for the six repeated measurements was 1.17%, indicating a high degree of repeatability for the PL method using a CNDs probe.

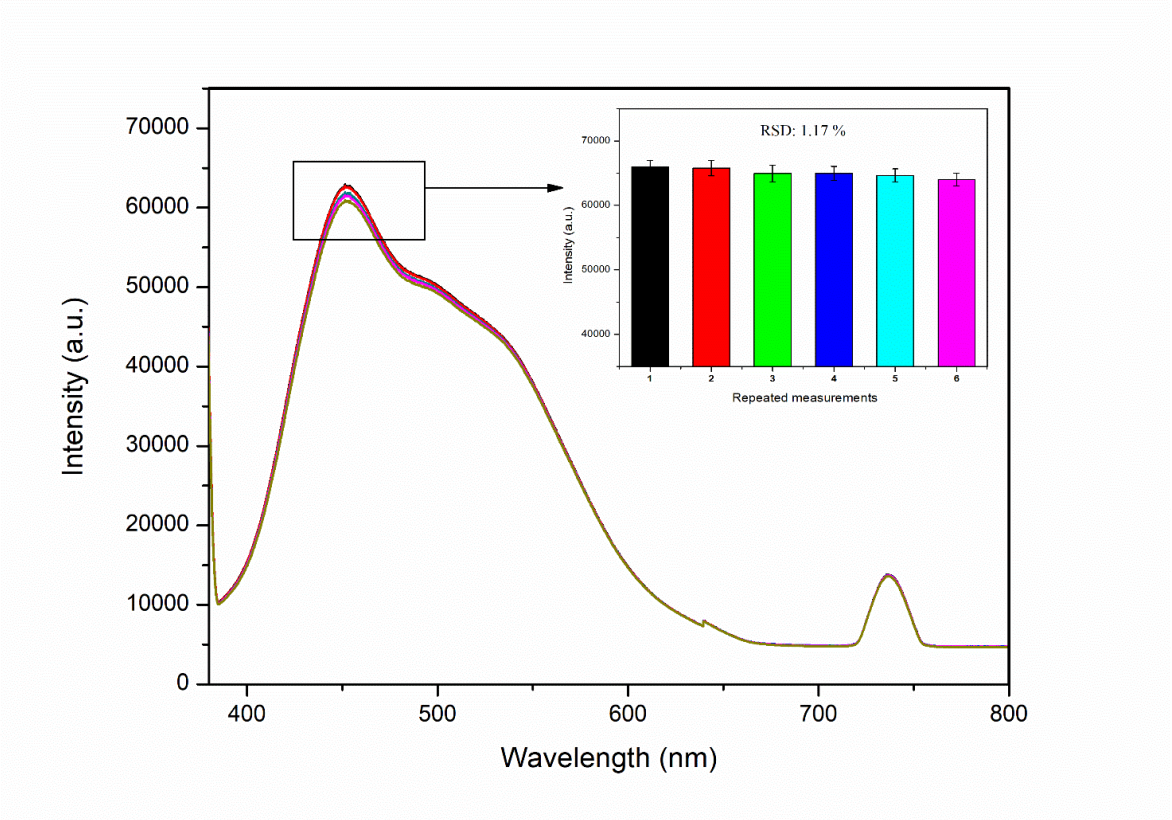

Figure 3.2.10. PL Measurement repeatability

The electrochemical behavior of the electrodes has been investigated. Cyclic voltammetry (CV) analysis was performed by immersing the bare SPCE and the modified CNDs/SPCE sensors in 10 mM $K_3[Fe(CN)_6]$ solution with a scanning speed of 50 mVs^{-1} in a potential window between −0.4 V and 0.8 V (see Figure 3.2.11a). The peak-to-peak separation (ΔEp) is lower in CNDs/SPCE compared to bare SPCE, respectively 160 mV and 270 mV. This finding indicates that the CNDs deposited onto the working electrode promote the redox reaction more effectively than the bare electrode, thereby improving the sensor's performance. By varying the scan speeds, (from 10mV/s to 400mV/s, Figure 3.2.11b), under the same analytical conditions, the

CNDs/SPCE showed a slight shift in potential with increasing scanning speed confirming the capability of the modified sensor to promote the electrochemical process under diffusion control. The plot of the results obtained by varying the scan rate exhibited high linearity (**Figure 3.2.11c**, R^2=0.99). EIS analysis was performed to confirm this behaviour, studying the electron transfer capacity of modified sensor, compared with SPCE. The analysis was carried out in 10 mM $K_3[Fe(CN)_6]$, in the frequency range from 0.1 Hz to 105 Hz (amplitude 5 mV), with an applied potential of 0.3 V (this potential was first selected developing a cyclic voltammetry to select the exactly potential for the redox couple Fe^{3+}/Fe^{2+}). The Nyquist data plotted (as shown in **Figure 3.2.11d**) confirms the modification of the sensor by revealing two distinct behaviours between the bare sensor and the modified one. Furthermore, it exhibited two semicircles for the CNDs/SPCE. The presence of these two semicircles could indicate the presence of two active electrochemical layers on the surface of the electrode, one more external which acts immediately, represented by a smaller semicircle, indicating the modified sensor's capability to promote the electrons transfer by improving the ability to start redox processes, necessary for heavy metal ions' detection. On the other hand, the linear portion indicates the diffusion process occurring on the sensor.

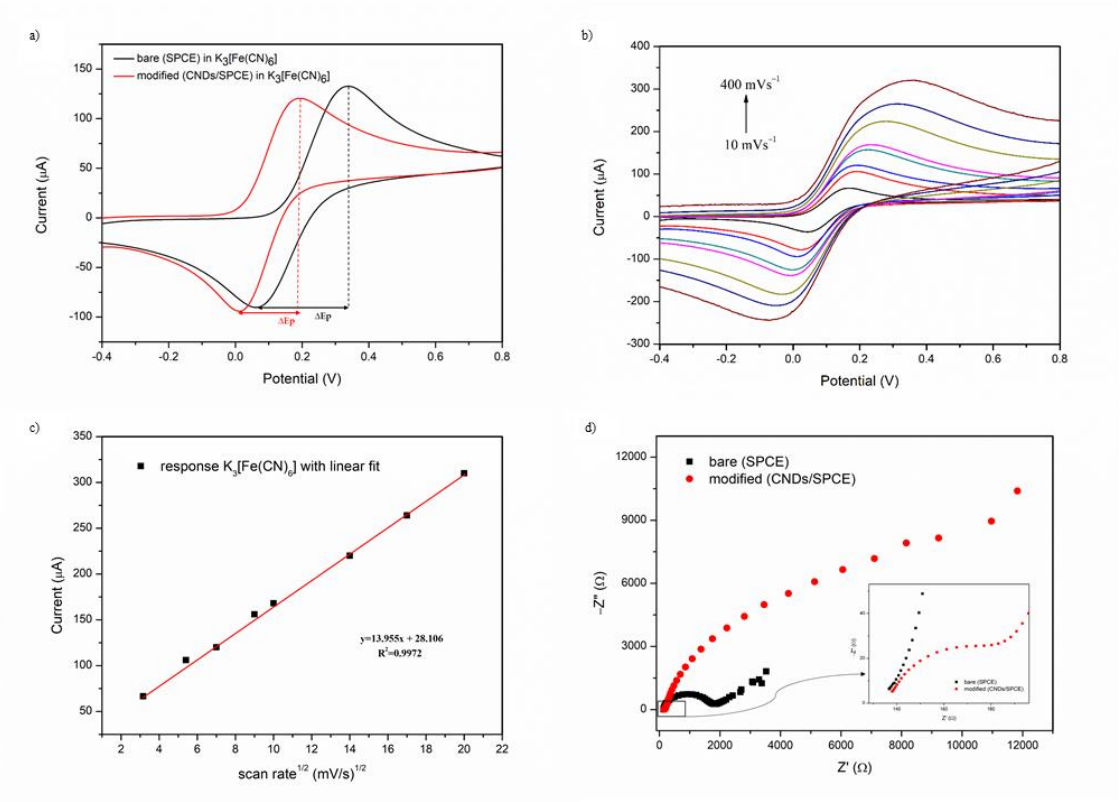

Figure 3.2.11. a) Cyclic voltammogram of modified sensor CNDs/SPCE (red curve) and bare SPCE (black curve) in 10 mM $K_3[Fe(CN)_6]$, scan rate 50 mVs^{-1}, potential range from−0.4 V to 0.8 V; **b)** cyclic voltammogram of modified sensor CNDs/SPCE in 10 mM $K_3[Fe(CN)_6]$, at different scan rate (between 10 and 400 mV/s) potential range from−0.4 V to 0.8 V and **c)** linear plot of current (μA) vs scan rate$^{1/2}$; **d)** EIS of modified sensor (CNDs/SPCE) and bare (SPCE) in 10 mM $K_3[Fe(CN)_6]$, amplitude 5mV, frequency range from 0.1 Hz to 105 Hz, applied potential of 0.3 V

CNDs fluorescent sensor for heavy metal ions detection

The fluorescence quenching was calculated as the percentage reduction in fluorescence using the following formula:

$$\text{Reduced PL Intensity } \% = \frac{(PL_0 - PL_{Hm})}{PL_0} \times 100 \quad (1)$$

where PL_0 is the CNDs fluorescence before the addition of heavy metal ions and PL_{Hm} is the CNDs fluorescence after adding of a selected concentration of heavy metal ions. The PL response of CNDs upon adding of aqueous solutions

of heavy metal ions at the highest tested concentration [300 µM] is displayed in **Figure 3.2.12**. As shown, the metal ions have different influences on the fluorescence emission intensity of CNDs: the PL intensity decreased significantly in the presence of Hg^{2+} and Pb^{2+} with a % quenching of 90% and 63% respectively, and slightly in addition of Ni^{2+} (23%). In contrast, the other studied metal ions showed no noticeable effect on the PL intensities. Cobalt and copper responses show minimal variations and the trend is not even proportional to the additions. Cd^{2+} addition caused the lowest fluorescence quenching with a maximum fluorescence reduction of less than 5%.

The extinction mechanism may be due to a dynamic or static effect. It is possible to define dynamic extinction when the energy transfer occurs through collisions between fluorophore and ions. Consequently the absorption profile does not change (Yarur *et al.*, 2019). The obtained data show that it is a static mechanismsince the fluorophore and the quenching molecule form a complex, drastically reducing the availability of free fluorophores. The lack of changes in fluorescence lifetime suggests the formation of a stable non-fluorescent complex between the two metal ions and the CNDs (Sekar*et al.*, 2021). This also explains the transformation of CNDs' absorbance when the complex CNDs-metals are exposed to UV light (see inset in **Figure 3.2.13** and **Figure 3.2.14**). The interaction could be due to a strong electrostatic bond between the negatively charged CNDs and the positively charged metal ions (Balakrishnan *et al.*, 2022).

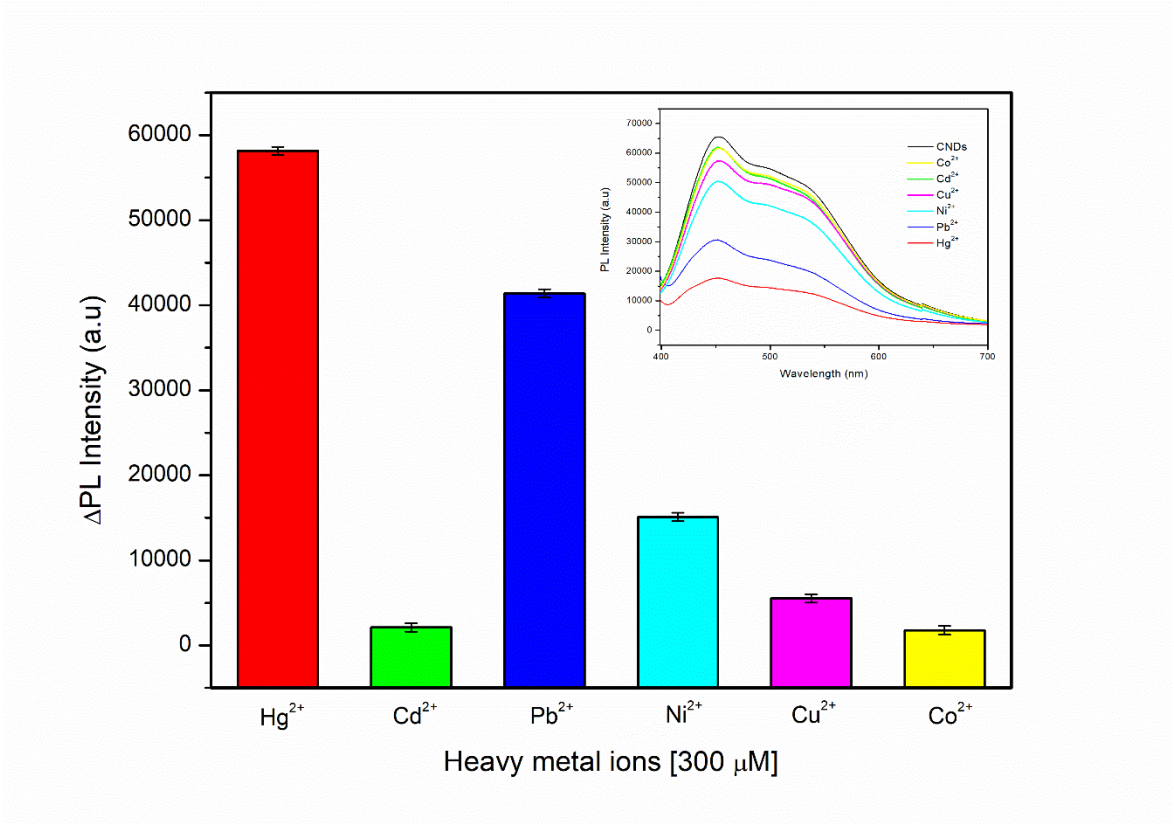

Figure 3.2.12. CNDs PL response to different heavy metal ions [300 μM]

Based on these results, the most significant quenching was observed for Hg^{2+} and Pb^{2+} with a complete turn-off at mercury ion concentrations up to 300 μM. According to the literature, the active adsorption sites of the two cations promote the adhesion of CNDs, leading to the blocking of radioactive recombination of electron holes by an effective electron transfer process and, subsequently, to the extinction of fluorescent CNDs (Lin *et al.*, 2018). The interactions between the functional groups of CNDs (i.e. carboxyl, phenolic, and hydroxyl groups) and the heavy metal ions are based on coordination bonds with unshared electron pairs; carboxyl and phenolic groups are electron donors whose interactions with the heavy metal ions are determined by electrostatic forces and entropy gains. This finding is supported by several studies (Balakrishnan *et al.*, 2022; Anusuya *et al.*, 2021; Ng *et al.*, 2021). From these

results, it emerged that the affinity towards Pb^{2+} and Hg^{2+} ions could be attributed to the interaction between the empty orbitals of the ions and the amino groups present on the surface of the CNDs, which may hinder the bonding with the other cations.

In the PL spectra of the CNDs in the presence of Pb^{2+} (**Figure 3.2.13**), the damping of the fluorescence is evident since the first additions and proportional to the increase in the concentration range of the metal.

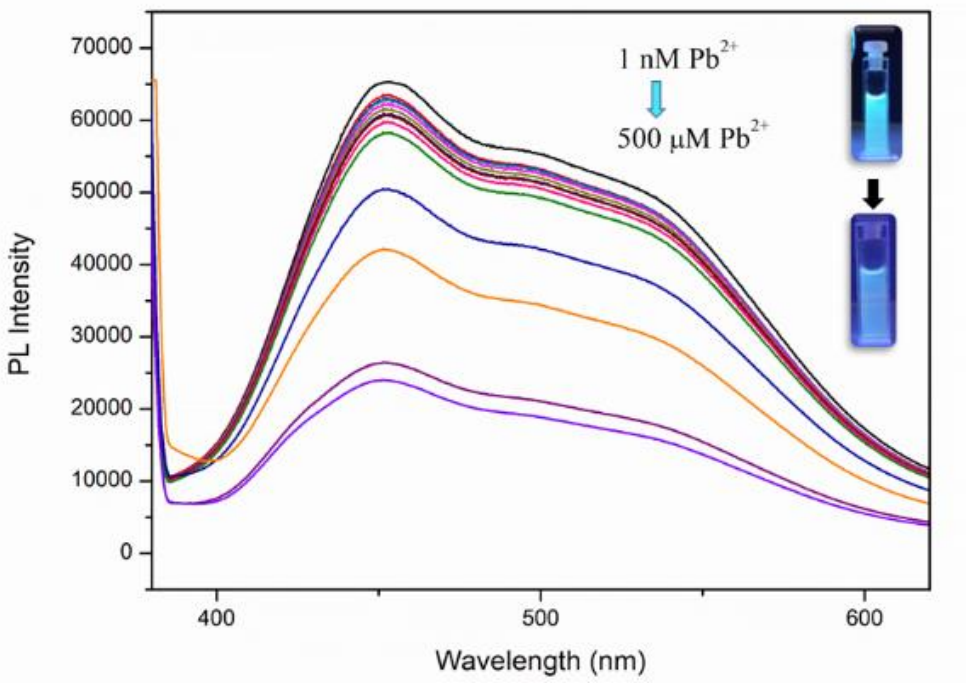

Figure 3.2.13. CNDs PL intensity emission (black line) and PL response to Pb^{2+} addition from 1 nM up to 500 µM

Hg^{2+} also reduces the PL intensity of CNDs; at 400 µM, can completely switch off the fluorescence of the nanomaterials (**Figure 3.2.14**). The figure's inset

shows the fluorescence intensity quenching after adding mercury ions [300

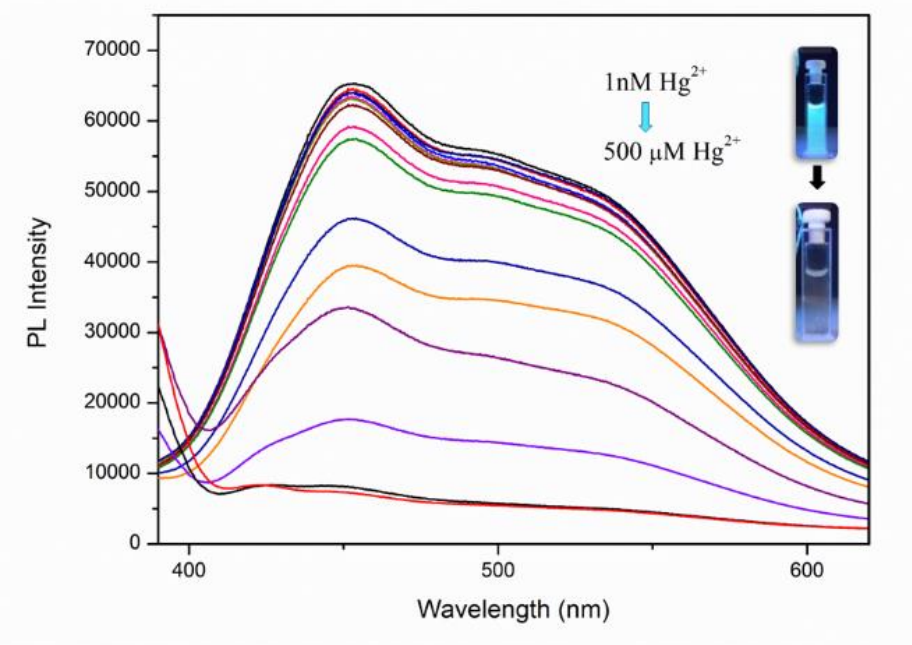

μM].

Figure 3.2.14. CNDs PL intensity emission (black line) and PL response to Hg^{2+} addition from 1 nM up to 500 μM

Interesting is the response to the metals at low concentrations. As shown in **Figure 3.2.15**, up to 50nM, the response of CNDs is greater for Pb^{2+} than Hg^{2+}. This effect could be attributed to stronger coordination of Pb^{2+} by the hydroxyl groups on the surface of CNDs than other metal ions (Liu *et al.*, 2016). The calculated fluorescence limit of detection (LOD) was 11.3 nM for Hg^{2+} and 78.8 nM for Pb^{2+}, with a R^2 of 0.97 and 0.99, respectively.

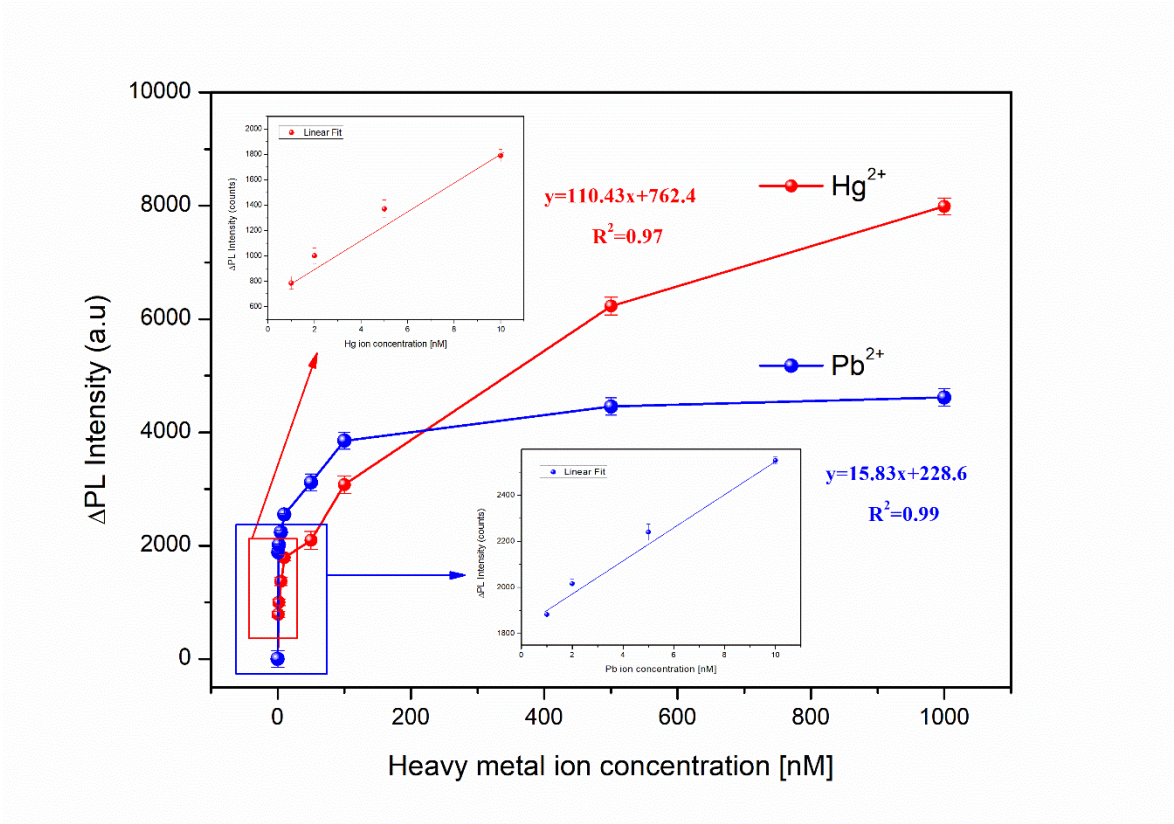

Figure 3.2.15. CNDs PL response to Hg^{2+} and Pb^{2+} addition in nanomolar concentrations range

Figure 3.2.16 shows the stability tests of the response of CNDs solution performed in 5 μM Hg^{2+} solution after different times. The PL intensity emission changes were monitored immediately, after 20 minutes, after 40 minutes, and after 60 minutes: the resulting RSD was less than 1 (0.54%), confirming the excellent stability of the PL method.

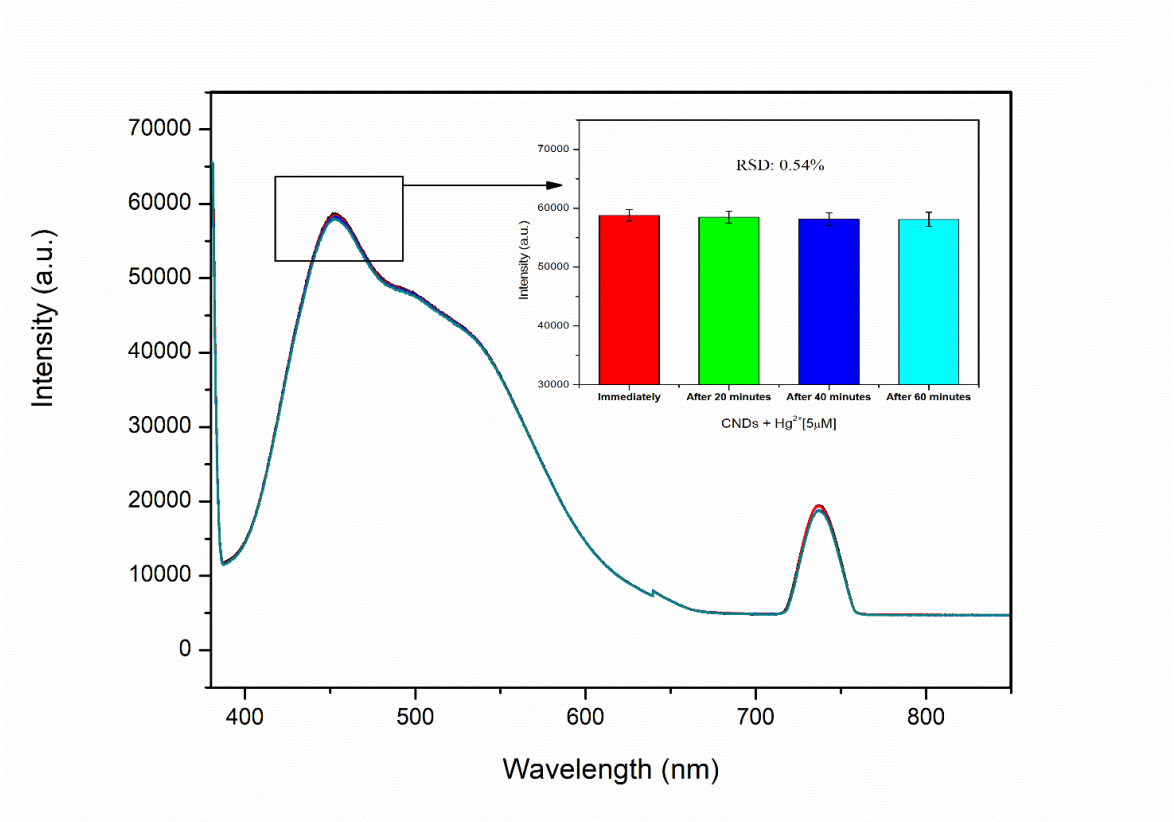

Figure 3.2.16. Stability PL response of CNDs with 5 μM of Hg^{2+} monitored after 20 minutes, 40 minutes and 60 minutes

The second harmonic was also observed to investigate the binding mechanism between the metals and the CNDs. The second harmonic is also known as "twice frequency" because it occurs precisely twice the incident radiation intensity. This is a nonlinear optical phenomenon in which two photons of the same frequency interact with a nonlinear material, "combining" and producing a new photon with twice the energy of the original one (Qi *et al.*, 2019). Studies on the second harmonic are interesting because usually carbon nanomaterials consist of ordered structures. However an external factor (such as the addition of metals in solution, which creates a bond with the functional groups) destabilizes and breaks the center of symmetry, resulting in a saturation or a total signal loss. As seen in **Figures 3.2.17a-b**, the second harmonic in both studies is inversely proportional to the increase in cations concentrations, even

going off the scale when it comes to high concentrations of lead ions; this increase is justified when the aggregation of particles increases. Since it is stable in the absence of cations (see **Figure 3.2.10**), this implies that the cations in solution increase the aggregation between the individual carbon dots and probably act as a bridge between the surface functional groups of the individual CNDs. The insets in **Figures 3.2.17a-b** show the DLS measurements confirming this behavior, with an average diameter of around 20 nm for CNDs after adding 300 µM of mercury and 40 nm for CNDs after adding 300 µM of Lead.

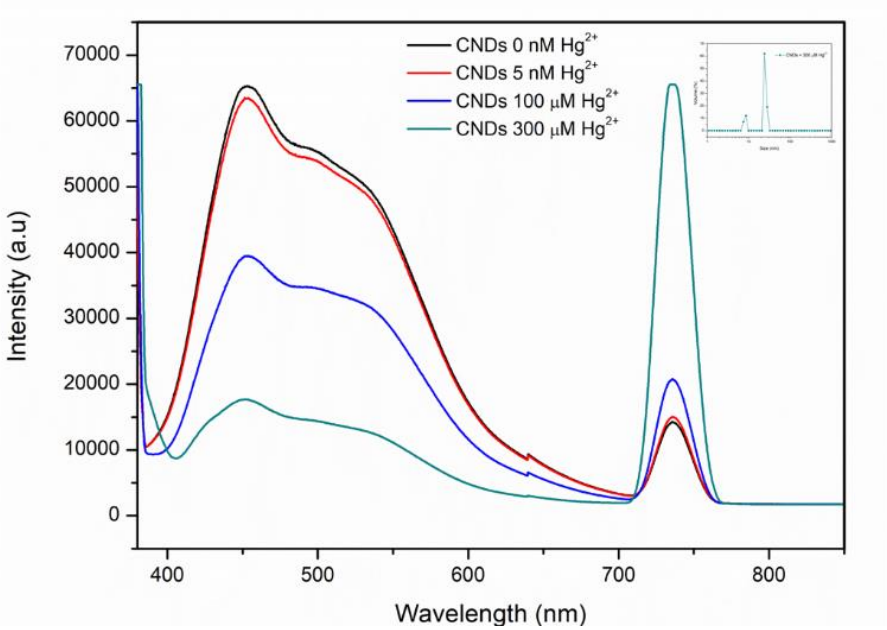

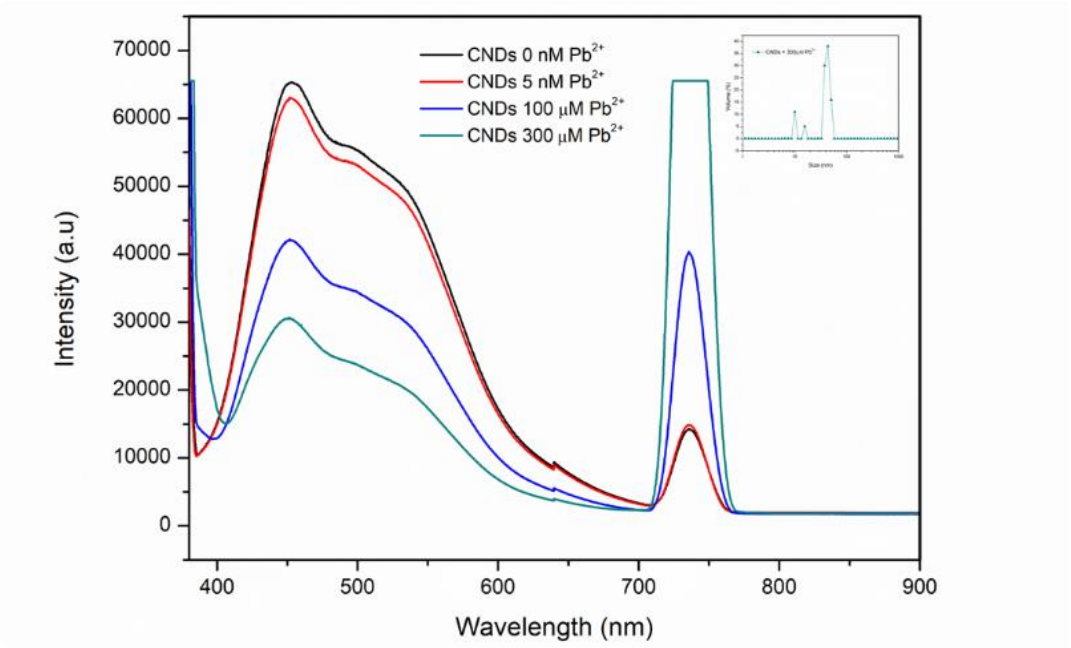

Figure 3.2.17. Second harmonic PL CNDs at different addition of **a)** Hg^{2+} and (inset) related increasing of CNDs aggregation after 300 µM of Hg^{2+} addition revealed by DLS measurement, and **b)** Pb^{2+} and (inset) related increasing of CNDs aggregation after 300 µM of Pb^{2+} addition revealed by DLS measurement

CNDs electrochemical sensor for the simultaneous detection of heavy metal ions

Based on the existing literature, electrochemical methods are less reported for detecting heavy metals using CNDs (Song *et al.*, 2022; Zhang *et al.*, 2019). Unlike the fluorimetric method, the electrochemical one allows the simultaneous determination of these species. Hence, an electrochemical study was conducted to explore both the potential of electrochemical detection of heavy metal ions with CNDs/SPCE sensor and their simultaneous detection. Before attempting the simultaneous determination of heavy metal ions, the responses of the sensors have been evaluated for the single metal ions by using the SWV technique. With the bare SPCE and CNDs/SPCE, stripping peaks for Ni (II), Cd (II), Pb (II), and Hg (II) were observed at −1.1, −0.78, −0.42, and −0.05 V, respectively. For example, the peak of Cd^{2+} for both sensors is

reported in **Figure 3.2.18a**. As noted, at the tested concentration of 1 µM (Figure 12a), the modified electrode shows a very high current variation (31.4 µA) as compared with bare SPCE (10.7 µA). Furthermore, as depicted in **Figure 3.2.18b**, no peak for Cd^{2+} [0.08 µM] is observed when the analysis is performed with bare SPCE (black line). In contrast, the electrode modified with CNDs exhibits a well-resolved peak, indicating that using CNDs/SPCE enhances the detection of very low concentrations of Cd^{2+}. As shown in **Figure 3.2.18c**, the peak current increased with the Cd^{2+} ions concentration with an excellent linear relationship (R^2=0.99).

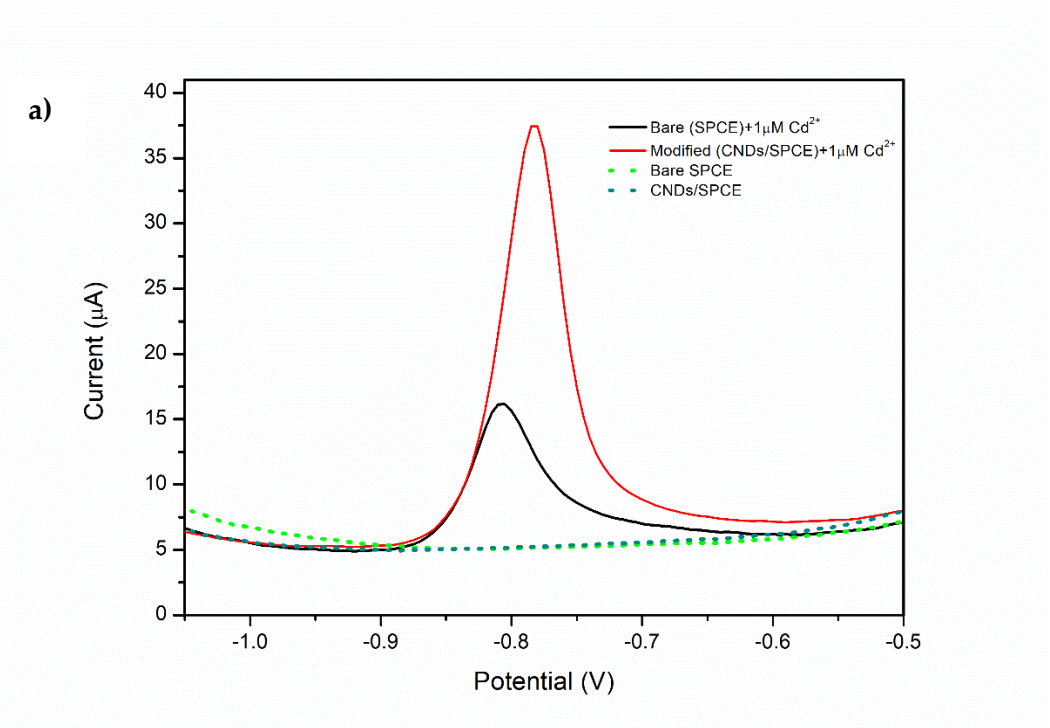

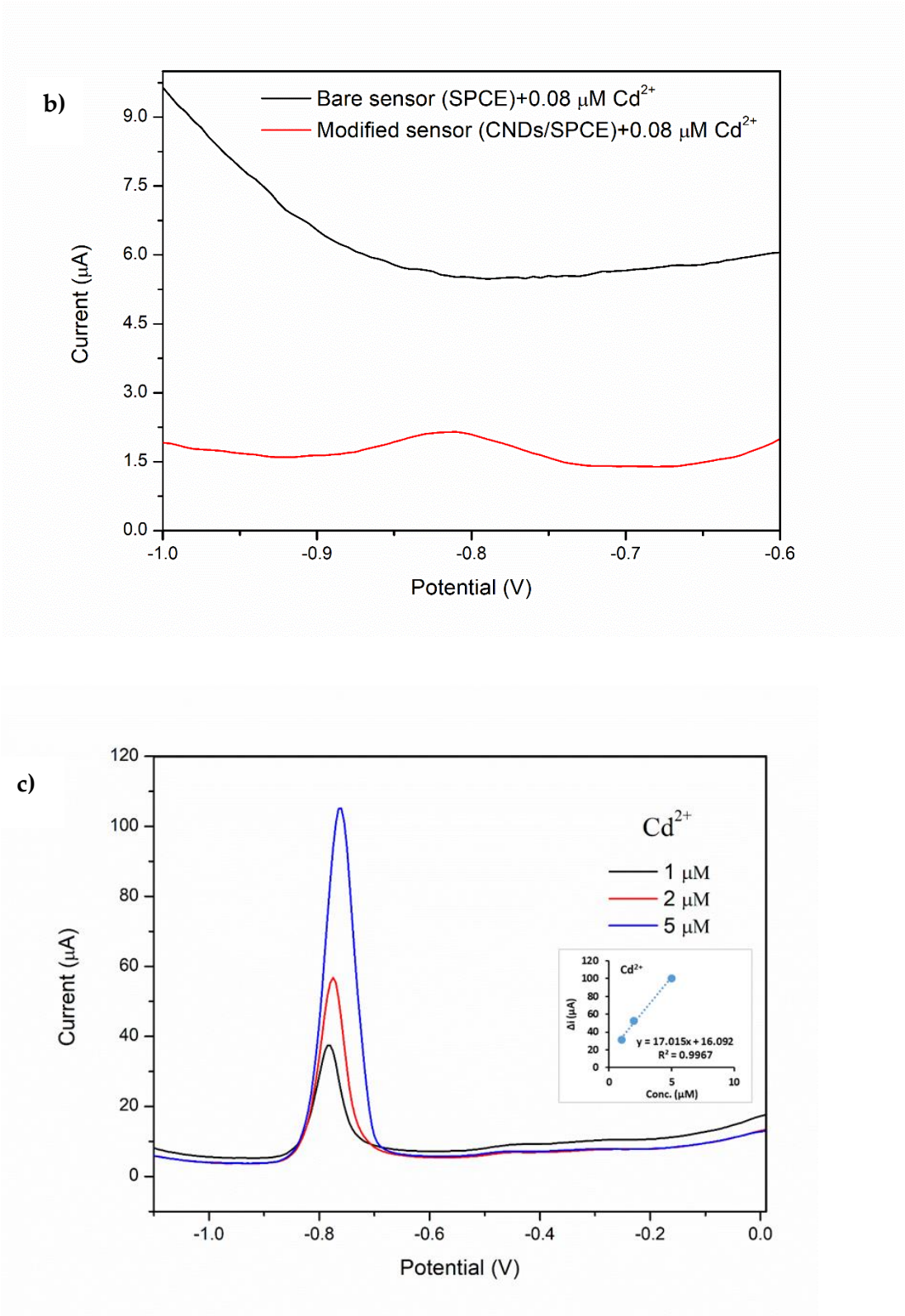

Figure 3.2.18. a) SWV analysis for Cd^{2+}, with SPCE (black line) and CNDs/SPCE (red line) sensors in acetate buffer pH 4.5 in the potential range from −1.1 V to −0.5 V ; **b)** SWV response at low concentration of Cd^{2+} [0.08 μM] with bare SPCE (black line) and modified CNDs/SPCE (red line) sensors (potential range from −1 V to −0.6 V; **c)** SWV analysis for Cd^{2+} [from 1 to 5 μM] with CNDs/SPCE sensor in acetate buffer (pH 4.5) in the potential range from

−1.1 V to 0 V, and (inset) related calibration curve. SWV conditions: E_{cond} 0.6V, t_{cond} 60s , E_{dep} −1V, t_{dep} 240s, t_{eq} 15s, E_{amp} 25mV, E_{step} 5mV, Freq 5Hz.

The CNDs/SPCE sensor can simultaneously and selectively detect heavy metal ions when added at different concentrations, as depicted in **Figure 3.2.19a**. The peak current of the stripping reaction shows a proportional increase with concentration, establishing a strong linear relationship (R^2 ranging from 0.96 to 0.98) across the concentration range of 0.1 nM to 100 µM for all metals reaching an apparent plateau at high concentrations due to the saturation, more evident for Hg^{2+}, Pb^{2+}, and Cd^{2+} (**Figure 3.2.19b**). The insets in the figure illustrate the fit linear trend at nanomolar concentrations, showcasing a low detection limit and high sensitivity ("*Progress on Household Drinking Water, Sanitation and Hygiene 2000-2020: Five Years into the SDGs*", 2020), as detailed in **Table 3.2.3**. The capability to detect heavy metal ions at very low concentrations is crucial for environmental applications.

Heavy metal ions	Max concentration in water (WHO limit)	LOD (ng/L)	Sensitivity ($\mu AnM^{-1}cm^{-2}$)
Hg^{2+}	1 µg/L	124	34.1
Pb^{2+}	10 µg/L	551	21.3
Cd^{2+}	5 µg/L	453	32.3
Ni^{2+}	20 µg/L	608	11.4

Table 3.2.3. LOD and sensitivity of CNDs/SPCE calculated through fit linear calibration curves (**Figure 3.2.19b**) in nanomolar concentration of heavy metals ions compared with the WHO limits of concentrations

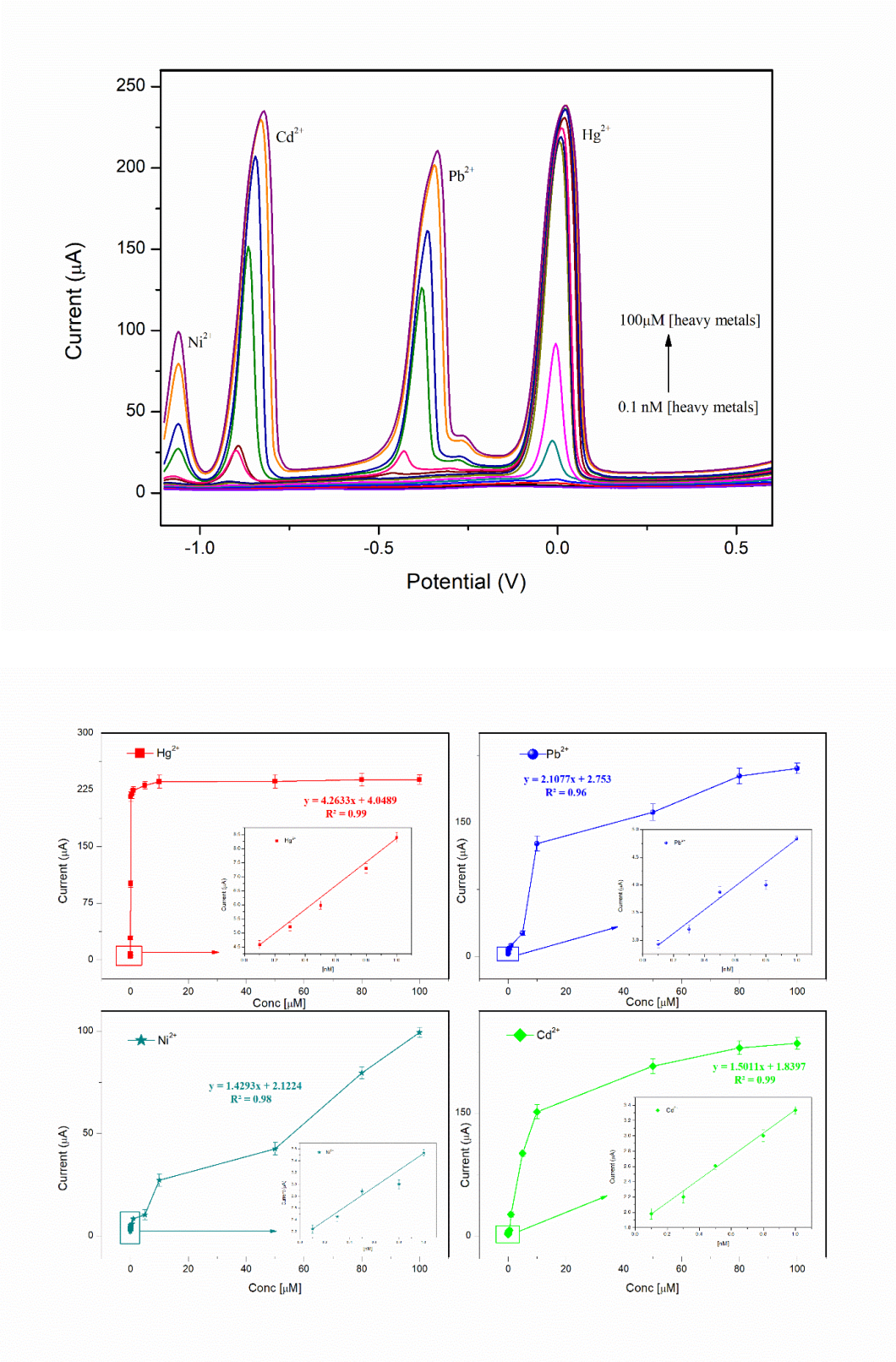

Figure 3.2.19. a) SWASV response of CNDs/SPCE at concentration range between 0.1nM and 100 µM of heavy metals ions; **b)** CNDs/SPCE response to heavy metal ions addition in the studied concentration range [0.1 nM to 100µM]; insets: calibration graphs for peak current at low concentrations [0.1 to 1 nM] and related fit linear equations (sd ≤ 3). SWASV condition: E_{cond} 0.6V, t_{cond} 60s, E_{dep} −1V, t_{dep} 240s, t_{eq} 15s, E_{amp} 25mV, E_{step} 5mV, Freq 5Hz, potential range between −1.2 to 0.6 V

The repeatability of the modified electrode's response to adding heavy metal ions was evaluated by performing five replicate tests in an acetate buffer solution (pH 4.5) with a final concentration of 50 μM for each metal. The results obtained and the average standard deviations related to the SWASV oxidation peaks are presented in **Figure 3.2.20a**. The outcomes showed that the CNDs/SPCE has high and good repeatability, especially for mercury and nickel ions detection. **Figure 3.2.20b** depicts the response reproducibility, which was evaluated using three modified sensors prepared in the same way, and the resulting RSDs were found to be less than 2% for all the performed tests, indicating outstanding repeatability.

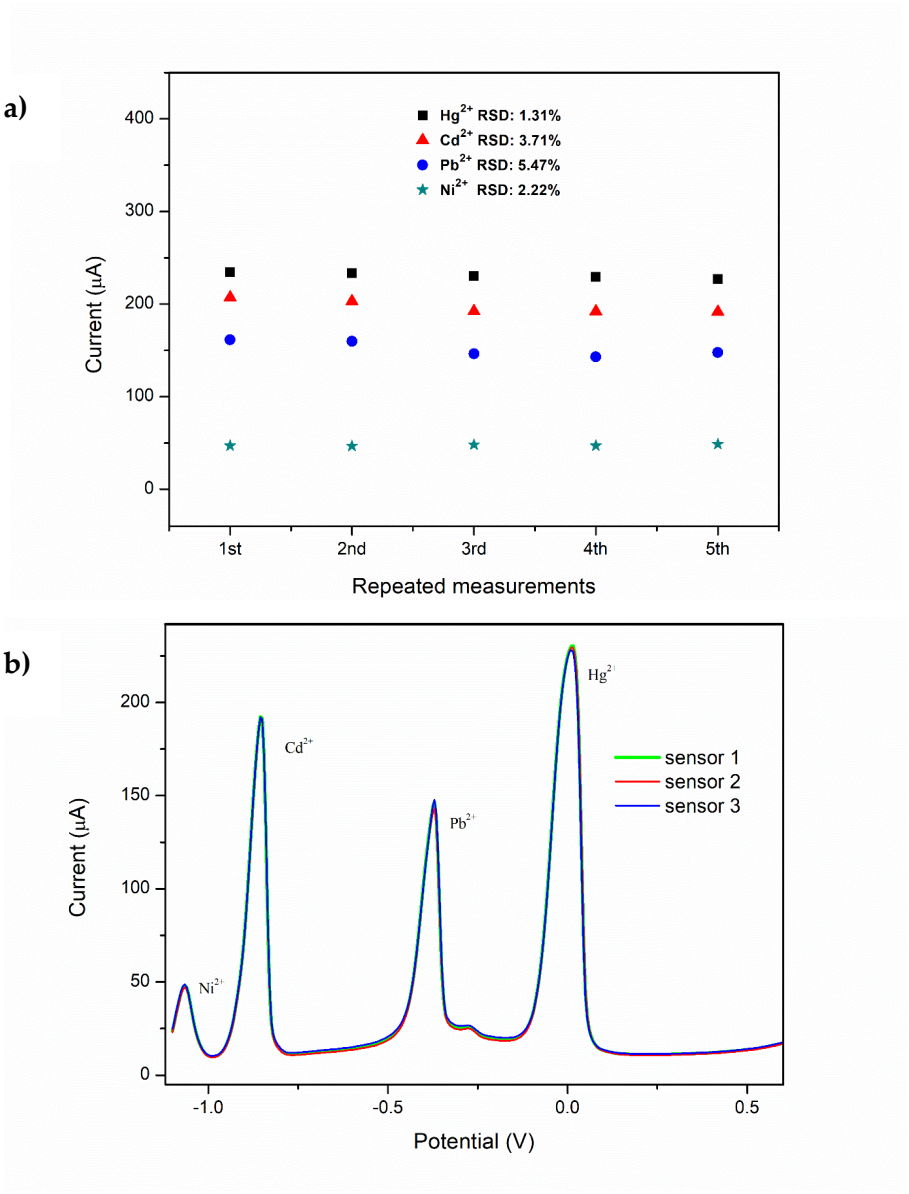

Figure 3.2.20. Repeatability results obtained **a)** after several tests performed with the same sensor, and **b)** by using three modified sensors (CNDs/SPCE), carring out a SWASV in acetate buffer (pH 4.5) by stripping heavy metals at final concentration of 50 µM working in the potential range from −1.2 V to 0.6V. SWV condition: E_{cond} 0.6V, t_{cond} 60s , E_{dep} −1V, t_{dep} 240s, t_{eq} 15s, E_{amp} 25mV, E_{step} 5mV, Freq 5Hz, potential range between −1.2 V to 0.6V

Real samples analysis

To explore the capability of CNDs/SPCE for detecting heavy metal ions in real samples, seawater collected from Mar Jonio (Siderno, Calabria, Italy) and wastewater collected from the Port of Messina (Sicilia, Italy) were subjected to

SWASV analysis without any pre-treatment carrying out the proposed sensing approach. The procedure involved spiking two different heavy metal concentrations (50 and 100 nM) into real water samples, previously diluted with acetate buffer (ratio 1:9, water: acetate buffer). The experiments were repeated three times, and high recoveries were obtained for all heavy metals except for Ni^{2+}. The recoveries for all metals ranged between 95.5% and 102.6%, indicating that the recommended electrochemical method has the potential to accurately and simultaneously detect heavy metal ions in water samples. Table 3 presents the results of these experiments.

Real sample	**Added (nM)**	**Recovery (%) ± SD**			
		Hg^{2+}	Cd^{2+}	Pb^{2+}	Ni^{2+}
Seawater	0	-	-	-	-
	50	102.1 ± 0.86	96.3 ± 1.2	99.1 ± 0.90	ND
	100	102.4 ± 0.81	98.2 ± 0.90	100.3 ± 0.90	91.4 ± 2.17
Wastewater	0	-	-	-	-
	50	99.8 ± 1.2	95.5 ± 1.92	101.4 ± 1.6	ND
	100	102.6 ± 0.90	98.1 ± 0.88	98.9 ± 0.85	98.7 ± 1.8

Table 3.2.4. Recovery values for heavy metals detection in water real samples

Conclusions

This study presents a simple approach for synthesizing carbon nanomaterials from hydrochar produced through the hydrothermal treatment of bagasse beer, intending to improve the properties of natural biomass and harness the advantages of carbon nanomaterials. The resultant carbon nanodots were thoroughly characterized and exibited desirable properties such as good water solubility, interesting functional groups, and excellent photoluminescent and electrochemical properties. First, it has been demonstrated that the fluorescent carbon nanodots possess excellent sensitivity towards Hg^{2+} and Pb^{2+} ions, with a low detection limit of 11.3 nM and 78.8 nM, respectively. Moreover, the carbon nanodots were successfully tested as a disposable sensor for simultaneous electrochemical detection of heavy metals in wastewater without any pre/post-treatment, exhibiting low limit of detection for all the tested heavy metals. These remarkable properties make them highly attractive sensing materials for rapid and selective detection of heavy metals in water.

References

Anusuya, T.; Kumar, V.; Kumar, Vivek. Hydrophilic Graphene Quantum Dots as Turn-off Fluorescent Nanoprobes for Toxic Heavy Metal Ions Detection in Aqueous Media. *Chemosphere*, **2021**, 28, 131019. https://doi.org/10.1016/j.chemosphere.2021.131019

Balakrishnan, T.; Ang, W. L.; Mahmoudi, E.; Wahab Mohammad, A.; Sambudi, N. S. Formation Mechanism and Application Potential of Carbon Dots Synthesized from Palm Kernel Shell via Microwave Assisted Method. *Carbon Resources Conversion* **2022**, 5 (2), 150–66. https://doi.org/10.1016/j.crcon.2022.01.003

Bressi, V.; Balu, A.M.; Iannazzo, D.; Espro, C. Recent advances in the synthesis of carbon dots from renewable biomass by high-efficient hydrothermal and microwave green approaches. *Current Opinion in Green and Sustainable Chemistry*, **2023**, 40, 100742. https://doi.org/10.1016/j.cogsc.2022.100742

Bressi, V.; Chiarotto, I.; Ferlazzo, A.; Celesti, C.; Michenzi, C.; Len, T.; Iannazzo, D.; Neri, G.; Espro, C. Voltammetric Sensor Based on Waste-Derived Carbon Nanodots for Enhanced Detection of Nitrobenzene. *ChemElectroChem*, **2023**, e202300004. https://doi.org/10.1002/celc.202300004

Carbonaro, C. M.; Chiriu, D.; Stagi, L.; Casula, M. F.; Thakkar, S.V.; Malfatti, L.; Suzuki, K.; Ricci, P. C.; Corpino, R. Carbon Dots in Water and Mesoporous Matrix: Chasing the Origin of Their Photoluminescence. *The Journal of Physical Chemistry C*, **2018**, 122 (44), 25638–50. https://doi.org/10.1021/acs.jpcc.8b08012

Demirci, S.; McNally, A. B.; Ayyala, R. S.; Lawson, L. B.; Sahiner, N. Synthesis and Characterization of Nitrogen-Doped Carbon Dots as Fluorescent Nanoprobes with Antimicrobial Properties and Skin Permeability. *Journal of Drug Delivery Science and Technology*, **2020**, 59, 101889. https://doi.org/10.1016/j.jddst.2020.101889

'*International Union of Pure and Applied Chemistry'*, (accessed June 2023). https://publications.iupac.org/compendium/index.html

Kainth, S.; Maity, B.; Shetti, N. P.; Basu, S.; Kakarla, R. R. Dual Emissive Carbon Dots: Synthesis Strategies, Properties and Its Ratiometric Sensing Applications. *Nano-Structures & Nano-Objects*, **2023**, 33, 100931. https://doi.org/10.1016/j.nanoso.2022.100931

Kalpana, R.; Vignesh, N. S.; Vinothini, K.; Rajan, M.; Ashokkumar, B.; Brindhadevi, K.; Lan Chi, N. T.; Pugazhendhi, A.; Varalakshmi, P. Carbon Quantum Dots (CQD) Fabricated from Exiguobacterium Sp. VK2 Exopolysaccharide (EPS) Using Hydrothermal Reaction and Its Biodiesel Applications. *Fuel*, **2023**, 333, 126426. https://doi.org/10.1016/j.fuel.2022.126426

Lin, H.; Ding, L.; Zhang, B.; Huang, J. Detection of Nitrite Based on Fluorescent Carbon Dots by the Hydrothermal Method with Folic Acid. *Royal Society Open Science*, **2018**, 5 (5), 172149. https://doi.org/10.1098/rsos.172149

Liu, M. L.; Chen, B. B.; Li, C. M.; Huang, C. Z. Carbon Dots: Synthesis, Formation Mechanism, Fluorescence Origin and Sensing Applications. *Green Chemistry*, **2019**, 21 (3), 449–71. https://doi.org/10.1039/C8GC02736F

Liu, Y.; Zhou, Q.; Li, J.; Lei, M.; Yan, X. Selective and Sensitive Chemosensor for Lead Ions Using Fluorescent Carbon Dots Prepared from Chocolate by One-Step Hydrothermal Method. *Sensors and Actuators B: Chemical*, **2016**, 237, 597–604. https://doi.org/10.1016/j.snb.2016.06.092

Locquet, N.; Aït-Kaddour, A.; Cordella, C. B.Y. 3D Fluorescence Spectroscopy and Its Applications. In *Encyclopedia of Analytical Chemistry*, **2018**, 1–39. John Wiley & Sons, Ltd. https://doi.org/10.1002/9780470027318.a9540

Ng, H. K. M.; Lim, G. K.; Leo, C. P. Comparison between Hydrothermal and Microwave-Assisted Synthesis of Carbon Dots from Biowaste and Chemical for Heavy Metal Detection: A Review. *Microchemical Journal*, **2021**, 165, 106116. https://doi.org/10.1016/j.microc.2021.106116

Pang, S. C.; Voon, L. K.; Chin, S. F. Controlled Depolymerization of Cellulose Fibres Isolated from Lignocellulosic Biomass Wastes. *International Journal of Polymer Science*, **2018**, 1–11. https://doi.org/10.1155/2018/6872893

Pourmahdi, N.; Sarrafi, A. H. M.; Larki, A. Carbon Dots Green Synthesis for Ultra-Trace Determination of Ceftriaxone Using Response Surface Methodology. *Journal of Fluorescence*, **2019**, 29 (4), 887–97. https://doi.org/10.1007/s10895-019-02400-5

'*Progress on Household Drinking Water, Sanitation and Hygiene 2000-2020: Five Years into the SDGs*' (accessed June 2023). https://apps.who.int/iris/handle/10665/345081

Qi, X.; Liu, H.; Guo, W.; Lin, W.; Lin, B.; Jin, Y.; Deng, X. New Opportunities: Second Harmonic Generation of Boron-Doped Graphene Quantum Dots for Stem Cells Imaging and Ultraprecise Tracking in Wound Healing. *Advanced Functional Materials*, **2019**, 29 (37), 1902235. https://doi.org/10.1002/adfm.201902235

Saha, N.; McGaughy, K.; Reza, M. T. Elucidating Hydrochar Morphology and Oxygen Functionality Change with Hydrothermal Treatment Temperature Ranging from Subcritical to Supercritical Conditions. *Journal of Analytical and Applied Pyrolysis*, **2020**, 152, 104965. https://doi.org/10.1016/j.jaap.2020.104965

Satira, A.; Paone, E.; Bressi, V.; Iannazzo, D.; Marra, F.; Calabrò, P.S.; Mauriello, F.; Espro, C. Hydrothermal Carbonization as Sustainable Process for the Complete Upgrading of Orange Peel Waste into Value-Added Chemicals and Bio-Carbon Materials. *Applied Sciences*, **2021**, 11, 10983. https://doi.org/10.3390/app112210983

Sekar, A.; Yadav, R.; Basavaraj, N. Fluorescence Quenching Mechanism and the Application of Green Carbon Nanodots in the Detection of Heavy Metal Ions: A Review. *New Journal of Chemistry*, **2021**, 45 (5), 2326–60. https://doi.org/10.1039/D0NJ04878J

Song, H.; Huo, M.; Zhou, M.; Chang, H.; Li, J.; Zhang, Q.; Fang, Y.; Wang, H.; Zhang, D. Carbon Nanomaterials-Based Electrochemical Sensors for Heavy Metal Detection. *Critical Reviews in Analytical Chemistry*, **2022**, 0, 1–20. https://doi.org/10.1080/10408347.2022.2151832

Souza, T. G. F.; Ciminelli, V. S. T.; Mohallem, N. D. S. A Comparison of TEM and DLS Methods to Characterize Size Distribution of Ceramic Nanoparticles. *Journal of Physics: Conference Series*, **2016**, 733 (1), 012039. https://doi.org/10.1088/1742-6596/733/1/012039

Spagnuolo, D.; Iannazzo, D.; Len, T.; Balu, A. M.; Morabito, M.; Genovese, G.; Espro, C.; Bressi, V. Hydrochar from Sargassum Muticum: A Sustainable Approach for High-Capacity Removal of Rhodamine B Dye. *RSC Sustainability*, **2023**. https://doi.org/10.1039/D3SU00134B

Varsha Raveendran, P. T.; Renuka, N. K. Hydrothermal Synthesis of Biomass-Derived Carbon Nanodots: Characterization and Applications. *Materials Chemistry and Physics*, **2022**, 288, 126236. https://doi.org/10.1016/j.matchemphys.2022.126236

Wareing, T. C.; Gentile, P.; Phan, A. N. Biomass-Based Carbon Dots: Current Development and Future Perspectives. *ACS Nano*, **2021**, 15 (10), 15471–501. https://doi.org/10.1021/acsnano.1c03886

Wu, Y.; Liu, X.; Wu, Q.; Yi, J.; Zhang, G. Differentiation and Determination of Metal Ions Using Fluorescent Sensor Array Based on Carbon Nanodots. *Sensors and Actuators B: Chemical*, **2017**, 246, 680–85. https://doi.org/10.1016/j.snb.2017.02.132

Yarur, F.; Macairan, J-R.; Naccache, R. Ratiometric Detection of Heavy Metal Ions Using Fluorescent Carbon Dots. *Environmental Science: Nano*, **2019**, 6 (4), 1121–30. https://doi.org/10.1039/C8EN01418C

Zhang, Y.; Niu, Q.; Gu, X.; Yang, N.; Zhao, G. Recent Progress on Carbon Nanomaterials for the Electrochemical Detection and Removal of Environmental Pollutants. *Nanoscale*, **2019**, 11 (25), 11992–14. https://doi.org/10.1039/C9NR02935D

3.3 Electrochemical Determination of Nitrites and Sulfites by Using Waste-derived Nanobiochar

Published: Journal of Electroanalytical Chemistry, ***2023***

This study presents an electrochemical sensor employing nanobiochar for the detection of nitrite and sulfite ions, representing the first instance where nanobiochar, sourced from discarded waste, has showcased its potential for the simultaneous electrochemical detection of sulfites and nitrites in real samples. The nanobiochar material was derived from the hydrothermal carbonization of orange peel waste carried out at 180 °C and later subjected to alkaline activation, resulting in the synthesis of NBC_{180}. Various characterizations, such as SEM, XRD, FT-IR, and optical analyses, were conducted to evaluate its chemical, physical, morphological, and microstructural properties, and these were subsequently compared to the original hydrochar material, HTC_{180}. A screen printed carbon electrode was modified through drop-casting of NBC_{180} solution and its electrochemical abilities were examined through cyclic voltammetry (CV) and electrochemical impedance spectroscopy (EIS). The modified sensor demonstrated enhanced electrochemical performance in comparison to the bare SPCE when used for the detection of sulfite and nitrite ions with a linear relationship established between the anodic peaks and the concentrations of the analytes, with valid correlations observed up to concentrations of 3200 µM and 1400 µM, respectively.

Experimental

Synthesis of Nanobiochar (NBC)

20 g of orange peel waste (OPW) was placed in an autoclave reactor containing 50 mL of deionized water, mantained at 180°C for 60 min under continuous

stirring and autogenic pressure. This procedure was adopted from previously published works by our research group (Espro *et al.*, 2021; Satira *et al.*, 2021). The resulting hydrochar (HTC_{180}), was subsequently treated with a 2M NaOH solution and filtered through a 0.1 mm millipore membrane. The filtered solution was further purified through four dialysis days to yield the nanobiochar sample, designated as NBC_{180}. **Figure 3.3.1** provides a visual representation of the described process for synthesizing the nanobiochar.

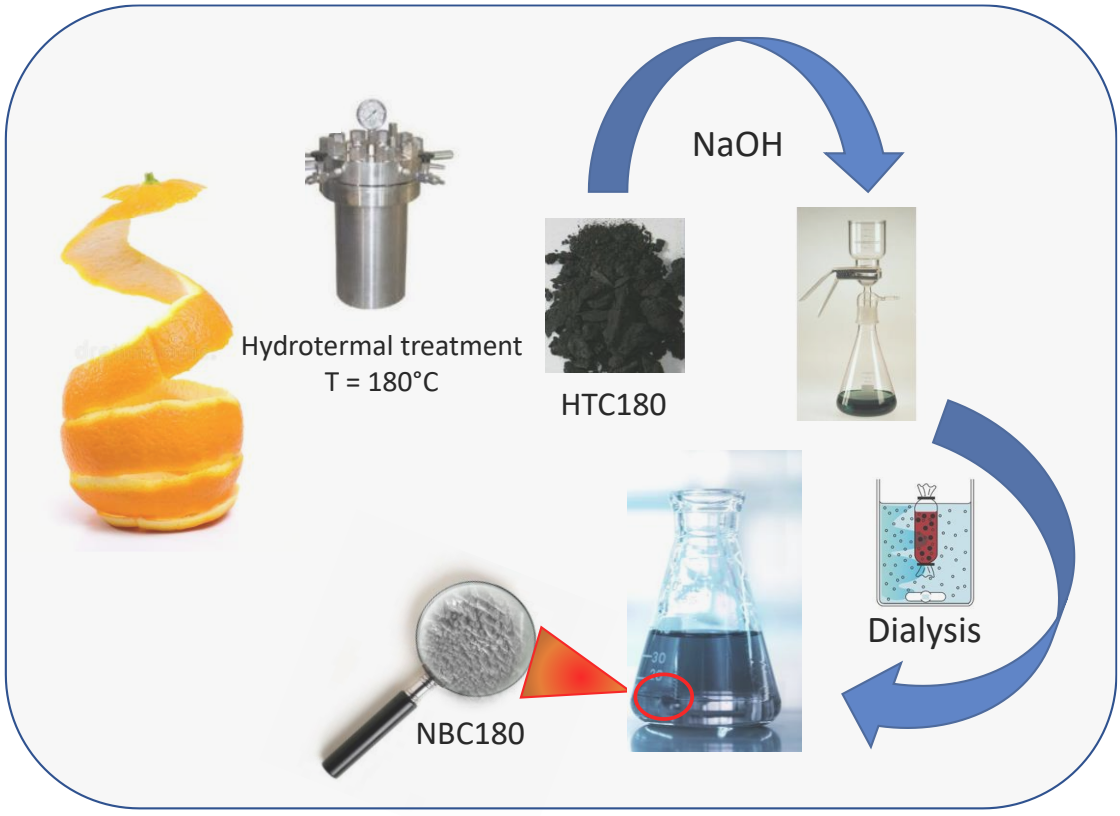

Figure 3.3.1. Illustration outlining the process for synthesizing NBC_{180}

In prior studies (Espro *et al.*, 2021; Iannazzo *et al.*, 2022), hydrothermal treatment of OPW was performed at varying reaction times and temperatures, producing different hydrochars. Before the start of electrochemical studies, the distinct types of nanobiochars derived from these hydrochars were analyzed.

Among them, the nanobiochar obtained at 180 °C for 60 minutes emerged as the most promising candidate for potential electrochemical applications. This preference is likely a consequence of excessively high temperatures causing the depolymerization of cellulose, hemicellulose, pectin, and lignin within the orange peels (Satira *et al.*, 2021). In contrast, lower reaction temperatures result in the retention of numerous residual oxygenated groups onto the surface of the hydrochar, as evidenced by a notably high oxygen content (approximately 20 wt%) and a lower carbon content (around 78 wt%). This disparity in composition may elucidate the enhanced affinity of the nanobiochar produced from HTC_{180} for the tested analytes. The morphological and structural properties of the starting material and the NBC_{180} are reported in subsequent sections.

Results and discussion

Characterization of the materials

Figure 3.3.2 provides the representative SEM images of HTC_{180} and NBC_{180}. The images reveal a similar amorphous appearance for both samples but highlight that in HTC_{180}, small spherical carbon aggregates are still present, becoming imperceptible in NBC_{180}, while the characteristic cellulose and hemicellulose structure, as previously observed in hydrochars obtained from the same raw material during hydrothermal activation at lower temperatures and shorter reaction time (Ramanayaka *et al.*, 2020), remains apparent. On the other hand, the NBC displays a different structure due to the subsequent treatment with NaOH, which enables the formation of nanoscale structures (Chausali *et al.*, 2021). The XRD spectra (**Figure 3.3.3**) confirm this observation, with the pattern of the HTC sample exhibiting two prominent peaks at around 15° and 22° 2 theta, which are attributed to the incomplete depolymerisation of the lignocellulosic structure (Satira *et al.*, 2021) and

associated with the (002) graphitic plane and the turbostratic structure of disordered carbon assigned to the (100) graphite plan, respectively (Mewada *et al.*, 2013). These peaks are absent in the nanobiochar sample, underscoring that the NaOH treatment induced significant changes in the surface compared to the starting material.

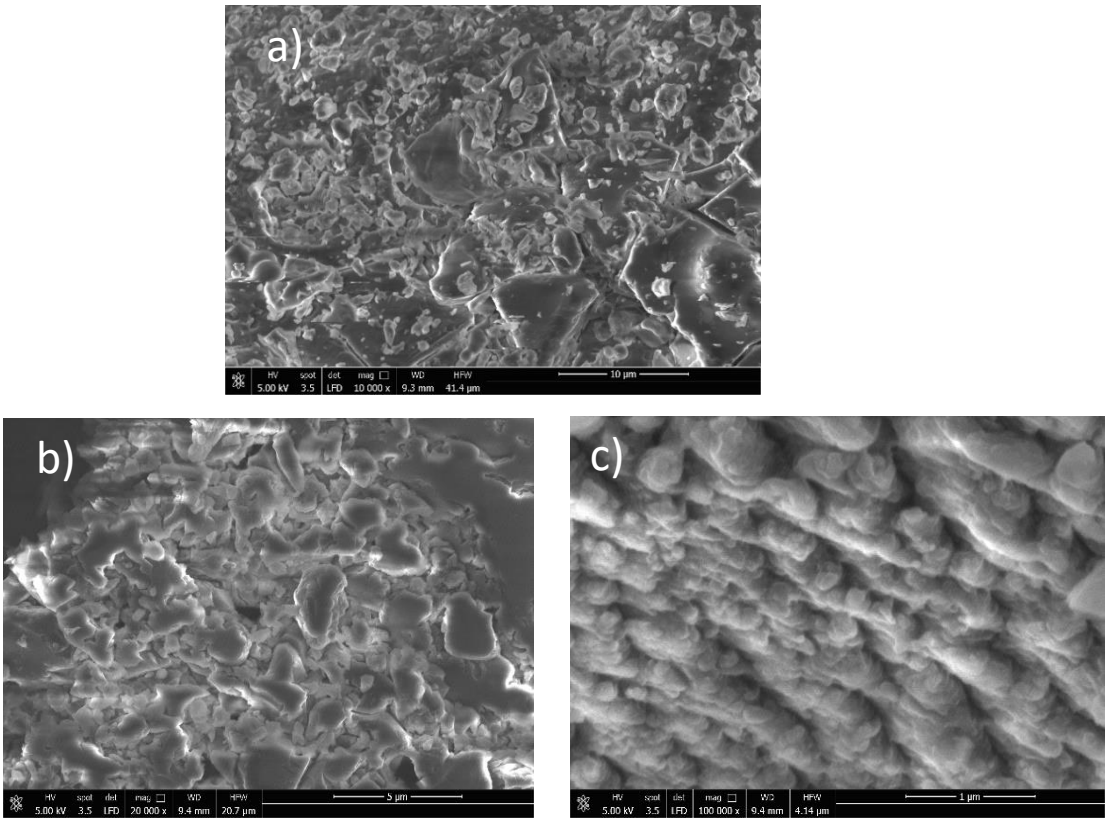

Figure 3.3.2. SEM images of **a)-b)** HTC_{180} and **c)** NBC_{180}

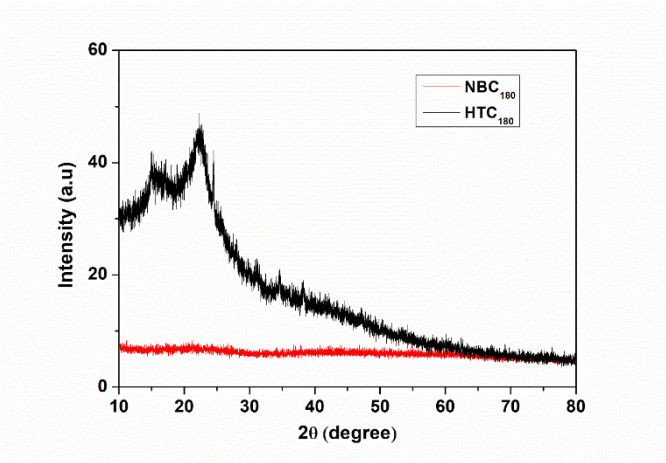

Figure 3.3.3. XRD patterns of **black)** HTC_{180} and **red)** NBC_{180}

Figure 3.3.4 depicts the FTIR spectra of the samples with the absorption bands interpreted as follows:

-the band at 3350 cm^{-1} corresponds to the stretching of O-H bonds in carboxyl and hydroxyl functional groups;

-the band at 2920 cm^{-1} is related to aliphatic C-H groups;

-at 1690 cm^{-1} there is evidence of the vibration associated with the carboxyl-derived C=O group, as well as at 1380 cm^{-1}, which may correspond to the asymmetric and symmetric stretching of the carboxylate group (COO^{-});

-the band at 1580 cm^{-1} can be attributed to the C=C vibrations of the aromatic groups present in the nanomaterial following carbon matrix graphitization;

- the peaks observed at 1270 and 1020 cm^{-1} are likely due to the stretching of the C-O group derived from alcohols, particularly phenolic groups.

Comparing the FTIR spectrum of NBC_{180} to that of the precursor, it becomes apparent that the signal at 1020 cm^{-1}, characteristic of the C-O single bond in the lignocellulosic component, disappears. In contrast, there is a noticeable increase in the presence of OH and C=O groups. This observation aligns with the higher water solubility of the NBC_{180} sample compared to HTC_{180} (Espro *et al.*, 2021).

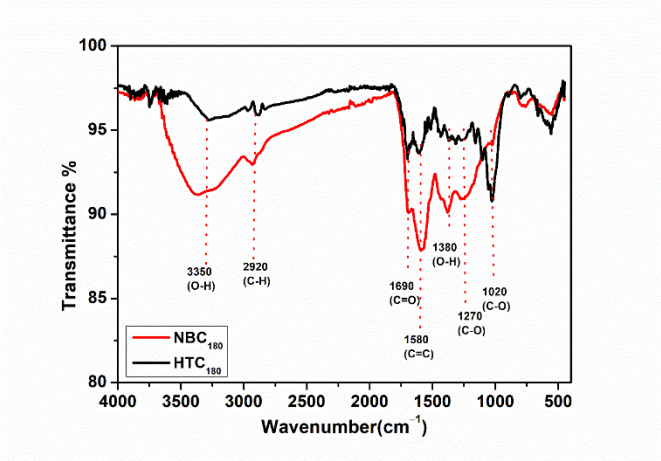

Figure 3.3.4. FTIR spectra of **black)** HTC_{180} and **red)** NBC_{180}

The optical property of NBC_{180} was compared to HTC_{180} by developing a photoluminescence analysis utilizing an excitation wavelength of 360 nm (see **Figure 3.3.5**). In the original HTC_{180} sample, a prominent fluorescence emission peak is visible at 448 nm, primarily attributable to the substantial presence of graphitic carbon, with an additional smaller peak at 538 nm. Conversely, in NBC_{180}, two emission peaks are discerned, one at 455 nm and the other at 545 nm. Notably, the intensity of the emission peak associated with graphitic carbon is significantly reduced, and it shifts to longer wavelengths, by the XRD analysis results. The emission peak at 545 nm is linked to the increased quantity of nanoscale material generated due to the NaOH treatment. The photoluminescence characterization findings indicate that the NaOH

activation and purification procedures effectively lead to the formation and selection of carbon nanoparticles over graphitic carbon.

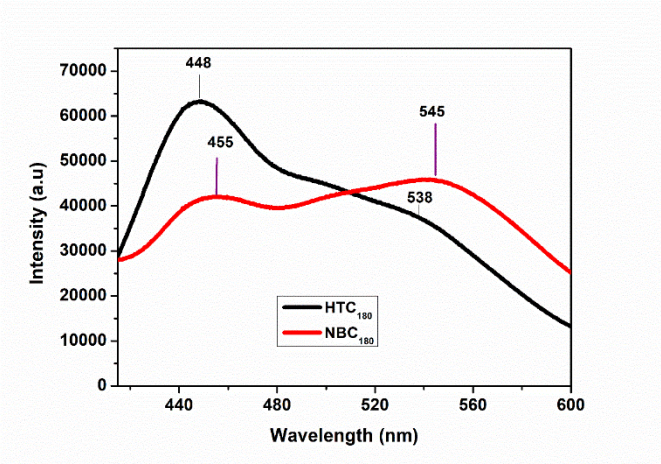

Figure 3.3.5 Photoluminescence spectra of **black)** HTC_{180} and **red)** NBC_{180}

Electrochemical Behavior

The bare screen-printed electrode was modified by drop-casting 10 µL of an aqueous suspension of both materials onto the carbon working electrode. This solution was then allowed to dry overnight at room temperature. Initially, an electrochemical investigation was performed on the prepared electrodes to identify the one exhibiting superior performance for nitrite detection. Cyclic voltammetry (CV) tests were executed within the potential range of −0.1 to 1.2 V, both in the absence and presence of 700 µM nitrite. The tests focusing on nitrite monitoring revealed that the sensor modified with NBC_{180} exhibited superior performance, with higher current intensity and a lower potential (as shown in **Figure 3.3.6**). Consequently, NBC_{180} was selected as the sensitive material for nitrite detection.

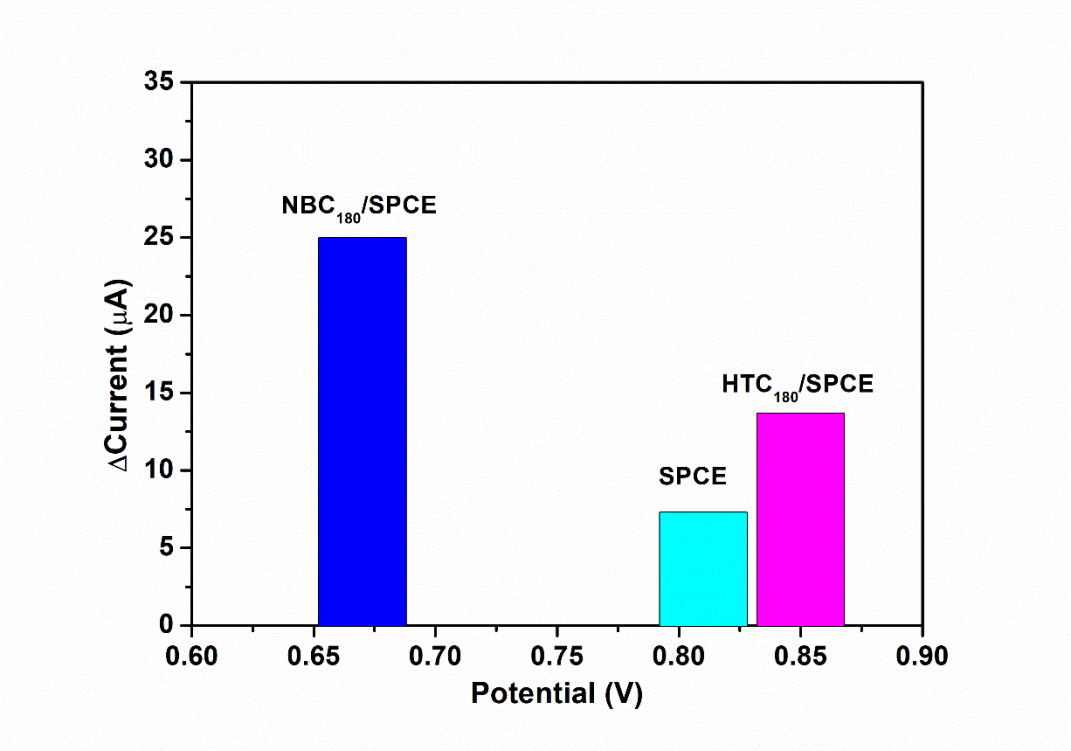

Figure 3.3.6. Electrochemical response of bare SPCE, HTC_{180}/SPCE, and NBC_{180}/SPCE, which was examined by CV carried out in 0.01 M PBS electrolyte, scan rate of 50 mV/s, within the potential range of −0.1 to 1.2 V, with the presence of 700 µM $NaNO_2$

The electrochemical performance of NBC_{180}/SPCE was investigated by conducting CV in 10 mM $K_3[Fe(CN)_6]$ solution at a scan rate of 50 mV/s (as reported in **Figure 3.3.7a**). The same analysis condition was performed using bare SPCE to compare the findings. The NBC_{180}/SPCE displays redox peaks at potentials of +0.20 V and +0.21 V vs. SPCE which shows redox peaks at +0.26 V and +0.16 V, indicative of iron oxidation and reduction, respectively. These outcomes suggest that the NBC_{180}/SPCE exhibits high electrical conductivity, probably due to the nanoparticles facilitating rapid electron transfer onto the electrode (Niranjana *et al.*, 2009). This outcome is further supported by the EIS analysis performed in a solution containing 10 mM $[Fe(CN)_6]^{3-/4-}$ and 0.1 M KCl, within a frequency range of 0.1 Hz to 105 Hz (using a 5 mV amplitude) and an applied potential of 0.25 V, as shown in **Figure 3.3.7b**. In this analysis, the bare SPCE shows a large semicircle, indicative of a diffusion-limited

electrochemical process, with a series resistance of 141 Ω. In contrast, the NBC_{180}/SPCE sensor exhibits a reduced semicircle with a series resistance to electron transfer (Rs. R) of 96.57 Ω. This resistance reduction emphasizes improved kinetics in electron transfer during the redox process at the electrode-electrolyte interface.

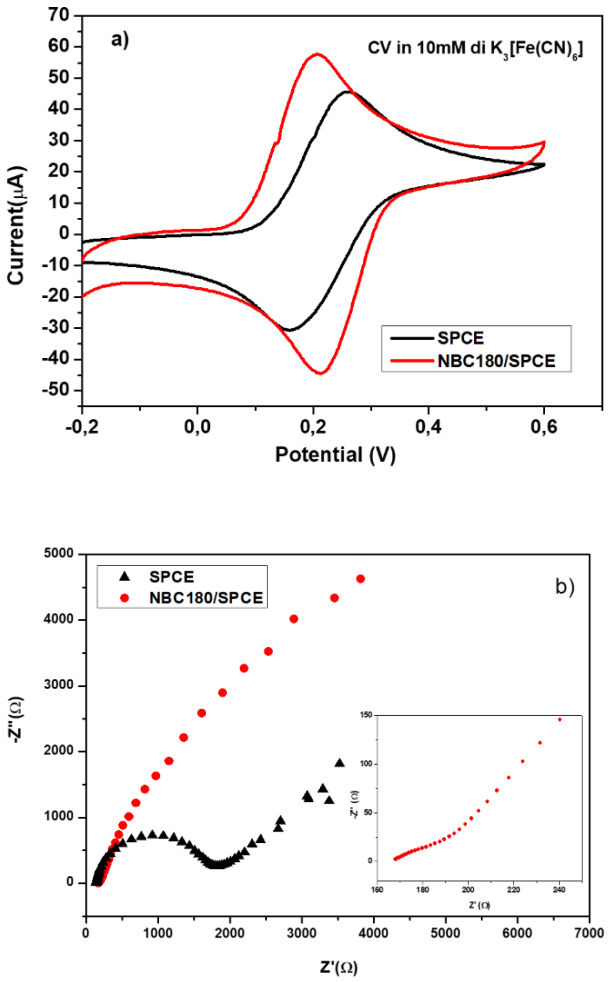

Figure 3.3.7. a) CV of bare SPCE and modified NBC_{180}/SPCE in 0.01 M PBS (pH 7.4), scan rate 50 mV/s. **b)** EIS of bare SPCE and NBC_{180}/SPCE in a solution containing 10 mM $[Fe(CN)_6]^{3-/4-}$ and 0.1 M KCl with a frequency range from 0.1 Hz to 105 Hz; Amplitude 5 mV

The CV of the NBC_{180}/SPCE sensor, conducted at varying scan rates in 10 mM solution of $K_3[Fe(CN)_6]$, reveals the influence of scanning speed on the electrocatalytic oxidation of redox species. As the scanning rate increases from 25 to 400 mVs^{-1}, the iron oxidation peak current and the peak potentials shift

toward a more positive direction. Notably, the current peak demonstrates a linear relationship when plotted against the square root of the velocity, as shown in **Figure 3.3.8**. This suggests that the electrocatalytic behavior of the NBC_{180}/SPCE sensor is attributed to a diffusion - controlled electron transfer process.

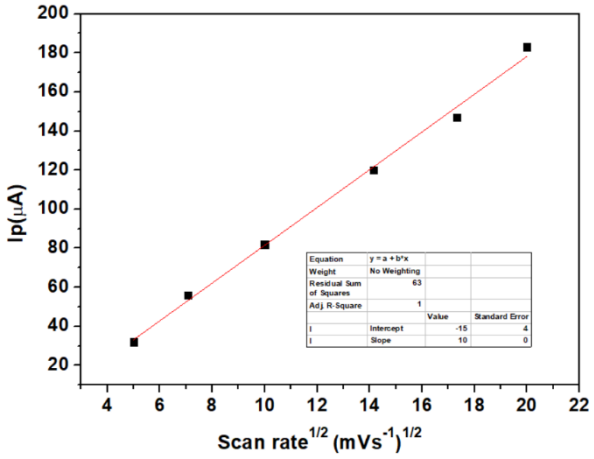

Figure 3.3.8. Plot of Ip vs $\upsilon^{1/2}$ obtained from cyclic voltammogram of NBC_{180}/SPCE in presence of 10 mM $K_3[Fe(CN)_6]$ at different scan rates from 25 to 400 mV/s in 0.01 M PBs (pH 7.4)

The impact of the scanning rate was also investigated by studying the electrocatalytic oxidation of nitrite [1 mM] in a 0.01 M phosphate buffer (pH 7.4) using the NBC_{180}/SPCE sensor, with a scanning rate range spanning from 25 to 400 mVs^{-1}. This analysis revealed an increase in the anodic peak current of nitrite, as shown in **Figure 3.3.9a**. The peak current of nitrite exhibited a linear correlation with the scan rate, indicating that the oxidation of nitrite ions on the NBC_{180}/SPCE sensor is an adsorption-controlled process. Additionally, the oxidation peak potential (Ep) shifted toward more positive values with increasing scan rate, confirming the irreversibility of the nitrite oxidation process (**Figure 3.3.9a**).

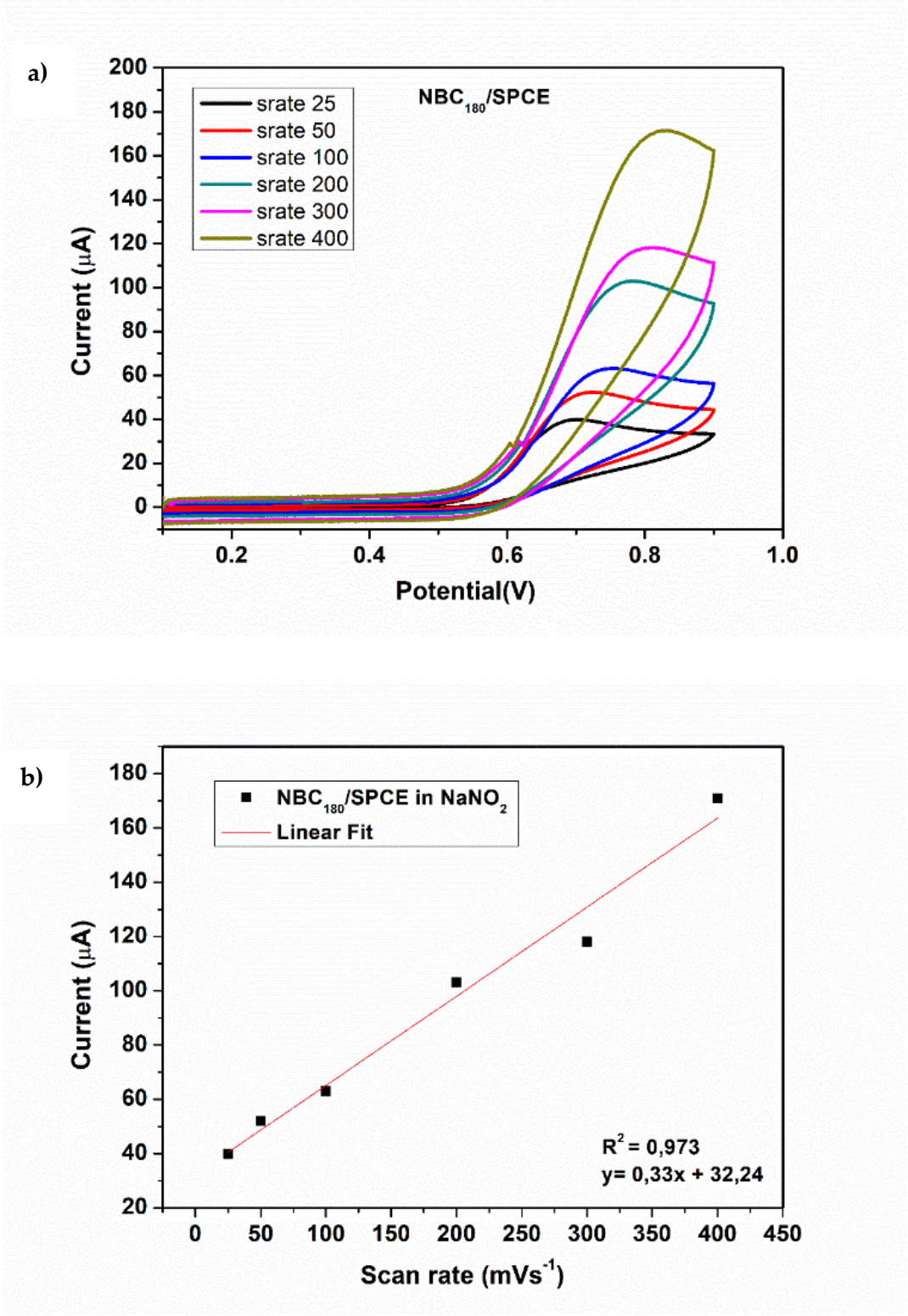

Figure 3.3.9. b) Plot of the anodic peak current (Ipa) vs. scan rate. Ipa values were derived by **a)** CV curves performed with the modified NBC_{180}/SPCE in 1 mM of $NaNO_2$ at different scan rate.

The electrochemical active surface area (EASA) associated with the redox reaction can be calculated by using the following Randles–Sevcik equation:

$$Ip = (2.69 \times 10^5)\, n^{3/2} D^{1/2} A\, \nu^{1/2} C$$

where: ν represents the scan rate, C is the bulk concentration of oxidized and reduced species, Ip is the peak current response, D is the diffusion coefficient (7.26×10^{-6} cm^2 s^{-1}), and *n* denotes the number of electrons participating in the electrochemical reaction. The EASA values for both bare and modified electrodes were determined from the slopes obtained in the plot of Ipa versus scan rate$^{1/2}$ (mV s^{-1}), as depicted in **Figure 3.3.8**. These calculations yielded EASA values of 0.0278 cm^2 for the bare SPCE and 0.0352 cm^2 for the modified electrodes.

Electrochemical Nitrite ions Determination

CV was employed to investigate the electrochemical behaviour NBC_{180}/SPCE in nitrite detection, as illustrated in **Figure 3.3.10**. A distinct oxidation current peak was evident at an oxidation potential of +0.69 V, compared to +0.82 V for the unmodified SPCE sensor. The shift in peak potential values and the amplification of oxidation current values indicate a faster electron transfer kinetics of the modified sensor for nitrite detection. The oxidation of nitrite is facilitated by its high electrocatalytic activity in the exchange of electrons due to the small dimensions of the particles and the presence of oxygenated functional groups, especially carbonyl and carboxyl groups that catalyze the oxidation to nitrite into nitrate (Ishizaki *et al.*, 2014; Qi *et al.*, 2013; Zheludkevich *et al.*, 2005). Developing CV analysis (as depicted in **Figure 3.3.11a**), the NBC_{180}/SPCE sensor underwent testing at various $NaNO_2$ concentrations. The results demonstrate a current increase corresponding to the solution's rising concentration of nitrite ions. The calibration data exhibits a

linear relationship as nitrite ions concentration increases, with a sensitivity calculated as 0.276 μA $\mu M^{-1}cm^{-2}$.

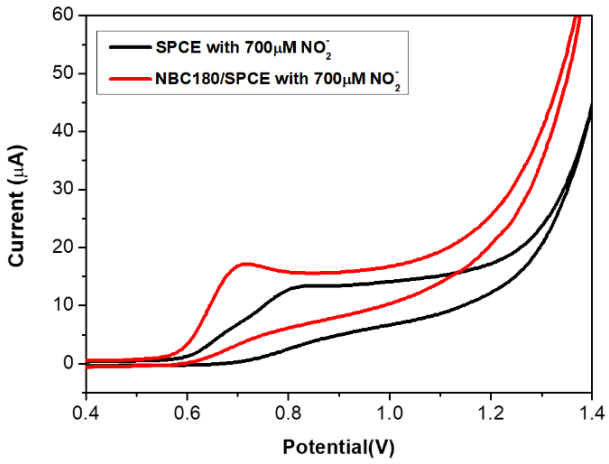

Figure 3.3.10. CV of SPCE and NBC_{180}/SPCE in the 0.4-1.4 V potential window, in response to the presence of 700 μM $NaNO_2$, performed in 0.01 M PBS at a scan rate of 50 mV/s

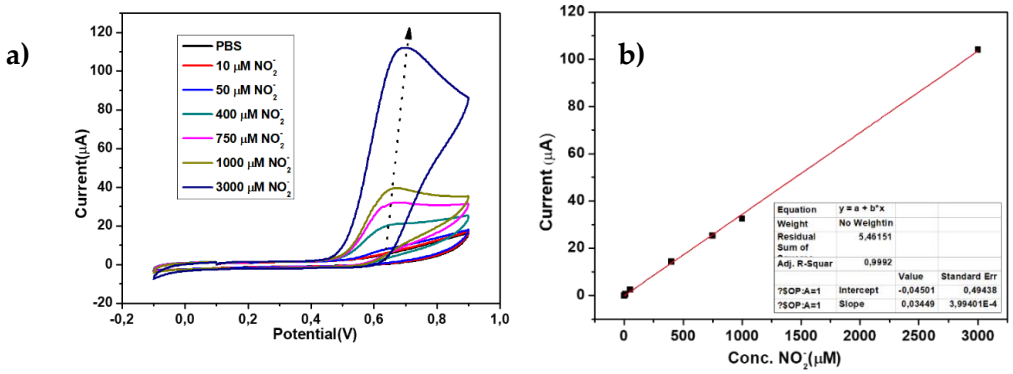

Figure 3.3.11. a) CV curves of NBC_{180}/SPCE in different concentrations of nitrite (0 to 3 mM) in 0.01 M PB (pH 7.4) at a scan rate 50 mV $s^{-1}$and potential range between 0.2 to 0.7 V; **b)** plot of the anodic peak current (Ipa) vs concentration. Ipa values were derived by CVs performed with the modified sensor at different concentration of $NaNO_2$

Electrochemical Sulfite ions Determination

To assess the ability to detect sulfite ions, a CV study was conducted in a 0.01 M PBS solution at a scan rate of 50 mV/s, comparing the unmodified sensor with the NBC_{180}/SPCE sensor. The bare exhibited no noticeable response to the

progressive increase in sulfite concentration, which ranged from 0 to 300 µM (**Figure 3.3.12a**). Conversely, the NBC_{180}/SPCE sensor demonstrated an elevation at 0.45 V peak current (**Figure 3.3.12b**).

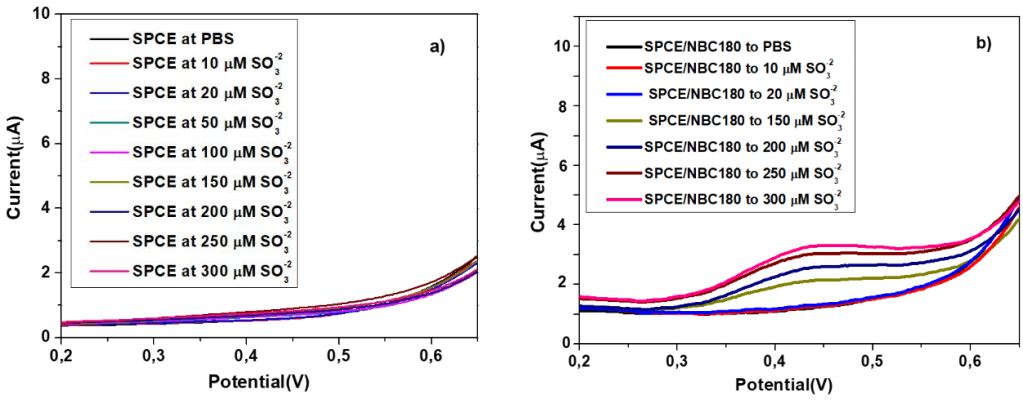

Figure 3.3.12. CV curves at different sulfite ions concentrations from 0 to 300 mM in 0.01 M PBS (pH 7.4) of **a)** bare SPCE, and **b)** NBC_{180}/SPCE. Scan rate 50 mV s^{-1}, potential range between 0.2 to 0.7 V

Simultaneous Analysis of Sulfite and Nitrite

Building upon the findings, LSV analysis was conducted to determine the simultaneous detection capability of sulfite and nitrite ions through the modified sensor NBC_{180}/SPCE. The curves shown in **Figure 3.3.13** illustrate the response in the presence of various concentrations of both analytes in a 0.01 M PBS at pH 7.4. Two distinct peaks were observed, one at 0.45 V for sulfites and another at 0.67 V for nitrites, which are evaluable even at low concentrations. There was a linear increase in the peak oxidation current with concentrations of both analytes within the linear range of 100 up to 400 µM (**Figure 3.3.13b**).

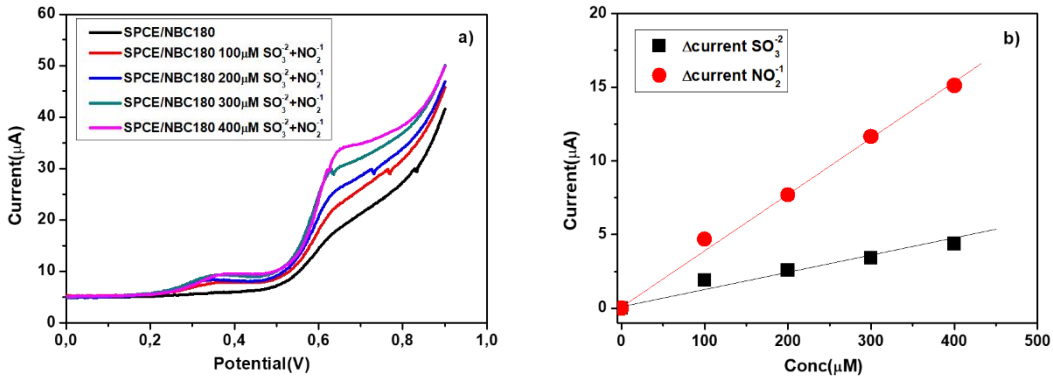

Figure 3.3.13. a) LSV at different nitrite and sulfite concentrations from 0 to 400 μM in 0.01 M PBS (pH 7.4), scan rate 50 mV/s; **b)** plot of the anodic peak current (Ipa) vs concentration

Subsequently, the Differential Pulse Voltammetry (DPV) technique was selected to detect nitrite and sulfite ions by using the NBC_{180}/SPCE sensor. Nitrites and sulfites were examined over a concentration range of 0 to 1400 μM (**Figure 3.3.14a**) and 0 to 3200 μM (**Figure 3.3.14b**), respectively. Nitrites demonstrated a linear relationship between current and concentration (**Figure 3.3.14c**), with a sensitivity of 0.352 $\mu A \mu M^{-1} cm^{-2}$. For sulfites, a sensitivity of 0.133 $\mu A \mu M^{-1} cm^{-2}$ was obtained from the calibration curve (**Figure 3.3.14d**). The Limit of Detection (LOD) was calculated using the formula: LOD = 3.3 σ/S, where S represents the slope of the calibration curve and σ is the standard deviation of the response. The calculated LOD values were 2.08 μM and 43 μM for nitrite, and sulfite ions, respectively.

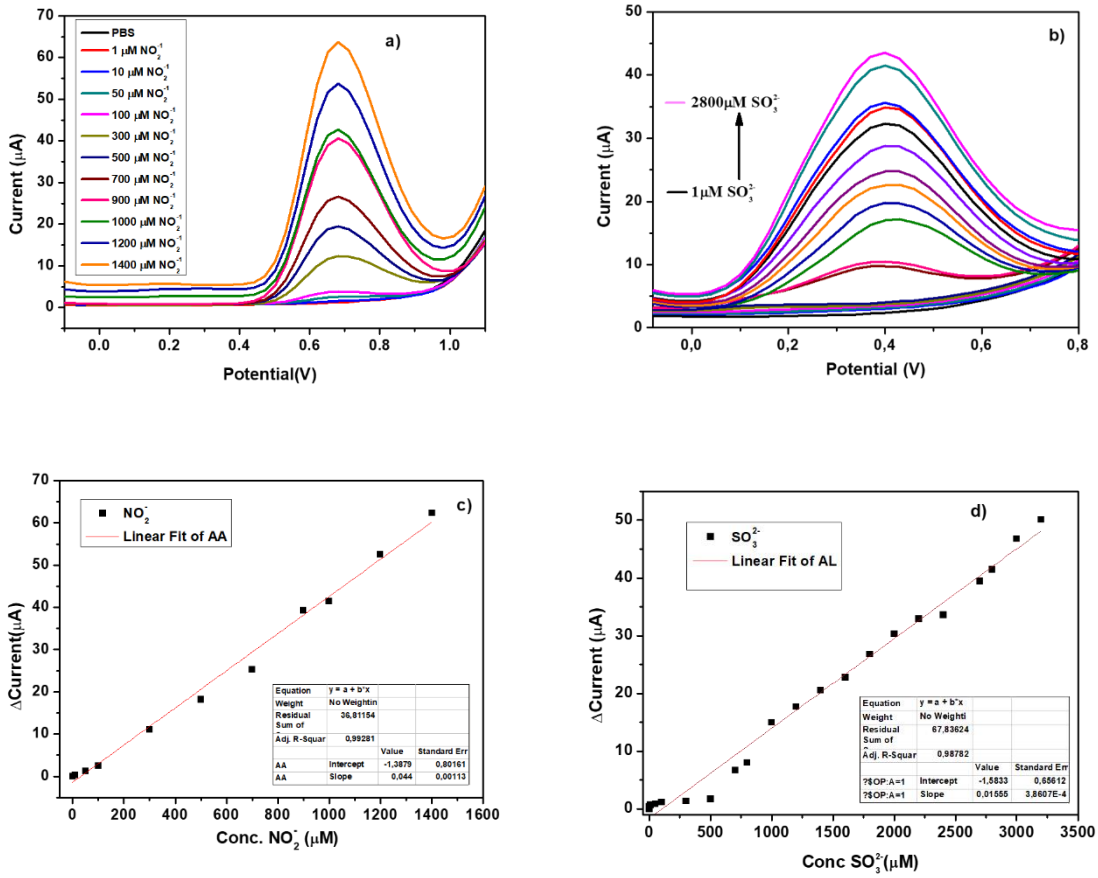

Figure 3.3.14. a) DPV at different nitrite ions concentrations from 0 to 1400 µM in 0.01 M PBS (pH 7.4). **b)** DPV at different sulphite ions concentrations from 0 to 3200 µM in 0.01 M PBS. **c)** Plot of the anodic peak current (Ipa) vs concentration nitrites. **d)** Plot of the anodic peak current (Ipa) vs concentration sulfites

Figure 3.3.15 shows DPV curves of NBC_{180}/SPCE encompassing both 600 µM nitrite and sulfite, added simultaneously. The DPV curve revealed distinct anodic oxidation peaks, each corresponding to its respective target analyte.

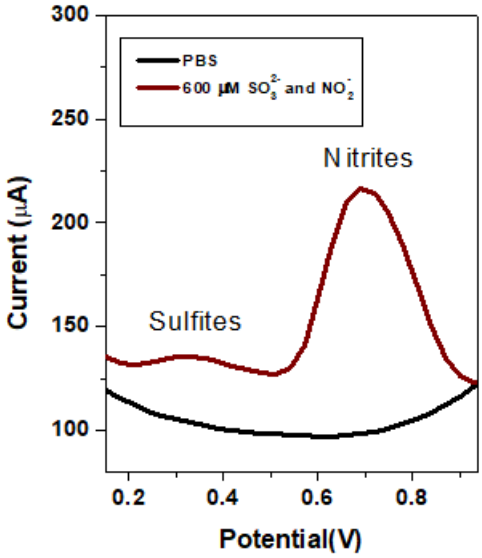

Figure 3.3.15. DPV curve acquired in PBS solution in absence and in co-presence of nitrite and sulfite at the concentration of 600 µM

In **Figure 3.3.16a**, the DPV technique illustrated the NBC_{180}/SPCE sensor's capability to detect sulfite ions in the presence of 200 µM nitrite ions, while **Figure 3.3.16b** showcased the variation in nitrite concentration when exposed to 600 µM sulfite ions. Based on these observations, it is strongly indicated that SO_3^{2-} and NO_2^- do not mutually interfere when simultaneously present during tests. Consequently, the prepared modified electrode enables the simultaneous determination of both sulfites and nitrites.

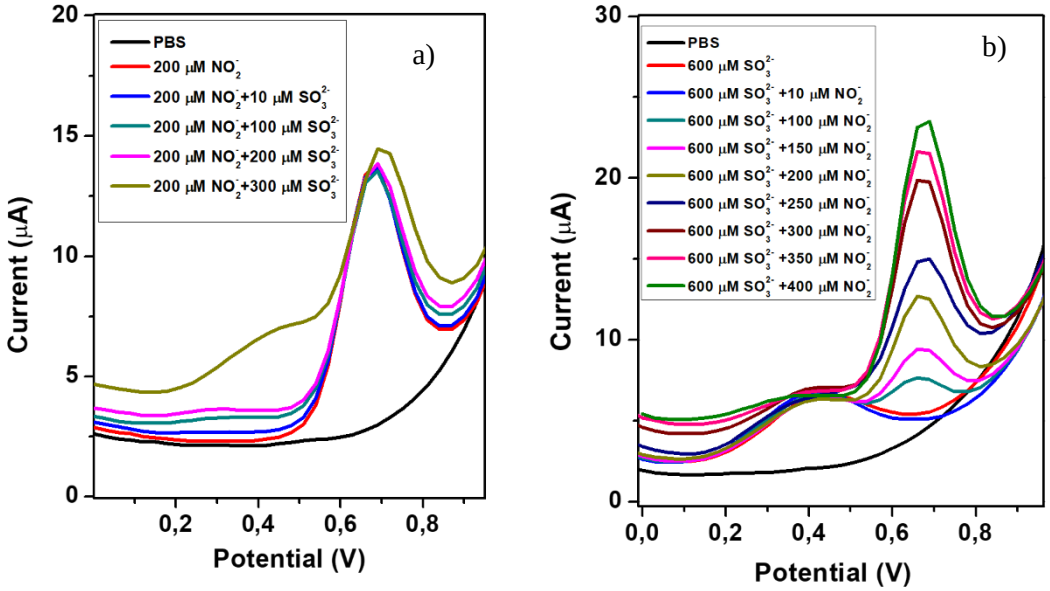

Figure 3.3.16. a) DPV curves acquired in solutions with co-presence of 200 μM nitrite and sulfite in a concentration up to 300 μM. **b)** DPV curves acquired in solutions with co-presence of 600 μM sulfite and nitrite in a concentration up to 400 μM

Assessment of Sensor Repeatability and Stability

To evaluate the repeatability and stability of the NBC_{180}/SPCE sensor, experiments were conducted in solutions containing 200 μM nitrites and 600 μM sulfites. By conducting four repeated tests in the presence of these analytes, the standard deviation was calculated, resulting in 1.02% for nitrites and 3.36% for sulfites. The sensor's stability study was carried out at 7 day intervals, revealing a 6.13% variation in nitrite detection and a 9.18% variation in sulfite detection after a week of sensor use. Therefore, the NBC_{180}/SPCE sensor demonstrates worthy repeatability and stability.

Analysis of Nitrite and Sulfite in Real Samples

The analysis of nitrite and sulfite in real samples was conducted in mineral water and wine, respectively. The certified analysis of the mineral water developed indicated an absence of nitrite. Therefore, the analysis was performed using the standard addition method within the range of 10–50 µM nitrite (**Figure 3.3.17**). The results resumed in **Table 3.3.1** demonstrate the sensor's effective ability to detect nitrite in mineral water samples, with a recovery rate ranging from 94% to 102%.

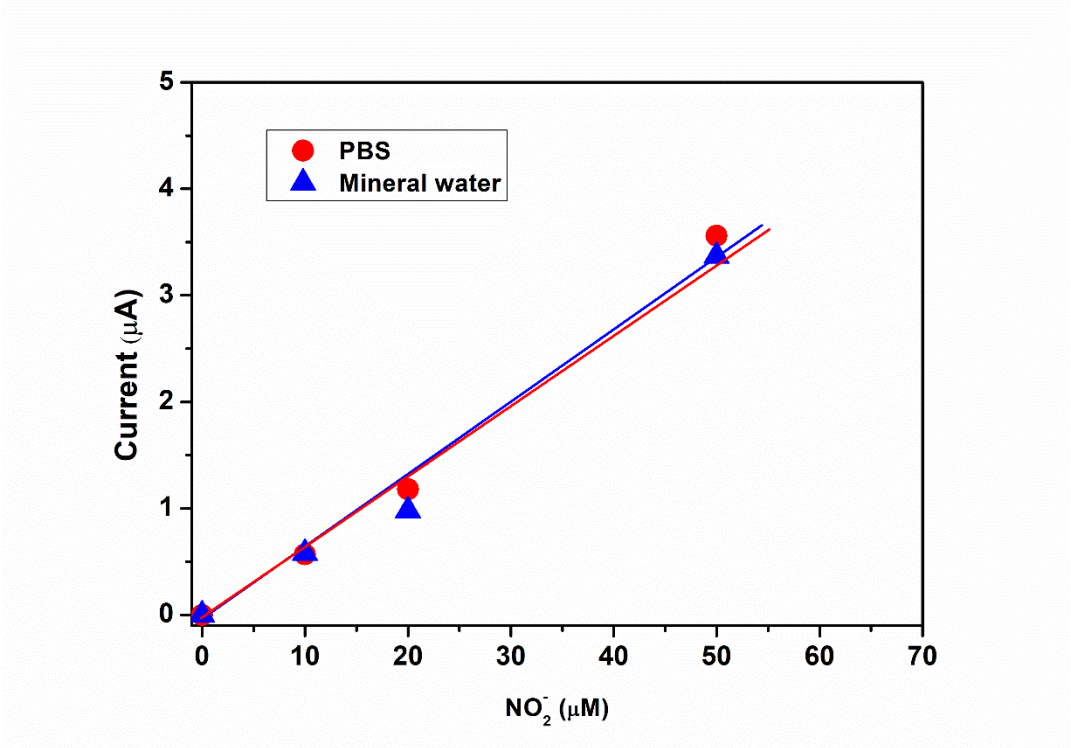

Figure 3.3.17. Plot of the anodic peak current (Ipa) vs. concentration for determination nitrite mixtures in water samples

Table 3.3.1. Determination of nitrite mixtures in water samples

Samples	Analytes	Added (µM)	(µA) Current	Recovery (%)
		10	0,57	-
		20	0,91	-
PBS	Nitrite	50	3,56	-
		10	0,58	101,7

		20	0,78	85,71
Mineral water	Nitrite	50	3,37	94,66

The determination of sulfites was performed in white wine, and the results can be observed in **Figure 3.3.18a**. According to current regulations permits the presence of sulfites in wine is acceptable at a maximum concentration of 200 mg/L. To perform these measurements, the DPV technique was employed, involving the dilution of white wine in a 0.01 M PBS solution (at 1:40 v/v ratio). The data resulting from the addition of sulfites within the range of 0 to 500 µM were plotted and are depicted in **Figure 3.3.18b,** demonstrating a linear correlation with sulfite additions. The measured concentration of sulfites in the analyzed wine was determined to be 178.6 mg/L, which falls below the maximum allowable limit established by current regulations.

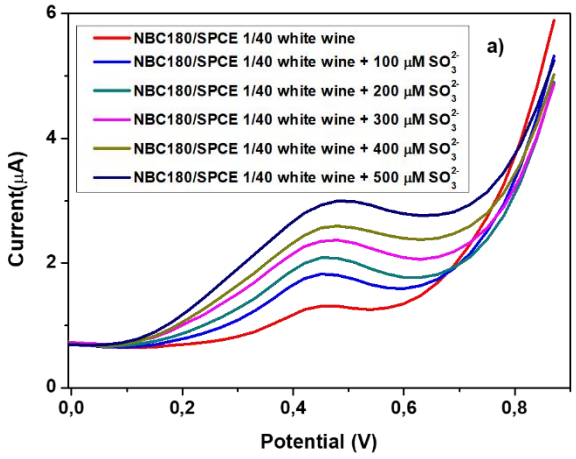

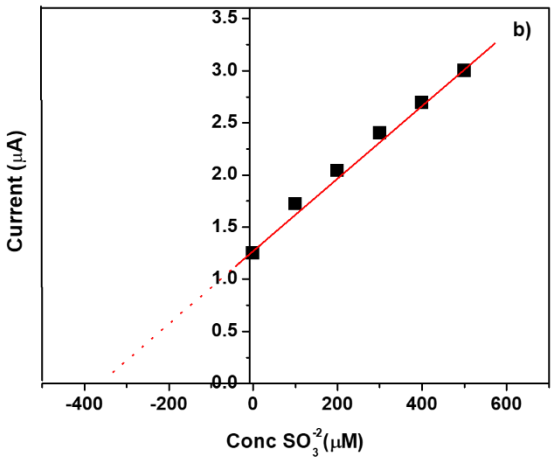

Figure 3.3.18. a) DPV of a real sample of commercial white wine by sulfite additions from 0 to 500 mM. **b)** Plot of the anodic peak current (Ipa) vs concentration for determination of sulfite in wine sample.

Conclusions

An electrochemical sensor based on nanobiochar derived from biomass waste was developed. Several instrumental techniques were employed to verify the morphological and microstructural properties of nanobiochar. The NBC-modified electrode displayed superior electrochemical and electroanalytical properties in the determination of nitrite and sulfite ions compared to the unmodified SPCE electrode. Furthermore, the modified sensor offers several practical advantages, including a simple preparation process, cost-effectiveness, and excellent stability, repeatability, reproducibility, and stability.

References

Chausali, N.; Saxena, J.; Prasad, R. Nanobiochar and biochar based nanocomposites: Advances and applications. *Journal of Agriculture and Food Research*, **2021**, 5, 100191. https://doi.org/10.1016/j.jafr.2021.100191

Espro, C.; Satira, A.; Mauriello, F.; Anajafi, Z.; Moulaee, K.; Iannazzo, D.; Neri, G. Orange Peels-Derived Hydrochar for Chemical Sensing Applications. *Sensors and Actuators B: Chemical*, **2021**, 341, 130016. https://doi.org/10.1016/j.snb.2021.130016

Iannazzo, D.; Celesti, C.; Espro, C.; Ferlazzo, A.; Giofrè, S.V.; Scuderi, M.; Scalese, S.; Gabriele, B.; Mancuso, R.; Ziccarelli, I.; Visalli, G.; Di Pietro, A. Orange-Peel-Derived Nanobiochar for Targeted Cancer Therapy. *Pharmaceutics*, **2022**, 14, 2249. https://doi.org/10.3390/pharmaceutics14102249

Ishizaki, T.; Chiba, S.; Kaneko, Y.; Panomsuwan, G. Electrocatalytic activity for the oxygen reduction reaction of oxygen-containing nanocarbon synthesized by solution plasma. *Journal of Material Chemistry A*, **2014**, 2, 10589–10598. https://doi.org/10.1039/C4TA01577K

Mewada, A.; Pandey, S.; Shinde, S.; Mishra, N.; Oza, G.; Thakur, M.; Sharon, M.; Sharon, M. Green synthesis of biocompatible carbon dots using aqueous extract of Trapa bispinosa peel. *Materials Science and Engineering: C Materials for Biological Applications*, **2013**, 33, 2914–2917. https://doi.org/10.1016/j.msec.2013.03.018

Niranjana, E.; Swamy, K.; Raghavendra Naik, B.E.; Sherigara, R.; Jayadevappa, B.S. H. Electrochemical investigations of potassium ferricyanide and dopamine by sodium dodecyl sulphate modified carbon paste electrode: A cyclic voltammetric study. *Journal of Electroanalytical Chemistry*, **2009**, 631, 1–9. https://doi.org/10.1016/j.jelechem.2009.02.011

Qi, W.; Liu, W.; Zhang, B.; Gu, X.; Guo, X.; Su, D. Oxidative Dehydrogenation on Nanocarbon: Identification and Quantification of Active Sites by Chemical Titration. *Angewandte Chemie International Edition*, **2013**, 52, 14224–14228. https://doi.org/10.1002/anie.201306825

Ramanayaka, S.; Vithanage, M.; Alessi, D.S.; Liu, W.-J.; Jayasundera, A.C.A.; Ok, Y.S. Nanobiochar: production, properties, and multifunctional applications. *Environmental Science: Nano*, **2020**, 7, 3279–3302. https://doi.org/10.1039/D0EN00486C

Satira, A.; Paone, E.; Bressi, V.; Iannazzo, D.; Marra, F.; Calabrò, P.S.; Mauriello, F.; Espro, C. Hydrothermal Carbonization as Sustainable Process for the Complete Upgrading of Orange Peel Waste into Value-Added Chemicals and Bio-Carbon Materials. *Applied Sciences*, **2021**, 11, 10983. https://doi.org/10.3390/app112210983

Zheludkevich, M.L.; Serra, R.; Montemor, M.F.; Ferreira, M.G.S. Oxide nanoparticle reservoirs for storage and prolonged release of the corrosion inhibitors. *Electrochemistry Communications*, **2005**, 7, 836–840. https://doi.org/10.1016/j.elecom.2005.04.039

3.4 On the Electroanalytical Detection of Zn Ions by a Novel Schiff Base Ligand-SPCE Sensor

*Published: Sensors, **2022***

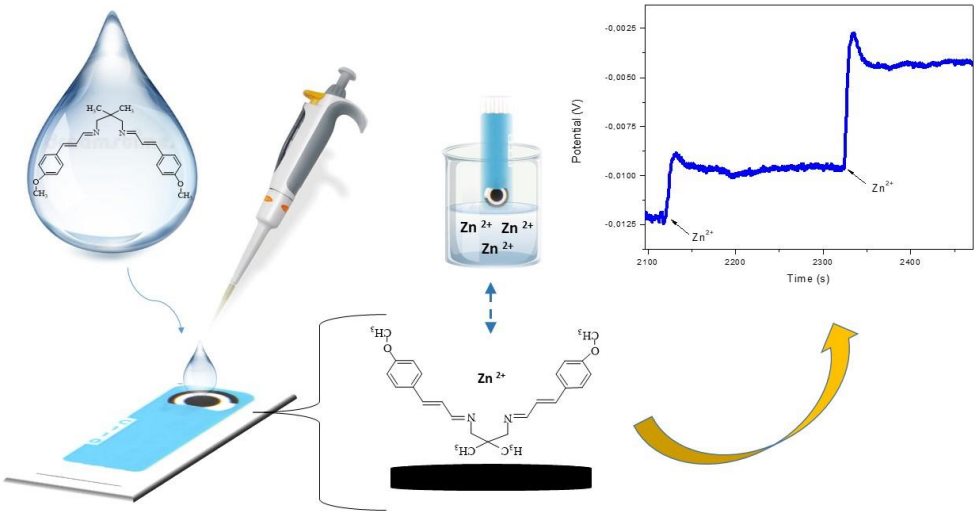

A novel bidentate Schiff base (L2) is proposed for the detection of Zn ions in water. The structure of the synthesized L2 Schiff base was characterized by FT-IR, ^{1}H NMR, and ^{13}C NMR. Optical characteristics were addressed by UV-Visible spectroscopy and Photoluminescence (PL) measurements. PL demonstrated that L displays a "turn-off" type fluorescence quenching in the presence of Zn^{2+} ion in an aqueous solution, indicating its ability to coordinate preferentially with this ion. Based on these findings, an L-M (where M is a suitable membrane) modified screen-printed carbon electrode (SPCE) has been developed to evaluate the electrochemical behavior of the L2 Schiff base with the final objective to perform the electroanalytical determination of Zn ions in water. By using various electrochemical techniques, the modified L-M/SPCE sensor demonstrated high sensitivity and selectivity to Zn ions over some common interferents ions, such as Ca^{2+}, Mg^{2+}, K^{+}, Ni^{2+}, and Cd^{2+}. The

potentiometric response of the L2-M/SPCE sensor to Zn ions was found to be linear over a relatively wide concentration range from 1 μM to 100 mM.

Experimental

Synthesis of bidentate Schiff base ligand (L2)

The Schiff base L2 (whose chemical name is: N1, N3-bis((E)-3-(4-methoxyphenyl)allylidene)-2,2-dimethylpropane-1,3-diamine) was synthesized under ultrasonic irradiation as follows. An ethanolic solution of 2,2-dimethylpropane-1,3-diamine (1 mmol in 10 mL) was drop wisely added to an ethanolic solution of (E)-3-(4-methoxyphenyl) acrylaldehyde (2 mmol in 10 mL). The reaction progress was monitored by TLC. After completion of the condensation reaction (30 min), the product was obtained as a milky precipitate. After evaporation of solvent, the ligand was obtained. Yield: 49%. m.p: 149–151 °C. UV–Vis in DMF [λ_{max}; nm (λ; $cm^{-1}M^{-1}$)]: 318(99164), 380(70958). Molar conductivities in DMF [Λ°M; $cm^2\ \Omega^{-1}\ mol^{-1}$]: 1.12. Selected FT-IR data (KBr, cm^{-1}): 3058 (ν C–H aromatic), 3014 (ν C–H alkenic), 2965 (ν C–H aliphatic), 2868 (ν C–H iminic), 1632 (ν C=N), 1462 (ν C=C), 1171 (ν C-N). ^{1}H NMR (DMSO-d6): [δ; ppm]: 8.02(s, 2Hc,c′, J=8.7 Hz), 7.57(d, 4Hf,f′, J=8.87 Hz), 7.03(d, 2He,e′, J=16.0 Hz), 6.97(d, 4Hg,g′, J=8.8 Hz), 6.85(dd, 2Hd,d′, J1=16.0 Hz and, J2=8.7 Hz), 3.80(s,6Hh,h'), 3.35(s, 4Hb,b'), 0.92(s, 6Ha,a') ppm. ^{13}C NMR (DMSO-d6): 163.57 (C4,4′), 160.48 (C10,10′), 141.46 (C6,6′), 129.26 (C8,8′),128.79 (C7,7′), 126.42 (C9,9′), 114.76 (C5,5′), 70.40 (C3,3′), 55.69 (C11,11′), 37.00 (C1,1′), 24.79 (C2,2′) ppm.

Electrochemical tests

Cyclic voltammetry (CV) and potentiometric measurements were performed using DropSens μStat 400 Potentiostat empowered by Dropview 8400 software for data acquisition. As already reported in section 2.3, bare screen-printed carbon electrodes (SPCEs) were easily modified as follows: 1.0 mg of L2 was ultrasonically dissolved in 0.5 mL of DMSO. Thereafter, 2 μL of the solution was directly dropped onto the surface of the carbon working electrode and was allowed to dry at room temperature until further use. Moreover, a L2-M/SPCE sensor was obtained by mixing the Shiff base ligand with a conductive membrane (M). The membrane was prepared by mixing: 0,5mg of sodium tetraphenylborate (NaTBP), 33mg of polyviniylchloride (PVC), 65,71mg of 2-nitrophenyloctylether (2-NPOE) and 1 mg of L2. The components were dissolved in 1.0 mL of THF and 2 μL of the mixture was deposited on the sensor. The solvent was allowed to dry overnight at room temperature to give a transparent membrane. Linear sweep voltammetry (LSV) and potentiometric calibration curves at SPCE were performed by adding small volumes of the metal ions stock standard solutions into the electrochemical cell containing 3 mL of distilled water. Three scans are made for each new unit in a buffer solution before taking reliable measurements to equilibrate the SPCEs. To ensure the elimination of the metal ions from the working SPCE surface, a conditioning potential of 1.3 V for 30 s was applied before each measurement. All experiments were carried out without any oxygen elimination and at room temperature (25 °C).

Results and Discussion

Characterization of Schiff base ligand

A schematic representation of L2 is shown in **Figure 3.4.1**. Data related to FT-IR, NMR, UV-Vis spectra, and molar conductivities of Schiff base ligand L2 have been described in the previous paragraph.

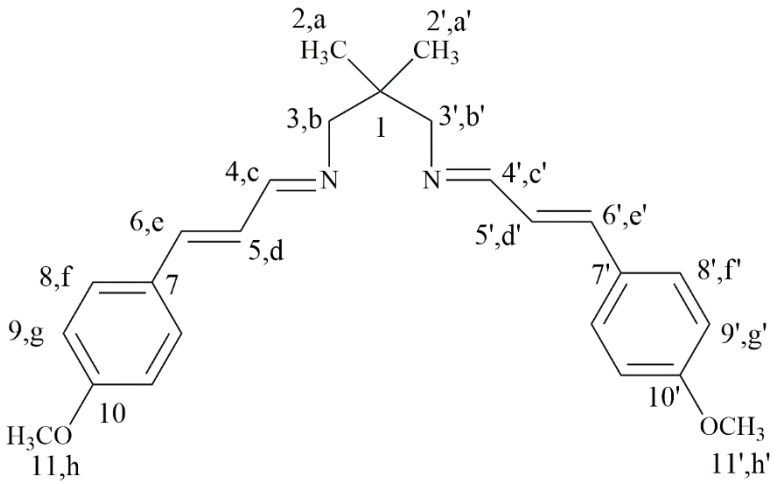

Figure 3.4.1. Atom numbering representation of Schiff base ligand L2

FT-IR spectroscopy is the first and easiest step to identify novel synthetic compounds via functional groups. **Figure 3.4.2** shows the IR spectrum of the Schiff base ligand. Compared to the expected bands related to reactants, the lack of stretching vibrations of NH_2 of primary amine at 3285 cm^{-1} and C=O of 4-methoxycinnamaldehade at 1685 cm^{-1} as initial reactants and on the other hand appearance of a new sharp and strong peak at 1632 cm^{-1} indicating formation of azomethine or aminic (C=N) bond as characteristic functional agent of the Schiff base compounds well support that the titled Schiff base ligand has been successfully synthesized. Moreover, the weak vibrations at 3058 and 2965 cm^{-1} are assigned to the stretching vibrations of C-H bonds of aromatic and aliphatic, respectively. Further bands between 2900 cm^{-1} and 2800 cm^{-1} are associated with stretching vibrations of the aliphatic C–H groups, whereas C-H bending of the methyl group is associated with the peak at 1400 cm^{-1}. At last, the strong band at 1275-1200 cm^{-1} is due to the C-O stretching of aryl ether.

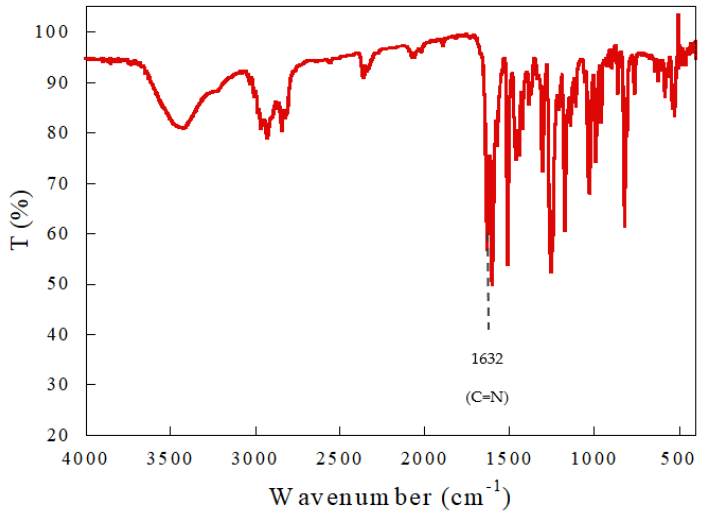

Figure 3.4.2. FT-IR spectra of ligand L2

^{1}H NMR and ^{13}C NMR of L2 based on **Figure 3.4.1** is exhibited in **Figure 3.4.3**. In ^{1}H NMR spectrum of ligand, azomethine hydrogens of cc' are observed at 8.02 ppm as a doublet signal with a coupling constant of 8.7 Hz. Olefinic hydrogens of ee' and dd' in the ligand spectrum appear at 7.03 ppm and 6.85 as doublet and doublet of doublet, respectively. Aromatic hydrogens of gg' and ff' in the ligand spectrum are seen at 6.97 and 7.57 ppm as doublet peaks. Aliphatic hydrogens of aa', bb' and hh' in ligand appear at 0.92, 3.35 and 3.80 ppm as singlet peaks, respectively. In ^{13}C NMR spectrum of ligand, the characteristic signal related to azomethine carbon appeared at 163.57 ppm. Aromatic, olefinic, and aliphatic carbons of ligand L2 appear at 126.42-160.48, 114.76-141.46 and 24.79-70.40 ppm, respectively.

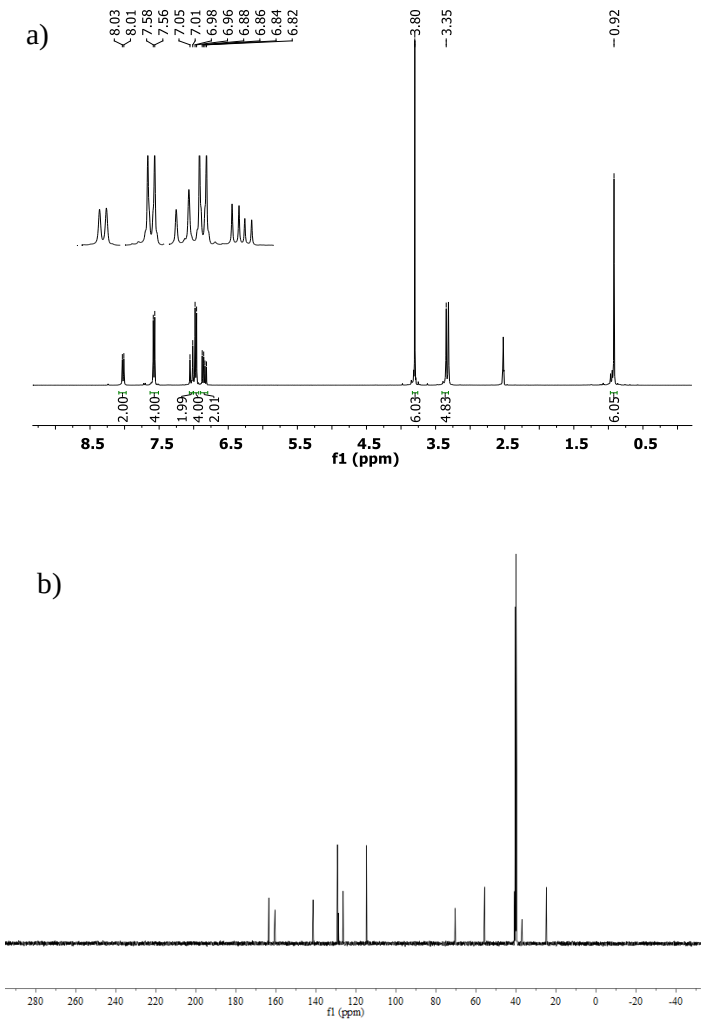

Figure 3.4.3.a) ^{1}H NMR spectra of ligand (L2), and **b)** ^{13}C NMR spectra of L2

The electronic spectrum of L2 in the DMF solution (10^{-5} M) was recorded in the range of 200–800 nm at room temperature and the relevant information is found in **Figure 3.4.4** In the UV–visible spectrum of the ligand, two intense absorption bands were observed. The first band that appeared at 318 nm is attributed to π→π* electronic transitions of ligands (aromatic rings and alkene moiety). The second absorption band of ligand at 380 nm may attributed to n →π*/ π→π* of imine groups.

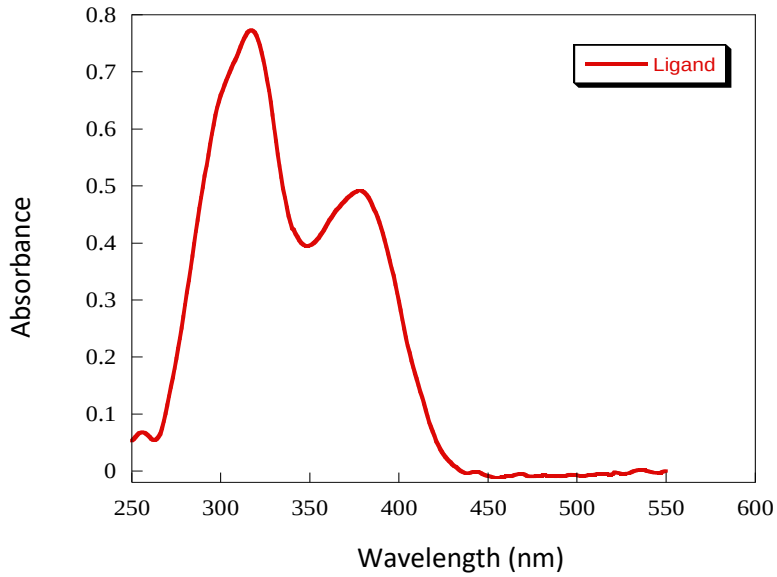

Figure 3.4.4. UV-Vis spectrum of the Schiff base ligand L2

Fluorescence studies

Schiff bases are known to exhibit fluorescence characteristics in both solution and solid state. The fluorescence from L2 in the visible region (see **Figure 3.4.5a**) can be explained due to the presence of the extended conjugation. At the excitation length of 340 nm, the base shows a fluorescent emission behavior with a well-defined band at 435 nm.

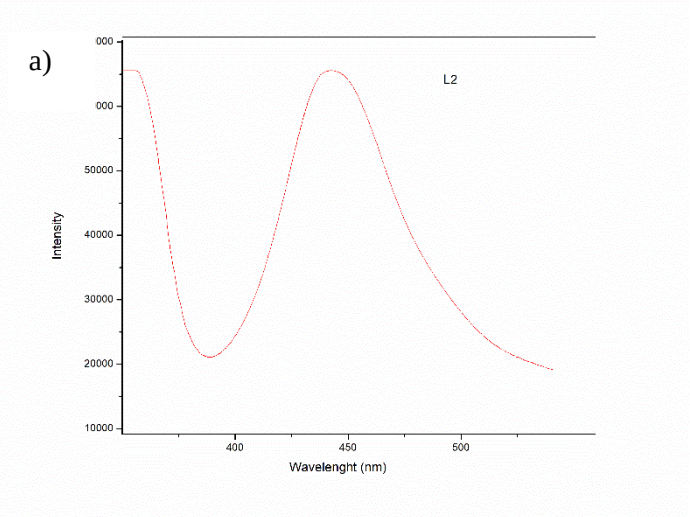

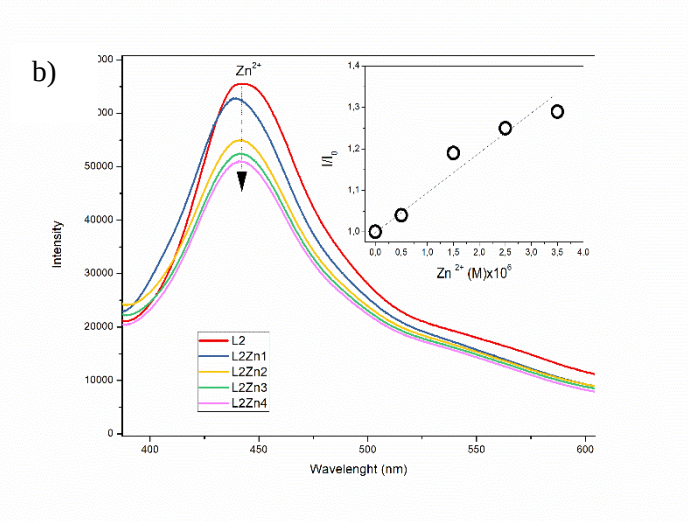

Figure 3.4.5. a) Photoluminescence emission peak of the Shiff base ligand L2; **b)** variation of the photoluminescence peak at the addition of different Zn ions concentrations from 0 to $3.5x10^{-5}$ M. Inset shows the fluorescence quenching Stern-Volmer plot of with increasing concentration of Zn ions

Schiff bases display versatile coordination chemistry with transition metal ions due to the preferred coordinative interaction with the imine –N and –OH groups. Therefore, in recent years, Schiff bases have been investigated for the detection of various toxic metal ions (Faridbod *et al.*, n.d.; Saleh *et al.*, 2017). In dependence of the ligands and the metal ion, fluorescence tuning both in intensity and/or emission maximum can be observed. A fluorescence enhancement (Lee *et al.*, 2012) or fluorescence reduction (fluorescence quenching (Deems *et al.*, 2020)) can occur upon metal ion coordination. Investigating the fluorescence properties of L2, we found that the addition of Zn ions caused remarkable changes in the intensity of the fluorescence peak (**Figure 3.4.5b**). The interaction between the Zn ion and the L2 Schiff base compound is likely assumed to transfer energy from L2 to Zn(II) and hinder the ligand-centered emission, thus resulting in the luminescent quenching of L2 (Yu *et al.*, 2020). The inset in the figure shows the analysis of data on the basis of the Stern–Volmer I/Io = 1 + Ksv[Zn^{2+}] equation, where I and I0 are the fluorescence intensities of the L2 solution in the presence and absence of Zn

ions, Ksv is the Stern-Volmer constant, and [Zn^{2+}] is the concentration of the Zn ions (quencher). The Ksv value calculated was in the order of 10^4-10^5 M^{-1}, suggesting that there is a significant interaction of Zn ions with L, which leads to the quenching of the fluorescence intensity, and the quenching pattern observed was likely due to the formation of a non-fluorescent Zn-L2 coordination complex (see **Scheme 3.4.1**).

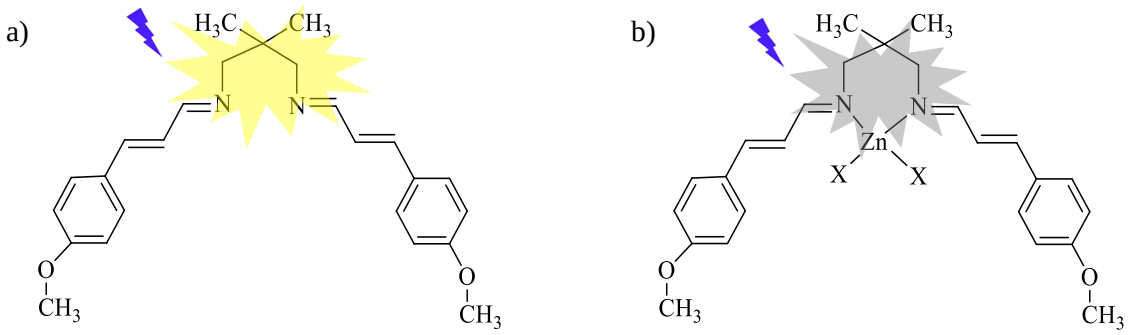

Scheme 3.4.1. Schematization of the fluorescent emission behavior for: **a)** ligand L2; **b)** Zn-Ligand coordination complex. Wavelength excitation is 340 nm.

Electrochemical studies

Based on the promising coordination ability for Zn ions, the ligand was used to modify a commercial screen printed electrode for developing a simple electrochemical device for the possible electroanalytical determination of these ions. Preliminarly, the electrochemical properties related to the sensors fabricated were evaluated by cyclic voltammetry (CV). CV measurements were recorded in 1.0 mM phosphate buffered saline (PBS) solution at pH 7.4 as an electrolyte and in the presence of the ferro/ferrocyanide $Fe(CN)_6^{3-/4-}$ redox couple. Cyclic voltammograms were recorded in 10 mM $Fe(CN)_6^{3-/4-}$ solution at a scan rate of 50 mV s^{-1}. For all the bare SPCE and modified SPCEs, a pair

of distinct, well-defined redox couple peaks were observed between −0.3 V and +1 V (**Figure 3.4.6**).

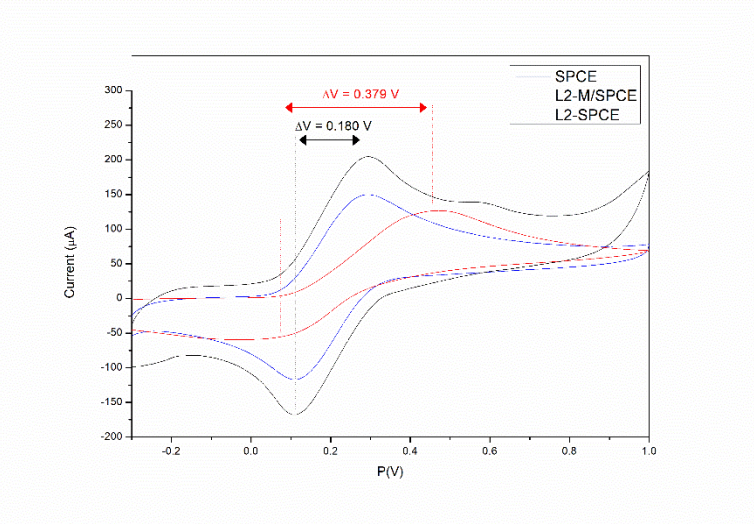

Figure 3.4.6. CV measurements of SPCE, L2-SPCE and L2-M/SPCE in PBS solution; CV of 10 mM $(Fe(CN)_6^{3-/4-})$ solution at a scan rate of 50 mVs^{-1}

On the bare SPCE a pair of redox peaks with the peak-to-peak separation (ΔEp) of 0.180 V was observed. On the L2/SPCE redox peaks are largely suppressed, likely due to the insulating layer formed after the Schiff base deposition on the working layer. Further, the (ΔEp) extended to 0.379 V which is due to the presence of L2 which limits the diffusion process. On the L2-M/SPCE a higher peak current than on both SPCE and L2/SPCE was observed. The presence of the membrane restores the electrochemical properties of the L2-M based electrode which could be ascribed to the high ionic conductivity of the M membrane used together the ligand. The effective electrochemical active surface area of the prepared electrode was also determinates from these data based on the Randlese-Sevcik equation. The formula was employed to find out the active surface area of the SPCE and L2-M/SPCE by using the ferro/ferrocyanide as the redox probe:

$$Ip = \pm 0{,}4463nFAC\sqrt{\frac{nFvD}{RT}}$$

where, Ip is the voltammetric current (A) using the forward peak of the electrochemical process, n=1 is the number of electrons transferred in the electrochemical reaction, F= 96485,3365 C/mol is the Faraday constant, A is the electrode surface area (cm^2), C=10-5 M/cm3 is the concentration of the redox probe, v= 0,05 V/s is the applied voltammetric scan rate, D=7.6 × 10^{-6} cm^2/s is the analytic diffusion coefficient, R=8,314 J/mol is the universal gas constant and T=298,15 K is the Kelvin temperature. We found an increase in the effective electrochemical active surface area from SPCE to L-M/SPCE of about 16 %. Further investigation of the electron transfer properties at the bare and modified electrodes was performed using electrochemical impedance spectroscopy (EIS). Here, the changes in the impedance and interface properties during the electrode surface modification procedure were measured and are shown in **Figure 3.4.7**.

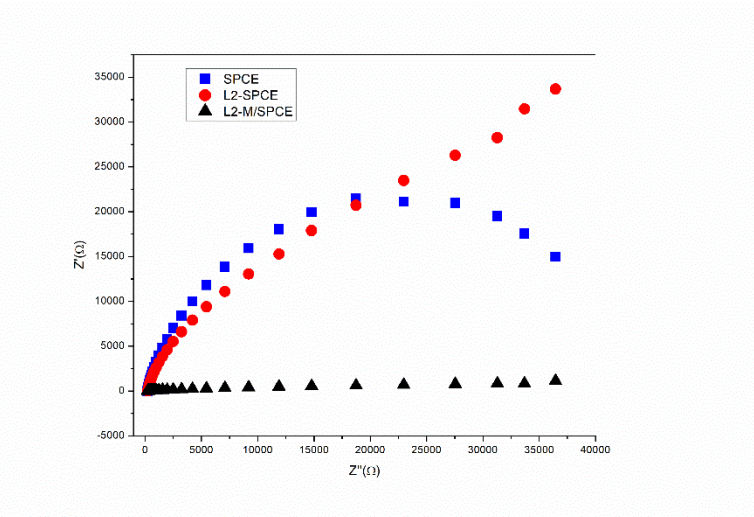

Figure 3.4.7. EIS of the fabricated sensors in 10 mM ($Fe(CN)_6^{3-/4-}$) solution

EIS experiments were carried out in a 10 mM $Fe(CN)_6^{3-/4-}$ solution over the 0.1–100000 Hz range. Impedance spectra typically consist of semi-circular and

linear regions representing electron transfer and diffusion processes, respectively. Electron transfer processes occur at higher frequencies, while diffusion processes occur at lower frequencies. The reported results highlight that the L2-M layer causes a notable decrease in the impedance concerning bare SPCE and L2/SPCE, thus confirming the beneficial role of the ionic membrane in cooperation with the Schiff base ligand. These enhanced electrochemical properties encouraged us to investigate the developed L2-M/SPCE as a sensor for the analytical determination of metal ions, particularly Zn (II).

Electroanalytical applications

Several voltammetric methods can be applied for the analytical application of the fabricated electrochemical sensors (Lu *et al.*, 2018). To investigate the capabilities of bare and modified SPCE fabricated electrodes, in the detection of Zn ions in distilled water, the LSV method was first applied. The curves in the graph in **Figure 3.5.8a**, report the current of the L2-M/SPCE sensor subjected at an increasing potential from 0.25 to 0.90 V in the presence of different concentrations of Zn ions in solution. The registered current increase with the applied potential and concentrations of Zn ions. Plotting the current registered at the potential of 1.2 V, we observe a good linearity vs. zinc ions concentration in the range of 10^{-3} - 1 M (**Figure 3.5.8b**This figures also reports the data collected in the same conditions for the bare SPCE, M/SPCE and L2/SPCE sensors. A different response of the sensor investigated to Zn^{2+} is noted. The response of L2-M/SPCE sensor resulted in higher compared to other sensors tested.

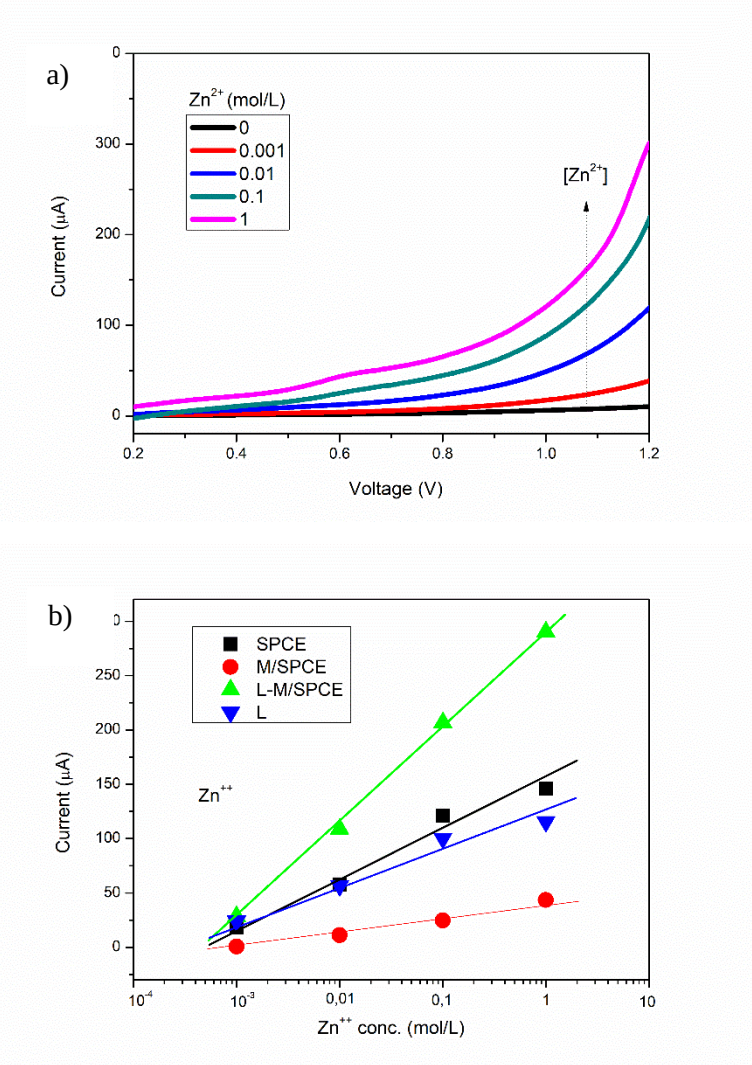

Figure 3.5.8. a) I-V tests carried out on L2-M modified SPCE in the presence of different concentrations of zinc ion. **b)** Current registered at 1.2 V vs. concentration of Zn ions in solution for the various fabricated sensors

Results from LSV method demonstrate that the modification of the bare SPCE electrode with the combination of L2 as ionophore and M as ionic membrane contributes to the improved electrochemical detection of zinc ions compared to bare SPCE. As a support for this, we present in **Figure 3.4.9** data obtained with K ions. This ion was chosen because it is not coordinated at the modified L2-M/SPCE electrode. We can observe on bare SPCE and L2-M-SPCE sensor a different response in solutions containing K ions compared to behavior reported

in **Figure 3.4.8** in the presence of Zn ions, confirming that the characteristics of L2-M/SPCE sensor are linked to the coordination ability towards Zn ions.

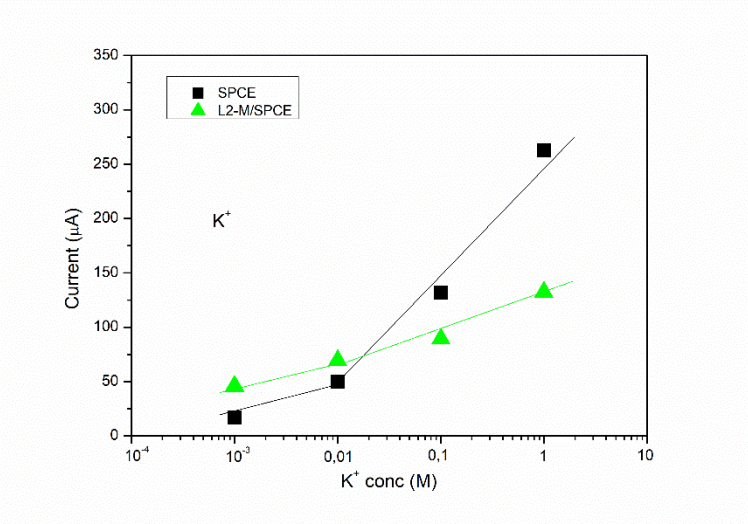

Figure 3.5.9. Current registered on bare SPCE and L2-M/SPCE sensors at 1.2 V vs concentration of K ions in solution

Potentiometry is another of the most commonly developed electrochemical methods, based on the measurement of a potential difference when the target ionic species in an aqueous phase complex with target selective ionophores present in an organic membrane (Abd El-Rahman *et al.*, 2021). Potentiometric sensing can be an attractive alternative to the existing electrochemical analytical tools due to its simplicity and fast responses (Dehabadi *et al.*, 2021). **Figure 3.4.9** shows the selective response of the bare SPCE and L2-M/SPCE sensors to zinc ion addition. It can be observed that the response of the modified electrode is highly amplified with respect to the bare electrode with a sensitivity of 50.1 mV/dec. The dynamic response time of the L2-M/SPCE sensor was also evaluated. Inset in **Figure 3.4.10** shows the potential variation of the sensor to step change in the concentration of Zn^{2+} ion. A fast response was noted; indeed, the time required for the Zn^{2+} sensor to reach the new potential value was evaluated in about 10 s.

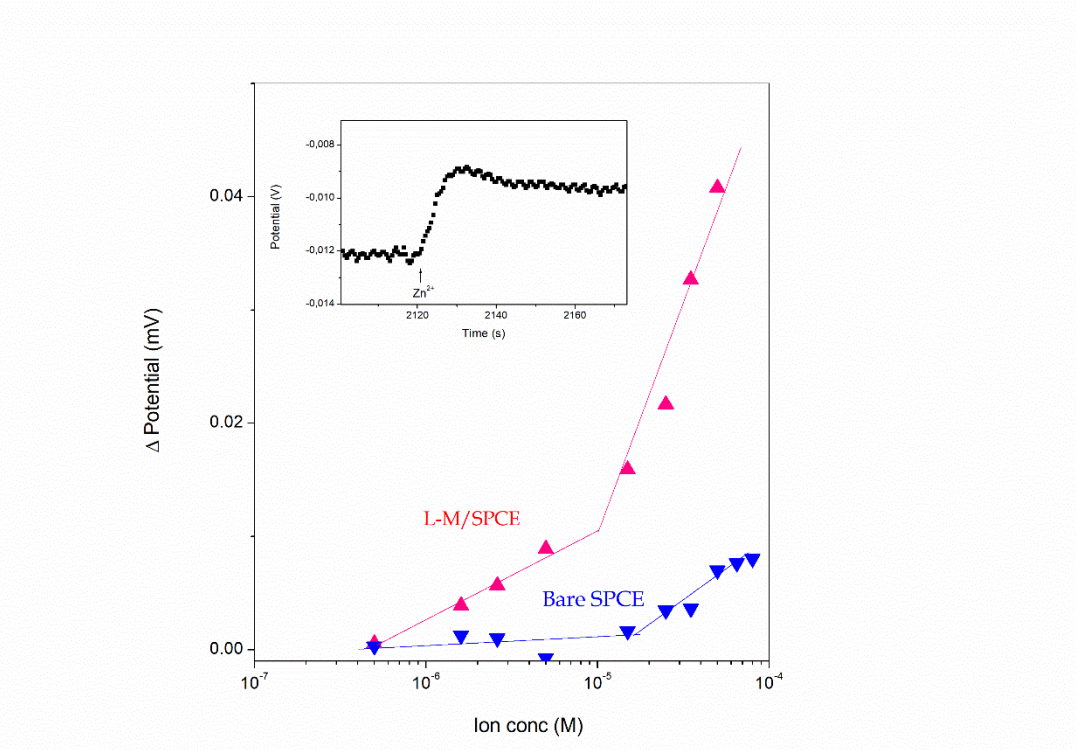

Figure 3.4.10. Calibration curves for the bare SPCE and L2-M/SPCE sensor to different concentrations of Zn ions. Dynamic response time of the L2-M/SPCE sensor for a step change in the concentration of Zn^{2+} ion

Aqueous solutions of both monovalent and divalent cations were also added, measuring the potential changes for each addition, for evaluating the selectivity of the sensor. The concentration was kept the same for all cations (5.5×10^{-5} mol/L) and the additions made directly into the solution kept under mechanical stirring. According to the potentiometric results, the sensitivity towards Zn ions of the proposed sensor is much higher compared to other ions, also evidencing its good selectivity (**Figure 3.4.11**). As for the LSV method, the high selectivity registered with the potentiometric method is due to the higher affinity of the L2-M/SPCE sensor for Zn against the other metal ions.

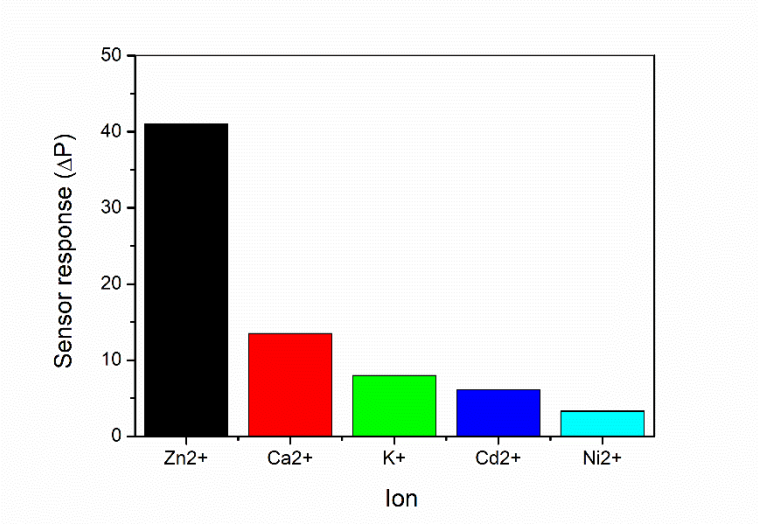

Figure 3.4.11. Response of the L2-M/SPCE sensor to different ions. The concentration of the ions is equal to 5.5×10^{-5} mol/L

To explain the observed behavior, we believe the sensor response is generated by: i) the electric double layer at the interface between the solution and ii) the L2-M membrane and the ion transfer from the solution to the L2-M membrane. In other words, the observed response results from the combined effects of the ionic conductivity of the ion solution and the resistance at the electrode/ion solution interface. At a specific concentration of Zn^{2+}, the first contribution is constant, so the electrode/ion solution interface resistance is the dominant factor, and this agrees with the different EIS spectra obtained on the various electrodes. However, the higher response of the L2-M/SPCE potentiometric sensor can be explained by the preferential adsorption of Zn^{2+} onto the electrode surface. Indeed, as demonstrated by the photoluminescence study, nitrogen as donor atoms in the ligand acts as a strong coordination site for binding zinc, enhancing the electrochemical properties of the L2-M/SPCE membrane towards the zinc ion. **Table 3.4.1** compares the Zn^{2+} sensing performances of our electrochemical sensor with others reported in the literature. As is well known, electrochemical techniques based mainly on stripping voltammetry (ASV) methods have been widely reported in the scientific literature for Zn ion detection because of their high sensitivity (de Oliveira *et al.*, 2004; Israel *et al.*,

1978). These electrochemical sensors undoubtedly performe highly, some toxic components (especially the mercury-based electrodes) limit their acceptance in wide-scale routine analysis. Therefore, the novel synthesized Schiff base may be a strong competitor, with similar or better electrochemical properties, in contrast to other Schiff bases (see **Table 3.4.1**) proposed, with the advantages deriving by a simple and easy preparation process.

Sensing Material	Linear Range	LOD	Ref.
Ionophore (SMS-3) Schiff base moiety modified SPCE	0.47 to 5.56 µM	0.92 µM	(Rana *et al.*, 2019)
Aminoacid Schiff base modified GCE	10 to 150 µM	-	(Kavitha and Easwaramoorthy, 2020)
3-D printed carbon nanofiber–graphite–polystyrene	12.7 µg/L to 450 µg/L	8.6 µg/L	(Honeychurch *et al.*, 2018)
Screen printed bismuth oxide	75 to 600 mg/L	33 mg/L	(Khairy *et al.*, 2010)
Coumarin-based fluorescent sensor	100 pM to 1 mM	3 µM	(Narakathu *et al.*, 2012)
L-SPCE	1 µM to 100 mM	3.5 µM	This work

Table 3.4.1. Comparison of the Zn^{2+} sensing performances of electrochemical sensors

The issue of selectivity is of particular importance for the practical applicability of these sensors. Most metal ions, particularly Ca^{2+}, are usually present in high concentrations in water samples and can interfere with detecting zinc ions. Very selective modified electrodes with Schiff base such as SMS-3 having high affinity toward Zn ions, have been proposed (Rana *et al.*, 2019). Other Schiff bases have been reported in the literature for developing high performances electrochemical/fluorescent sensors for Zn ions, but the selectivity issue is not addressed (see ref. Kavitha and Easwaramoorthy, 2020; Narakathu *et al.*, 2012). Schiff bases are also fluorescent probes to detect zinc ions (Kaur *et al.*,

2020; Narakathu *et al.*, 2012). This technique displays better performances regarding the selectivity issue, but needs more complicated instruments than the electrochemical one. Instead, the proposed electrochemical sensor for Zn ions is low- cost and simple to use. In case of high concentrations of interferent ions such as Ca^{2+}, a selective preconcentration step, must be applied to overcome this problem (Saçmacı *et al.*, 2012). On the other hand, in determining Zn in foods and pharmaceutical tablets, the preconcentration step is not necessary (Lutka *et al.*, 2004; Wang and Dewald, 1983).

Conclusions

In conclusion, the novel synthesized Schiff base L2 was suitable as a sensing material for detecting Zn ions in water. Photoluminescence studies showed that L2 displays a fluorescence turn-off in the presence of Zn^{2+} due to its high coordination ability for this ion. A simple electrochemical sensor was then fabricated by modification of SPCEs with L2 as a recognition element showing a micromolar detection limit and good linearity with a high sensitivity of ~50.1 mV/dec for sensing Zn^{2+} ions. A fast response time of about 10 s with good selectivity to some common interferent ions was also demonstrated. Further, these sensors are easy to fabricate and are intrinsically safe compared to the traditionally used mercury-based electrodes. Based on the know-how acquired in this first study, our future work will be focused on developing novel probes for heavy metal ions, and the fabrication of electrochemical sensors based on these receptors is in advancement.

References

Abd El-Rahman, M.K.; Mazzone, G.; Mahmoud, A.M.; Sicilia, E.; Shoeib, T. Novel choline selective electrochemical membrane sensor with application in milk powders and infant formulas. *Talanta*, **2021**, 221, 121409. https://doi.org/10.1016/j.talanta.2020.121409

de Oliveira, M.F.; Saczk, A.A.; Okumura, L.L.; Fernandes, A.P.; de Moraes, M.; Stradiotto, N.R. Simultaneous determination of zinc, copper, lead, and cadmium in fuel ethanol by anodic stripping voltammetry using a glassy carbon–mercury-film electrode. *Anal Bioanal Chem*, **2004**, 380, 135–140. https://doi.org/10.1007/s00216-004-2733-8

Deems, J.C.; Reibenspies, J.H.; Lee, H.-S.; Hancock, R.D. Strategies for a fluorescent sensor with receptor and fluorophore designed for the recognition of heavy metal ions. *Inorganica Chimica Acta*, **2020**, 499, 119181. https://doi.org/10.1016/j.ica.2019.119181

Dehabadi, M.; Legin, E.; Legin, A.; Yaghmaei, S.; Nechaev, A.; Babain, V.; Kirsanov, D. Developing potentiometric sensors for scandium. *Sensors and Actuators B: Chemical*, **2021**, 348, 130699. https://doi.org/10.1016/j.snb.2021.130699

Faridbod, F.; Ganjali, M.R.; Dinarvand, R.; Norouzi, P. Ion Recognition: Application of Symmetric and Asymmetric Schiff Bases and Their Complexes for the Fabrication of Cationic and Anionic Membrane Sensors to Determine Ions in Real Samples. *Combinatorial Chemistry & High Throughput Screening*, **2007**, 10, 527–546. https://www.eurekaselect.com/article/4976

Honeychurch, K.C.; Rymansaib, Z.; Iravani, P. Anodic stripping voltammetric determination of zinc at a 3-D printed carbon nanofiber–graphite–polystyrene electrode using a carbon pseudo-reference electrode. *Sensors and Actuators B: Chemical*, **2018**, 267, 476–482. https://doi.org/10.1016/j.snb.2018.04.054

Israel, Y.; Ofir, T.; Rezek, J. Determination of trace impurities in high-purity reagents by mercury thin-film anodic-stripping voltammetry. *Mikrochimica Acta*, **1978**, 69, 151–163. https://doi.org/10.1007/BF01196989

Kaur, P.; Singh, R.; Kaur, V. Dual role of silatranized Schiff base as a fluorimetric probe and a linker to functionalize graphene oxide for the selective detection and adsorption of zinc ions. *Inorganica Chimica Acta*, **2020**, 512, 119859. https://doi.org/10.1016/j.ica.2020.119859

Kavitha, A.; Easwaramoorthy, D. Aminoacid Schiff base Fabricated Glassy carbon Electrode for Efficient Sensing of Zinc, Copper, Mercury ions in Water. IOP Conf. Ser.: *Mater. Sci. Eng.*, **2020**, 988, 012042. https://doi.org/10.1088/1757-899X/988/1/012042

Khairy, M.; Kadara, R.O.; Kampouris, D.K.; Banks, C.E. Disposable Bismuth Oxide Screen Printed Electrodes for the Sensing of Zinc in Seawater. *Electroanalysis*, **2010**, 22, 1455–1459. https://doi.org/10.1002/elan.200900519

Lee, H.; Lee, H.-S.; Reibenspies, J.H.; Hancock, R.D. Mechanism of "Turn-on" Fluorescent Sensors for Mercury(II) in Solution and Its Implications for Ligand Design. *Inorganic Chemistry*, **2012**, 51, 10904–10915. https://doi.org/10.1021/ic301380w

Lu, Y.; Liang, X.; Niyungeko, C.; Zhou, J.; Xu, J.; Tian, G. A review of the identification and detection of heavy metal ions in the environment by voltammetry. *Talanta*, **2018**, 178, 324–338. https://doi.org/10.1016/j.talanta.2017.08.033

Lutka, A.; Kokot, Z.; Powidzka, H. Validation of electrochemical determination of zinc in selected pharmaceutical preparations. *Acta poloniae pharmaceutica*, **2004**, 61(4), 243-7. https://www.ptfarm.pl/pub/File/Acta_Poloniae/2004/4/243.pdf

Narakathu, B.; Abebe, F.; Eribal, C.; Atashbar, M.; Sinn, E. Detection of Zn^{2+} ions using a novel chemosensor based on coumarin Schiff-base derivatives by electrochemical and fluorescence spectroscopy. *Chemistry*, **2012**. https://doi.org/10.5162/IMCS2012/8.2.5

Rana, S.; Mittal, S.K.; Kaur, N.; Banks, C.E. Pseudo Cavity of Schiff Base Ionophore Incorporated in Screen Printed Electrode for Sensing of Zn (II). *Journal of Electrochemical Society*, **2019**, 166, B464. https://doi.org/10.1149/2.1041904jes

Saçmacı, Ş.; Kartal, Ş.; Saçmaci, M. Selective back-extraction and preconcentration of zinc(II) from metal-1,3,5-triketone extracts prior to its determination by flame atomic absorption spectrometry. *International Journal of Environmental Analytical Chemistry*, **2012**, 92, 1626–1637. https://doi.org/10.1080/03067319.2011.581463

Saleh, S.M.; Ali, R.; Ali, I.A.I. A novel, highly sensitive, selective, reversible and turn-on chemi-sensor based on Schiff base for rapid detection of Cu(II). *Spectrochimica Acta Part A: Molecular and Biomolecular Spectroscopy*, **2017**, 183, 225–231. https://doi.org/10.1016/j.saa.2017.04.019

Wang, J.; Dewald, H.D. Determination of Trace Elements in Pharmaceutical Tablets Using Anodic stripping Voltammetry. *Analytical Letters*, **1983**, 16, 925–939. https://doi.org/10.1080/00032718308065230

Yu, Y.; Wang, Y.; Yan, H.; Lu, J.; Liu, H.; Li, Y.; Wang, S.; Li, D.; Dou, J.; Yang, L.; Zhou, Z. Multiresponsive Luminescent Sensitivities of a 3D Cd-CP with Visual Turn-on and Ratiometric Sensing toward Al^{3+} and Cr^{3+} as Well as Turn-off Sensing toward Fe^{3+}. *Inorganic Chemistry*, **2020**, 59, 3828–3837. https://doi.org/10.1021/acs.inorgchem.9b03496

3.5 Hydrochar from Sargassum Muticum: a Sustainable Approach for High-capacity Removal of Rhodamine B dye

Published: RSC Sustainability, ***2023***

This study presented, an environmentally friendly protocol for the recovery of hydrochar by hydrothermal carbonization (HTC) of the macroalga *Sargassum muticum*. HTC conditions such as temperature (180-300 °C) and reaction time (60-300 min) were investigated to study the differences between the obtained samples and find the optimal conditions that maximize the yield of hydrochar. The acquired results demonstrate that the highest hydrochar yield is reached after 180 min at a reaction temperature of 180 °C. The obtained biocarbons were characterized by several techniques (XRD, FTIR, XPS, SEM-EDX, and BET) and their adsorption capability was evaluated in the environmental recovery of water organic pollutants.

Experimental

Synthesis of hydrochar and hydrothermal carbonization (HTC) process

A mixture of defrosted thalli of *Sargassum muticum* (5 g of dry starting material) and deionized water (100 mL) was placed into a 300 mL stainless steel autoclave (series 4540 Parr Instrument Company, IL, USA). The reactor was heated with a rated speed of 10 °C min^{-1} and the operative reaction times were recorded once the set temperature was reached. The process was carried out under stirring, autogenous pressure and a N_2 atmosphere. At the end of the HTC, the reactor was cooled and the solid phase was separated from the liquid by a vacuum filtration setup. The recovered solid was washed several times with distilled water and left to dry for 24 h under vacuum at 100 °C. The obtained hydrochar samples are here named SM-$HC_{T–t}$, with T, the reaction temperatures (180, 240, and 300 °C), and t, the reaction time (60, 180, and 300 min). Subsequently they will be named from SM1 to SM9, to enhance simplicity, with detailed reference to: SM1, SM2, and SM3 the hydrochars obtained after 60 minutes under 180 °C, 240 °C and 300 °C respectively; SM4, SM5, and SM6 the hydrochars obtained after 180 minutes under 180 °C, 240 °C and 300 °C respectively; SM7, SM8, and SM9 the hydrochars obtained after 300 minutes under 180 °C, 240 °C and 300 °C respectively. The yield of the hydrochar was determined using the following formula:

$$mass\ yield\ (wt\%) = \frac{gr\ of\ product}{gr\ of\ initial\ dry\ SM} \times 100 \quad (1)$$

The combined effect of time and temperature on the process can be evaluated by the so-called severity factor ($logR_0$) firstly described by Overend *et al.* (Overend *et al.*, 1997). In this field, numerous studies have been using this metric since it is also related to the distributions, chemical compositions and properties of the starting materials (Ruiz *et al.*, 2021). Therefore, the role of

reaction time and temperatures in the HTC of the algae was deduced by the severity factor, which is expressed as:

$$\log_{10} R_0 = log\left[t \times exp\left(\frac{T - T0}{14{,}75}\right)\right] \quad (2)$$

where t is the time (min), T is the temperature (°C), and T_0 is the reference temperature (generally set at 100 °C).

Adsorption tests

The adsorption efficiency of the hydrochars SM1, SM2, and SM3 for Rhodamine B removal was assessed via dispersing different amounts of hydrochars into 50 mL of Rhodamine B solutions 50 µM under stirring (350 rpm) by monitoring the adsorbent amount (5, 10, 30, 50, and 100 mg), the contact time (5, 15, 30, and 60 minutes) and the temperature (25, 35, and 45 °C). The samples were filtered, and their absorbance was measured using a UV-Vis spectrophotometer (PerkinElmer, Lambda 365). All the measurements were repeated three times, and corresponding linear models fit all the adsorption spectra. The calculation of pollutant removal percentage was determined using the following empirical formula:

$$removal\ \% = \frac{(C_0 - C_e)}{C_0} \times 100 \quad (3)$$

where C_0 (mg L^{-1}) represents the initial concentration of Rhodamine B, while C_e (mg L^{-1}) indicates the concentration of Rhodamine B at equilibrium. **Figure 3.5.1a** shows the absorbance readings recorded at different concentrations of Rhodamine B solutions (0 µM, 10 µM, 20 µM, 30 µM, 50 µM), which were

then used to construct a calibration curve based on the Beer-Lambert law (**Figure 3.5.1b**). The UV-Vis spectrum of Rhodamine B presents a prominent peak at 533 nm, corresponding to the wavelength of maximum absorption.

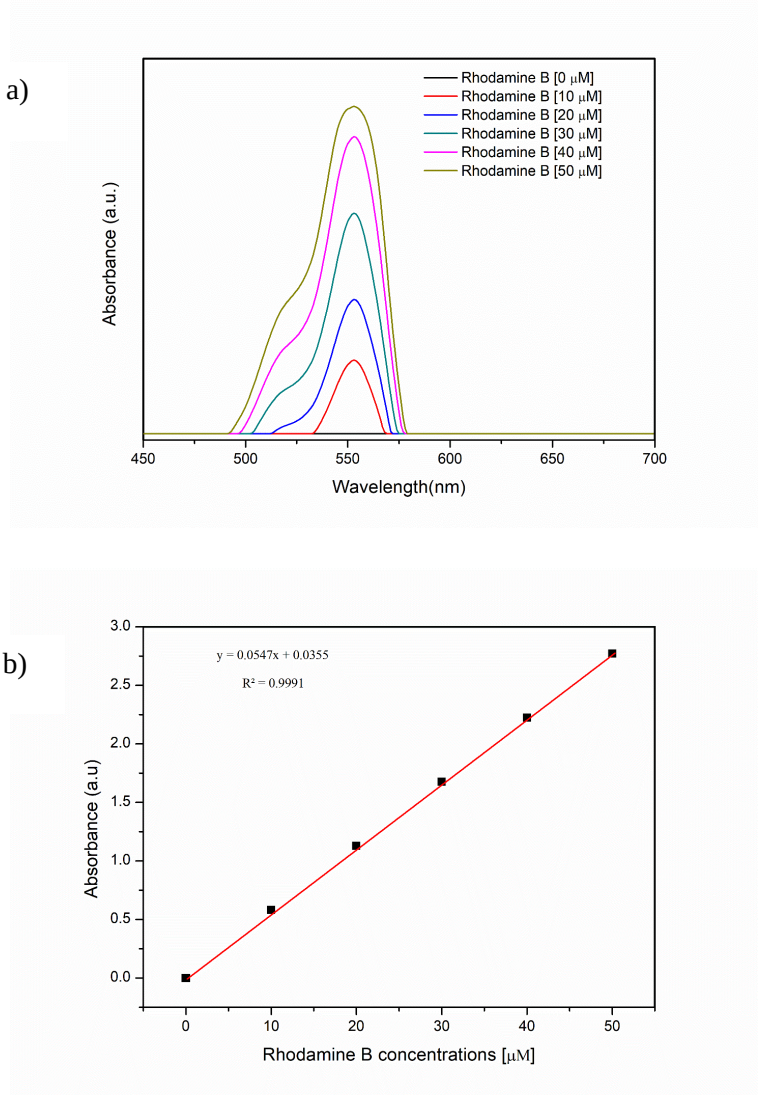

Figure 3.5.1. a) UV-Vis spectra of Rhodamine B solutions at different concentrations and **b)** calibration curve based on Beer's-Lambert law, sd ≤ 1.

Adsorption kinetics

The adsorption kinetics are determined by analysing experimental data collected during an adsorption process. Several kinetic models, including

pseudo-first order and pseudo- second order models can be used to describe the adsorption behavior over time. The first-order model describes adsorption as a reaction of the first order, where the adsorption rate is directly proportional to the concentration of the remaining solute. The equation for the pseudo first-order model is typically expressed as:

$$ln(q_e - q_t) = ln(q_e) - k_1 t \quad (4)$$

where q_e is the equilibrium adsorption capacity, q_t is the adsorption capacity at time t, k_1 is the first-order rate constant, and t represents time. On the other hand, the second-order model takes into account not only the solute concentration but also the available surface area for adsorption. The equation for the second-order model is typically represented as:

$$\frac{t}{q_t} = \left(\frac{1}{q_e}\right) \times t + \frac{1}{(k_2 q_e^2)} \quad (5)$$

where t represents time, q_t is the concentration of the solute at time t, q_e denotes the equilibrium adsorption capacity, and k_2 is the second-order rate constant.

Results and discussion

HTC data

Assuming that the overall reaction follows first-order kinetics and the Arrhenius temperature relation, the empirical parameters were obtained by fitting the model to the experimental data. In this and most other studies, the fitted parameter is assigned a value of 14.75, which corresponds to a reaction rate that doubles for every 10 °C increase in temperature. The severity factor

values were then correlated with the percent yields, as reported in **Table 3.5.1** and **Figure 3.5.2**.

Table 3.5.1. Hydrochar yields at different $LogR_0$.

Sample	$LogR_0$	HC Yields (wt%)
SM1 ($HC_{180–60}$)	4.13	22.82
SM2 ($HC_{240–60}$)	5.90	21.02
SM3 ($HC_{300–60}$)	7.66	12.98
SM4 ($HC_{180–180}$)	4.61	24.18
SM5 ($HC_{240–180}$)	6.37	18.14
SM6 ($HC_{300–180}$)	8.14	13.22
SM7 ($HC_{180–300}$)	4.83	20.54
SM8 ($HC_{240–300}$)	6.59	16.19
SM9 ($HC_{300–300}$)	8.36	11.33

Figure 3.5.2 illustrates that lower log R_0 values produce higher hydrochar yield percentages. Recent studies have indicated that residence time is a critical factor in hydrochar formation, as longer residence times increase reaction severity. While temperature has a more significant effect on solid product recovery, residence time also plays a role, albeit to a lesser degree. A shorter residence time led to a higher solid hydrochar content (60 and 180 minutes), which decreased gradually with increasing residence time (300 minutes). Additionally, the simultaneous effect of reaction time and temperature significantly influences yield. Decreasing the reaction temperature resulted in higher yields, with the maximum yield of 24.18% achieved at 180 °C and 3 hours of reaction time. The anomalous trend of the increase in hydrochar yield after 180 min, compared to 1 hour and 5 hours, could be attributed to several factors: the HTC process involves several chemical transformations, such as

hydrolysis, dehydration, and condensation reactions. These reactions require sufficient time to occur and reach equilibrium (Castro *et al.*, 2021). Therefore, the initial stages of the reaction can involve the breakdown of the labile components, while longer reaction times allowed for the conversion of more recalcitrant components into carbonaceous materials until a plateau (Liu *et al.*, 2019). A decreasing trend in yield was observed at 240 °C, inversely proportional to reaction duration, which is directly proportional to log R_0. At 300 °C, the yield was almost similar for reaction times of 60 and 180 minutes but lower for 300 minutes. Compared to other biomasses, the response of algae to increasing reaction temperatures shows a distinct pattern. Recent research suggests that the solid content of seaweed hydrochar decreases under more severe temperature conditions (Castro *et al.*, 2021; Khoo *et al.*, 2020; Del Río *et al.*, 2021). This outcome is potentially attributed to increased biomass solubilization, leading to the release of compounds into the liquid phase. Furthermore, the higher activation energy required to break the chemical bonds of the biomass components into their corresponding monomers may facilitate further decomposition of the solid residue (Liu *et al.*, 2019).

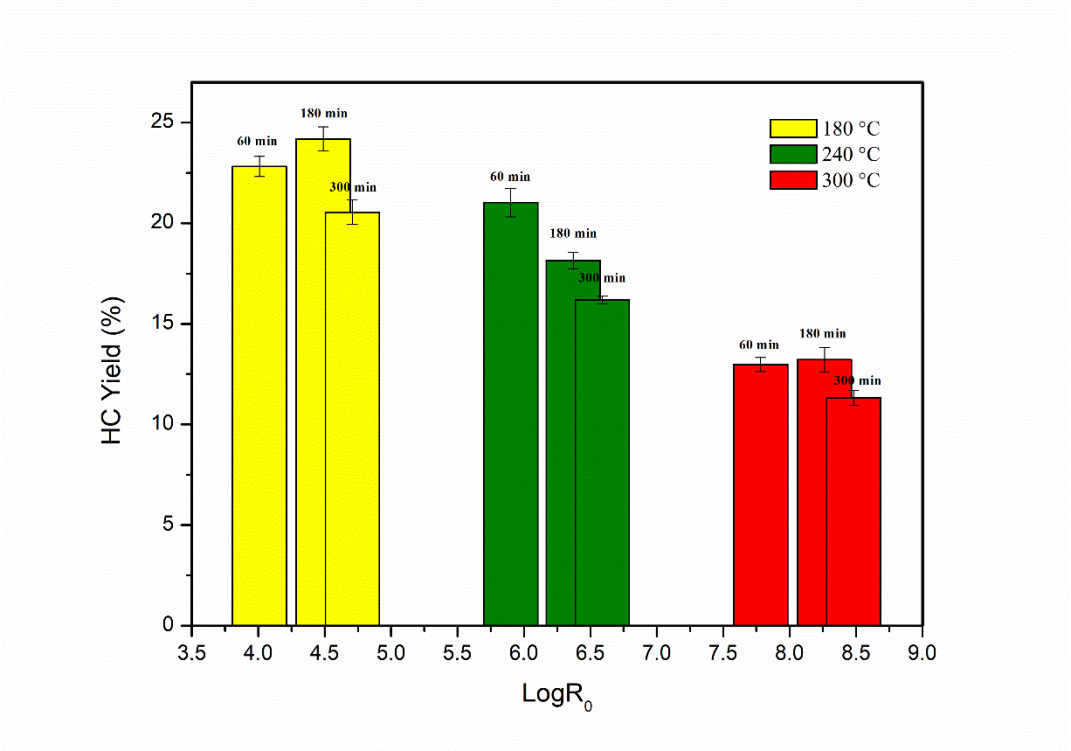

Figure 3.5.2. Percentage yield of hydrochar as a function of log R_0, sd≤1.

Characterization data

Figure 3.5.3a, **b**, and **c** illustrate the obtained Infrared spectra. As observed, all hydrochar samples exhibited similar absorption bands. The variations in the intensity of the absorption peaks are not reflected in the FTIR spectra. The wide band located between 3000 cm^{-1} and 3700 cm^{-1} is attributed to the stretching vibration of the hydroxyl groups. The intensity of this band decreases at 240 °C and 300 °C, probably caused by dehydration reactions occurring at higher temperatures. The small peak at 3330 cm^{-1} particularly evident at 180 °C could be attributed to the symmetrical and asymmetrical vibrations of the N–H group or O–H group. The bands at 2925 cm^{-1} and 2850 cm^{-1} are ascribed to the stretching vibrations of the aliphatic C–H groups and strain vibrations. The transmittance intensity of these bands increases with increasing temperature, probably due to the reduction of aromatic O and C following the carbonization process (Biswas *et al.*, 2022). The peak at 1613 cm^{-1} could be responsible for

the stretching of C−C and C−O, which agrees with the XPS results. The peak at 1490 cm^{-1} suggests the presence of amino groups. The signal at 1300 cm^{-1} could be related to the stretching vibration of the aromatic ring, which agrees with the XRD spectra showing the loss of the amorphous structure. The band around 1061 cm^{-1} can be ascribed to the β-glycosidic bond of cellulose and hemicellulose (Kale and Gorade, 2019). This band is reduced as the reaction time increases (also by the XRD outcomes). As observed for other hydrochars derived from biomass (Röhrdanz *et al.*, 2016; Satira *et al.*, 2021), FTIR spectra indicate that the reaction time does not influence on the structural properties of the samples, whereas temperature plays a crucial role in determining the surface functional groups due to the rearrangement of chemical bonds, the reaction of dehydration, the degree of carbonization, and the decomposition. Furthermore, the lack of significant changes in surface functional groups over time suggests that the composition of hydrochars remains relatively stable within the duration of the experiment.

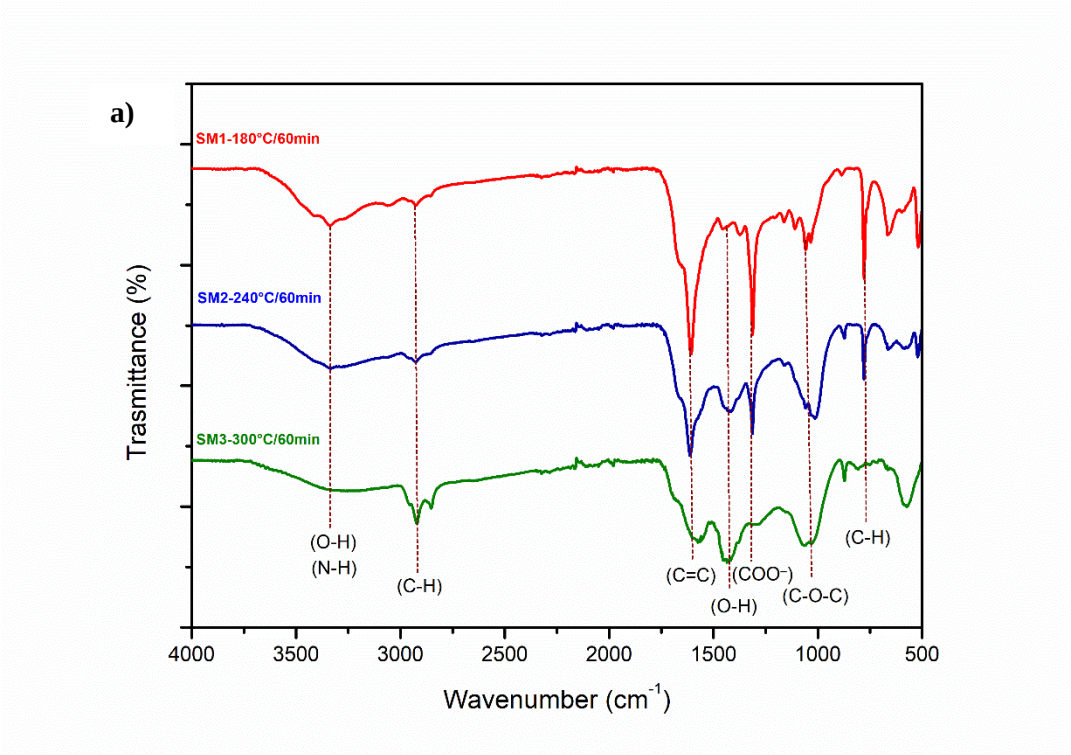
a)
SM1-180°C/60min
SM2-240°C/60min
SM3-300°C/60min
Trasmittance (%)
(O-H)
(N-H)
(C-H)
(C=C)
(O-H)
(COO⁻)
(C-O-C)
(C-H)
4000
3500
3000
2500
2000
1500
1000
500
Wavenumber (cm-1)

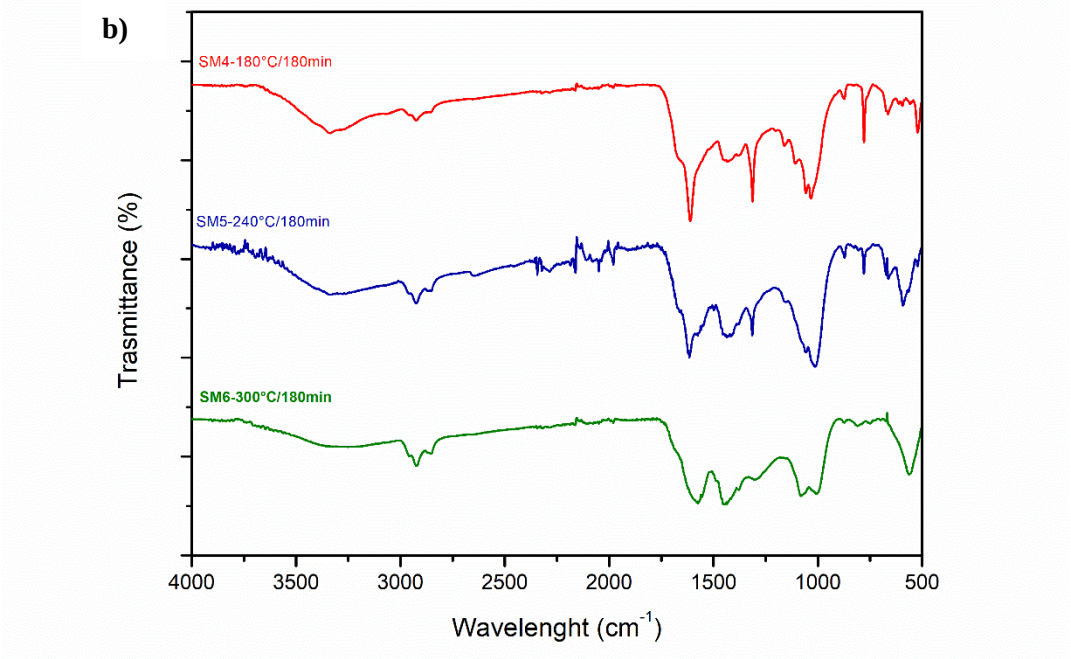
b)
SM4-180°C/180min
SM5-240°C/180min
SM6-300°C/180min
Trasmittance (%)
4000
3500
3000
2500
2000
1500
1000
500
Wavelenght (cm-1)

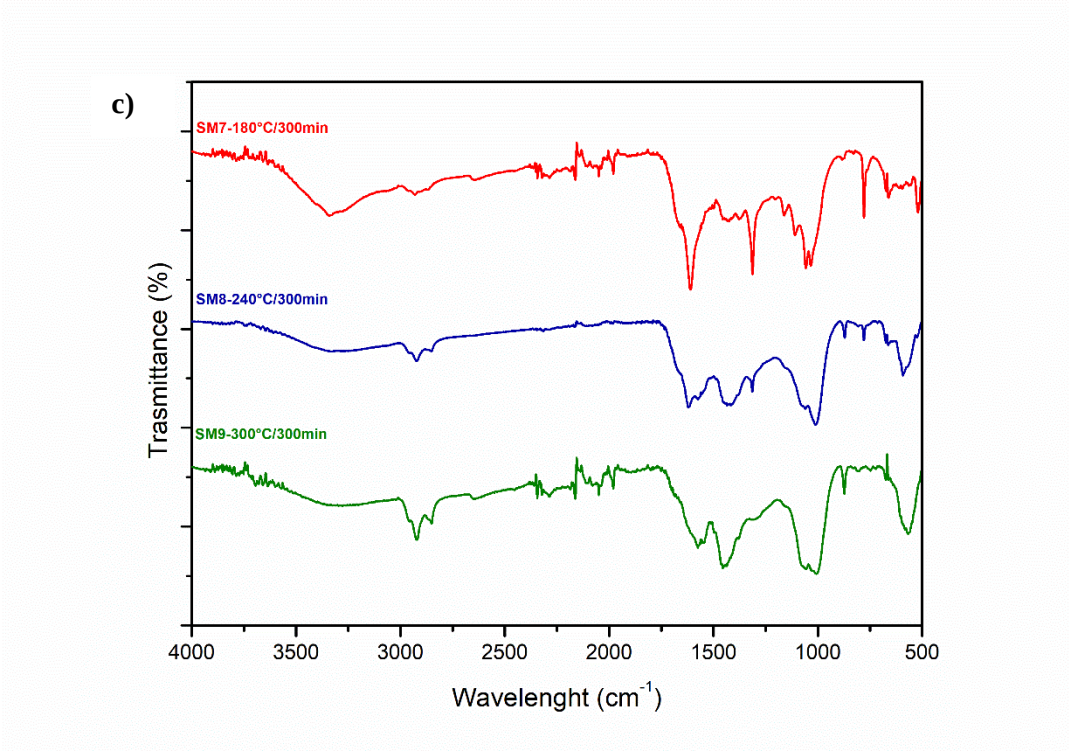

Figure 3.5.3. FT-IR spectra of hydrochar obtained from the hydrothermal process of algae at three different reaction temperatures (180 °C, 240 °C, 300 °C) and reaction times: **a)** 60 min, **b)** 180 min, and **c)** 300 min.

Figures 3.5.4a, b and **c** show the X-ray diffraction spectra (XRD) of the hydrochars produced under different HTC conditions of time (60, 180 and 300 min) and temperature (180, 240, 300 °C). The samples showed similar XRD patterns: as reported in the literature, the diffraction peaks at 2θ 15 and 25 represent the ordered structure of microcrystalline cellulose (Rustamaji *et al.*, 2022). With the increase in the reaction temperature, the peak at 15 2θ degrees disappears, underlining that the cellulose components begin to degrade and its microcrystalline structure gives way to a more amorphous one. The reaction time doesn't play a fundamental role, however, the hydrochar obtained at 240 °C and 300 °C for 300 minutes showed a stronger peak at the 25.79 2θ angle, demonstrating the formation of carbon layer planes which may be indicative of the disordered diffraction plane of the graphite (Masoumi and Dalai, 2020). The XRD analysis is in agreement with that observed previously for other

biomasses. The spectra show the presence of lower intensity peaks indicative of inorganic compounds derived from algal ash content (Clemente *et al.*, 2018): in particular, the 2θ diffraction peaks at 41.13 and 44 are assignable to phosphates of Al and Cu, while the peak at 25.32 indicates the presence of $CaSO_4$ (Liu *et al.*, 2019).

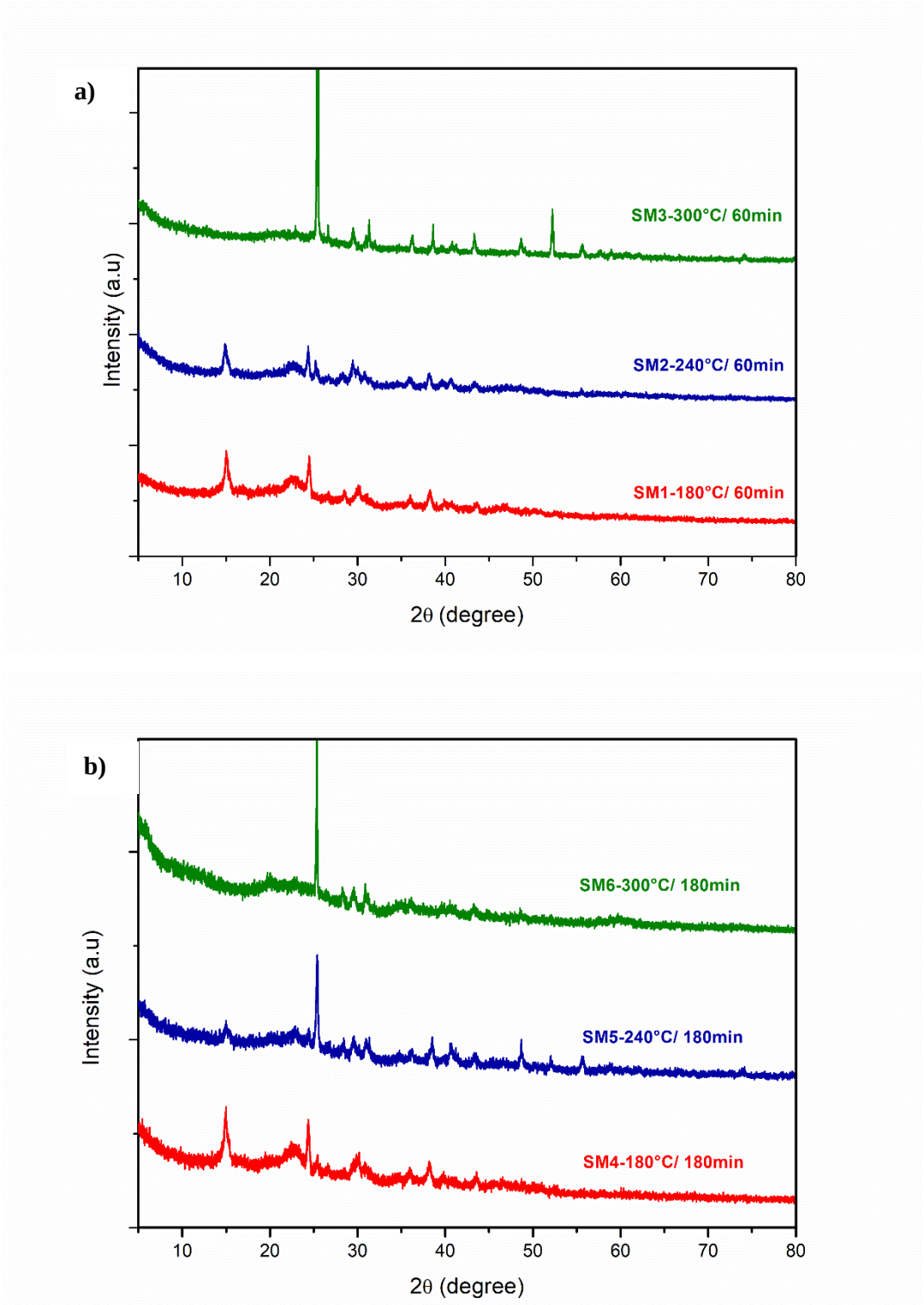
a)
SM3-300°C/ 60min
SM2-240°C/ 60min
SM1-180°C/ 60min
Intensity (a.u)
10
20
30
40
50
60
70
80
2θ (degree)
b)
SM6-300°C/ 180min
SM5-240°C/ 180min
SM4-180°C/ 180min
Intensity (a.u)
10
20
30
40
50
60
70
80
2θ (degree)

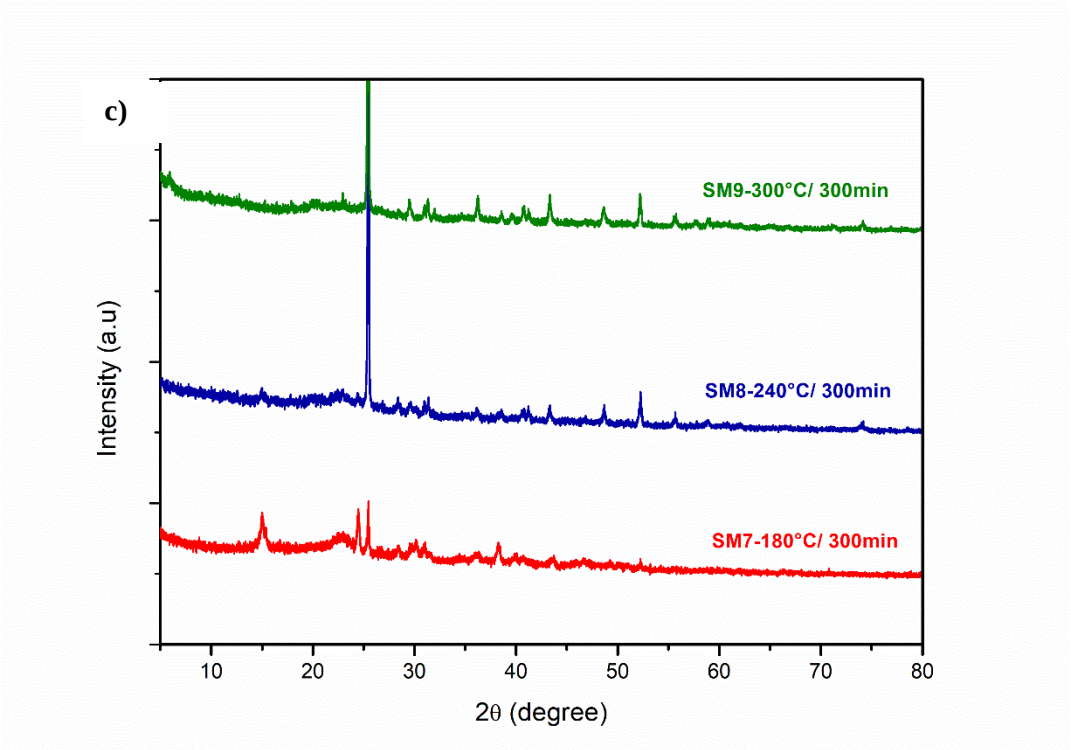

Figure 3.5.4. XRD spectra of hydrochar obtained from the hydrothermal process of algae at three different reaction temperatures (180 °C, 240 °C, 300 °C) and a reaction times: **a)** 60 min, **b)** 180 min, and **c)** 300 min.

The SEM images of the hydrochar samples collected at varying magnifications are illustrated in **Figure 3.5.5**. These images are indicative of the porous structure of the hydrochar sample. To gain insights into the morphology of the algae, SEM images of the raw material were also obtained (**Figure 3.5.5a-b**). In **Figure 3.5.5b**, several spherical aggregations with an average diameter of 874 mm and a smooth surface without whiskers are evident. As shown in **Figure 3.5.5c-f** at the same magnification, variations in the reaction conditions lead to cracks on the surface and the spheres become smaller microspheres. Longer residence time (300 min, **Figure 3.5.5e-f**) had a visible effect on surface morphology because cellulose and hemicellulose did not completely react at shorter residence times. A longer residence time resulted in the polymerization of monomers in the liquid phase, leading to the formation of secondary hydrochar with a polyaromatic structure (He *et al.*, 2013).

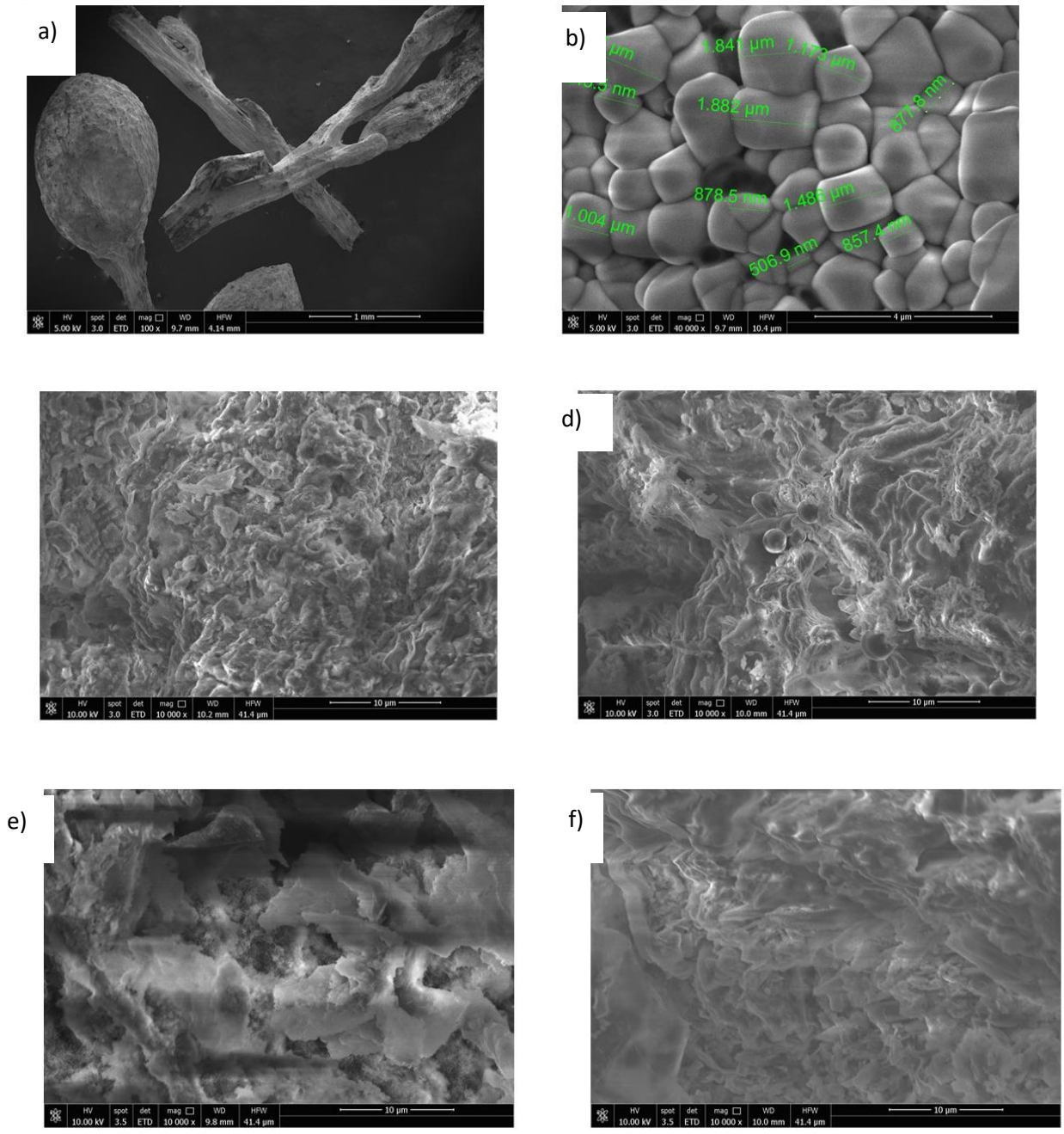

Figure 3.5.6 SEM images of *Sargassum muticum*: **a)** fragments of the thallus before the process; **b)** magnification of the thallus surface showing algal cells; **c)** sample SM4; **d)** sample SM5; **e)** sample SM7; **f)** sample SM8.

As reported in the literature for lignocellulosic biomasses, the residence time heavily influences the secondary hydrochar formation because the fading of fragments requires extensive polymerization (Wang *et al.*, 2018). The abundant

presence of C and O, as well as elements such as Mg, K, and Ca, which are widely dispersed in the matrix, was confirmed by EDX spectroscopy (**Figure 3.5.7**). These elements were particularly abundant in the samples obtained after 60 min of treatment. The porous structure of hydrochar is formed through carbonization, which involves releasing of volatile matter: as the matter is liberated, pores and cracks emerge on the surface of the hydrochar.

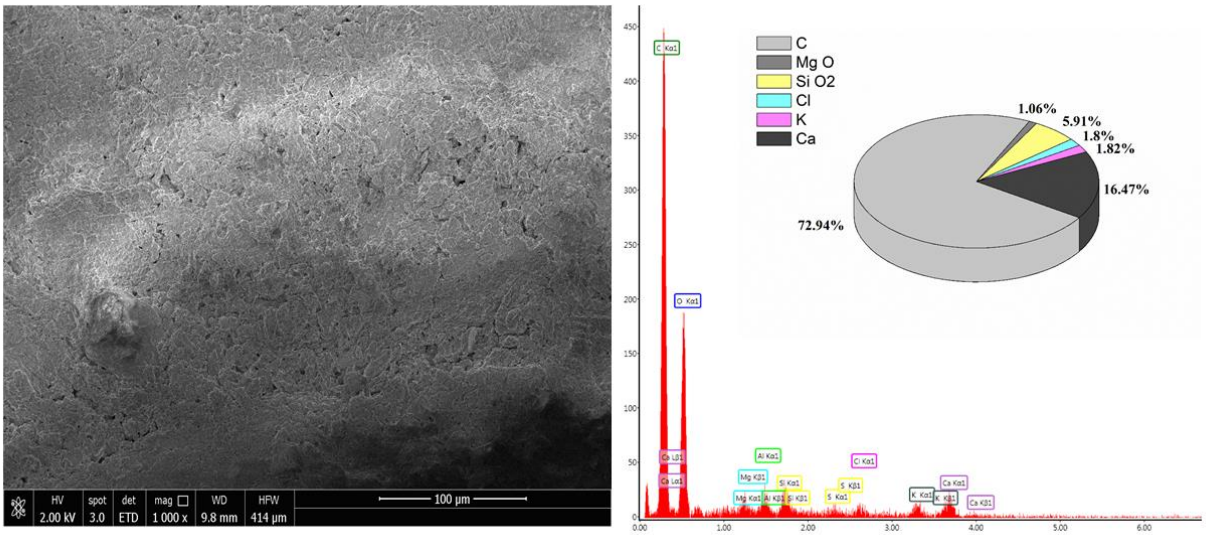

Figure 3.5.7. SEM image of sample SM1-$HC_{180–60}$ and relative EDX spectrum.

As shown in **Table 3.5.2** and according to the literature (Masoumi and Dalai, 2020; Espro *et al.*, 2021), BET surface areas were relatively low. As reported by Qin *et al.* (Qin *et al.*, 2017) the low surface area of hydrochar can be attributed to dehydration, polymerization and condensation reactions during the hydrothermal treatment, which hinder pore formation. In contrast to the hydrochars described in the literature, these samples, especially those obtained after 60 minutes of treatment have a good surface area with the largest surface area exhibited by the sample SM2. Moreover, the samples obtained at 240 °C show the highest values compared to the other samples.

Table 3.5.2. Surface area, Pore radius and Pore Volume of hydrochar samples

Sample	Surface Area (m^2/g)	Pore radius (Å)	Pore Volume (cc/g)
SM1	29.09	20.856	0.078
SM2	60.86	21.774	0.126
SM3	38.40	21.002	0.135
SM4	21.77	25.125	0.027
SM5	29.84	17.220	0.063
SM6	13.18	16.622	0.031
SM7	18.81	16.992	0.012
SM8	22.02	18.072	0.057
SM9	26.40	20.151	0.081

The surface compositions of the hydrochar, especially the three hydrochars formed after 60 min at various temperatures (SM1, SM2 and SM3) were studied by XPS. The results are compiled in **Figure 3.5.8**. Clearly and logically the materials are mainly composed of carbon, oxygen and nitrogen. However, small traces of calcium and silicium were detected. While the presence of calcium is consistent with the previously discussed results, the detection of silicium was ascribed to a contamination of the hydrochars. The analysis of the C 1s spectra reveals the existence of several functional groups such as aromatic and aliphatic C–C/C–H, carboxyl and carbonyl groups. The nitrogen spectra seem to indicate the presence of quaternary nitrogen species. This could derive from the biomolecules in the starting materials, which possess this nitrogen. As expected, the XPS characterization led to valuable information about the surface chemistry of the hydrochars, which is needed to evaluate their potential in various applications including in environmental or energy-related fields

(Guo *et al.*, 2020). The percentages of the elements are summarized in the following **Table 3.5.3**. It can be noted that increasing the synthesis temperature leads to an enrichment of carbon combined with an important loss of oxygen.

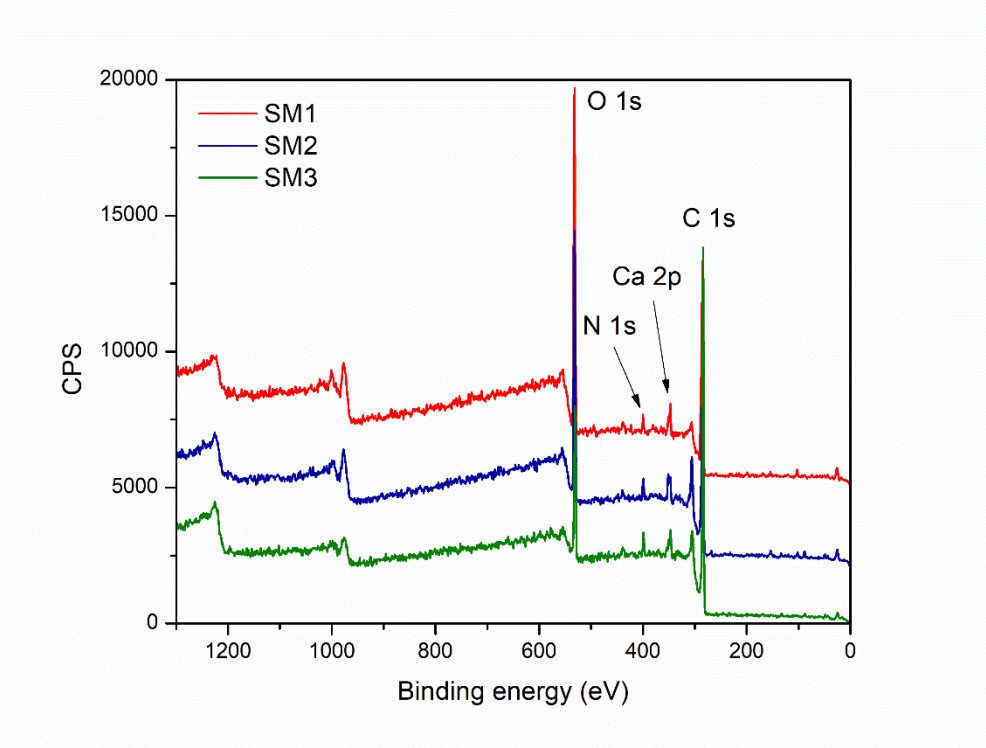

Figure 3.5.8. Full-scale XPS survey scan of the hydrochars SM1, SM2, and SM3

SM1			**SM2**			**SM3**		
O	1s	29.85 %	O	1s	24.66 %	O	1s	13.86 %
C	1s	64.66 %	C	1s	69.07 %	C	1s	82.23 %
N	1s	1.84 %	N	1s	2.63 %	N	1s	2.47 %
Ca	2p	1.98 %	Ca	2p	2.55 %	Ca	2p	1.44 %
Si	2p	1.67 %	Si	2p	1.08 %			

Table 3.5.3. XPS elements and relative percentages

Adsorption of Rhodamine B dye

According to the literature (El-Bery *et al.*, 2022; Masoumi and Dalai, 2020), hydrochar does not show high adsorbing power probably due to the low surface area, and therefore it could be activated by chemical and physical processes. In this study, the hydrochars obtained after 60 minutes at different temperatures exhibited superior surface areas, so they were used without any activation, showing an excellent adsorption capacity. The adsorption mechanism could be due to the surface area of the samples under investigation. The results agree, showing that the SM2 sample, with the highest surface area, exhibited the best response, even at low concentrations. Nevertheless, all the samples investigated displayed good adsorption performance. Therefore, in addition to the adsorption mechanism, a surface chemical interaction between the polar groups of the hydrochar and Rhodamine B could also contribute, indicating the existence of hydrogen bonding (Masoumi and Dalai, 2020) and π- π interactions between the aromatic rings (Hou *et al.*, 2021).

Effect of hydrochars amount

In this study, the effect of adsorbent dosage was investigated by using different amounts of hydrochar (5 mg, 10 mg, 30 mg, 50 mg, and 100 mg) at 25 °C in 50 mL of Rhodamine B solution [50 μM], under stirring for 60 minutes. **Figure 3.5.9** illustrates that as the adsorbent dosage increases from 5 to 30 mg, the dye removal rate increases for all the samples, reaching 67.02% for SM1, 83.6% for SM2, and 71.12% for SM3. However, as the dosage of hydrochars is further increased from 30 to 100 mg, the removal percentage decreases, indicating probably the saturation of adsorption sites. This observation suggests that the availability of active sites for the adsorption of Rhodamine B is directly proportional to the quantity of adsorbents employed in the experiment. Accordingly, an increase in the dosage of adsorbents leads to a linear increase

in the number of available sites and thus to an increase in the amount of Rhodamine B adsorbed by the hydrochars. However, beyond 30 mg, no significant change is observed, indicating that adsorption sites have reached equilibrium. Therefore, 30 mg was chosen as the optimal dosage for subsequent studies.

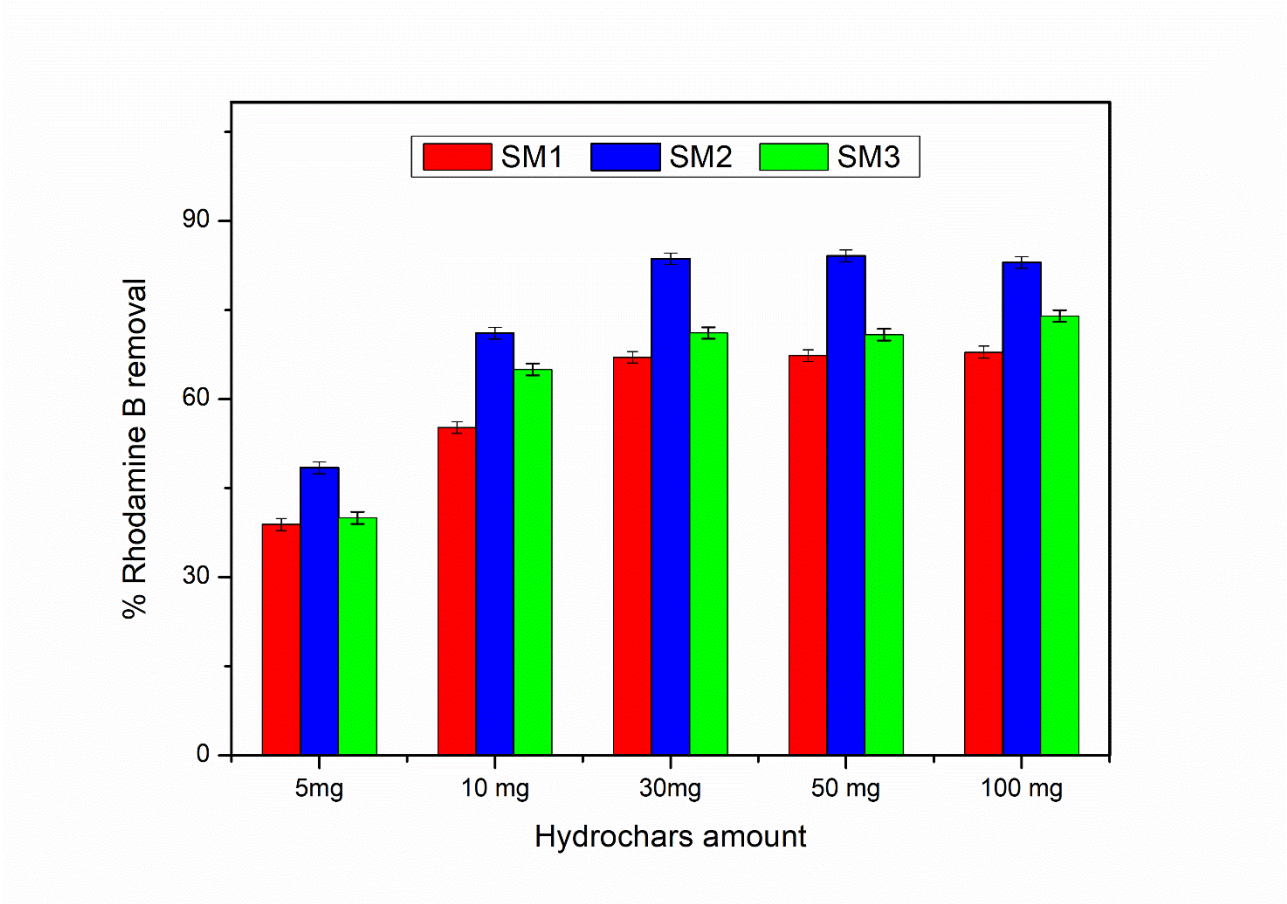

Figure 3.5.9. Adsorbent amount effect on % Rhodamine B removal, sd ≤1.

Effect of contact time

Figure 3.5.10 presents the effect of contact time (from 5 to 60 min) on Rhodamine B adsorption. The experiments were conducted at 25 °C with an adsorbent amount of 30 mg for all samples, and 50 mL of Rhodamine B

solution with a concentration of 50 μM, under stirring. The adsorption of Rhodamine B rapidly increased in the first 30 minutes, followed by a gradual increase up to 60 minutes, with the highest removal rate achieved by SM2, increasing from 25.8% to almost 84%. The adsorption capacity of the hydrochar was efficient, as indicated by the percentage removal of the adsorbent at time zero and the high affinity for the contaminant. **Figure 3.5.11** displays the solutions and the significant color quenching resulting from the adsorption of the organic compound by hydrochar SM2.

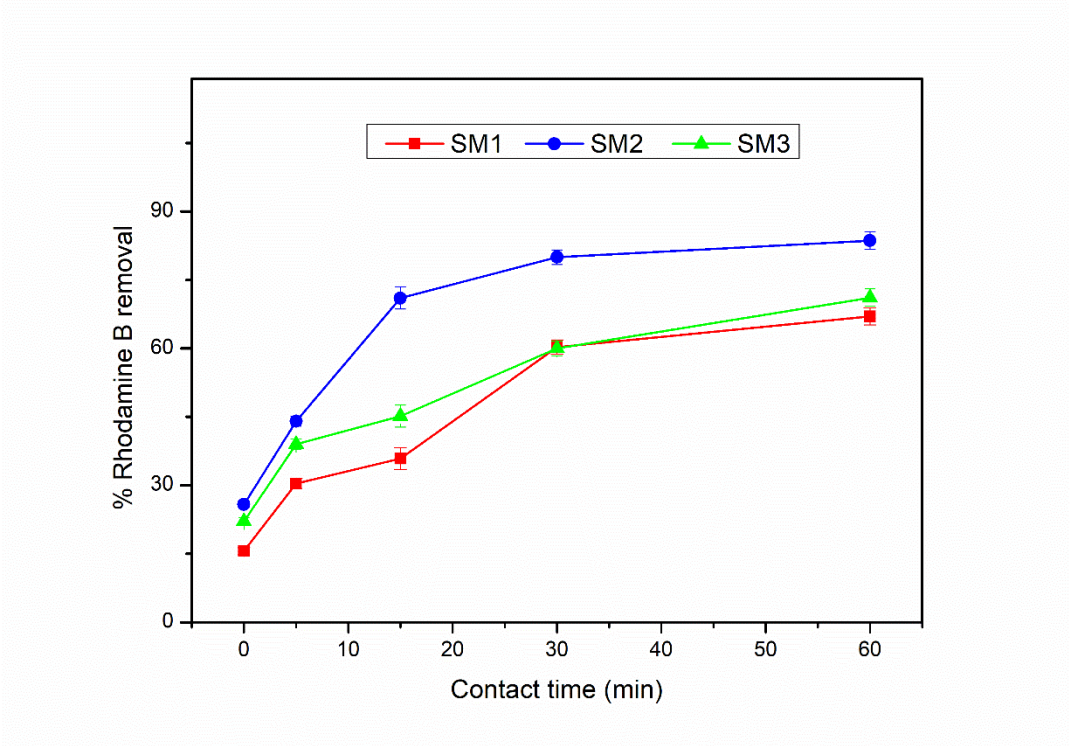

Figure 3.5.10. Time effect on % Rhodamine B removal, sd≤2.

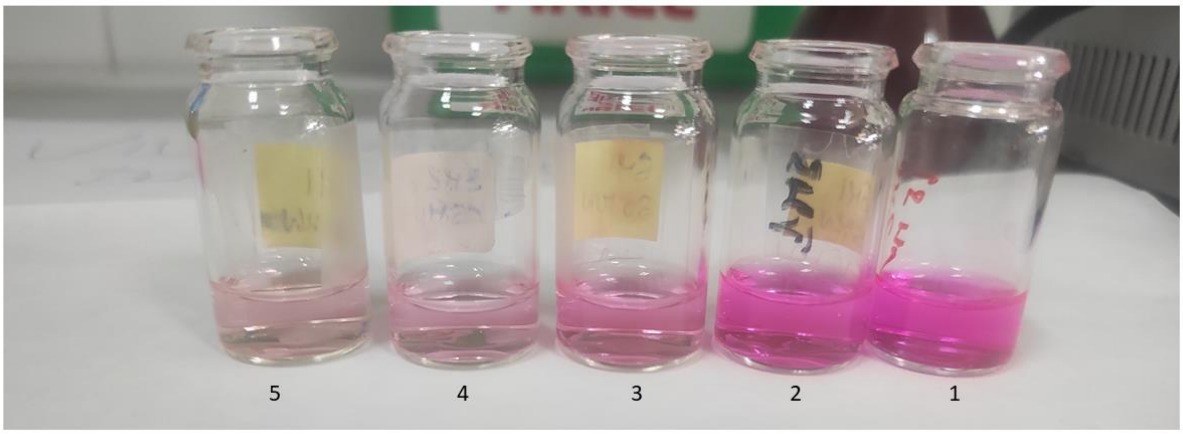

Figure 3.5.11. Impact of contact time by hydrochar SM2 in Rhodamine B solution evaluated **1)** immediately, **2)** after 5 min, **3)** after 15 min, **4)** after 30 min, and **5)** after 60 min.

Effect of temperature

The effect of the operating temperature on the removal of Rhodamine B [50 µM] was evaluated at three temperature values (25 °C, 35 °C, and 45 °C), establishing the reaction time as 30 minutes. As depicted in **Figure 3.5.12**, at the maximum temperature the samples showed 74.9%, 97.8%, and 80% Rhodamine B removal respectively for SM1, SM2 and SM3. Therefore, the removal efficiency is higher when the temperature is high, indicating that the temperature affects the enhancement of the chemical-physical bonds between the adsorbate and the adsorbent.

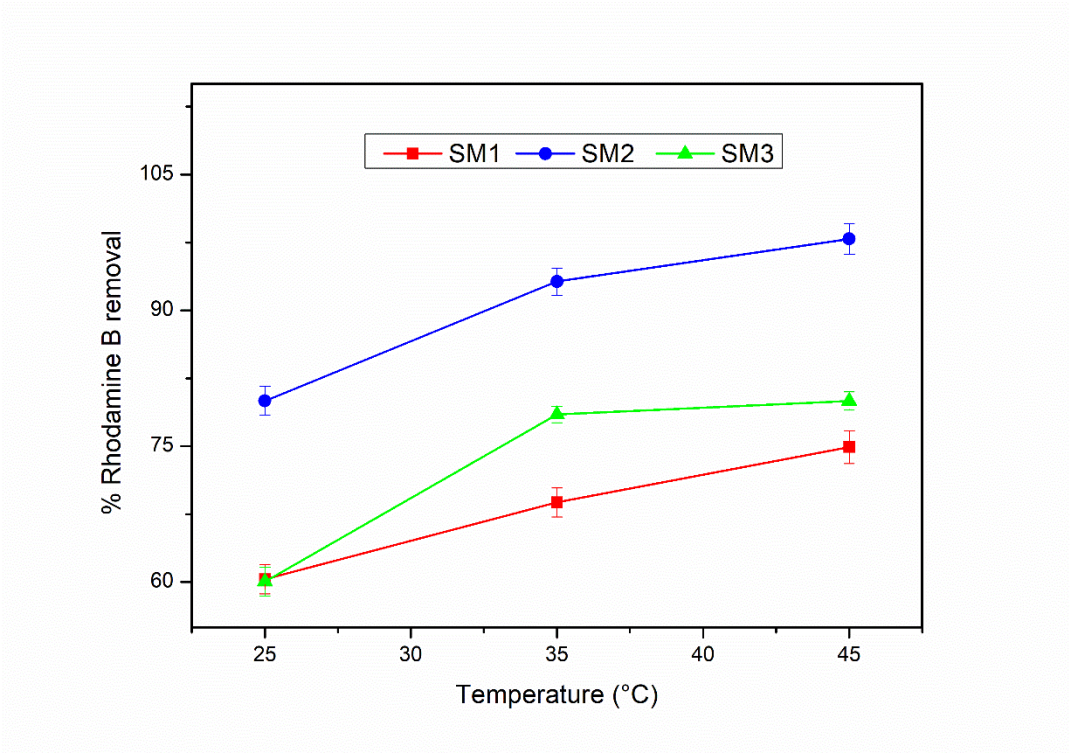

Figure 3.5.11. Temperature effect on % Rhodamine B removal, sd≤3.

Adsorption kinetic results

The adsorption kinetic values of q_e, k_t and R^2 were evaluated and calculated from eqn (3) and eqn (4) and the data are plotted in **Figure 3.5.12**. The corresponding results are summarized in **Table 3.5.4**. The calculated pseudo-second order correlation coefficient (R^2) values were superior to those obtained from the pseudo-first order kinetic model for all the samples. This suggests that the pseudo-second order model fits well with the experimental data, supporting that the hydrochar-mediated adsorption process is primarily governed by chemisorption (Xie *et al.*, 2019), involving the formation of chemical bonds between the polar groups and aromatic groups present on the hydrochar surface and Rhodamine B molecules in solution.

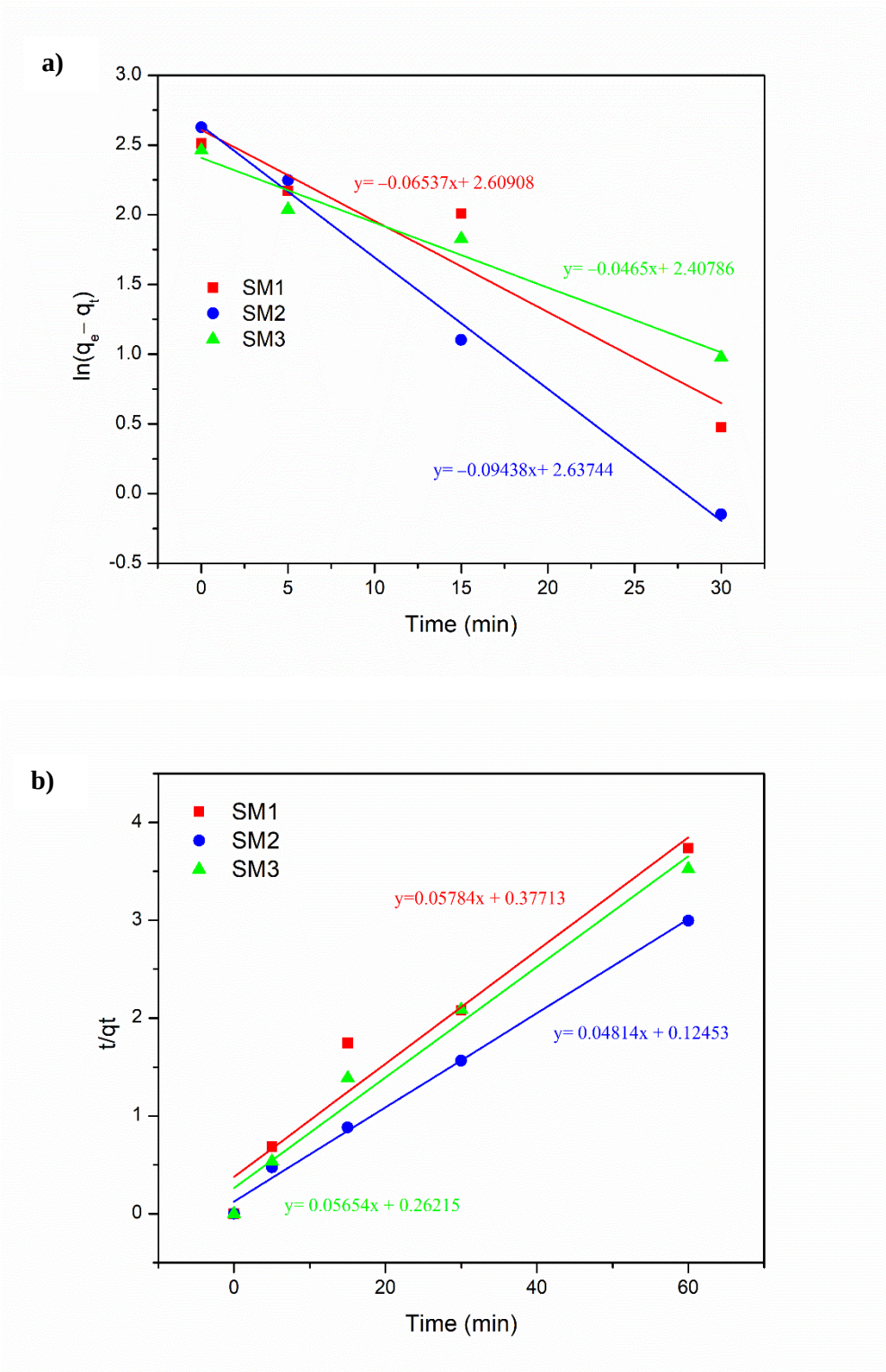

Figure 3.5.12. Kinetic of Rhodamine B adsorption by SM1, SM2, and SM3, fitted by **a)** pseudo-first order model and **b)** pseudo-second order model.

Table 3.5.4. Adsorption kinetics' parameters

Samples	Pseudo-first order kinetic model			Pseudo-second order kinetic model		
	q_e (mg·g^{-1})	k_t (min^{-1})	R^2	q_e (mg·g^{-1})	k_t (g·mg^{-1}·min^{-1})	R^2
SM1	13.59	0.065	0.92	17.29	0.009	0.95
SM2	13.98	0.094	0.94	20.77	0.019	0.99
SM3	11.11	0.046	0.97	17.69	0.012	0.98

Comparison with literature data

The table below (**Table 3.5.5**) displays the adsorbent potential of various samples derived from *Sargassum muticum* and other *Sargassum*-based adsorbents. Its purpose is to compare the adsorptive capacities of the hydrochars obtained in this study with those reported in recent research. According to the available data, there is limited literature on hydrochars derived from *Sargassum muticum* for direct adsorption purposes. However, the results are comparable to those obtained from other macroalgae sources or even chemically treated *Sargassum muticum*. These promising findings show that these hydrochars have the potential to be exploited as effective adsorbents without the requirement of additional physical or chemical activation processes, thus promoting the use of environmentally friendly materials.

Table 3.5.5. Comparison between *Sargassum*-derived adsorbents

Samples	Pollutants	Technique	% removal	Ref.
Sargassum muticum hydrochar activated by KOH treatment	Methylene Blue	Adsorption	91	(Chambers *et al.* 2023)

dried *Sargassum muticum*	Cr (VI)	Adsorption	84.4	(González Bermúdez *et al.* 2012)
dried *Sargassum muticum* treated with $CaCl_2$ dried *Sargassum muticum* treated with HCl dried *Sargassum muticum* treated with H_2CO	Methylene Blue	Adsorption	97 98 98	(Rubin *et al.* 2005)
dried *Sargassum muticum*	Hg (II)	Adsorption	86	(Carro *et al.* 2013)
dried and grinded *Sargassum muticum*	Methylene Blue Pb (II)	Adsorption	96.13 96	(Hannachi and Hafidh 2020)
dried and sieved *Sargassum ilicifolium*	Hydrazine	Adsorption	94	(Tabaraki and Nateghi 2016)
Sargassum muticum fabricated AgNPs	Methylene Blue Methyl Orange	Adsorption	63.5 66.5	(Trivedi *et al.* 2021)
Sargassum oligocystum treated with $CaCl_2$	Cr (VI)	Adsorption	> 95	(Foroutan, Mohammadi, and Ramavandi 2018)
Sargassum horneri hydrochar	Methylene Blue	Adsorption	99	(Soroush *et al.* 2022)
dried and sieved *Sargassum hemiphyllum*	Methylene Blue	Adsorption	> 86	(Liang, Xia, and Long 2017)

dried and grinded *Sargassum dentifolium*	Methylene Blue	Adsorption	99.2	(Moghazy, Labena, and Husien 2019)
dried *Sargassum glaucescens*	Acid black 1	Adsorption	94	(Daneshvar *et al.* 2012)
Sargassum fusiforme hydrochar	Heavy metals	Adsorption	> 86	(Poo *et al.* 2018)
dried *Sargassum hemiphyllum*	Ni (II)	Adsorption	67.4	(Fan, Xia, and Long 2019)
Sargassum honeri magnetically modified	Dyes pollutants	Adsorption	> 90	(Angelova *et al.* 2016)
Sargassum muticum hydrochar SM1 *Sargassum muticum* hydrochar SM2 *Sargassum muticum* hydrochar SM3	Rhodamine B	Adsorption	75 98 80	This work

Conclusions

In this study, thalli of the alga *Sargassum muticum* were converted to hydrochar by hydrothermal carbonization, and the role of temperature and residence time was investigated, showing a maximum hydrochar yield at 180 °C after 180 min. Based on the characterization data, the samples contained many oxygen, carboxyl, and amino functional groups and showed a stable mesoporous structure. The SM2 sample showed the highest surface area and it proved to be the best adsorbent for Rhodamine B in water with a removal rate of up to 98% when left at 45 °C for 30 minutes. The present research fits in a larger project dealing with the exploitation of algal biomass, such as those produced by blooms of natural populations of invasive algae in dystrophic environments. In this scenario, huge algal biomasses, which disturb the equilibrium of the

ecosystem, the wellness of native species, the provision of ecosystem services, and the realization of human activities, are usually treated as waste. A potential use of unwanted algal biomasses is suggested, involving their conversion into a valuable resource, laying the foundations for a sustainable, economic, and efficient process.

References

Angelova, R.; Baldikova, E.; Pospiskova, K.; Maderova, Z.; Safarikova, M.; Safarik, I. Magnetically Modified Sargassum Horneri Biomass as an Adsorbent for Organic Dye Removal. *Journal of Cleaner Production*, **2016**, 137, 189–94. https://doi.org/10.1016/j.jclepro.2016.07.068

Biswas, B.; Bisht, Y.; Kumar, J.; Reddy Yenumala, S.; Bhaskar, T. Effects of Temperature and Solvent on Hydrothermal Liquefaction of the Corncob for Production of Phenolic Monomers. *Biomass Conversion and Biorefinery*, **2022**, 12 (1), 91–101. https://doi.org/10.1007/s13399-020-01012-5

Carro, L.; Barriada, J. L.; Herrero, R.; Sastre de Vicente, M. E. Surface Modifications of Sargassum Muticum Algal Biomass for Mercury Removal: A Physicochemical Study in Batch and Continuous Flow Conditions'. *Chemical Engineering Journal*, **2013**, 229, 378–87. https://doi.org/10.1016/j.cej.2013.06.014

Castro, J.; Peixoto Assemany, P.; Cássia de Oliveira, A.; Carneiro; Ferreira, J.; Magno de Jesus Júnior, M.; de Ávila Rodrigues, F.; Calijuri, M.L. Hydrothermal Carbonization of Microalgae Biomass Produced in Agro-Industrial Effluent: Products, Characterization and Applications. *Science of The Total Environment*, **2021**, 768, 144480. https://doi.org/10.1016/j.scitotenv.2020.144480

Chambers, C.; Saha, S.; Grimes, S.; Calhoun, J.; Reza, M. T. Physical and Morphological Alteration of Sargassum-Derived Ultraporous Superactivated Hydrochar with Remarkable Cationic Dye Adsorption. *Biomass Conversion and Biorefinery*, **2023**. https://doi.org/10.1007/s13399-023-04326-2

Clemente, J.; Beauchemin, S.; Thibault, Y.; MacKinnon, T.; Smith. D. Differentiating Inorganics in Biochars Produced at Commercial Scale Using Principal Component Analysis. *ACS Omega*, **2018**, 3, 6931–44. https://doi.org/10.1021/acsomega.8b00523

Daneshvar, E.; Kousha, M.; Jokar, M.; Koutahzadeh, N.; Guibal, E. Acidic Dye Biosorption onto Marine Brown Macroalgae: Isotherms, Kinetic and Thermodynamic Studies.

Chemical Engineering Journal, **2012**, 204–206, 225–34. https://doi.org/10.1016/j.cej.2012.07.090

Del Río, P. G.; Gullón, B.; Pérez-Pérez, A.; Romaní, A.; Garrote, G. Microwave Hydrothermal Processing of the Invasive Macroalgae Sargassum Muticum within a Green Biorefinery Scheme. *Bioresource Technology*, **2021**, 340, 125733. https://doi.org/10.1016/j.biortech.2021.125733

El-Bery, H. M.; Saleh, M.; El-Gendy, R.A.; Saleh, M.R.; Thabet, S. M. High Adsorption Capacity of Phenol and Methylene Blue Using Activated Carbon Derived from Lignocellulosic Agriculture Wastes. *Scientific Reports*, **2022**, 12(1), 5499. https://doi.org/10.1038/s41598-022-09475-4

Espro, C.; Satira, A.; Mauriello, F.; Anajafi, Z.; Moulaee, K.; Iannazzo, D.; Neri, G. Orange Peels-Derived Hydrochar for Chemical Sensing Applications. *Sensors and Actuators B: Chemical*, **2021**, 341, 130016. https://doi.org/10.1016/j.snb.2021.130016

Fan, X.; Xia, J.; Long, J. The Potential of Nonliving Sargassum Hemiphyllum as a Biosorbent for Nickel(II) Removal—Isotherm, Kinetics, and Thermodynamics Analysis. *Environmental Progress & Sustainable Energy*, **2019**, 38 (s1), S250–59. https://doi.org/10.1002/ep.12997

Foroutan, R.; Mohammadi, R.; Ramavandi, B. Treatment of Chromium-Laden Aqueous Solution Using $CaCl_2$-Modified Sargassum Oligocystum Biomass: Characteristics, Equilibrium, Kinetic, and Thermodynamic Studies. *Korean Journal of Chemical Engineering*, **2018**, 35(1), 234–45. https://doi.org/10.1007/s11814-017-0239-2

González Bermúdez, Y.; Rodríguez Rico, I. L.; Guibal, E.; Calero de Hoces, M.; Martín-Lara, M. A. Biosorption of Hexavalent Chromium from Aqueous Solution by Sargassum Muticum Brown Alga. Application of Statistical Design for Process Optimization. *Chemical Engineering Journal*, **2012**, 183, 68–76. https://doi.org/10.1016/j.cej.2011.12.022

Guo, S.; Wang, Y.; Wei, X.; Gao, Y.; Xiao, B.; Yang, Y. Structural Analysis and Heavy Metal Adsorption of N-Doped Biochar from Hydrothermal Carbonization of

Camellia Sinensis Waste. *Environmental Science and Pollution Research*, **2020**, 27 (15), 18866–74. https://doi.org/10.1007/s11356-020-08455-3

Hannachi, Y.; Hafidh, A. Biosorption Potential of Sargassum Muticum Algal Biomass for Methylene Blue and Lead Removal from Aqueous Medium. *International Journal of Environmental Science and Technology*, **2020**, 17 (9), 3875–90. https://doi.org/10.1007/s13762-020-02742-9

He, C.; Giannis, A.; Wang, J-Y. Conversion of Sewage Sludge to Clean Solid Fuel Using Hydrothermal Carbonization: Hydrochar Fuel Characteristics and Combustion Behavior. *Applied Energy*, **2013**, 111, 257–66. https://doi.org/10.1016/j.apenergy.2013.04.084

Hou, Z.; Tao, Y.; Bai, T.; Liang, Y.; Huang, S.; Cai, J. Efficient Rhodamine B Removal by N-Doped Hierarchical Carbons Obtained from KOH Activation and Urea-Oxidation of Glucose Hydrochar. *Journal of Environmental Chemical Engineering*, **2021**, 9 (4), 105757. https://doi.org/10.1016/j.jece.2021.105757

Kale, R. D.; Gorade, V. G. Potential Application of Medical Cotton Waste for Self-Reinforced Composite. *International Journal of Biological Macromolecules*, **2019**, 124, 25–33. https://doi.org/10.1016/j.ijbiomac.2018.11.196

Khoo, C. G.; Lam, M. K.; Mohamed, A. R.; Lee, K. T. Hydrochar Production from High-Ash Low-Lipid Microalgal Biomass via Hydrothermal Carbonization: Effects of Operational Parameters and Products Characterization. *Environmental Research*, **2020**, 188, 109828. https://doi.org/10.1016/j.envres.2020.109828

Liang, J.; Xia, J.; Long, J. Biosorption of Methylene Blue by Nonliving Biomass of the Brown Macroalga Sargassum Hemiphyllum. *Water Science and Technology*, **2017**, 76 (6), 1574–83. https://doi.org/10.2166/wst.2017.343

Liu, H.; Chen, Y.; Yang, H.; Gentili, F. G.; Söderlind, U.; Wang, X.; Zhang, W.; Chen, H. Hydrothermal Carbonization of Natural Microalgae Containing a High Ash Content. *Fuel*, **2019**, 249, 441–48. https://doi.org/10.1016/j.fuel.2019.03.004

Masoumi, S.; Dalai, A.K. Optimized Production and Characterization of Highly Porous Activated Carbon from Algal-Derived Hydrochar. *Journal of Cleaner Production*, **2020**, 263, 121427. https://doi.org/10.1016/j.jclepro.2020.121427

Moghazy, R. M.; Labena, A.; Husien, Sh. Eco-Friendly Complementary Biosorption Process of Methylene Blue Using Micro-Sized Dried Biosorbents of Two Macro-Algal Species (Ulva Fasciata and Sargassum Dentifolium): Full Factorial Design, Equilibrium, and Kinetic Studies. *International Journal of Biological Macromolecules*, **2019**, 134, 330–43. https://doi.org/10.1016/j.ijbiomac.2019.04.207

Overend, R. P.; Chornet, E.; Gascoigne, J. A.; Hartley, B. S.; Broda, P.M.A.; Senior, P.J. Fractionation of Lignocellulosics by Steam-Aqueous Pretreatments. *Philosophical Transactions of the Royal Society of London. Series A, Mathematical and Physical Sciences*, **1997**, 321 (1561), 523–36. https://doi.org/10.1098/rsta.1987.0029

Poo, K-M.; Son, E-B.; Chang, J-S.; Ren, X.; Choi, Y-J.; Chae, K-J. Biochars Derived from Wasted Marine Macro-Algae (Saccharina Japonica and Sargassum Fusiforme) and Their Potential for Heavy Metal Removal in Aqueous Solution. *Journal of Environmental Management*, **2018**, 206 (January): 364–72. https://doi.org/10.1016/j.jenvman.2017.10.056

Qin, T.; Song, M.; Jiang, K.; Zhou, J.; Zhuang, W.; Chen, Y.; Liu, D.; Chen, X.; Ying, H.; Wu, J. Efficient Decolorization of Citric Acid Fermentation Broth Using Carbon Materials Prepared from Phosphoric Acid Activation of Hydrothermally Treated Corncob. *RSC Advances*, **2017**, 7 (59), 37112–21. https://doi.org/10.1039/C7RA04813K

Röhrdanz, M.; Rebling, T.; Ohlert, J.; Jasper, J.; Greve, T.; Buchwald, R.; von Frieling, P.; Wark, M. Hydrothermal Carbonization of Biomass from Landscape Management – Influence of Process Parameters on Soil Properties of Hydrochars. *Journal of Environmental Management*, **2016**, 173, 72–78. https://doi.org/10.1016/j.jenvman.2016.03.006

Rubin, E.; Rodriguez, P.; Herrero, R.; Cremades, J.; Barbara, I.; Sastre de Vicente, M. E. Removal of Methylene Blue from Aqueous Solutions Using as Biosorbent

Sargassum Muticum: An Invasive Macroalga in Europe. *Journal of Chemical Technology & Biotechnology*, **2005**, 80 (3), 291–98. https://doi.org/10.1002/jctb.1192

Ruiz, H. A.; Galbe, M.; Garrote, G.; Ramirez-Gutierrez, D. M.; Ximenes, E.; Sun, S-N.; Lachos-Perez, D.; Rodríguez-Jasso, R. M.; Sun, R-C.; Yang, B.; Ladisch, M. R. Severity Factor Kinetic Model as a Strategic Parameter of Hydrothermal Processing (Steam Explosion and Liquid Hot Water) for Biomass Fractionation under Biorefinery Concept. *Bioresource Technology*, **2021**, 342, 125961. https://doi.org/10.1016/j.biortech.2021.125961

Rustamaji, H.; Prakoso, T.; Rizkiana, J.; Devianto, H.; Widiatmoko, P.; Guan, G. Synthesis and Characterization of Hydrochar and Bio-Oil from Hydrothermal Carbonization of Sargassum Sp. Using Choline Chloride (ChCl) Catalyst. *International Journal of Renewable Energy Development*, **2022**, 11 (2), 403–12. https://doi.org/10.14710/ijred.2022.42595

Satira, A.; Paone, E.; Bressi, V.; Iannazzo, D.; Marra, F.; Calabrò, P.S.; Mauriello, F.; Espro, C. Hydrothermal Carbonization as Sustainable Process for the Complete Upgrading of Orange Peel Waste into Value-Added Chemicals and Bio-Carbon Materials. *Applied Sciences*, **2021**, 11, 10983. https://doi.org/10.3390/app112210983

Soroush, S.; Ronsse, F.; Verberckmoes, A.; Verpoort, F.; Park, J.; Wu, D.; Heynderickx, P, M. Production of Solid Hydrochar from Waste Seaweed by Hydrothermal Carbonization: Effect of Process Variables. *Biomass Conversion and Biorefinery*, **2022**. https://doi.org/10.1007/s13399-022-02365-9

Tabaraki, R.; Nateghi, A. Application of Taguchi L16 Orthogonal Array Design to Optimize Hydrazine Biosorption by Sargassum Ilicifolium. *Environmental Progress & Sustainable Energy*, **2016**, 35 (5), 1450–57. https://doi.org/10.1002/ep.12377

Trivedi, S.; Alshehri, M. A.; Aziz, A. T.; Panneerselvam, C.; Al-Aoh, H. A.; Maggi, F.; Sut, S.; Dall'Acqua, S. Insecticidal, Antibacterial and Dye Adsorbent Properties of Sargassum Muticum Decorated Nano-Silver Particles. *South African Journal of Botany*, **2021**, 139, 432–41. https://doi.org/10.1016/j.sajb.2021.03.002

Wang, T.; Zhai, Y.; Zhu, Y.; Li, C.; Zeng, G. A Review of the Hydrothermal Carbonization of Biomass Waste for Hydrochar Formation: Process Conditions, Fundamentals, and Physicochemical Properties. *Renewable and Sustainable Energy Reviews*, **2018**, 90, 223–47. https://doi.org/10.1016/j.rser.2018.03.071

Xie, L.; Ding, K.; Liu, Y.; Zou, M.; Han, C. Experimental, Thermodynamic and Kinetic Studies for the Adsorption of Phenolic Compounds Derived from Oilfield Wastewater by the Corncob Hydrochar. *Open Journal of Yangtze Oil and Gas*, **2019**, 04, 286–301. https://doi.org/10.4236/ojogas.2019.44023

Concluding Remarks and Future Perspectives

Innovation and the development of sustainable materials have become increasingly crucial in the current context of climate change and the growing concern about environmental pollution. Specifically, pollution from heavy metal ions and organic molecules that accumulate in water and soil seriously threatens the environment and human health. These pollutants can have a range of harmful effects in both the short and long term. In pollutant detection, several environmentally friendly and sustainable materials have emerged. These materials include “carbon dots,” “nanobiochar”, and “hydrochar.” They have their high carbon content in common, and they can all be obtained from biomass, making them ecologically sustainable and reducing our dependence on fossil carbon sources. These materials offer significant potential to enhance the ability of the actual system to detect and monitor pollutants efficiently and in an environmentally responsible manner. This thesis work explores the methods, advantages, and applications of these sustainable products in the context of pollutant detection. Carbon nanodots have garnered significant interest in the scientific community due to their versatility, photoluminescent properties, biocompatibility, and stability in aqueous solutions. The synthesis of CDs involves environmentally friendly and economically advantageous techniques, such as the hydrothermal conversion of waste biomass. The accumulation of waste biomass poses a significant management problem. Biomass-derived CDs have the advantage of being self-functionalized with specific chemical groups, which can easily be used to chelate or bind divalent metals or organic groups. Their high sensitivity and selectivity have made them excellent candidates for developing systems to detect heavy metal ions in solutions like lead, cadmium, and mercury, as well as organic pollutants like

nitrobenzene, which can severely affect human health and the ecosystem. Nanobiochar is an innovative material obtained through the hydrothermal processing of biomass, and it possesses nanometer-scale dimensions slightly more extensive than carbon nanodots. Nanobiochar has demonstrated promising properties, including a high surface area, thermal and chemical stability, and a porous structure. These characteristics have made it a key player in various applications, such as water filtration processes and soil quality monitoring. Thanks to its studied properties, the char produced from nanobiochar has proven to be an intriguing alternative for efficiently removing organic and inorganic contaminants. These contaminants include pesticides, heavy metals, and volatile organic compounds. As a result, nanobiochar contributes significantly to providing safe drinking water in numerous regions across the globe.

Furthermore, using nano biochar derived from waste biomass sources, such as orange peels, positively impacts waste management. It offers opportunities to reduce waste and alleviate the environmental burden of disposal facilities. Hydrochar can be a potent adsorbent for removing pollutants from industrial and domestic wastewater. Its remarkable capacity to adsorb pollutants, including persistent organic contaminants (POPs), plays a pivotal role in purifying water before it is released into the environment. Moreover, during hydrothermal conversion, hydrochar can be transformed into biochar, which can subsequently be utilized as a renewable energy source through combustion or gasification. This conversion process contributes to the generation of clean energy but also aids in reducing carbon emissions.

The choice of the system used in an environmental monitoring application is closely tied to the material, significantly influencing the final performance. In this context, we monitored three key areas: electrochemical, fluorescent, and chemical adsorption systems. Each of these systems offers unique advantages

and considerations. The fluorescence-based detection system stands out for its speed and high selectivity. However, it is essential to note that this system applies only to materials that possess fluorescent properties. In this regard, carbon dots have emerged as the ideal candidates, enabling the monitoring of heavy metals in water. Carbon dots have the intrinsic property of fluorescence, which becomes particularly valuable when introduced into a solution containing heavy metals. In the presence of heavy metals, carbon dots respond by diminishing the intensity of their fluorescence emission or even wholly extinguishing it. This response depends on the chemical affinities established with the relevant ions, allowing for a susceptible and selective detection mechanism. Adsorption techniques eliminate pollutants or other substances from a matrix, such as water, soil, or air, by inducing these substances to adhere to a solid surface called an adsorbent. These approaches leverage the extensive surface areas or significant porosity of certain materials and find widespread use in various applications, encompassing environmental, industrial, and laboratory contexts. Specifically, liquid-phase adsorption entails the passage of a liquid through a solid adsorbent material. For instance, columns filled with adsorbent material in wastewater treatment are deployed to extract organic contaminants, heavy metals, or other impurities from the liquid. In this study, the selection of the adsorbent material centered on hydrochar derived from aquatic weeds. Thanks to its inherent high porosity and surface area, this carbonaceous material, without the need for functionalization or activation, exhibited outstanding adsorption capabilities, effectively removing a substantial percentage of organic pollutants.

However, electrochemical sensors have emerged as the most promising techniques. A sensor is a technological device meticulously engineered to detect and measure specific quantities or characteristics in the surrounding environment or within a system. It accomplishes this by converting these

measurements into electrical or digital signals, which are subsequently recorded and processed by specialized instruments. In environmental monitoring, electrochemical sensors present many advantages, including ease of operation, high sensitivity, and the capacity to monitor a broad spectrum of measurements. The electrochemical analysis is intricately influenced by an array of aspects encompassing those tied to the instrument itself (for instance, in a voltammetric analysis, the choice of the deposition voltage and its duration), aspects linked to the ongoing redox process (such as the ability to scrutinize the oxidation or reduction peak and ascertain if the process is reversible), considerations regarding the material employed (including whether it necessitates the incorporation of a membrane-like Nafion to improve sensor stability), and factors associated with the operational environment (ranging from external temperature to solution pH and the potential formation of precipitates, among others). These parameters are pivotal in determining the most suitable material for a specific analyte and the optimal methodology (potentiometric, voltammetric, amperometric, etc.). The screen-printed electrochemical sensors used in this work are cost-effective, easy to customize, and rapid response times. The selectivity of their response to the compounds employed hinged on the specific material chosen for the respective analysis.

Continuous advancements in synthesizing novel green materials pave the way for very effective pollutant detection technologies. These measures protect human health and contribute to environmental preservation, presenting a vision of a cleaner and more sustainable society in the future.

Other Activities

Scientific production (chronological order)

nanomaterials

MDPI

Review

Graphene Quantum Dots by Eco-Friendly Green Synthesis for Electrochemical Sensing: Recent Advances and Future Perspectives

Viviana Bressi, Angelo Ferlazzo, Daniela Iannazzo and Claudia Espro *

Dipartimento di Ingegneria, Università di Messina, Contrada di Dio, Vill. S. Agata, I-98166 Messina, Italy; viviana.bressi@unime.it (V.B.); angelo.ferlazzo@unime.it (A.F.); diannazzo@unime.it (D.I.)
* Correspondence: espro@unime.it

Abstract: The continuous decrease in the availability of fossil resources, along with an evident energy crisis, and the growing environmental impact due to their use, has pushed scientific research towards the development of innovative strategies and green routes for the use of renewable resources, not only in the field of energy production but also for the production of novel advanced materials and platform molecules for the modern chemical industry. A new class of promising carbon nanomaterials, especially graphene quantum dots (GQDs), due to their exceptional chemical-physical features, have been studied in many applications, such as biosensors, solar cells, electrochemical devices, optical sensors, and rechargeable batteries. Therefore, this review focuses on recent results in GQDs synthesis by green, easy, and low-cost synthetic processes from eco-friendly raw materials and biomass-waste. Significant advances in recent years on promising recent applications in the field of electrochemical sensors, have also been discussed. Finally, challenges and future perspectives with possible research directions in the topic are briefly summarized.

Keywords: graphene quantum dots; electrochemical sensors; biomass; green synthesis

check for updates

Citation: Bressi, V.; Ferlazzo, A.; Iannazzo, D.; Espro, C. Graphene Quantum Dots by Eco-Friendly Green Synthesis for Electrochemical Sensing: Recent Advances and Future Perspectives. Nanomaterials 2021, 11, 1120. https://doi.org/10.3390/nano11051120

Academic Editor: Yurii K. Gun'ko

Received: 2 April 2021
Accepted: 22 April 2021
Published: 26 April 2021

Publisher's Note: MDPI stays neutral with regard to jurisdictional claims in published maps and institutional affiliations.

1. Introduction

Over the last thirty years, both academic and industrial chemical research has increasingly oriented towards a holistic vision focused on pollution, use of renewable sources, and waste reduction, leading to the generation of a new concept of chemistry, called Green Chemistry, which with its 12 principles aims to redirect the chemical industry along paths of eco-sustainability. Indeed, sustainable development, which has become increasingly central to scientific and technological progress in the last century, requires chemistry to play a primary role in the conversion of old technologies into new "clean" processes and in the design of new products and new processes that are more eco-friendly, breaking the old paradigms based on the generation of large amounts of waste and the wide use of petrochemicals. One of the most important goals of green chemistry and resource efficiency, as stated in the seventh principle, is the design and development of synthetic approaches

REVIEW: **Bressi, V**., Ferlazzo, A., Iannazzo, D., Espro, C. "*Graphene Quantum Dots by Eco-Friendly Green Synthesis for Electrochemical Sensing: Recent Advances and Future Perspectives*", Nanomaterials 2021, 11, https://doi.org/10.3390/nano11051120

applied sciences

MDPI

Article

Hydrothermal Carbonization as Sustainable Process for the Complete Upgrading of Orange Peel Waste into Value-Added Chemicals and Bio-Carbon Materials

Antonella Satira [1,2], Emilia Paone [1,3,*], Viviana Bressi [2], Daniela Iannazzo [2], Federica Marra [4], Paolo Salvatore Calabrò [4], Francesco Mauriello [1] and Claudia Espro [2,*]

[1] Dipartimento DICEAM, Università Mediterranea di Reggio Calabria, Loc. Feo di Vito, 89122 Reggio Calabria, Italy; antonella.satira@unirc.it (A.S.); paolo.calabro@unirc.it (P.S.C.); francesco.mauriello@unirc.it (F.M.)
[2] Dipartimento di Ingegneria, Università di Messina, Contrada di Dio—Vill. S. Agata, 98166 Messina, Italy; viviana.bressi@unime.it (V.B.); diannazzo@unime.it (D.I.)
[3] Consorzio Interuniversitario per la Scienza e la Tecnologia dei Materiali (INSTM), 50121 Firenze, Italy
[4] Dipartimento di Agraria, Università Mediterranea di Reggio Calabria, Loc. Feo di Vito, 89122 Reggio Calabria, Italy; fede.marra6@gmail.com
* Correspondence: emilia.paone@unirc.it (E.P.); espro@unime.it (C.E.)

Featured Application: Hydrothermal carbonization process can be efficiently used for the simultaneous production of value-added chemicals, including furans and levulinates, and carbon-based materials.

Abstract: In this study, a simple and green protocol to obtain hydrochar and high-added value products, mainly 5-hydroxymethylfurfural (5-HMF), furfural (FU), levulinic acid (LA) and alkyl levulinates, by using the hydrothermal carbonization (HTC) of orange peel waste (OPW) is presented. Process variables, such as reaction temperature (180–300 °C), reaction time (60–300 min), biomass:water ratio and initial pH were investigated in order to find the optimum conditions that maximize both the yields of solid hydrochar and 5-HMF and levulinates in the bio-oil. Data obtained evidence that the highest yield of hydrochar is obtained at a 210 °C reaction temperature, 180 min residence time, 6/1 w/w orange peel waste to water ratio and a 3.6 initial pH. The bio-products distribution strongly depends on the applied reaction conditions. Overall, 180 °C was found to be the best reaction temperature that maximizes the production of furfural and 5-HMF in the presence of pure water as a reaction medium.

Keywords: orange peel waste (OPW); hydrothermal carbonization; hydrochar; 5-hydroxymethylfurfural (5-HMF); furfural (FU); levulinic acid (LA)

Citation: Satira, A.; Paone, E.; Bressi, V.; Iannazzo, D.; Marra, F.; Calabrò, P.S.; Mauriello, F.; Espro, C. Hydrothermal Carbonization as Sustainable Process for the Complete Upgrading of Orange Peel Waste into Value-Added Chemicals and Bio-Carbon Materials. *Appl. Sci.* **2021**, *11*, 10983. https://doi.org/10.3390/app112210983

Academic Editor: Luca Fiori

Received: 19 October 2021
Accepted: 17 November 2021
Published: 19 November 2021

Publisher's Note: MDPI stays neu-

ARTICLE: Satira, A., Paone, E., **Bressi, V**., Iannazzo, D., Marra, F., Calabrò, P. S., Mauriello, F., Espro, C. "*Hydrothermal carbonization as sustainable process for the complete upgrading of orange peel waste into value-added chemicals and bio-carbon materials*", Applied Sciences 2021, 11, https://doi.org/10.3390/app112210983

sensors

MDPI

Article

On the Electroanalytical Detection of Zn Ions by a Novel Schiff Base Ligand-SPCE Sensor

Viviana Bressi [1], Zahra Akbari [1,2], Morteza Montazerozohori [2], Angelo Ferlazzo [1], Daniela Iannazzo [1], Claudia Espro [1,*] and Giovanni Neri [1,*]

[1] Department of Engineering, University of Messina, I-98166 Messina, Italy; vbressi@unime.it (V.B.); zakbari@unime.it (Z.A.); angelo.ferlazzo@unime.it (A.F.); daniela.iannazzo@unime.it (D.I.)
[2] Department of Chemistry, Yasouj University, Yasouj 75914-4831, Iran; mzerozohori@mail.yu.ac.ir
* Correspondence: espro@unime.it (C.E.); gneri@unime.it (G.N.)

Abstract: A novel bidentate Schiff base (L) is here proposed for the detection of Zn ions in water. The structure of the synthesized Schiff base L was characterized by FT-IR, ^{1}H NMR and ^{13}C NMR. Optical characteristics were addressed by UV-Visible spectroscopy and Photoluminescence (PL) measurements. PL demonstrated that L displays a "turn-off" type fluorescence quenching in the presence of Zn^{2+} ion in aqueous solution, indicating its ability to preferentially coordinate this ion. Based on these findings, an L-M (where M is a suitable membrane) modified screen-printed carbon electrode (SPCE) was developed to evaluate the electrochemical behavior of the Schiff base (L) with the final objective of undertaking the electroanalytical determination of Zn ions in water. Using various electrochemical techniques, the modified L-M/SPCE sensor demonstrates high sensitivity and selectivity to Zn ions over some common interferents ions, such as Ca^{2+}, Mg^{2+}, K^+, Ni^{++} and Cd^{++}. The potentiometric response of the L-M/SPCE sensor to Zn ions was found to be linear over a relatively wide concentration range from 1 µM to 100 mM.

Keywords: Schiff base; fluorescence; electrochemical sensors; heavy metals; trace analysis of pollutants and contaminants

check for updates

Citation: Bressi, V.; Akbari, Z.; Montazerozohori, M.; Ferlazzo, A.; Iannazzo, D.; Espro, C.; Neri, G. On the Electroanalytical Detection of Zn Ions by a Novel Schiff Base Ligand-SPCE Sensor. *Sensors* **2022**, *22*, 900. https://doi.org/10.3390/s22030900

Academic Editor: Katarzyna Tyszczuk-Rotko

Received: 20 December 2021
Accepted: 20 January 2022
Published: 25 January 2022

1. Introduction

Schiff base ligands have been known about for a very long time and can be easily synthesized by condensation reactions of primary amines and carbonyl compounds in which the characteristic azomethine bond is formed [1]. Interest in Schiff bases has rapidly grown, and they played a central role in the development of coordination chemistry due to their unique properties, including high stability and selectivity to metal coordination, good reproducibility, more active sites and good homogeneity, making them particularly attractive in the field of metal ion recognition, especially by means of optical techniques [2–4].

In recent decades, electrochemical sensors have received great attention due to their good versatility in heavy metal ion detection. Several Schiff bases have been used in the

ARTICLE: **Bressi, V.**, Akbari, Z., Montazerozohori, M., Ferlazzo, A., Iannazzo, D., Espro, C., Neri, G. "*On the Electroanalytical Detection of Zn Ions by a Novel Schiff Base Ligand-SPCE Sensor*", Sensors 2022, 22, https://doi.org/10.3390/s22030900

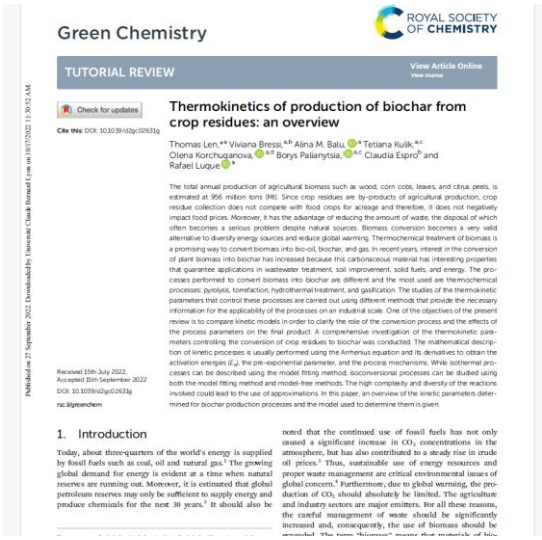

Green Chemistry

ROYAL SOCIETY OF CHEMISTRY

TUTORIAL REVIEW

View Article Online

Check for updates

Thermokinetics of production of biochar from crop residues: an overview

Thomas Len,[a,b] Viviana Bressi,[a,b] Alina M. Balu,[a] Tetiana Kulik,[a,c] Olena Korchuganova,[a,d] Borys Palianytsia,[a,c] Claudia Espro[b] and Rafael Luque[a]

Cite this: DOI: 10.1039/d2gc02631g

Received 15th July 2022,
Accepted 15th September 2022
DOI: 10.1039/d2gc02631g
rsc.li/greenchem

The total annual production of agricultural biomass such as wood, corn cobs, leaves, and citrus peels, is estimated at 956 million tons (Mt). Since crop residues are by-products of agricultural production, crop residue collection does not compete with food crops for acreage and therefore, it does not negatively impact food prices. Moreover, it has the advantage of reducing the amount of waste, the disposal of which often becomes a serious problem despite natural sources. Biomass conversion becomes a very valid alternative to diversify energy sources and reduce global warming. Thermochemical treatment of biomass is a promising way to convert biomass into bio-oil, biochar, and gas. In recent years, interest in the conversion of plant biomass into biochar has increased because this carbonaceous material has interesting properties that guarantee applications in wastewater treatment, soil improvement, solid fuels, and energy. The processes performed to convert biomass into biochar are different and the most used are thermochemical processes: pyrolysis, torrefaction, hydrothermal treatment, and gasification. The studies of the thermokinetic parameters that control these processes are carried out using different methods that provide the necessary information for the applicability of the processes on an industrial scale. One of the objectives of the present review is to compare kinetic models in order to clarify the role of the conversion process and the effects of the process parameters on the final product. A comprehensive investigation of the thermokinetic parameters controlling the conversion of crop residues to biochar was conducted. The mathematical description of kinetic processes is usually performed using the Arrhenius equation and its derivatives to obtain the activation energies (E_a), the pre-exponential parameter, and the process mechanisms. While isothermal processes can be described using the model fitting method, isoconversional processes can be studied using both the model fitting method and model-free methods. The high complexity and diversity of the reactions involved could lead to the use of approximations. In this paper, an overview of the kinetic parameters determined for biochar production processes and the model used to determine them is given.

1. Introduction

Today, about three-quarters of the world's energy is supplied by fossil fuels such as coal, oil and natural gas.[1] The growing global demand for energy is evident at a time when natural reserves are running out. Moreover, it is estimated that global petroleum reserves may only be sufficient to supply energy and produce chemicals for the next 30 years.[1] It should also be noted that the continued use of fossil fuels has not only caused a significant increase in CO_2 concentrations in the atmosphere, but has also contributed to a steady rise in crude oil prices.[2] Thus, sustainable use of energy resources and proper waste management are critical environmental issues of global concern.[3] Furthermore, due to global warming, the production of CO_2 should absolutely be limited. The agriculture and industry sectors are major emitters. For all these reasons, the careful management of waste should be significantly increased and, consequently, the use of biomass should be

REVIEW: Len, T., **Bressi, V.**, Balu, A. M., Kulik, T., Korchuganova, O., Palianytsia, B., Espro, C., Luque, R. "*Thermokinetics of production of biochar from crop residues: an overview*", Green Chemistry 2022, 24, https://doi.org/10.1039/D2GC02631G

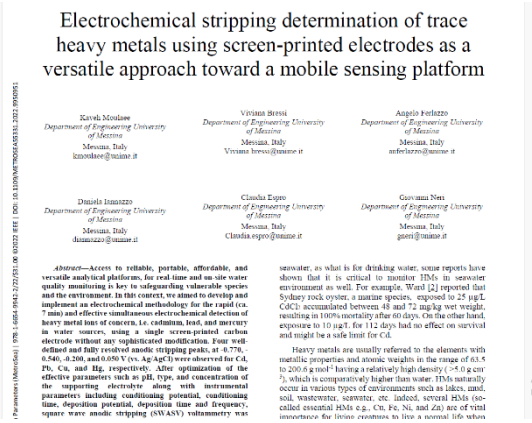

Electrochemical stripping determination of trace heavy metals using screen-printed electrodes as a versatile approach toward a mobile sensing platform

Kaveh Moulaee
Department of Engineering University of Messina
Messina, Italy
kmoulaee@unime.it

Viviana Bressi
Department of Engineering University of Messina
Messina, Italy
Viviana.bressi@unime.it

Angelo Ferlazzo
Department of Engineering University of Messina
Messina, Italy
anferlazzo@unime.it

Daniela Iannazzo
Department of Engineering University of Messina
Messina, Italy
diannazzo@unime.it

Claudia Espro
Department of Engineering University of Messina
Messina, Italy
Claudia.espro@unime.it

Giovanni Neri
Department of Engineering University of Messina
Messina, Italy
gneri@unime.it

Abstract—Access to reliable, portable, affordable, and versatile analytical platforms, for real-time and on-site water quality monitoring is key to safeguarding vulnerable species and the environment. In this context, we aimed to develop and implement an electrochemical methodology for the rapid (ca. 7 min) and effective simultaneous electrochemical detection of heavy metal ions of concern, i.e. cadmium, lead, and mercury in water sources, using a single screen-printed carbon electrode without any sophisticated modification. Four well-defined and fully resolved anodic stripping peaks, at -0.770, -0.540, -0.200, and 0.050 V (vs. Ag/AgCl) were observed for Cd, Pb, Cu, and Hg, respectively. After optimization of the effective parameters such as pH, type, and concentration of the supporting electrolyte along with instrumental parameters including conditioning potential, conditioning time, deposition potential, deposition time and frequency, square wave anodic stripping (SWASV) voltammetry was

seawater, as what is for drinking water, some reports have shown that it is critical to monitor HMs in seawater environment as well. For example, Ward [2] reported that Sydney rock oyster, a marine species, exposed to 25 µg/L CdCl2 accumulated between 48 and 72 mg/kg wet weight, resulting in 100% mortality after 60 days. On the other hand, exposure to 10 µg/L for 112 days had no effect on survival and might be a safe limit for Cd.

Heavy metals are usually referred to the elements with metallic properties and atomic weights in the range of 63.5 to 200.6 g mol-1 having a relatively high density (>5.0 g cm-3), which is comparatively higher than water. HMs naturally occur in various types of environments such as lakes, mud, soil, wastewater, seawater, etc. Indeed, several HMs (so-called essential HMs e.g., Cu, Fe, Ni, and Zn) are of vital importance for living creatures to live a normal life when

CONFERENCE PAPER: Moulaee, K., **Bressi, V.**, Ferlazzo, A., Iannazzo, D., Espro, C., Neri, G. "*Electrochemical stripping determination of trace heavy metals using screen-printed electrodes as a versatile approach toward a mobile sensing platform*", IEEE International Workshop on Metrology for the Sea; MetroSea 2022, 164–167.

Available online at www.sciencedirect.com
ScienceDirect
Current Opinion in Green and Sustainable Chemistry
ELSEVIER

Recent advances in the synthesis of carbon dots from renewable biomass by high-efficient hydrothermal and microwave green approaches

Viviana Bressi[1,2], Alina M. Balu[2], Daniela Iannazzo[1] and Claudia Espro[1]

Abstract
Carbon dots (CDs), a class of novel zero-dimensional nanomaterials, have recently emerged as excellent candidates for versatile applications in several fields due to their superior properties such as excellent photostability and biocompatibility, low cytotoxicity, small size, fluorescence, and ease of surface modification. The use of a more environmentally friendly source to produce high-quality CDs remains a crucial issue to be addressed. "Green" CDs have attracted a lot of attention recently and renewable biomass, especially waste biomass, is a good choice for large-scale CDs synthesis because it not only promotes outstanding properties, has excellent properties but also provides a green solution to balance waste management goals with those of the circular economy. Here, we highlight recent advances in green synthesis and formation mechanism of CDs from biomass, focusing on innovative one-pot hydrothermal and microwave processes.

Addresses
[1] Department of Engineering, University of Messina, C.da di Dio S. Agata, 1-98166 Messina, Italy
[2] Departamento de Química Organica, Universidad de Cordoba, Campus de Rabanales, Edificio Marie Curie (C-3), Ctra Nnal IV-A, Km 396, Cordoba, Spain

Corresponding author: Espro, Claudia (claudia.espro@unime.it)

Current Opinion in Green and Sustainable Chemistry 2023, **40**:100742

This review comes from a themed issue on **New Synthetic Methods (2023)**

Edited by **Salvatore V. Giofré** and **Daniela Iannazzo**

Available online 14 December 2022

For complete overview of the section, please refer the article collection - New Synthetic Methods (2023)

https://doi.org/10.1016/j.cogsc.2022.100742

2452-2236/© 2022 Elsevier B.V. All rights reserved.

Keywords

Green processes for carbon dots (CDs) synthesis from biomass renewable precursors

Green chemistry's roots in the Pollution Prevention Act of 1990 and the subsequent formulation of the 12 principles for chemical synthesis by Anastas and Warner [12], have addressed our future challenges aiming to design and produce cost-competitive chemical products and processes that attain the highest level of the pollution-prevention hierarchy by reducing contamination at its source. Therefore, with a view to the implementation of the Green Chemistry principles, correlated to conventional sources, natural carbon precursors are more favourable for the production of CDs due to their low cost, environmental friendliness, and increased

nanotubes, and later, identified by Sun et al. [2]. Since their exceptional structure and size afford them outstanding chemical, physical, and optical features, recently, much attention has been paid to the synthesis methods of CDs [3]. Early CDs syntheses employed top-down approaches whereby, through multiple steps, strong chemicals, and expensive equipment were used to convert larger grains into smaller ones on the nanometer scale via electrochemical oxidation [4], arc discharge [5], and laser ablation [6]. The synthesis of CDs is still challenging, but recently, bottom-up green approaches, whereby, small renewable molecules undergo pyrolysis or carbonization to form nanosized CDs, are more and more striking meeting the urgent need for large-scale synthesis of CDs, with a view on the sustainable development and the circular economy concept. A great interest of the scientific community is focused on the implementation of technologies not yet widely explored, exhibiting low cost, eco-friendliness, and easy chemical functionalization [7–11] to obtain CDs from biomass and biowastes. On these bases, our attempt is to provide an overview of the latest two year's trends in the innovative strategies and the renewable feedstock used.

REVIEW: **Bressi, V.**, Balu, A.M., Iannazzo, D., Espro, C. "*Recent advances in the synthesis of carbon dots from renewable biomass by high-efficient hydrothermal and microwave green approaches*", Current Opinion in Green and Sustainable Chemistry 2023, 40, https://doi.org/10.1016/j.cogsc.2022.100742

ChemElectroChem

Research Article
doi.org/10.1002/celc.202300004

Chemistry Europe

www.chemelectrochem.org

Voltammetric Sensor Based on Waste-Derived Carbon Nanodots for Enhanced Detection of Nitrobenzene

Viviana Bressi,[a, b] Isabella Chiarotto,*[c] Angelo Ferlazzo,[a] Consuelo Celesti,[a, d] Cinzia Michenzi,[c] Thomas Len,[b] Daniela Iannazzo,[a] Giovanni Neri,[a] and Claudia Espro*[a]

Carbon dots (CDs) samples were synthesized from orange peel waste (OPW) via a simple and eco-friendly hydrothermal carbonization (HTC) and electrochemical (EC) bottom-up synthesis integrated approach. The comprehensive chemical-physical characterization of CDs samples, carried out by various techniques such as TEM, EDX, XRD, FT-IR, underlined their morphological and microstructural features. The CDs exhibited attractive electrochemical properties, and thus an electrochemical sensor by modifying a screen printed carbon electrode (CDs/SPCE) for the detection of nitrobenzene (NB) in water was developed. Electroanalytical performances of CDs/SPCE sensor using differential pulse voltammetry (DPV) demonstrated its high sensitivity (9.36 μA μM^{-1} cm^{-2}) towards NB in a wide linear dynamic range (0.1–2000 μM) and a low limit of detection (LOD = 13 nM). The electrochemical sensor also shown high selectivity, long-term stability, and repeatability. This paper might open the way to a new synergistic HTC-EC approach for the synthesis of CDs from waste biomass material and their advanced application in highly efficient electrochemical sensors.

Introduction

The orange juice industry produces large amounts of orange peel waste (OPW) each year, which requires proper management, taking into account the high biodegradability of orange processing waste, which causes rapid fermentation.[1–4] Both from the economical and eco-friendly points of point of view, wastes of industrial and agricultural processes are very attractive for their low cost and to chance to recover the manufactured side-products and reconvert them to useful materials. Therefore, the production of new carbon nanostructures from these wastes is highly demanding and covers a wide range of application fields.[5] Natural raw materials such as biomass and plant wastes are the most interesting feedstock for the synthesis of carbonaceous nanomaterials due to their high availability, environmental compatibility, and affinity with Green Chemistry principles.[6–8] Carbon dots (CDs), a new class of carbon-based zero-dimensional materials, typically less than ≈10 nm in diameter, exhibiting excellent photostability and biocompatibility, low cytotoxicity, fluorescence, and ease of surface modification, have attracted much attention due to their interesting properties, leading to diverse applications in catalysis, bio-imaging, drug delivery, and so on. In recent years, hydrothermal carbonization (HTC) has become the cornerstone of the synthesis of nanomaterials from natural sources thanks to the mild reaction conditions and the large amount of products obtained.[9–11] The HTC of the OPW, provides solid (hydro-char), liquid, and non-condensable gaseous products.[12,13] However, the aqueous phases generated from HTC treatment of OPW are generally considered as by-products, and there are few studies addressing their use as a resource for value-added chemicals.[14]

The electrochemical (EC) approach represents an efficient and easily repeatable method for the preparation of high-quality CDs,[15] starting from the liquid fraction obtained via the

[a] Dr. V. Bressi, Dr. A. Ferlazzo, Dr. C. Celesti, Prof. D. Iannazzo, Prof. G. Neri, Prof C. Espro
Department of Engineering
University of Messina
Contrada di Dio–Ms. S. Agata, I-98166 Messina (Italy)
E-mail: claudia.espro@unime.it
Homepage: https://archivio.unime.it/it/persona/claudia-espro
[b] Dr. V. Bressi, Dr. T. Len
Department of Organic Chemistry
University of Cordoba
Campus de Rabanales, Marie Curie (C-3), Ctra Nnal IV–A, Km 396 Cordoba (Spain)
[c] Prof. I. Chiarotto, Dr. C. Michenzi
Department of Basic and Applied Sciences for Engineering (SBAI)
Sapienza University of Rome
Via Castro Laurenziano, 7, 00161 Rome (Italy)
E-mail: isabella.chiarotto@uniroma1.it
Homepage: https://corsidilaurea.uniromal.it/it/users/isabellachiarottouniroma1it
[d] Dr. C. Celesti

Journal of Electroanalytical Chemistry 928 (2021) 117071

Contents lists available at ScienceDirect

Journal of Electroanalytical Chemistry

journal homepage: www.elsevier.com/locate/jelechem

ELSEVIER

Electrochemical determination of nitrites and sulfites by using waste-derived nanobiochar

A. Ferlazzo [a,*], V. Bressi [a,b], C. Espro [a], D. Iannazzo [a], E. Piperopoulos [a], G. Neri [a]

[a] Department of Engineering, University of Messina, Cda Di Dio, I-98166 Messina, Italy
[b] Department of Organic Chemistry, Institute of Fine Chemistry and Nanochemistry, University of Cordoba, Campus de Rabanales, Edificio Marie Curie (C-3), Ctra Nnal IV-A, Km 396, Cordoba E1-14014, Spain

ARTICLE INFO

Keywords:
Nanobiochar
Orange peels waste
Electrochemical sensors
Nitrites
Sulfites

ABSTRACT

In this work, the development of an electrochemical sensor based on nanobiochar for the determination of nitrites and sulfites is reported. Nanobiochar was obtained from orange peel waste derived hydrochar synthesized by hydrothermal carbonization 180 °C. This nanomaterial (NBC180) was characterized by SEM, FT-IR, PL, XRD analysis and its chemical, physical, morphological and microstructural properties were compared with the starting hydrochar material (HTC180). NBC180 was deposited on a commercial screen-printed carbon electrode (SPCE) and its electrochemical characteristics were investigated through CV and EIS analysis. The NBC180/SPCE sensor exhibits better electrochemical properties than the bare SPCE sensor for the detection of sulfites and nitrites in water, showing two well-defined and separated anodic peaks at +0.45 and +0.67 V, respectively. Linear correlations between anodic peaks and sulfites and nitrites concentration were found up to 3200 μM and 1400 μM, respectively. This study demonstrates, for the first time, the promising capability of nanobiochar derived from orange peels waste product for the simultaneous electrochemical oxidation of sulfites and nitrites in real samples.

1. Introduction

In recent years, there has been an increase in interest in monitoring chemical substances used in the food industry and released into the environment. Among them, nitrites have a significant impact on human health. Nitrite ions are widely present in waters, [1] due to excessive use of fertilizers, wastewater pollution [2], and are widely used as preservatives in the production of meat and fishery products [3]. Excessive nitrites entering the human body introduced with food can lead to the formation of intestinal cancers, due to the transformation of nitrites into N-nitrosamines in the stomach [4]. In addition, nitrites can bind to the hemoglobin in the blood and reduce its ability to oxygen transport [5–7].

Like nitrites, sulfites are also found in many drinks and foods, which can lead to numerous allergic reactions and various illnesses such as nausea, asthma, headaches, etc. [8,9]. Therefore, the Food and Drug Administration (FDA) asks not to exceed the dose of 50 mgL^{-1} in beer and 350 mgL^{-1} in wine [10]. The presence, of nitrites and sulfites in everyday life, is then very common. Therefore, the need arises to develop selective, rapid, and easy-to-use methods for detect-

develop sensors capable of simultaneously detecting these two contaminants [11,12]. For the single determination of these compounds, several analytical techniques, such as spectrophotometry [13,14], chemiluminescence [15,16], electrochemical [17,18], etc., have been proposed. There are, instead, few examples in the literature of their simultaneous and selective determination. Electrochemical sensors, based on gold nanoparticles [19], graphene-gold nanocomposite [20], potassium-doped graphene [21], and graphene nanocomposites [20,22], are the most investigated for the monitoring of these toxic ions. In recent years there has been growing interest in the use of carbon-derived nanomaterials for sensor development, such as graphene quantum dots used for the formation of various sensors, from metal ion detection [23] to cancer cell determination [24]. The excellent properties of carbon nanomaterials enable researchers to develop novel electrochemical detection strategies thanks to improved sensitivity, selectivity, and stability. In particular, the use of green and renewable sources for the synthesis of these nanomaterials shows considerable interest [25].

Among the several sources to produce carbon-derived nanomaterials, biomass such as forestry waste, municipal solid waste, and agricul-

ARTICLE: **Bressi, V**., Chiarotto, I.; Ferlazzo, A.; Celesti, C.; Michenzi, C.; Len, T.; Iannazzo, D.; Neri, G.; Espro, C. "*Voltammetric Sensor Based on Waste-Derived Carbon Nanodots for Enhanced Detection of Nitrobenzene*", ChemElectroChem 2023, 10, https://doi.org/10.1002/celc.202300004

ARTICLE: Ferlazzo, A.; **Bressi, V**.; Espro, C.; Iannazzo, D.; Piperopoulos, E.; Neri, G. "*Electrochemical determination of nitrites and sulfites by using waste-derived nanobiochar*", Journal of Electroanalytical Chemistry2023,928 https://doi.org/10.1016/j.jelechem.2022.117071

Molecular Catalysis 544 (2023) 113182

Contents lists available at ScienceDirect

Molecular Catalysis

journal homepage: www.journals.elsevier.com/molecular-catalysis

Electrochemical *bottom-up* synthesis of biomass-derived carbon dots for promoting Knoevenagel condensation

Cinzia Michenzi, Claudia Espro, Viviana Bressi, Consuelo Celesti, Fabrizio Vetica, Chiara Salvitti, Isabella Chiarotto

ARTICLE INFO

ABSTRACT

Introduction

ARTICLE: Michenzi, C.; Espro, C.; **Bressi, V.**; Celesti, C.; Vetica, F.; Salvitti, C.; Chiarotto, I. "*Electrochemical bottom-up synthesis of biomass-derived carbon dots for promoting Knoevenagel condensation*", Molecular Catalysis 2023, 544, https://doi.org/10.1016/j.mcat.2023.113182

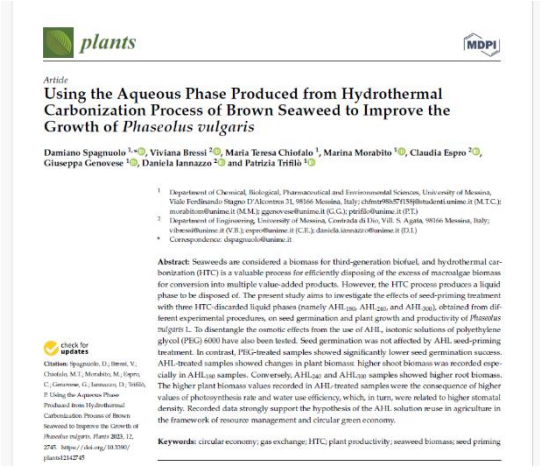

plants

MDPI

Article

Using the Aqueous Phase Produced from Hydrothermal Carbonization Process of Brown Seaweed to Improve the Growth of *Phaseolus vulgaris*

Damiano Spagnuolo, Viviana Bressi, Maria Teresa Chiofalo, Marina Morabito, Claudia Espro, Giuseppa Genovese, Daniela Iannazzo and Patrizia Trifilò

Abstract: Seaweeds are considered a biomass for third-generation biofuel, and hydrothermal carbonization (HTC) is a valuable process for efficiently disposing of the excess of macroalgae biomass for conversion into multiple value-added products. However, the HTC process produces a liquid phase to be disposed of. The present study aims to investigate the effects of seed-priming treatment with three HTC-discarded liquid phases (namely AHL_{180}, AHL_{240}, and AHL_{300}), obtained from different experimental procedures, on seed germination and plant growth and productivity of *Phaseolus vulgaris* L. To disentangle the osmotic effects from the use of AHL, isotonic solutions of polyethylene glycol (PEG) 6000 have also been tested. Seed germination was not affected by AHL seed-priming treatment. In contrast, PEG-treated samples showed significantly lower seed germination success. AHL-treated samples showed changes in plant biomass: higher shoot biomass was recorded especially in AHL_{180} samples. Conversely, AHL_{240} and AHL_{300} samples showed higher root biomass. The higher plant biomass values recorded in AHL-treated samples were the consequence of higher values of photosynthesis rate and water use efficiency, which, in turn, were related to higher stomatal density. Recorded data strongly support the hypothesis of the AHL solution reuse in agriculture in the framework of resource management and circular green economy.

Keywords: circular economy; gas exchange; HTC; plant productivity; seaweed biomass; seed priming

ARTICLE: Spagnuolo, D.; **Bressi, V.**; Chiofalo, M.T.; Morabito, M.; Espro, C.; Genovese, G.; Iannazzo, D.; Trifilò, P. "*Using the Aqueous Phase Produced from Hydrothermal Carbonization Process of Brown Seaweed to Improve the Growth of Phaseolus vulgaris*", Plants (Basel) 2023, 12, https://doi.org/10.3390/plants12142745

chemosensors

MDPI

Article

A Sensitive and Selective Non-Enzymatic Dopamine Sensor Based on Nanostructured Co_3O_4–Fe_2O_3 Heterojunctions

Madiha Khan [1,2], Khoulood Abid [1,3], Angelo Ferlazzo [1], Viviana Bressi [1], Claudia Espro [1], Mozaffar Hussain [2], Antonino Foti [3], Pietro Giuseppe Gucciardi [3] and Giovanni Neri [1,*]

Abstract: In the present work, a study was carried out with the aim of enhancing the performance of electrochemical biosensors based on Co_3O_4-Fe_2O_3 heterojunctions. Specifically, the redox behavior of screen-printed carbon electrodes (SPCEs) modified with Co_3O_4-Fe_2O_3 (0.5 wt%± wt%) nanocomposites, where x ranged from 0.1 to 0.5 wt%, was examined in detail. The hybrid nanocomposites were synthesized using the sol-gel auto-combustion method. Several characterization methods were performed to investigate the morphology, microstructure, and surface area of the pure Co_3O_4, pure Fe_2O_3, and the synthesized Co_3O_4-Fe_2O_3 nanocomposites. Using cyclic voltammetry (CV) tests, the electrochemical behavior of the modified electrodes toward the dopamine (DA) molecules was investigated. The modified Co_3O_4-Fe_2O_3 (0.5 wt%, x = 0.4 wt%)/SPCE resulted in a sensor with the best electrochemical performance toward DA. A high linear relationship between DA concentrations and the faradic current variation (I_{pa} (μA) = 0.0736 + 0.1031 C_{DA} (μA) and R^2 = 0.99) was found in the range of 10–100 μM. The sensitivity value was computed to be 0.604 μA μM^{-1} cm^{-2} and the limit of detection (LOD) 0.24 μM. Based on the characterization and electrochemical results, it can be suggested that the formation of Co_3O_4-Fe_2O_3 heterostructures provides a large specific surface area, an increased number of electroactive sites at the metal oxide interface and a p–n heterojunction, thus ensuring a remarkable enhancement in the electrochemical response towards DA.

Keywords: metal oxide; nanocomposites; dopamine electrochemical detection; biosensors

1. Introduction

Dopamine (DA) is a neurotransmitter secreted directly by the brain, capable of activating cellular response. It is also related to spreading pleasure and the habit of drugs. Low levels of DA are responsible for the onset of diseases such as Parkinson's disease. Accumulation can also lead to numerous diseases, such as cardiovascular disease, Alzheimer's disease, and cancer [1–4]. Thus, it is fundamental to detect DA precisely and efficiently. Numerous approaches have been established to identify this biomolecule, including photoluminescence, spectrophotometry, electrochemical sensors, and chemoluminescence [5]. Electrochemical sensors appeal to our consideration because of their high sensitivity, low cost, and time-saving features [6].

ARTICLE: Khan, M.; Abid, K.; Ferlazzo, A.; **Bressi, V.**; Espro, C.; Hussain, M.; Foti, A.; Gucciardi, P.G.; Neri, G. "*A Sensitive and Selective Non-Enzymatic Dopamine Sensor Based on Nanostructured Co_3O_4–Fe_2O_3 Heterojunctions*", Chemosensors 2023, 11. https://doi.org/10.3390/chemosensors11070379

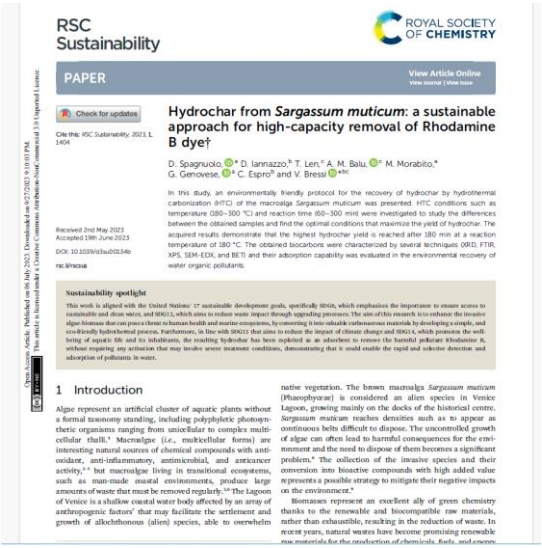

RSC Sustainability

ROYAL SOCIETY OF CHEMISTRY

PAPER

View Article Online

Check for updates

Hydrochar from *Sargassum muticum*: a sustainable approach for high-capacity removal of Rhodamine B dye†

D. Spagnuolo, D. Iannazzo, T. Len, A. M. Balu, M. Morabito, G. Genovese, C. Espro and V. Bressi

In this study, an environmentally friendly protocol for the recovery of hydrochar by hydrothermal carbonization (HTC) of the macroalga *Sargassum muticum* was presented. HTC conditions such as temperature (180–300 °C) and reaction time (60–300 min) were investigated to study the differences between the obtained samples and find the optimal conditions that maximize the yield of hydrochar. The acquired results demonstrate that the highest hydrochar yield is reached after 180 min at a reaction temperature of 180 °C. The obtained biocarbons were characterized by several techniques (XRD, FTIR, XPS, SEM-EDX, and BET) and their adsorption capability was evaluated in the environmental recovery of water organic pollutants.

Sustainability spotlight

This work is aligned with the United Nations' 17 sustainable development goals, specifically SDG6, which emphasizes the importance to ensure access to sustainable and clean water, and SDG12, which aims to reduce waste impact through upgrading processes. The aim of this research is to enhance the invasive algae biomass that can pose a threat to human health and marine ecosystems, by converting it into valuable carbonaceous materials by developing a simple, and eco-friendly hydrothermal process. Furthermore, in line with SDG13 that aims to reduce the impact of climate change and SDG14, which promotes the well-being of aquatic life and its inhabitants, the resulting hydrochar has been exploited as an adsorbent to remove the harmful pollutant Rhodamine B, without requiring any activation that may involve severe treatment conditions, demonstrating that it could enable the rapid and selective detection and adsorption of pollutants in water.

1 Introduction

Algae represent an artificial cluster of aquatic plants without a formal taxonomy standing, including polyphyletic photosynthetic organisms ranging from unicellular to complex multicellular thalli.[1] Macroalgae (*i.e.*, multicellular forms) are interesting natural sources of chemical compounds with antioxidant, anti-inflammatory, antimicrobial, and anticancer activity,[2–5] but macroalgae living in transitional ecosystems, such as man-made coastal environments, produce large amounts of waste that must be removed regularly.[6] The Lagoon of Venice is a shallow coastal water body affected by an array of anthropogenic factors' that may facilitate the settlement and growth of allochthonous (alien) species, able to overwhelm native vegetation. The brown macroalga *Sargassum muticum* (Phaeophyceae) is considered an alien species in Venice Lagoon, growing mainly on the docks of the historical centre. *Sargassum muticum* reaches densities such as to appear as continuous belts difficult to dispose. The uncontrolled growth of algae can often lead to harmful consequences for the environment and the need to dispose of them becomes a significant problem.[4] The collection of the invasive species and their conversion into bioactive compounds with high added value represents a possible strategy to mitigate their negative impacts on the environment.[4]

Biomasses represent an excellent ally of green chemistry thanks to the renewable and biocompatible raw materials, rather than exhaustible, resulting in the reduction of waste. In recent years, natural wastes have become promising renewable raw materials for the production of chemicals, fuels, and energy;

ARTICLE: Spagnuolo, D.; Iannazzo, D.; Len, T.; Balu, A. M.; Morabito, M.; Genovese, G.; Espro, C.; **Bressi, V.** "*Hydrochar from Sargassum muticum: a sustainable approach for high-capacity removal of Rhodamine B dye*", RSC Sustainability 2023, 1, https://doi.org/10.1039/d3su00134b

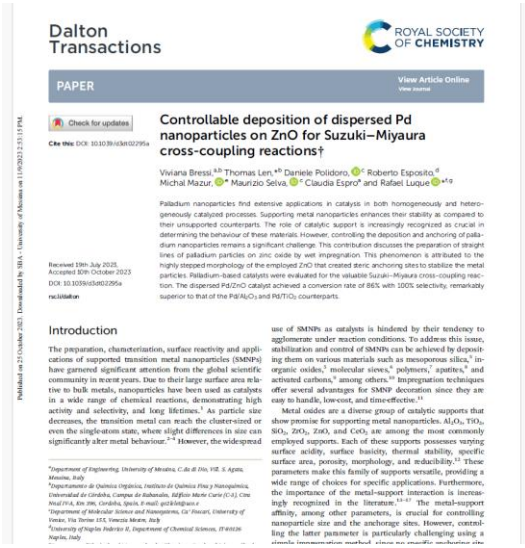

Dalton Transactions

ROYAL SOCIETY OF CHEMISTRY

PAPER

View Article Online

Check for updates

Controllable deposition of dispersed Pd nanoparticles on ZnO for Suzuki–Miyaura cross-coupling reactions†

Introduction

ARTICLE: **Bressi, V**.; Len, T.; Polidoro, D.; Esposito, R.; Mazur, M.; Selva, M.; Espro, C.; Luque, R. "*Controllable deposition of dispersed Pd nanoparticles on ZnO for Suzuki-Miyaura cross-coupling reactions*", Dalton Transactions, October 2023.

Scientific work submitted

ARTICLE: Guesmi, S.; **Bressi, V**.; Moulaee; K.; Kahri, H.; Khaskhoussi, A.; Espro, C.; Barhoumi, H.; Neri, G. "*Room Temperature Synthesis of Cu-MOF for Enzyme-Free Glucose Electrochemical Sensing*", Materials Advances, August 2023.

ARTICLE: **Bressi, V**.; Celesti, C.; Ferlazzo, A.; Len, T.; Moulaee, K.; Neri, G.; Espro, C.; Luque, R. "*Waste-derived Carbon Nanodots for Fluorimetric and Simultaneous Electrochemical Detection of Heavy Metals in Water*", Environmental Science: Nano, September 2023.

ARTICLE: **Bressi, V**.; Len, T.; Espro, C.; Luque, R. "*From Waste to Fuel: Metal-free Carbon Nanodots for Selective CO_2 Photoreduction into Methanol*", Journal of Materials Chemistry A, September 2023.

List of Conferences attended (chronological order)

- ***Oral communications***

"Sensors for monitoring and detection of heavy metals in the waters". **Bressi, Viviana**; Espro, Claudia; Iannazzo, Daniela; Ferlazzo, Angelo; Neri, Giovanni, XII Congresso Nazionale Associazione Italiana Chimica per l'Ingegneria (AICIng 2021), Reggio Calabria 5-8/09/2021

"Sviluppo di nuove metodologie e di sensori elettrochimici per il monitoraggio dei metalli pesanti nelle acque". **Bressi, Viviana**; Espro, Claudia; Iannazzo, Daniela; Ferlazzo, Angelo; Neri, Giovanni, Convegno della Sezione Sicilia 2021 (SCI), Catania 02/12/2021

"Zn ions detection by a schiff base/spce sensor". **Bressi, Viviana**; Ferlazzo, Angelo; Iannazzo, Daniela; Espro, Claudia; Neri, Giovanni, 21a Conferenza Nazionale Sensori e Microsistemi: AISEM 2022, Roma (virtual edition), 10-11/02/2022

"Rilevamento elettroanalitico di ioni metallici pesanti in acqua di mare mediante sensori TPYP-SPEEK/SPCE". **Bressi, Viviana**; Iannazzo, Daniela; Espro, Claudia; Neri, Giovanni. IX workshop AICIng: Chemistry for sustainable materials, Ancona 16-17/06/2022

"Electrochemical detection of Pb^{2+}, Cd^{2+} and Hg^{2+} in sea water by sPEEK/TpyP sensor". **Bressi, Viviana**; Moulaee, Kaveh; Iannazzo, Daniela; Espro, Claudia; Neri, Giovanni, 1° Congresso Nazionale della Divisione di Chimica per le Tecnologie della Società Chimica Italiana, Napoli 4-7/09/2022

"Innovative selective chemosensor based on orange peel waste-derived carbon nanodots for enhanced electrochemical detection of nitrobenzene". **Bressi, Viviana**; Chiarotto, Isabella; Ferlazzo, Angelo; Michenzi, Cinzia; Espro, Claudia, Merck Young Chemists' Symposium XXI edition, Rimini 21-23/11/2022

"Orange peel waste-derived carbon nanodots by an integrated hydrothermal and electrochemical approach towards environmental pollutants detection". **Bressi, Viviana;** Espro, Claudia; Balu Balu, Alina Mariana, XI Congreso científico de Personal Investigador en Formación (PIF) de la

Universidad de Córdoba, Córdoba (Spain) 04/05/2023. ***Award for the best oral communication.***

"Sustainable Ru-Supported Hydrochar from Biomass Waste for N-Containing Chemicals via Biomass Reductive Amination". **Bressi, Viviana**; Minio, Francesco; Balu, Alina Mariana; Vaccaro, Luigi; Espro, Claudia; Luque, Rafa; Chhabra, Tripti. Merck Young Chemists' Symposium XXII edition, Rimini 13-15/11/2023

- ***Poster communication***

"Zn ions detection by a schiff base/spce sensor". **Bressi, Viviana**; Ferlazzo, Angelo; Iannazzo, Daniela; Espro, Claudia; Neri, Giovanni, 21a Conferenza Nazionale Sensori e Microsistemi: AISEM 2022, Roma (virtual edition), 10-11/02/2022

"Innovative approach for the synthesis of carbon dots by conversion of beer bagasse via Hydrothermal Carbonization Processes". **Bressi, Viviana**; Celesti, Consuelo; Ferlazzo, Angelo; Espro, Claudia; Luque, Rafa; Neri, Giovanni, 1° Congresso Nazionale della Divisione di Chimica per le Tecnologie della Società Chimica Italiana, Napoli 04-07/09/2022

"Bottom-up hydrothermal and electrochemical synthesis of carbon dots derived from orange peel waste for the selective electrochemical detection of nitrobenzene in water solution". **Bressi, Viviana**; Chiarotto, Isabella; Ferlazzo, Angelo; Michenzi, Cinzia; Neri, Giovanni; Espro, Claudia. SciCaSi 2022 Convegno congiunto delle sezioni Calabria e Sicilia della Società Chimica Italiana, Reggio Calabria 1-2/12/2022. ***Award for the best poster.***

"Synthesis of carbon-based nanomaterials via environmentally sustainable approach for enhanced sensing applications". **Bressi, Viviana**; Espro, Claudia; Balu Balu, Alina Mariana. QUIEMA-23, I CONGRESO DE QUÍMICA APLICADA A LA ENERGÍA Y EL MEDIO AMBIEMTE, Córdoba (Spain) 12-13/06/2023

"Organosolv Treatment of Bagasse Beer for Enhanced Biomass Valorization and Microwave-Assisted Conversion of Hemicellulose to Platform Chemicals", **Bressi, Viviana***;* Espro, Claudia; Luque, Rafa. XIII Congresso Nazionale AICIng | II Congresso Nazionale della Divisione di Chimica per le Tecnologie - SCI |, Milano 25-28/06/2023

Attendance at Doctoral School (chronological order)

Advances in Functional Materials: Fundamentals, Technology and Sustainable Energy Productions. Erice (virtual edition) 6-7/07/2021

Società Chimica Italiana
Divisione di Chimica Ambiente e Beni Culturali

VI Scuola Nazionale di Monitoraggio Ambientale: i Siti Contaminati. Taranto (virtual edition), 24-26/11/2021

Scuola di Chimica Industriale 2023.

Torino, 27/05-01/06/2023

Additional Academic and Institutional Initiatives (chronological order)

Tutoring *service for disabled/learning-disabled students from the DIMED and CHIBIOFARAM departments for educational-integrative activities in support of the students at the University of Messina,* Messina, March 2021 – November 2021

Participation at the **formative lessons** offered by the Department of Engineering at the University of Messina, Messina, 2021–2023

Terza Missione, *Sea in SHELL (Sea in Science, Health, Environment, Literature, Law & economy),* Messina, September 2021

Chemistry Course ***Tutor*** *for Engineering Department students,* Messina, September 2021 and September 2023

Research period abroad as ***Ph.D. Visiting Scholar*** at the University of Córdoba (Spain), Department of Organic Chemistry (from January 2022 to July 2022 and from February 2023 to June 2023) and currently in **thesis co-supervision** between the two Universities

Participation at the "*Laboratory Waste Management*" **course** organized by the University of Córdoba on March 2022

Attendance at **seminar** organized for the Engineering students of the University of Messina (POT-ING) titled "*Valorization of Biomass into High-Value Compounds for Detection and Sustainable Applications*", Messina (virtual presentation), May 2022

Participation at the "*Laboratory Safety and Health: III Edition*" **course** organized by the University of Córdoba on July 2022

Participation in the course "*Contesti applicativi di materiali macroporosi silossanici: dalla progettazione alla verifica sperimentale*" organized by Elpida Piperopoulos, Luigi Calabrese, and Claudia Espro, Messina, September 2022

Research activity and visiting scholar at the Faculty of Science at Charles University for the use of sophisticated instrumentation (STEM) for research purposes, Prague (Czech Republic), October 2022

Participation at the **seminar** titled "*Academia Tour NPI: Tips & Tricks sobre cromatografía y espectroscopia de masas*" organized by the University of Córdoba (Spain) on March 2023

Teaching Collaborations in Laboratory Sessions for the Elective Course *"Organic Structural Determination and Pharmaceutical-chemistry"* in the 3rd Year of the Chemistry Degree Program, Córdoba (Spain), March 2023

Terza Missione, *Giochi della Chimica,* Messina, April 2023

Participation at the **seminar** titled "*La protección del conocimiento: aspectos de interés para el personal investigador*" organized by the University of Córdoba, Córdoba (Spain), May 2023

Attendance at the event "*Thinking Green: il salotto dell'economia sostenibile*" with an **oral communication** at the roundtable titled "Innovazione e sostenibilità: le chiavi per la rigenerazione dei territori e la competitività delle PMI", Taormina on July 2023